

Chairman:	Prof. Dr Marlies Van Bael
Promoter:	Prof. Dr Wouter Maes
Copromoters:	Prof. Dr Dirk Vanderzande, UHasselt Prof. Dr Jean Manca, UHasselt
Members of the jury:	Dr. Laurence Lutsen, IMO-IMOMEC Prof. Dr Peter Adriaensens, UHasselt Prof. Dr Jan C. Hummelen, University of Groningen Prof. Dr Sabine Van Doorslaer, University of Antwerp



# TABLE OF CONTENTS

## Chapter 1: General Introduction

1.1	The energy challenge .....	2
1.2	Photovoltaics .....	3
1.3	Organic photovoltaics .....	4
1.3.1	Working principle of organic solar cells .....	4
1.3.2	Morphology and device structure .....	6
1.3.3	Characterization of solar cells.....	8
1.3.4	Design rules for organic semiconductors.....	10
1.4	Aims and outline of the thesis.....	13
1.5	References .....	15

## Chapter 2: High Dielectric Constant Conjugated Materials for Organic Photovoltaics

2.1	Introduction .....	19
2.2	Strategies toward increased dielectric constants in OPV materials .....	23
2.2.1	High- $\epsilon_r$ organic donor materials .....	23
2.2.2	High- $\epsilon_r$ acceptor materials .....	34
2.2.3	(In)organic additives to increase the blend $\epsilon_r$ .....	39
2.3	Conclusions and outlook .....	44
2.4	References .....	48

Table of Contents

---

**Chapter 3: CPDTPD-Based Low Bandgap Polymers Bearing Oligo(Ethylene Glycol) Side Chains – An Effective Strategy to Enhance the Dielectric Constant of Organic Semiconductors**

3.1	Introduction .....	55
3.2	Results and discussion .....	58
3.3	Conclusions .....	70
3.4	Experimental section .....	71
3.5	References .....	80
3.6	Supporting information .....	83

**Chapter 4: A CPDTPD-Based Narrow Bandgap Conjugated Polyelectrolyte for Organic Solar Cells**

4.1	Introduction .....	101
4.2	Results and discussion .....	103
4.3	Conclusions .....	111
4.4	Experimental section .....	112
4.5	References .....	120
4.6	Supporting information .....	123

**Chapter 5: Low Bandgap Polymers Based on Bay-Annulated Indigo for Organic Photovoltaics: Enhanced Sustainability in Material Design and Solar Cell Fabrication**

5.1	Introduction .....	133
5.2	Results and discussion .....	135
5.3	Conclusions .....	145
5.4	References .....	147
5.5	Supporting information .....	151

**Chapter 6: Summary and Outlook**

6.1	Summary .....	175
6.2	Outlook.....	178
6.3	References .....	179
6.4	Nederlandstalige samenvatting .....	180

**List of Publications**

**Dankwoord**

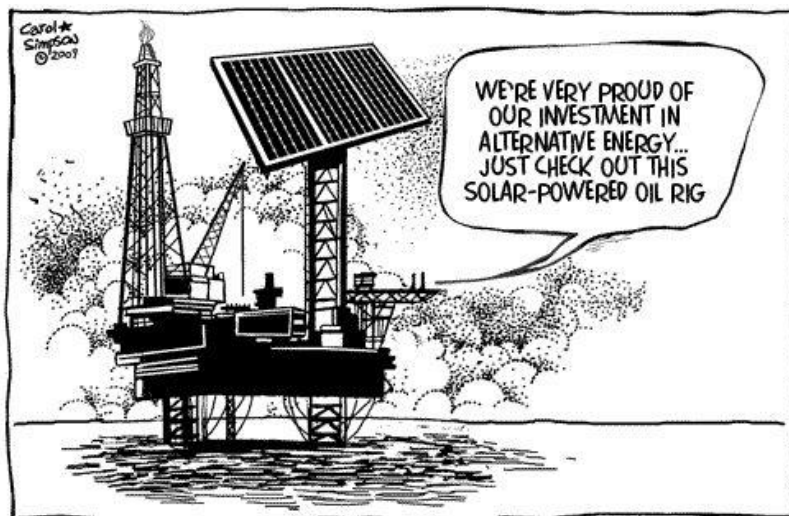


---

# Chapter 1

## General Introduction

---



## 1.1 The energy challenge

'Energy' is receiving large attention over the last decades and it is a key concern for the economy of the increasing world population. However, the most used resources nowadays have limited availability and/or are highly pollutant. Further scientific investigations and progress is necessary to tackle this challenge and to come up with new energy sources that are more sustainable and clean. Sustainability was initially triggered by the awareness that the reserves of oil, coal and natural gas are limited. It became clear that their increased use results in climate changes due to the production of hazardous greenhouse gasses (e.g. carbon dioxide). Sustainable energy production, drastically reducing the emission of hazardous gasses and, ideally, unlimitedly available, will obviously become more and more prominent. Several energy sources can meet these requirements, such as wind, geothermal energy, hydropower and solar power. Among these, solar energy production is the most appealing and promising option because of its wide availability and even distribution over the globe. The power the sun produces every year meets the energy demand of the entire world, as 17.4 TW was needed in 2015, while the sun produces on earth 120.000 TW every year.<sup>[1,2]</sup> Therefore, it can provide a permanent solution for our long-term energy demand and a further growth of the solar contribution to the renewable electricity generation can be expected (Figure 1).<sup>[3]</sup>

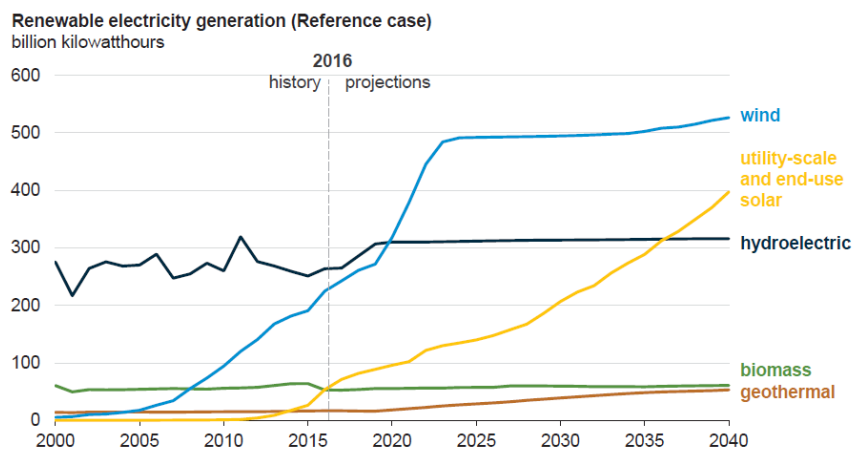


**Figure 1.** Prediction of the renewable energy generation until 2040 in the U.S.<sup>[3]</sup>

Furthermore, there is no emission of hazardous gasses when converting sunlight into electricity, making it a clean and environmentally friendly energy source. Nowadays, the standard devices for converting solar power into electricity are based on very pure silicon crystal wafers, which have the disadvantage of being expensive.<sup>[4]</sup> Furthermore, the production speed is limited since these high grade silicon crystals grow slowly over time. On the positive side, highly efficient solar cells can be made. To cope with the disadvantages of silicon solar cells, organic materials have been investigated over the last 20 years, with progresses pushing the power conversion efficiency (PCE) to record values over 13%.<sup>[5]</sup>

## 1.2 Photovoltaics

Already in the early 19<sup>th</sup> century (1839), Becquerel discovered that solar irradiation could be converted into a photocurrent by illuminating an aqueous solution containing a platina electrode covered with silver bromide/chloride.<sup>[6]</sup> Despite this early discovery, it took 44 years before the first working solar cell was fabricated by Charles Fritts, making use of selenium coated with a thin layer of gold.<sup>[7]</sup> The first solar cell device based on crystalline silicon was developed in 1954 by Chapin *et al.*, using a *p-n* junction for converting sun power into free charge carriers with a PCE of 6%.<sup>[8]</sup> Currently, crystalline silicon is still the most frequently used material in solar panels, occupying 90% of the total production.<sup>[9]</sup> The main reason for this is the high PCE, up to 26.3%.<sup>[10]</sup> Although highly efficient solar cells can be made, high-grade crystalline silicon has one major drawback: the amount of high-quality solar grade silicon needed is quite high, as silicon is a weak absorber, and 200-300  $\mu\text{m}$  thick wafers are necessary for efficient light absorption.<sup>[4]</sup> Furthermore, the production of crystalline silicon, mainly done via the Czochralski process, limits the production speed and gives rise to high production costs. Therefore, a second generation of photovoltaics has been developed, focusing on thin film technologies to reduce the production cost. Amorphous silicon (a-Si), copper indium gallium diselenide (CIGS) or cadmium telluride (CdTe) thin film solar cells were produced, but the scarcity (indium, selenium, tellurium) and toxicity (cadmium) of the required elements restricts the large-scale production and commercialization.<sup>[10]</sup> A third group that can provide an alternative to the silicon based solar cells are the organic solar cells (OSC's), dye-sensitized solar cells (DSSC's) and hybrid organic/inorganic solar cells. They

all have in common that they make use of organic semiconductors to convert solar photons. As for Si-based solar cells, the photoactive organic material needs to be semi-conductive, which implies that the structures typically consist of alternating double and single carbon bonds.<sup>[11]</sup> This causes an overlap of the  $p_z$  orbitals on adjacent carbon/hetero atoms, delocalizing the valence electrons over the entire molecule. The research into organic semiconductors drastically increased upon the discovery of Heeger, MacDiarmid and Shirakawa that via doping of polyacetylene with iodine, an increase of the conductivity by seven orders of magnitude can be achieved.<sup>[12]</sup> The Nobel Prize in chemistry was awarded in 2000 for this invention.<sup>[13]</sup> The applications of semiconducting polymers and small molecules are not limited to the field of solar cells, as they can also be used for organic field-effect transistors (OFET's),<sup>[14]</sup> light-emitting diodes (OLED's),<sup>[15]</sup> photodetectors (OPD's),<sup>[16]</sup> etc.

The main advantage of organic materials is their solution-processability, which allows low-cost large-area thin film fabrication by e.g. roll-to-roll printing.<sup>[17]</sup> This thin film OSC technology can be fabricated on flexible substrates, opening a broad and pristine market (e.g. portable applications).<sup>[18]</sup> Furthermore, because of the high extinction coefficients of organic materials, only very thin active layers (100 to 200 nm) are required for sufficient light absorption. The combination of a very thin photoactive layer and the printing ability lowers the production costs when compared to crystalline silicon. The recent developments and appealing features make organic photovoltaics (OPV's) a viable alternative technology to the present inorganic solar cells. However, before competitive market entrance can be realized, the efficiency and stability should be further enhanced.<sup>[5,10,19]</sup>

### **1.3 Organic photovoltaics**

#### **1.3.1 Working principle of organic solar cells**

Organic and inorganic materials show a different behavior when converting solar irradiation into electricity. Inorganic materials have higher dielectric constants. Upon illumination, photons with an energy equal or higher than the bandgap will give rise to weakly bound electron-hole pairs, which can easily be separated by thermal energy (kT) into free charge carriers. On the other hand, absorption of

incident photons in organic semiconductors results in the formation of a tightly bound charge pair, called exciton (electron-hole pair). These excitons have larger Coulombic interactions, resulting in a binding energy which is typically around 0.3 eV, and hence they cannot be separated via thermal energy (0.025 eV).<sup>[20]</sup> To provide the required driving force, a different organic material with stronger electron affinity (i.e. electron acceptor) in close vicinity is needed to split the exciton into free charge carriers. This is in contrast to what happens in traditional Si-based solar cells and why the working principle of OSC's is rather different and more complex, as illustrated in Figure 2.

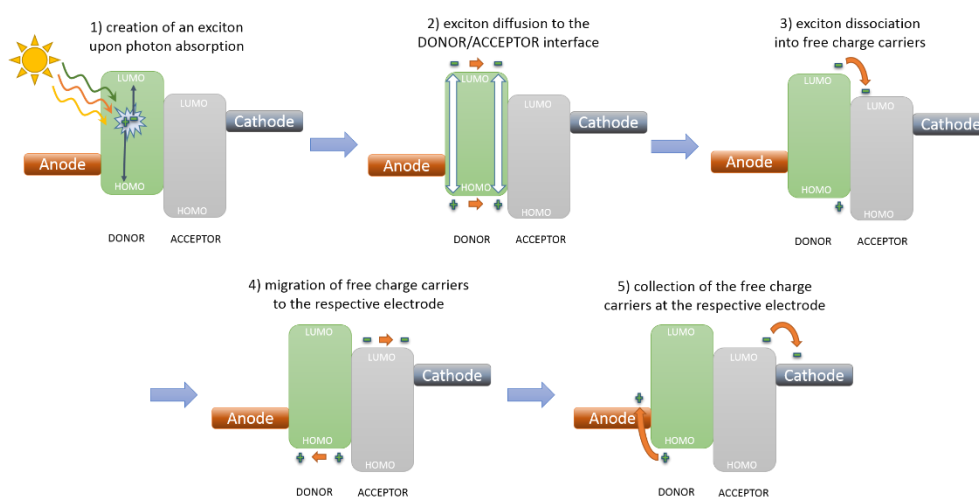


**Figure 2.** Band diagram illustrating the working principle of an organic solar cell.

Upon light absorption, an electron in the photoactive material is excited from the highest occupied molecular orbital (HOMO) to the lowest unoccupied molecular orbital (LUMO), resulting in the formation of an exciton (**1**). The excess of energy a photon has when exceeding the bandgap is rapidly thermalized. The formation of an exciton is a localized process, since its diffusion length is limited to about 10 nm, with a lifetime of 1 ns.<sup>[21]</sup> To overcome the Coulombic interactions, a second semiconducting material (acceptor) in the proximity is required, with a different electron affinity and ionization potential to trigger the dissociation. Hence, the LUMO of the acceptor material needs to be sufficiently lower ( $\sim 0.3$  eV) than that

of the donor to create a driving force for charge separation. When the exciton has diffused near the interface (**2**), the electron is transferred to the LUMO of the acceptor (**3**) and subsequently the charges are spatially separated (**4**). The spatial separation further reduces the attraction between the opposite charges ( $\sim 1/r^2$ ). Finally, collection of free charges at the different electrodes occurs due to the difference in work function (**5**).

The steps needed to convert sunlight into electricity in organic solar cells can hence be summarized as follows: **1**) creation of an exciton upon absorption of light, **2**) exciton diffusion to the donor-acceptor interface, **3**) exciton dissociation and generation of free charge carriers via CT states, **4**) migration of the charge carriers to the respective electrodes, and **5**) collection of the free charges at the respective electrodes. Despite the good understanding in how these processes occur, they are still prone to losses. Optimization of each step is necessary to get an optimal efficiency, as will be discussed in the following paragraphs.

### **1.3.2 Morphology and device structure**

The device structure and morphology of the active layer of organic solar cells have strongly evolved over the years. In 1959, Kallmann and Pope reported the first organic solar cell made of a single crystal of anthracene.<sup>[22]</sup> The low efficiency of  $2 \cdot 10^{-6}\%$  can be assigned to the primitive structure of the active layer based on a homojunction, i.e. a single organic material, which is not beneficial for the charge separation. The limited performance of single junction OSC's is related to the rather high exciton binding energy of organic semiconducting materials.<sup>[23]</sup> It was a real breakthrough when Tang published the new concept of a donor-acceptor heterojunction (based on a bilayer) in 1986 (Figure 3).<sup>[24]</sup> These organic solar cells were based on an organic double layer using complementary electron donor and acceptor organic molecules, sandwiched between two metal electrodes with different work functions. The photoactive layer consisted out of two different organic layers, with specific electron and hole transporting properties, evaporated on top of each other, and gave a rather moderate PCE of 1%.<sup>[6,25]</sup>

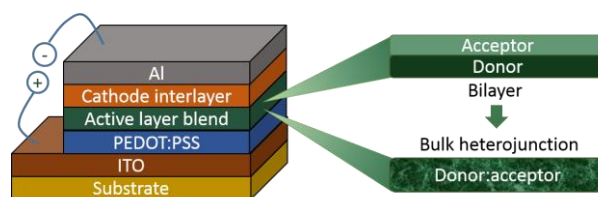


**Figure 3.** Typical device stack of an organic solar cell.

The drawback of such an architecture is the small interfacial area where the formation of free charge carriers can take place, due to the limited diffusion length of excitons ( $\sim 10$  nm) in organic semiconductors.<sup>[21]</sup> This implies that the number of excitons reaching the interface is restricted, with high losses of the photogenerated photons due to recombination. To solve these shortcomings of the bilayer structure, the concept of a bulk heterojunction (BHJ) was introduced by Yokoyama in 1991.<sup>[26]</sup> Co-evaporation of two dyes offers a strongly increased donor-acceptor interface area to improve exciton dissociation and charge transport. The groups of Heeger and Holmes successfully applied this concept in polymer solar cells in 1995.<sup>[27,28]</sup> A bulk heterojunction, as illustrated in Figure 3, typically consists of an electron donating material (a p-type semiconductor) and an electron accepting material (a n-type semiconductor) with an increased donor-acceptor surface area. This results in a high probability for the excitons to dissociate across the entire photoactive layer because of the large interface area in the intimately mixed phases. In addition, it should also offer an efficient charge transport pathway, a so-called bicontinuous pathway, to the electrodes, which facilitates the collection of charges formed in the BHJ.<sup>[29]</sup> The polymer-fullerene bulk heterojunction is still the most frequently used OSC architecture.

Obtaining a very specific nanostructured photoactive layer morphology is, however, a complex process, which is far from trivial to achieve and to reproduce.<sup>[30]</sup> The solvent (and possible co-solvent) used to deposit the photoactive layer has a major influence on the final BHJ film morphology. Traditionally, solvent optimization is done in a trial and error fashion. A wide range of organic solvents (e.g. chloroform, (*ortho*-di)chlorobenzene, 1,1,2,2-tetrachloroethane) and co-solvents (e.g. 1,8-diiodooctane, 1-chloronaphthalene) have been used to optimize the active layer morphology. With the aid of co-

solvents, favorable morphologies can be pursued as their higher boiling points allow to optimize the crystallization time given to a certain material.<sup>[31]</sup>

The device structure, on its turn, has been intensively investigated and adapted over the last decades. The most frequently used device stack typically consists of 5 different layers on top of each other (Figure 3). Indium tin oxide (ITO) with a thickness of around 100 nm serves as a transparent hole-collecting electrode and is mostly patterned on a glass substrate. On top of it, a layer of poly(3,4-ethylenedioxythiophene):poly(styrenesulfonate) (PEDOT:PSS) is spincoated, which enhances the hole transport to the ITO electrode because of its higher work function and smoothens the rough ITO bottom contact before depositing the photoactive layer blend. The photoactive layer, consisting of a blend of a donor and acceptor, is deposited on top with a thickness varying from 50 to 200 nm, depending on the nature of the organic dye used. The back contact consists of a thin cathode interlayer or calcium (30 nm) and aluminum (80-100 nm), serving as a low work function collecting electrode.<sup>[32]</sup> Insertion of an additional charge transporting layer (instead of Ca) has been suggested as an effective strategy to further optimize the device performance by diminishing unfavorable factors such as bad interface tuning, charge recombination, etc. Conjugated polyelectrolytes (CPE's) are typically used as electron transporting layer and serve as a simple and powerful tool to enhance the OPV parameters. Aluminum, on the other hand, serves as a back reflector for the light that is not absorbed upon the first pass, hence increasing the photon absorption and exciton generation in the active layer blend. Besides this 'regular' device architecture, a so-called 'inverted' structure is also used because of its better resistivity to ambient conditions, which is governed by the higher work function of the top metal electrode that can be used.<sup>[33]</sup>

### 1.3.3 Characterization of solar cells

The performance of a solar cell is characterized via a current density-voltage ( $J$ - $V$ ) plot, measured in dark and under illumination, resulting in different output parameters. The solar cell set-up typically uses a standard illumination of AM1.5G (air mass 1.5 global) with an intensity of  $1000 \text{ W/m}^2$ , which corresponds to the average light of the solar spectrum that strikes the earth when the sun is at an  $48.2^\circ$  angle with the zenith (see Figure 4).

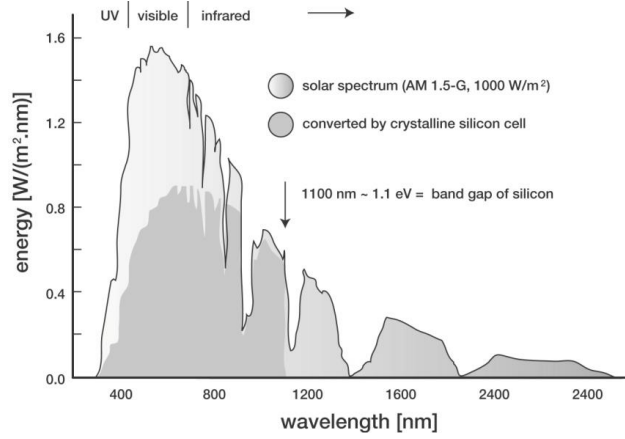


**Figure 4.** Solar spectrum (AM1.5G).<sup>[34]</sup>

The dark measurement shows the diode behavior of the corresponding diode generated by the cell. Ideally, a very low leakage current is observed in reverse bias and a high current density in forward bias, indicating that the active layer does not suffer from imperfections. Under illumination, an additional photocurrent is created and three parameters are determined in this state: the short-circuit current density ( $J_{sc}$ ,  $V = 0$ ), the open-circuit voltage ( $V_{oc}$ ,  $J = 0$ ) and the fill factor (FF) (Figure 5). The point on the  $J$ - $V$  curve where the product of  $J$  and  $V$  maximizes, determines the maximum power point (MPP). The fill factor is defined as the ratio of the maximum power density ( $P_{MPP}$ ) to the product of the open-circuit voltage and short-circuit current density. The  $P_{MPP}$ , on its turn, is related to the product of  $J_{MPP}$  and  $V_{MPP}$ , which results in the following equation (1):<sup>[35]</sup>

$$FF = \frac{P_{MPP}}{J_{sc} \cdot V_{oc}} = \frac{J_{MPP} \cdot V_{MPP}}{J_{sc} \cdot V_{oc}} \quad (1)$$

The FF gives an indication on the performance of the solar cell under illumination. The number should be as close as possible to unity. Due to several loss mechanisms in the device affecting the extraction and generation of charge carriers, the fill factor will drop and hence the efficiency will lower as well. The power conversion efficiency ( $\eta$ ) is then defined as the ratio of  $P_{MPP}$  and the power density of the incoming light ( $P_{in}$ ) (equation 2):<sup>[36]</sup>

$$\eta = \frac{P_{MPP}}{P_{in}} = \frac{J_{sc} \cdot V_{oc} \cdot FF}{P_{in}} \quad (2)$$

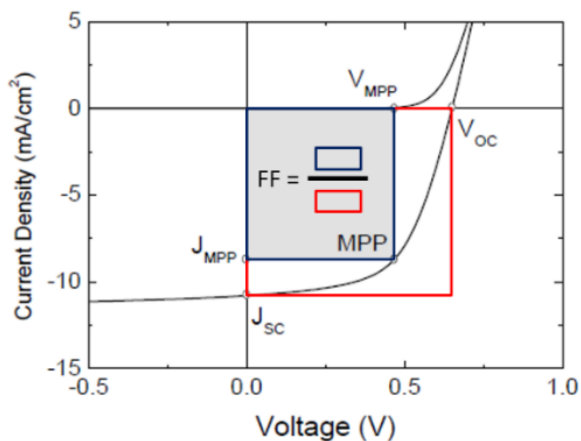


**Figure 5.** Typical  $J$ - $V$  characteristics of a solar cell.

Experimentally, it is challenging to accurately simulate the AM1.5G spectrum because a white light source with filters is used that can suffer from deviations over time. This has a major impact on the short-circuit current and hence can increase or decrease the effective efficiency of the organic solar cell. The spectrally resolved external quantum efficiency (EQE) measures  $J_{sc}$  more accurately. The EQE is defined as the fraction of incident photons that is converted to electrons at a certain wavelength ( $\lambda$ ) in the external circuit at short-circuit conditions.<sup>[29]</sup> This corrected  $J_{sc}$ , together with the other parameters measured, gives a more accurate value for the power conversion efficiency.

#### 1.3.4 Design rules for organic semiconductors

A crucial factor in achieving optimal OSC efficiencies is the design of the energy level alignment on a molecular level, resulting in an efficient conversion of sunlight into electricity without too much energy losses. Current high-performing devices typically consist of an electron donating low bandgap polymer and an electron accepting fullerene derivative ([60]PCBM or [70]PCBM).<sup>[37]</sup> On the other hand, recent advances in organic small molecule derivatives, creating small bandgap materials (donor and acceptor compounds) as in a similar fashion as conjugated polymers, have demonstrated similar device performances (Figure 6).<sup>[5]</sup>

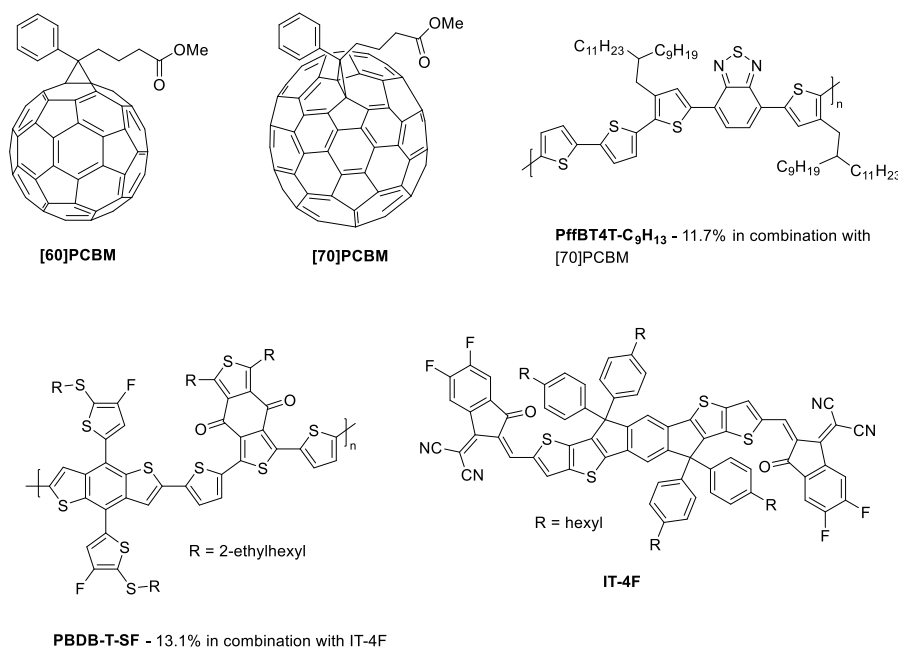


**Figure 6.** Molecular structures of polymers and small molecules used in highly efficient organic solar cells.

All these high-performing materials are fine-tuned on the molecular level in terms of getting the HOMO and LUMO levels right and having appropriate solubility and miscibility to achieve an ideal nanostructured active layer morphology. Furthermore, the active materials need to harvest as much light as possible through an optimal overlap with the solar spectrum. In order to absorb both high and low energy photons, the bandgap ( $E_g$ ) (of the donor material) need to be designed to match the maximum theoretical efficiency of a solar cell (Shockley-Queisser limit). Investigation into new narrow-bandgap materials has attracted a lot of interest. Light absorption from the UV-vis till the near-infrared can be realized when having bandgaps as low as the ideal 1.4-1.5 eV (Shockley-Queisser limit).<sup>[38,39]</sup>

Tuning the bandgap is mostly done by combining an electron rich and an electron poor moiety in an alternating fashion in a polymer backbone, which results in a bandgap smaller than the individual bandgaps of the building blocks. The donor component is electron rich and will therefore mainly determine the energetic

position of the HOMO, while the electron poor moiety (acceptor<sup>†</sup>) will determine the energetic position of the LUMO, as illustrated in Figure 7.<sup>[40]</sup>

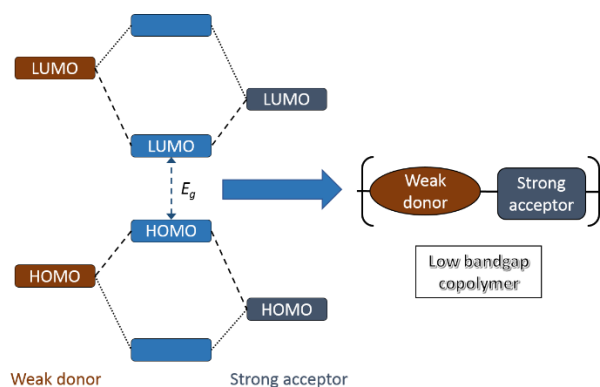


**Figure 7.** Lowering  $E_g$  by the use of an alternating donor-acceptor structure.<sup>[41]</sup>

Modifying the energy levels can additionally be realized on a molecular level via modifications to the molecular structure. Reducing the bandgap and hence absorbing a broader spectrum can be done by raising the HOMO or lowering the LUMO level of the donor polymer. However, this either affects the  $V_{oc}$  or  $J_{sc}$  and an optimum hence must be found (Figure 8). The introduction of electron withdrawing substituents will decrease the LUMO level, but the difference between the LUMO of the electron donor material and the electron acceptor ( $\Delta E_{LL}$ ) will also be reduced, which can be detrimental for the electron transfer and exciton dissociation. On the other hand, introducing stronger donor moieties will increase the HOMO level, also resulting in a lower bandgap. However, since the  $V_{oc}$  is proportional to the difference of the HOMO of the electron donor and the LUMO of the electron acceptor ( $\Delta E_{HL}$ ), it will drop and hence the efficiency of the OPV device decreases. Therefore, a balance should be found between efficient light harvesting and a high  $V_{oc}$ .

<sup>†</sup> This should not be confused with the earlier mentioned (fullerene) electron acceptor in the active layer blend.

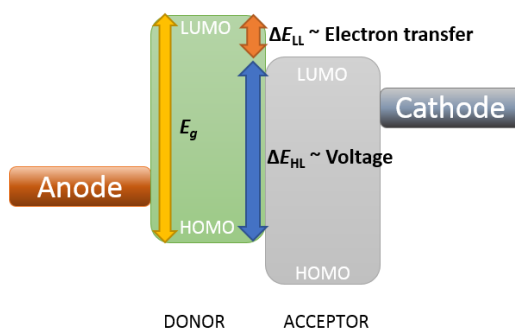


**Figure 8.** Finding an optimum between the bandgap and the HOMO/LUMO energy levels.

## 1.4 Aims and outline of the thesis

OPV is often claimed to be a truly environmentally friendly energy producing technology. The possibility to create OPV devices via roll-to-roll printing and coating technologies is one of the main benefits of this class of solar cells, allowing to rapidly produce large areas on a small timescale. However, to deposit many of the current high-performance materials, harsh processing conditions (e.g. halogenated processing (co)solvents) are needed to obtain a perfect (nano)morphology of the active layer blend. The use of such toxic solvents restrains the upscaling and hence commercialization of OPV's. Very strict (and expensive) safety precautions must be taken when working with these chlorinated solvents on an industrial scale. To cope with these issues, new low bandgap copolymers can be designed with more polar groups to enhance their solubility in more environmentally friendly solvents (e.g. alcohols, ethers, ...). Furthermore, an increased polarity of the active layer materials will also increase the dielectric properties of the blends. This can facilitate charge generation because of the lower exciton binding energies. Therefore, one of the main goals of this thesis is to synthesize novel low bandgap copolymers exhibiting enhanced polarizabilities and dielectric properties. Furthermore, sustainability improvements in the material synthesis and device production steps are pursued as well. The thesis contains 3 experimental chapters addressing these issues. These chapters are written in paper format.

**Chapter 2** provides an overview on the high dielectric constant materials used in OPV devices over the last decade. All data from literature are discussed, pointing out the different strategies used toward increased dielectric properties in OPV materials. Organic donor and acceptor materials and dopants are addressed, all used to enhance the permittivity of the active layer blend. As such, a literature background is provided toward the first experimental chapter.

**Chapter 3** discusses the synthesis of four novel alternating donor-acceptor copolymers based on an electron rich 4*H*-cyclopenta[2,1-*b*:3,4-*b'*]dithiophene (CPDT) and an electron deficient 4*H*-thieno[3,4-*c*]pyrrole-4,6(5*H*)-dione (TPD) subunit, with the aim to increase the dielectric constant of the materials using oligo(ethylene glycol) side chains. The number of glycol substituents on the polymer backbone is gradually raised to systematically investigate the influence on the dielectric properties and solar cell parameters. Impedance measurements reveal a doubling of the dielectric constant (up to  $\epsilon_r = 6.3$ ) with respect to the reference polymer. Furthermore, a non-halogenated processing solvent (anisole) is applied for the active layer deposition.

In **Chapter 4** a different application of polar low bandgap copolymers is targeted, also based on CPDT and TPD alternating units. An ionic moiety (methylimidazole) is introduced on the side chains to obtain a narrow bandgap conjugated polyelectrolyte, which is then used as a cathode interlayer to replace calcium in the solar cell device stack. A significant enhancement of the PCE (from 6.95% to 7.83%) was observed for the PBDTTPD:[70]PCBM system.

**Chapter 5** describes additional efforts to enhance the sustainability of OPV's. The photoactive polymers all contain an electron deficient building block inspired on the natural indigo dye, i.e. bay-annulated indigo (BAI), combined with electron rich thiophene and 4*H*-dithieno[3,2-*b*:2',3'-*d*]pyrrole units. Best solar cell efficiencies are obtained for polymer:fullerene blends spincoated from a pristine non-halogenated solvent (*o*-xylene). Additionally, MALDI-TOF mass spectrometry provides detailed information on the structural composition of the polymers.

To end (**Chapter 6**), a general summary of the thesis is presented and an outlook is formulated.

## 1.5 References

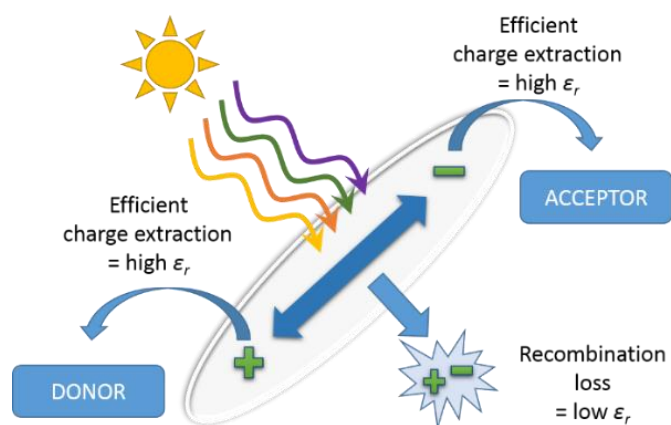
- [1] Basic Research Needs for Solar Energy Utilization, BES Workshop on Solar Energy Utilization, April 18–25, 2005.
- [2] <https://www.linkedin.com/pulse/global-energy-consumption-numbers-now-future-brian-seger>
- [3] [https://www.eia.gov/outlooks/aeo/pdf/0383\(2017\).pdf](https://www.eia.gov/outlooks/aeo/pdf/0383(2017).pdf)
- [4] Woditsch, P.; Koch, W. *Sol. Energy Mater. Sol. Cells* **2012**, *72*, 11.
- [5] Zhao, W.; Li, S.; Yao, H.; Zhang, S.; Zhang, Y.; Yang, B.; Hou, J. *J. Am. Chem. Soc.* **2017**, *139* (21), 7148.
- [6] Spanggaard, H.; Krebs, F. C. *Sol. Energy Mater. Sol. Cells* **2004**, *83*, 125.
- [7] Green, M. A. *Physica E* **2002**, *14*, 11.
- [8] Chapin, D. M.; Fuller, C. S.; Pearson, G. L. *J. Appl. Phys.* **1954**, *25*, 676.
- [9] Wen, C.; Fu, C.; Tang, J.; Liu, D.; Hu, S.; Xing, Z. *Sci. China Phys. Mech. Astron.* **2012**, *55*, 235.
- [10] Green, M. A.; Emery, K.; Hishikawa, Y.; Warta, W.; Dunlop, E. D.; Levi, D. H.; Ho-Baillie, A. W. Y. *Prog. Photovolt.: Res. Appl.* **2017**, *25*, 3.
- [11] Nalwa, H. S. *Handbook of Organic Conductive Molecules and Polymers: Conductive polymers: transport, photophysics, and applications* (Wiley, 1997).
- [12] MacDiarmid, A. G. *Angew. Chem. Int. Ed.* **2001**, *40*, 2581.
- [13] [https://www.nobelprize.org/nobel\\_prizes/chemistry/laureates/2000/](https://www.nobelprize.org/nobel_prizes/chemistry/laureates/2000/)
- [14] Sax, S.; Rugen-Penkalla, N.; Neuhold, A.; Schuh, S.; Zojer, E.; List, E. J. W.; Müllen, K. *Adv. Mater.* **2010**, *22*, 2087.
- [15] Kanimozhi, C.; Yaacobi-Gross, N.; Chou, K. W.; Amassian, A.; Anthopoulos, T. D.; Patil, S. J. *J. Am. Chem. Soc.* **2012**, *134*, 16532.
- [16] Jansen-van Vuuren, R. D.; Armin, A.; Pandey, A. K.; Burn, P. L.; Meredith, P. *Adv. Mater.* **2016**, *28*, 4766.
- [17] Bernier, P.; Bidan, G.; Lefrant, S. *Advances in Synthetic Metals: Twenty years of progress in science and technology* (Elsevier, 1999).
- [18] Krebs, F. C. *Sol. Energy Mater. Sol. Cells* **2009**, *93*, 394.
- [19] Jorgensen, M.; Norrman, K.; Gevorgyan, S. A.; Tromholt, T.; Andreasen, B.; Krebs, F. C. *Adv. Mater.* **2012**, *24*, 580.
- [20] Morgan, S. O.; Yager, W. A. *Ind. Eng. Chem.* **1940**, *32* (11), 1519.

- [21] Haugeneder, A.; Neges, M.; Kallinger, C.; Spirkl, W.; Lemmer, U.; Feldmann, J.; Scherf, U.; Harth, E.; Gügel, A.; Müllen, K. *Phys. Rev. B* **1999**, *59*, 15346.
- [22] Kallmann, H.; Pope, M. J. *Chem. Phys.* **1959**, *30*, 585.
- [23] Knupfer, M. *Appl. Phys. A* **2003**, *77* (5), 623.
- [24] Tang, C. W. *Appl. Phys. Lett.* **1986**, *48*, 183.
- [25] Hoppe, H.; Sariciftci, N. S. *J. Mater. Res.* **2004**, *19* (7), 1924.
- [26] Hiramoto, M.; Fujiwara, H.; Yokoyama, M. *Appl. Phys. Lett.* **1991**, *58*, 1062.
- [27] Yu, G.; Gao, J.; Hummelen, J. C.; Wudl, F.; Heeger, A. J. *Science* **1995**, *270*, 1789.
- [28] Halls, J. J. M.; Walsh, C. A.; Greenham, N. C.; Marseglia, E. A.; Friend, R. H.; Moratti, S. C.; Holmes, A. B. *Nature* **1995**, *376*, 498.
- [29] Benanti, T. L.; Venkataraman, D. *Photosynth. Res.* **2006**, *87* (1), 73.
- [30] Park, S. H.; Roy, A.; Beaupré, S.; Cho, S.; Coates, N.; Moon, J. S.; Moses, D.; Leclerc, M.; Lee, K.; Heeger, A. J. *Nat. Photon.* **2009**, *3*, 297.
- [31] Van Franeker, J. J.; Turbiez, M.; Li, W.; Wienk, M. M.; Janssen, R. A. J. *Nat. Commun.* **2015**, *6*, 6229.
- [32] Winder, C.; Sariciftci, N. S. *J. Mater. Chem.* **2004**, *14*, 1077.
- [33] Lloyd, M. T.; Peters, C. H.; Garcia, A.; Kauvar, I. V.; Berry, J. J.; Reese, M. O.; McGehee, M. D.; Ginley, D. S.; Olson, D. C. *Sol. Energy Mater. Sol. Cells* **2011**, *95*, 1382.
- [34] <http://www.vicphysics.org/documents/events/stav2005/spectrum.JPG>
- [35] Brabec, C. J.; Sariciftci, N. S.; Hummelen, J. C. *Adv. Funct. Mater.* **2001**, *11*, 15.
- [36] Servaites, J. D.; Ratner, M. A.; Marks, T. J. *Appl. Phys. Lett.* **2009**, *95*, 163302.
- [37] Zhao, J.; Li, Y.; Yang, G.; Jiang, K.; Lin, H.; Ade, H.; Ma, W.; Yan, H. *Nat. Energy* **2016**, *1*, 15027.
- [38] Thompson, B. C.; Fréchet, J. M. J. *Angew. Chem. Int. Ed.* **2008**, *47*, 58.
- [39] Scharber, M. C.; Mühlbacher, D.; Koppe, M.; Denk, P.; Waldauf, C.; Heeger, A. J.; Brabec, C. J. *Adv. Mater.* **2006**, *18* (6), 789.
- [40] Yuen, J. D.; Wudl, F. *Energy Environ. Sci.* **2013**, *6*, 392.
- [41] Zhou, H.; Yang, L.; You, W. *Macromolecules* **2012**, *45*, 607.

# Chapter 2

## High Dielectric Constant Conjugated Materials for Organic Photovoltaics

---



Brebels, J.; Manca, J.; Lutsen, L.; Vanderzande, D.; Maes, W. High Dielectric Constant Conjugated Materials for Organic Photovoltaics. *J. Mater. Chem. A* **2017**, DOI: 10.1039/C7TA06808E.

## Abstract

Organic photovoltaics (OPV) offer a low-cost and esthetically appealing thin-film alternative to the well-known silicon-based solar panels, opening up new applications and markets. A substantial increase in power conversion efficiency (to over 12%) has been achieved for these organic solar cells over the last decade, largely as a result of intensive research on novel electron donor and acceptor materials, combined in a bulk heterojunction device structure. Nevertheless, it is clear that further progress is required to be competitive with more efficient traditional and other emerging thin-film PV technologies. At this moment, the device performance is (among others) limited by the low dielectric constants ( $\epsilon_r = \sim 3-4$ ) of the state of the art photoactive organic materials. Important loss processes inherently connected to the strong Coulombic interactions within low-permittivity organic materials can be suppressed through the enhancement of  $\epsilon_r$ . High dielectric constant materials show lower exciton binding energies and hence bimolecular recombination can be reduced, improving the charge carrier extraction efficiency. Despite these promising prospects, limited research has been devoted to the development and OPV integration of high-dielectric organic semiconductors. In this chapter, an overview is provided of the approaches applied so far to enhance  $\epsilon_r$  of organic compounds specifically developed for OPV purposes, commenting on the insights obtained and the challenges remaining.

## 2.1 Introduction

Organic photovoltaics (OPV) have gained a lot of attention over the past 20 years as a result of their superior characteristics to produce light-weight, fully flexible and esthetically pleasing (colored) devices at reduced manufacturing costs.<sup>[1-4]</sup> Their thin-film character, ease of production by printing techniques and the employment of abundant, non-toxic organic photoactive materials render organic solar cells an attractive low-cost, complementary PV technology, enabling to target new markets such as building or automotive integration and numerous indoor and outdoor applications.<sup>[5-8]</sup> Over the years, OPV research has mainly focused on the quest for suitable electron donor and acceptor molecules, either of polymer or small molecule nature, which has resulted in organic solar cells with power conversion efficiencies (PCE's) exceeding 12%.<sup>[9-12]</sup> A major limitation of organic semiconductors is their restricted exciton (*i.e.* hole-electron pair) lifetime of  $\sim 1$  ns and exciton diffusion length of  $\sim 10$  nm.<sup>[13]</sup> The photo-generated holes and electrons experience a strong Coulombic interaction due to the low relative permittivity values in organic semiconductors ( $\epsilon_r = \sim 3-4$ ), which lead to significant recombination losses.<sup>[14]</sup> The limited exciton dissociation rate particularly restrains the photocurrent generation and fill factor (FF) of organic solar cells. To overcome these strong Coulombic interactions, a second semiconducting material in close proximity is required, with a different electron affinity or ionization potential to trigger the exciton dissociation, *i.e.* electron transfer from an electron donor material to an electron acceptor and hole transfer in the opposite direction. In 1991, Hiramoto *et al.* introduced the bulk heterojunction (BHJ) concept.<sup>[15]</sup> Co-evaporation of two dyes offered a strongly increased interfacial area to improve exciton dissociation and charge transport as compared to the bilayer concept used before. The groups of Heeger and Friend successfully applied this concept in polymer solar cells in 1995 (Figure 1).<sup>[16,17]</sup> However, a very specific nanostructured photoactive layer morphology is required to overcome the limited exciton diffusion length, which is far from trivial to achieve and to reproduce.<sup>[18]</sup> The solvent (and possible co-solvent) used to deposit the photoactive layer has a major influence on the final BHJ film morphology, traditionally in a trial and error fashion. A wide range of organic solvents (e.g. chloroform, (*ortho*-di)chlorobenzene, 1,1,2,2-tetrachloroethane) and co-solvents

(e.g. 1,8-diodooctane, 1-chloronaphthalene) have been used to optimize the active layer morphology. With the aid of co-solvents, favorable morphologies can be pursued as their higher boiling point allows to optimize the crystallization time given to a certain material.<sup>[19]</sup>

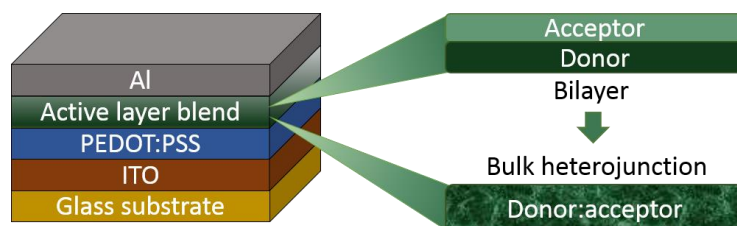


**Figure 1.** Illustration of a standard organic solar cell stack with either a bilayer or a bulk heterojunction donor:acceptor photoactive layer.

A major advantage of OPV over competing technologies is the fact that the molecular structures of the photoactive organic materials can be readily fine-tuned to achieve optimally balanced energy levels. Moreover, an appropriate solubility and miscibility can be targeted by dedicated structural variations to achieve a near-ideal, 'intimately mixed' nanostructured BHJ active layer. In 2006, Brabec and co-workers defined a set of design rules for electron donor molecules in BHJ organic solar cells (in combination with fullerene acceptors).<sup>[20]</sup> It was speculated that, if the desired material properties could be achieved, this would allow to reach the (at that time very ambitious) 10% efficiency limit. These molecular design rules have steadily been refined over the years, but essentially the same guidelines were always used as a basis for material development.<sup>[21,22]</sup> In 2012, Koster *et al.* outlined three different pathways to a novel efficiency regime for organic solar cells, with PCE's in excess of 20%:<sup>[23]</sup> i) a radiation limit was presented that clarifies the role of charge transfer (CT) absorption (which should be sufficiently weak), ii) a model based on exciton generation in both the electron donor and acceptor material was used to demonstrate how reduction of the reorganization energies can result in a significant improvement in PCE, and iii) the dielectric constant ( $\epsilon_r$ ) was put forward as a crucial parameter for high-efficiency organic solar cells, reducing relaxation and recombination processes. In 2009, Kirchartz *et al.* presented that among all loss mechanisms occurring in OPV, singlet exciton recombination accounts for almost 12% and charge transfer

exciton recombination causes an efficiency loss of more than 32%, both because of the rather low relative permittivity values of organic semiconductors.<sup>[24]</sup> Inorganic semiconductors typically have dielectric constants in the range of 10–15, which is considerably higher than their organic counterparts (~3–4). Organic materials therefore have much higher binding energies (0.3–1.0 eV), as the exciton binding energy ( $E_b$ ) is directly related to the intrinsic dielectric properties via

$$E_b = \frac{e^2}{4\pi\epsilon_r\epsilon_0 r} \quad (1)$$

where  $e$  is the elementary charge,  $\epsilon_0$  is the permittivity of vacuum,  $\epsilon_r$  is the relative permittivity of the material, and  $r$  is the distance between the electron and hole.<sup>[25]</sup> When dielectric constants in the same range as silicon (~11) could be achieved for organic materials, thicker active layers could be used, harvesting more of the incoming light and beneficial for roll-to-roll processing, and even single junction devices could be prepared, overruling all morphological issues BHJ organic solar cells are facing to date.<sup>[23,26,27]</sup> A recent study on the combined influence of charge mobility and the dielectric constant for instance showed that higher efficiencies could be achieved with lower optimum mobilities of the charge carriers when a suitable active layer blend with a high  $\epsilon_r$  of around 8 could be designed.<sup>[28]</sup>

The dielectric constant (i.e. static relative permittivity) is defined as the ratio of the relative permittivity of the material divided by the permittivity of free space. In practical terms, it represents the capacity of a material to store electrical energy under an applied electric field relative to vacuum, in which a part of the electrical energy is used to polarize the organic material. In this respect, the dielectric constant is directly correlated to the polarizability and the ability of organic compounds to polarize in the presence of an applied electric field. Consequently, synthetic approaches to increase  $\epsilon_r$  are mainly focusing on local changes on the conjugated backbone and/or periphery via the introduction of polar or polarizable substituents.<sup>[28-30]</sup> A beneficial side effect of this strategy is the fact that the resulting materials become more hydrophilic, which helps to reduce the environmental impact of the OPV production process.<sup>[31-33]</sup> At present, the active layer of the top-efficiency BHJ organic solar cells, combining a low bandgap electron donor (polymer or small molecule) and a fullerene (or alternative)

acceptor in the photoactive layer blend, is most often deposited from solutions of high-boiling chlorinated solvents such as (di)chlorobenzene.<sup>[12,34]</sup> To reduce the ecological footprint, processing from less harmful solvents (e.g. alcohols and ultimately water) is highly desirable.<sup>[11,35,36]</sup> High-permittivity hydrophilic organic materials hence have great potential for OPV applications.

Different techniques can be used to measure the dielectric constants of organic compounds, but impedance spectroscopy (IS) and charge extraction by linearly increasing voltage (CELIV) are the most commonly used methods. One of the most convenient approaches is to use a standard OPV device architecture (ITO/PEDOT:PSS/organic material/Al) to measure the capacitance of a parallel plate capacitor,

$$C = \frac{\epsilon_r \epsilon_0 A}{d} \quad (2)$$

where  $C$  is the capacitance of the sample,  $A$  is the capacitor's size defined by the electrode,  $d$  is the thickness of the organic layer,  $\epsilon_0$  is the permittivity of vacuum, and  $\epsilon_r$  is the relative dielectric constant of the organic material. The capacitance of the device is normally measured in the Hz to MHz (or even GHz) regime because bimolecular recombination is reversely proportional to the relative permittivity and occurs on a  $\mu\text{s}$  timescale.<sup>[29]</sup> Therefore, a relatively constant  $\epsilon_r$  up to the MHz (or even GHz) range is required when materials are applied in BHJ OPV layers. From equation 2, it is clear that the thickness of the dielectric material is very important and the active layer should be very smooth to get reliable results. To minimize the error on the measurement, PEDOT:PSS is used as an intermediate layer to reduce the surface roughness of the underlying ITO layer in order to achieve a smoother and more evenly distributed active layer. It is often also better to use thicker active layers (in the range of 100–200 nm) to minimize the errors made in these measurements.

## **2.2 Strategies toward increased dielectric constants in OPV materials**

If one desires to increase the dielectric constant (which is per definition a bulk property) of a conjugated polymer, small molecule or fullerene by local structural changes, several strategies can be adopted. The structural variations can involve either the backbone of the periphery/side chain pattern. The mobile (freely rotating) alkyl side chains are attractive targets for effective screening of the dissociated hole/electron pair formed upon light absorption by the photoactive material. In the sections below, the different strategies used so far to increase  $\epsilon_r$  are introduced in a stepwise manner. We will first focus on the electron donor materials and then move on to the electron acceptor materials. Finally, a completely different strategy is discussed, wherein high dielectric constant (in)organic dopants are added to the photoactive layer blend.

### **2.2.1 High- $\epsilon_r$ organic donor materials**

Push-pull low bandgap copolymers and related small molecules comprising of electron-donating and electron-accepting building blocks in an alternating fashion are currently the state of the art electron donor materials for BHJ OPV devices.<sup>[9,10]</sup> A lot of material optimization with respect to absorption, bandgap, energy levels, solubility, etc., has been realized over the past decade, but little efforts have been done to enhance the dielectric properties, using only a few general strategies. The structures of all donor materials discussed in this section are depicted in Figure 2 and the  $\epsilon_r$  values, HOMO-LUMO energy levels, hole mobilities ( $\mu_h$ ), and resulting organic solar cell output parameters are listed in Table 1.

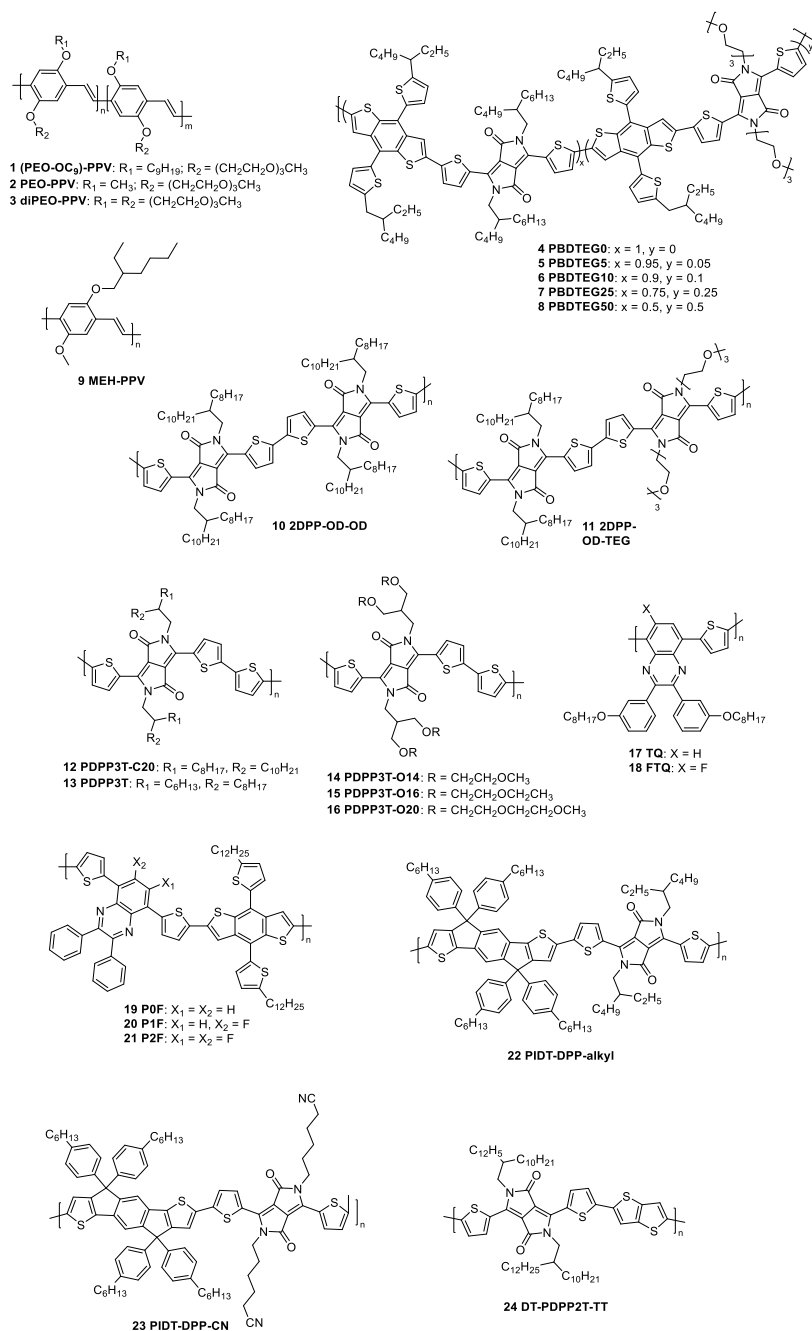


**Figure 2.** Donor polymers employed in  $\epsilon_r$  studies to improve the performance of organic solar cells.

**Table 1.** Dielectric constants, HOMO-LUMO values, and hole mobilities for donor materials employed in  $\epsilon_r$  studies and photovoltaic parameters of the resulting BHJ OPV devices.

Compound	$\epsilon_r^{(a)}$	HOMO [eV]	LUMO [eV]	$\mu_h$ [ $\text{cm}^2 \text{V}^{-1} \text{s}^{-1}$ ]	Active layer blend	$J_{sc}$ [ $\text{mA cm}^{-2}$ ]	$V_{oc}$ [V]	FF	PCE [%] <sup>(b)</sup>	Ref
<b>(PEO-OC<sub>3</sub>)-PPV 1</b>	4.1	-	-	$3-6 \times 10^{-4(b)}$	<b>1:PC<sub>61</sub>BM</b>	4.3	0.64	0.34	0.94	[37]
<b>PEO-PPV 2</b>	4.0	-	-	$1-5 \times 10^{-4(b)}$	<b>2:PC<sub>61</sub>BM</b>	1.8	0.38	0.26	0.18	[37]
<b>diPEO-PPV 3</b>	5.5	-	-	$1-4 \times 10^{-4(b)}$	<b>3:PC<sub>61</sub>BM</b>	0.006	0.61	0.24	0.0009	[37]
<b>PEO-PPV 2</b>	4.0	-	-	$1.8 \times 10^{-5(c,d)}$	<b>2:PCB-EH</b>	1.38	0.67	0.52	0.5	[38]
<b>PBDTEG0 4</b>	-	-5.32	-3.76	$\sim 9.5 \times 10^{-5(e)}$	<b>4:PC<sub>71</sub>BM</b>	13.4	0.73	0.63	6.2 (6.1)	[39]
<b>PBDTEG5 5</b>	-	-5.32	-3.76	$\sim 9.5 \times 10^{-5(e)}$	<b>5:PC<sub>71</sub>BM</b>	13.8	0.73	0.63	6.3 (6.1)	[39]
<b>PBDTEG10 6</b>	-	-5.31	-3.76	$\sim 9.5 \times 10^{-5(e)}$	<b>6:PC<sub>71</sub>BM</b>	14.3	0.72	0.68	7.0 (6.8)	[39]
<b>PBDTEG25 7</b>	-	-5.28	-3.78	$\sim 9.5 \times 10^{-5(e)}$	<b>7:PC<sub>71</sub>BM</b>	10.3	0.70	0.65	4.7 (4.6)	[39]
<b>PBDTEG50 8</b>	-	-5.25	-3.77	$\sim 9.5 \times 10^{-5(e)}$	<b>8:PC<sub>71</sub>BM</b>	8.1	0.68	0.58	3.2 (3.1)	[39]
<b>MEH-PPV 9</b>	$3 \pm 0.1$	-	-	$1.4 \times 10^{-6(c)}$	-	-	-	-	-	[29]
<b>PEO-PPV 2</b>	$6 \pm 0.1$	-	-	-	-	-	-	-	-	[29]
<b>2DPP-OD-OD 10</b>	$2.1 \pm 0.1$	-	-	-	-	-	-	-	-	[29]
<b>2DPP-OD-TEG 11</b>	$4.8 \pm 0.1$	-	-	$2 \times 10^{-4(c)}$	-	-	-	-	-	[29]

<b>PDPP3T-C20 12</b>	2.0 ± 0.1	-5.20	-3.50	1.55 × 10 <sup>-3</sup> <sup>e)</sup>	12:PC <sub>71</sub> BM	6.45	0.68	0.68	3.00	[40]
<b>PDPP3T 13</b>	-	-5.17	-3.61	0.04 <sup>b)</sup>	<b>13</b> :PC <sub>71</sub> BM	11.8	0.65	0.60	4.7	[41]
<b>PDPP3T-O14 14</b>	5.5 ± 0.3	-5.13	-3.65	4.14 × 10 <sup>-3</sup> <sup>e)</sup>	<b>14</b> :PC <sub>71</sub> BM	16.42	0.50	0.55	4.52	[40]
<b>PDPP3T-O16 15</b>	4.6 ± 0.2	-5.09	-3.61	2.53 × 10 <sup>-3</sup> <sup>e)</sup>	<b>15</b> :PC <sub>71</sub> BM	14.30	0.57	0.66	5.37	[40]
<b>PDPP3T-O20 16</b>	4.6 ± 0.2	-5.21	-3.60	1.10 × 10 <sup>-3</sup> <sup>e)</sup>	<b>16</b> :PC <sub>71</sub> BM	4.82	0.56	0.44	1.20	[40]
<b>TQ 17</b>	4.2	-5.36	-3.03	-	<b>17</b> :PC <sub>61</sub> BM	~5.0 <sup>h)</sup>	0.87	~0.60	~2.6	[43]
<b>FTQ 18</b>	5.5	-5.51	-3.08	2.0 × 10 <sup>-3</sup> <sup>f)</sup>	<b>18</b> :PC <sub>71</sub> BM	~6.5 <sup>h)</sup>	0.93	~0.53	3.21	[43]
<b>POF 19</b>	6.6 (4.2)	-4.98	-3.18	-	<b>19</b> :PC <sub>61</sub> BM	6.37	0.83	0.54	-(2.9)	[46]
<b>P1F 20</b>	7.2 (4.4)	-5.07	-3.27	-	<b>20</b> :PC <sub>61</sub> BM	6.52	0.87	0.55	-(3.1)	[46]
<b>P2F 21</b>	7.9 (5.4)	-5.08	-3.27	-	<b>21</b> :PC <sub>61</sub> BM	6.84	0.91	0.59	-(3.7)	[46]
<b>PIDT-DPP-alkyl 22</b>	3.5	-5.16	-3.18	0.015 <sup>b)</sup>	<b>22</b> :C <sub>60</sub> bilayer	2.40	0.63	0.47	-(0.72)	[49]
<b>PIDT-DPP-CN 23</b>	5.0	-5.18	-3.23	0.011 <sup>b)</sup>	<b>23</b> :C <sub>60</sub> bilayer	3.00	0.71	0.68	-(1.44)	[49]
<b>DT-PDPP2T-TT 24</b>	16.7 ± 0.4 (7.3 ± 0.75)	-	-	1.8 × 10 <sup>-3</sup> <sup>g)</sup>	<b>24</b> :PC <sub>61</sub> BM	9.2	0.71	0.62	4.0	[51]

<sup>a)</sup> Blend dielectric constant between brackets. <sup>b)</sup> Organic field-effect transistor (OFET) mobility for the donor polymer. <sup>c)</sup> Space-charge-limited current (SCLC) mobility for the donor polymer. <sup>d)</sup> A hole mobility of 4 × 10<sup>-7</sup> cm<sup>2</sup> V<sup>-1</sup> s<sup>-1</sup> was measured for the blend (**2**:PCB-EH, 1:4). <sup>e)</sup> Space-charge-limited current (SCLC) mobility of the active layer blend. <sup>f)</sup> Organic thin-film transistor (OTFT; glass/ITO/PVP/FTO/Ag) mobility. The hole mobility increased to 5.7 × 10<sup>-3</sup> cm<sup>2</sup> V<sup>-1</sup> s<sup>-1</sup> after heating at 110 °C for 1 min. <sup>g)</sup> Blend mobility (**24**:PC<sub>61</sub>BM, 1:3) measured by photo-CELLIV. <sup>h)</sup> Estimated values deduced from figures as no exact values were reported. <sup>i)</sup> Best efficiency (average between brackets).

*- Oligo(ethylene glycol) side chains*

Initial endeavors to increase the dielectric constant of an organic semiconductor were done by Cleij and co-workers in 2006 by introducing oligo(ethylene glycol) (OEG) side chains on a poly(*p*-phenylene vinylene) (PPV) polymer.<sup>[37]</sup> A maximum  $\epsilon_r$  of 5.5 was achieved for diPEO-PPV **3**, compared to  $\epsilon_r = 3$  for the reference material OC<sub>1</sub>C<sub>10</sub>-PPV (also called MDMO-PPV), via the introduction of 2 tri(ethylene glycol) (TEG) side chains on the polymer backbone (Figure 2). The hole mobility values of the PPV-based polymers reported were all in the same range ( $10^{-4}$  cm<sup>2</sup>/V s) and were hardly influenced by the side chains. On the other hand, the conductivity did improve with one order of magnitude ( $\sim 10^{-4}$  S/m) compared to the reference MDMO-PPV. This can be attributed to the higher  $\epsilon_r$  values, increasing the number of charge carriers in the channel for a given voltage. Initial solar cell results were, however, rather disappointing (Table 1). Lenes *et al.* further investigated why the efficiency was so low as compared to the standard PPV polymers, despite the increased dielectric constant.<sup>[38]</sup> The solar cells were remade and optimized using PCB-EH rather than [60]PCBM as the fullerene acceptor material (see Figure 6), aiming at a better miscibility of the donor and acceptor in the photoactive layer. However, PEO-PPV **2** (with only one TEG side chain; Figure 2) still afforded a non-optimal blend morphology, attributed to incompatible polarities of the materials in the blend, resulting in a low PCE of 0.5% (Table 1). The hole transporting features of the blend were investigated and the hole mobility turned out to be more than 3 orders of magnitude lower ( $4 \times 10^{-7}$  cm<sup>2</sup> V<sup>-1</sup> s<sup>-1</sup>) as compared to a regular MDMO-PPV:PC<sub>[60]</sub>BM blend ( $4 \times 10^{-4}$  cm<sup>2</sup> V<sup>-1</sup> s<sup>-1</sup>). Thin active layer blends of only 68 nm afforded the maximum PCE for PEO-PPV:PCB-EH devices, with a low short-circuit current density ( $J_{sc}$ ) of 1.38 mA cm<sup>-2</sup> (Table 1). Further measurements were done to study the effect of the raised dielectric constant on the charge dissociation rate. Despite the lower hole mobility, an enhanced charge dissociation at short circuit and a lower decay rate were achieved as compared to the standard PPV derivatives with lower  $\epsilon_r$  values, still showing the potential benefit of the higher relative permittivity.

Chang *et al.* gradually increased the number of TEG side chains on a diketopyrrolopyrrole (DPP) based low bandgap polymer (Figure 2) to slightly enhance the polarity without too much affecting the compatibility with

[70]PCBM.<sup>[39]</sup> The main goal of their study was to improve the photovoltaic properties by inducing a better self-assembly of the polymer chains, since OEG substituents are known to enhance the polymer-polymer interactions (*vide infra*). This concept was tested via a triple component random copolymerization, wherein the concentration of TEG units was gradually increased, up to a 50/50 TEG/alkyl ratio on the DPP units in copolymer **8**. A PCE increase from 6.2 to 7.0% was observed for the 10% TEGDPP-modified polymer **6**, especially enhancing the  $J_{sc}$  and FF, accompanied with a minor decrease of the open-circuit voltage ( $V_{oc}$ ) (Table 1). Further increasing the number of TEG resulted in a strong drop of (mainly)  $J_{sc}$ . Transmission electron microscopy (TEM) was used to examine the active layer morphology, which revealed that aggregation becomes stronger and a higher degree of phase separation is obtained upon increasing the density of TEG side chains on this polymer (Figure 3). Unfortunately, no  $\epsilon_r$  measurements were performed in this study.

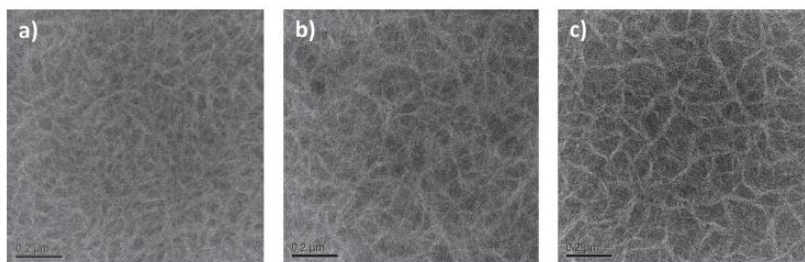


**Figure 3.** TEM images of a) **4**:[70]PCBM, b) **6**:[70]PCBM, and c) **8**:[70]PCBM blend thin films (scale bars: 200 nm). Reproduced with permission.<sup>[39]</sup> Copyright 2014, Wiley.

Hummelen, Koster and co-workers introduced OEG side chains to enhance the dielectric properties without affecting the mobilities of both charge carriers (electron and holes) and still providing good solubility in common processing solvents.<sup>[29]</sup> This was also done via the substitution of the donor (or acceptor) alkyl side chains. OEG substituents have a high flexibility, with active rotations along the chain in the GHz frequency domain and full rotation in the MHz range, without sacrificing the magnitude of the dipole moment. The ease by which these rotations can occur directly corresponds to the dielectric constant due to a fast reorientation of the dipole moments. Experimentally, this was tested on different

acceptors (fullerenes) and donors (DPP and PPV-based polymers) for BHJ organic solar cells. For the PPV-based polymer, one side chain was replaced for TEG (affording a material identical to polymer **2**) as compared to the reference MEH-PPV **9** (Figure 2). An impressive doubling of the dielectric constant ( $\epsilon_r = 6 \pm 0.1$ ) was obtained by impedance spectroscopy measurements (Table 1). A second, DPP-based polymer **11** with di(ethylene glycol) (DEG) side chains showed an increase in  $\epsilon_r$  from  $2.1 \pm 0.1$  to  $4.8 \pm 0.1$  compared to the DPP polymer **10** with simple hydrocarbon side chains (Figure 2, Table 1). Very low error bars were obtained for all  $\epsilon_r$  measurements. The authors suggest that the fast change of the dipole moments accounts for the higher  $\epsilon_r$  values of the OEG-functionalized materials and they illustrate that the polarization mechanism gives rise to enhanced dielectric constants rather than space-charge polarization or ionic movements. The effects on the OPV characteristics were not studied in this case.

In 2016, Chen *et al.* reported that the introduction of branched glycolated side chains on PDPP3T (Figure 2) results in polymers with a smaller  $\pi$ - $\pi$  stacking distance, reduced optical bandgap, higher relative permittivity and larger surface energy.<sup>[40]</sup> The hole mobilities of the different polymers did not vary that much and are all in the order of  $10^{-3} \text{ cm}^2 \text{ V}^{-1} \text{ s}^{-1}$ . The  $\pi$ - $\pi$  stacking distances as achieved from grazing incidence X-ray diffraction (GI-XRD) experiments were estimated to be  $3.80 \text{ \AA}$  for the alkylated PDPP3T-C20 reference polymer **12** and  $\sim 3.60 \text{ \AA}$  for the glycolated polymers, which can be attributed to the faster rotations along these side chains, providing a higher chain flexibility and closer packing. This is in agreement with the UV-Vis absorption spectra, exhibiting a bathochromic shift as an indication of the stronger interactions of the glycolated backbones. The influence of the side chain substitution on the energy levels was analyzed by means of cyclic voltammetry (CV). The glycolated polymers generally displayed slightly higher HOMO energy levels and lower LUMO levels (Table 1), reducing the bandgap of the corresponding polymers. The dielectric constants of the materials as obtained by impedance spectroscopy and measured over the range from 100 Hz to 1 MHz are  $5.5 \pm 0.3$ ,  $4.6 \pm 0.2$ ,  $4.6 \pm 0.2$  and  $2.0 \pm 0.1$  for polymers **14** (PDPP3T-O14), **15** (PDPP3T-O16), **16** (PDPP3T-O20) and **12** (PDPP3T-C20), respectively. All polymers were then also tested as donor materials for OPV devices in combination with [70]PCBM (Table 1). Although the highest  $\epsilon_r$  value was obtained for PDDP3-O14 **16**, PDPP3T-O16 **15** performed best, with a

maximum PCE of 5.37%, outperforming both their own reference material **12** with alkyl side chains and a similar PDPP3T polymer **13** reported by Bijleveld *et al.*<sup>[41]</sup> (Figure 2, Table 1). Higher short-circuit currents were obtained for the glycolated polymers, whereas the  $V_{oc}$  values were somewhat lower. The main issue for the devices based on polymer **16** (carrying the longest OEG side chains) was the rough active layer morphology for the blend with [70]PCBM (Figure 4). This could be attributed to the higher surface energy (deduced from contact angle measurements), which reduces the compatibility with PC<sub>[70]</sub>BM and thereby complicates intermixing of both phases. The larger  $\epsilon_r$  values should also reduce bimolecular recombination and this was analyzed by varying the thickness of the photoactive layer for the **14**: [70]PCBM devices from 100 to 290 nm, maintaining PCE's in the range from 4.2–4.5%.

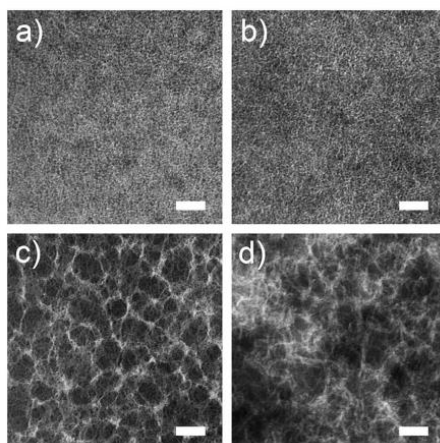


**Figure 4.** TEM images of the active layer blends of a) **14**: [70]PCBM, b) **15**: [70]PCBM, c) **16**: [70]PCBM, and d) **12**: [70]PCBM (scale bar = 200 nm).

Reproduced with permission.<sup>[40]</sup> Copyright 2016, Wiley.

The results observed by Wang and co-workers for their DPP-based polymers were in accordance with previous studies from the same group wherein they already investigated the effect of replacing alkyl side chains with OEG on a benzothiadiazole-fluorene based polymer.<sup>[42]</sup> For this system, it was already observed that the stacking distance in thin film decreased from 0.44 to 0.41 nm due to the enhanced flexibility of the side chains (Figure 5). Moreover, a red-shift in the absorption spectrum of the polymer and a higher hole mobility were

observed as well. The dielectric constant was not measured in this case, but polymer solar cells were made and they showed a slightly enhanced device efficiency from 2.28% to 2.58%. An alternative non-halogenated solvent (anisole) was also used and was found to provide a better device performance (PCE = 3.29%).

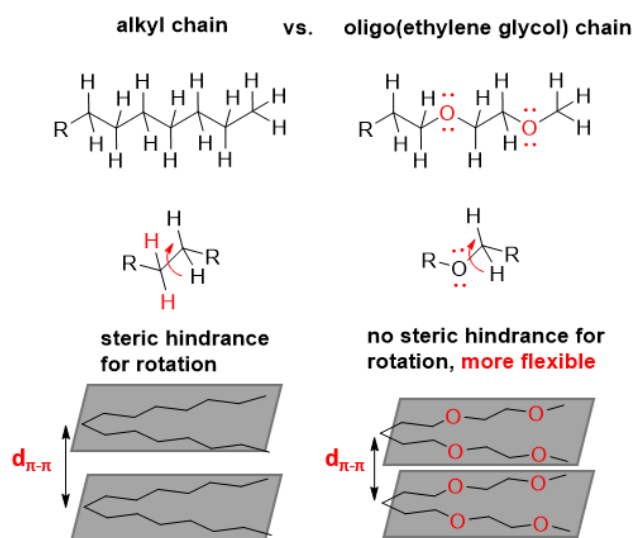


**Figure 5.** Schematic illustration of the superior flexibility of OEG chains (based on the Figure by Meng *et al.*<sup>[42]</sup>).

#### - Fluorination

A second strategy to increase the dielectric constant was initially presented by Lu *et al.*<sup>[43]</sup> They found that the introduction of fluorine directly on the polymer backbone causes an increase in  $\epsilon_r$  without sacrificing the  $V_{oc}$  of the resulting OPV devices, as generally observed upon glycolation. Fluorine introduction is in fact an established approach to reduce the HOMO energy level of electron donor materials, thereby increasing the  $V_{oc}$ .<sup>[44,45]</sup> In this case, fluorine was introduced on a thiophene-quinoxaline alternating copolymer (**18**, Figure 2). CV analysis showed that the HOMO level of the fluorinated low bandgap polymer **18** (FTQ) decreased with 0.15 eV as compared to the TQ reference polymer **17**. Fluorination also resulted in an overall increase of the OPV device efficiency, in particular due to enhanced  $J_{sc}$  and  $V_{oc}$  values, although the increase of the open-circuit voltage was slightly less than expected based on the CV results (Table 1). The dielectric

constants were measured for both polymers, showing an  $\epsilon_r$  of 5.5 at 10 kHz for FTQ, higher than the non-fluorinated TQ analogue with  $\epsilon_r = 4.2$  (Table 1).

Yang *et al.* also introduced fluorine on a quinoxaline-based polymer to investigate its effect on the  $V_{oc}$  and the dielectric constant.<sup>[46]</sup> To this extent, three different quinoxaline monomers (with 0, 1 and 2 fluorine atoms) were copolymerized with a benzodithiophene unit (**19-21**; Figure 2). CV analysis confirmed the decrease of the HOMO level when introducing 1 fluorine atom, but surprisingly no further significant decrease was observed upon the second fluorination. On the other hand, the OPV devices did show a stepwise increase in  $V_{oc}$  of 0.04 V for each additional fluorine atom (Table 1). This is not in accordance with the CV results, but the  $V_{oc}$  depends on different factors, such as the binding energy of the charge transfer excitation, which is correlated to the dielectric constant (Eq. 3):

$$V_{oc} = \frac{E_{LUMO}^A - E_{HOMO}^D - E_b}{q} - C \quad (3)$$

where  $E_{LUMO}^A$  is the LUMO energy level of the acceptor,  $E_{HOMO}^D$  is the HOMO energy level of the donor,  $E_b$  is the exciton binding energy,  $q$  is the elemental electron charge, and  $C$  is a constant related to illumination and temperature.<sup>[47]</sup>

Further analysis of the dielectric constant via impedance measurements revealed an  $\epsilon_r$  of 6.6 for the reference polymer POF, which is remarkably high for a standard reference polymer with no polar substituents. Adding fluorine substituents to the polymer backbone further increased the  $\epsilon_r$  with  $\sim 0.6$  for each fluorine addition, moving from 6.6 to 7.2 for P1F **20** and to 7.9 for P2F **21** (Figure 2, Table 1). On the other hand, only a slight enhancement of the blend dielectric constant was observed for the addition of 1 fluorine atom (from  $\epsilon_r = 4.2$  to 4.4), whereas the largest increase was seen for the second fluorine addition ( $\epsilon_r = 5.4$ , Table 1). This may explain the further increase of the  $V_{oc}$  for P2F **21**. However, a clear correlation of the dielectric constant to the enhanced device performance could not be made due to the influence of fluorine on various parameters (e.g. solubility and miscibility, active layer morphology, absorption range, *etc.*).

Chen *et al.* investigated the dependence of the open-circuit voltage on the dielectric constant in more detail.<sup>[48]</sup> Seven different active layer blends (based on PCDTBT, P3HT, PTB7, PDTs-TPD, PDTG-TPD, PDTB-TPD and PDTs-il) were

explored and dielectric constants of the photoactive layer blends were determined and correlated with the photovoltage loss due to the dielectric effect. The  $\epsilon_r$  values of the blends varied from  $3.36 \pm 0.24$  to  $4.95 \pm 0.14$  and a clear correlation could be made with the energy loss in organic solar cells. A  $V_{oc}$  loss of more than 0.3 V was observed for active layer blends with low dielectric constants in the range of 3–4, whereas these losses vanished for high- $\epsilon_r$  ( $\sim 5$ ) active layer blends. It was stated that organic donor materials should be designed with  $\epsilon_r$  values exceeding 6 to minimize the photovoltage losses due to the dielectric effect.

- *Cyano functionalization*

In 2014, the group of Jen reported a high dielectric constant for a PIDT-DPP polymer **23** (Figure 2) containing a cyano moiety at the outer ends of the DPP side chains.<sup>[49]</sup> Preceding studies from the same group already showed that the incorporation of a CN group on the side chains does not really affect the hole mobility, frontier orbital energy levels and absorption profile.<sup>[50]</sup> A dedicated device architecture was employed to eliminate possible interferences due to morphology, inherent to spin-coated BHJ polymer:fullerene blends. A non-conventional bilayer structure was used, wherein first the pure polymer (30 nm) was spin-coated and C<sub>60</sub> (40 nm) was deposited on top via thermal evaporation, followed by calcium and aluminum. The OPV device performance was investigated and an overall increase of all output parameters was reported for PIDT-DPP-CN **23**, doubling the PCE (from 0.7 to 1.4%) as compared to PIDT-DPP-alkyl **22** (Figure 2, Table 1). The dielectric properties of both polymers were investigated by impedance spectroscopy and  $\epsilon_r$  values of 3.5 and 5.0 for **22** and **23**, respectively, were obtained in the low frequency regime ( $10^3$ – $10^6$  Hz). Transient photovoltage (TPV) measurements done on both polymer solar cells showed suppression of the non-geminate charge recombination rates, which can be attributed to the dielectric constant increase. Because of the specific device architecture used and the similar opto-electrical material properties, it could be concluded that the observed increase in PCE can truly be attributed to the dielectric constant enhancement. This shows that there are definitely strong prospects for organic semiconductors with increased permittivities.

- *Other high- $\epsilon_r$  donor-type materials*

Zhang *et al.* studied the effect of bimolecular recombination for a high dielectric constant DPP-based polymer blended with [P60]CBM.<sup>[51]</sup> They found that the recombination coefficient was two times lower compared to a P3HT:[60]PCBM blend and one order of magnitude lower than in PCPDTBT:[60]PCBM. A smaller Coulomb capture radius was found for the DPP-based polymer blend, resulting in efficient charge extraction with active layers approaching 300 nm, which is significantly thicker than most organic photoactive layers reported in literature. Remarkably, the authors did not apply any specific strategy to enhance the dielectric constant, but just used a regular alkylated DPP-based polymer **24** without polar(izable) substituents (Figure 2). Yet, they measured a very high  $\epsilon_r$  of  $16.7 \pm 0.4$  for the pure material and an  $\epsilon_r$  of  $7.3 \pm 0.75$  for a 1:3 blend with [60]PCBM (at 1 kHz) by impedance and photo-CELIV (Table 1). For the pure materials, relatively low errors on the obtained  $\epsilon_r$  values were achieved, but the errors almost doubled for the blends. Moreover, batch to batch variations showed large differences for the blend dielectric constant, with a value varying from 4.5 to 7.3 despite the negligible difference in molar mass, dispersity, and impurity level (as judged by NMR) between the different polymer samples. The authors attribute the large difference in the blend dielectric constant to different film morphologies, affecting the domain size, crystallinity and phase purity. Yet, no further studies were performed to confirm this hypothesis. The reason for the very high dielectric constant compared to other analogous DPP-based low bandgap materials (e.g. compounds **12** and **13**) also remains to be elucidated.

### **2.2.2 High- $\epsilon_r$ acceptor materials**

(Methano)fullerene derivatives ([60]PCBM and [70]PCBM) are still the most widely applied electron acceptor materials in OPV devices, although the field of non-fullerene OPV has recently developed at an impressive pace and similar performances can now be realized without fullerenes.<sup>[12]</sup> Besides their relatively high cost, limited absorptivity and difficult structural fine-tuning, the standard fullerenes also show rather low dielectric constants ( $\sim 4$  for [60]PCBM). Similar approaches as discussed above for the donor materials have hence been applied to fullerene compounds as well with the general aim to increase  $\epsilon_r$ , although the

efforts done remain limited to only three research groups. The structures of all acceptor materials discussed in this section are depicted in Figure 6 and the  $\epsilon_r$  values, reduction potentials, electron mobilities ( $\mu_e$ ) and resulting OPV output parameters are listed in Table 2.

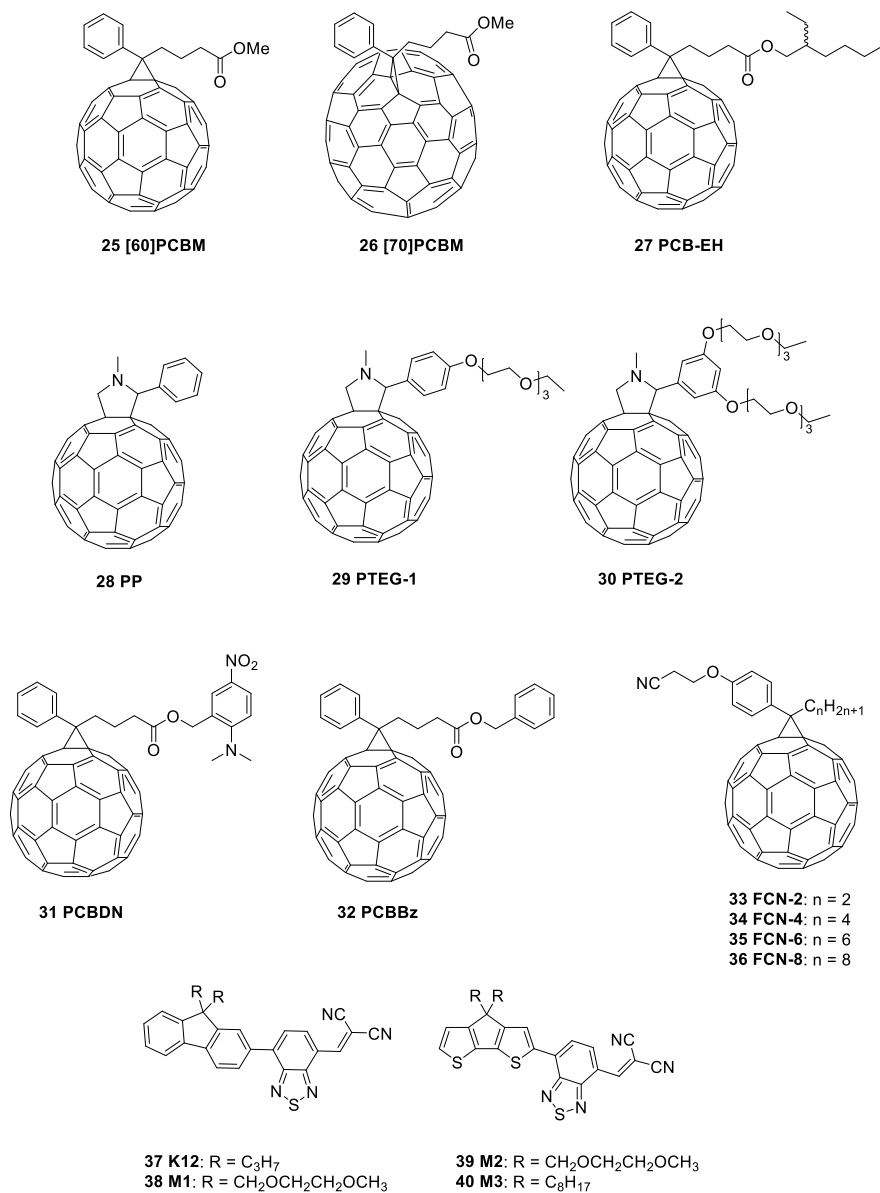


**Figure 6.** Acceptor materials employed in  $\epsilon_r$  studies to improve the performance of organic solar cells.

**Table 2.** Dielectric constants, reduction potentials and electron mobilities for acceptor materials employed in  $\epsilon_r$  studies and photovoltaic parameters of the resulting BHJ OPV devices.

Compound	$\epsilon_r$	$E_{1/2}^{\text{red}}$	$E_{1/2}^{\text{red}}$	$\mu_e$ [ $\text{cm}^2 \text{V}^{-1} \text{s}^{-1}$ ] <sup>b)</sup>	Active layer blend	$J_{\text{sc}}$ [ $\text{mA cm}^{-2}$ ]	$V_{\text{oc}}$ [V]	FF	PCE [%] <sup>c)</sup>	Ref
<b>PC<sub>61</sub>BM 25</b>	3.9 ± 0.1	-1.092	-1.482	2 × 10 <sup>-3</sup>	-	-	-	-	-	[29,52]
<b>PP 28</b>	3.6 ± 0.4	-1.114	-1.508	-	-	-	-	-	-	[29,52]
<b>PTEG-1 29</b>	5.7 ± 0.2	-1.113	-1.511	2 × 10 <sup>-3</sup>	-	-	-	-	-	[29,52]
<b>PTEG-2 30</b>	5.3 ± 0.2	-1.106	-1.504	3.5 × 10 <sup>-3</sup>	-	-	-	-	-	[29,52]
<b>PCBDN 31</b>	-	-1.089	-1.482	-	-	-	-	-	-	[53]
<b>PCBBz 32</b>	-	-1.095	-1.489	-	-	-	-	-	-	[53]
<b>FCN-2 33</b>	4.9 ± 0.1	-0.95 <sup>a)</sup>	-	4.8 × 10 <sup>-3</sup>	PCDTBT: <b>33</b>	8.66	0.90	0.71	5.55	[30]
<b>FCN-4 34</b>	4.9 ± 0.1	-0.93 <sup>a)</sup>	-	4.4 × 10 <sup>-3</sup>	PCDTBT: <b>34</b>	8.54	0.88	0.46	3.43	[30]
<b>FCN-6 35</b>	4.9 ± 0.1	-0.95 <sup>a)</sup>	-	4.0 × 10 <sup>-3</sup>	PCDTBT: <b>35</b>	8.36	0.93	0.64	4.97	[30]
<b>FCN-8 36</b>	4.9 ± 0.1	-0.94 <sup>a)</sup>	-	3.5 × 10 <sup>-3</sup>	PCDTBT: <b>36</b>	7.72	0.92	0.49	3.50	[30]
<b>PC<sub>61</sub>BM 25</b>	3.9 ± 0.1	-0.94 <sup>a)</sup>	-	2.1 × 10 <sup>-3</sup>	PCDTBT: <b>25</b>	7.73	0.91	0.65	4.56	[30]
<b>K12 37</b>	3.8	-1.2	-	5.0 × 10 <sup>-6</sup>	P3HT: <b>37</b>	0.22	0.70	0.25	0.04	[54]
					P3HT: <b>37</b> (cryst)	2.70	0.56	0.57	0.86	
<b>M1 38</b>	8.5	-1.3	-	1.3 × 10 <sup>-6</sup>	P3HT: <b>38</b>	0.81	0.52	0.25	0.10	[54]
<b>M2 39</b>	9.8	-1.2	-	3.0 × 10 <sup>-6</sup>	P3HT: <b>39</b>	0.86	0.40	0.35	0.12	[54]
<b>M3 40</b>	4.3	-1.1	-	3.0 × 10 <sup>-7</sup>	P3HT: <b>40</b>	0.51	0.38	0.35	0.07	[54]

<sup>a)</sup>  $E_{\text{onset}}^{\text{red}}$  potentials. <sup>b)</sup> Space-charge-limited current (SCLC) mobility for the acceptor material. <sup>c)</sup> Best efficiencies.

Hummelen, Koster and co-workers focused on the dielectric constant enhancement of fullerenes via the introduction of a TEG side chain.<sup>[29,52]</sup> An increase from  $3.6 \pm 0.4$  for the reference fullerene derivative PP **28** (without any side chains) to  $5.7 \pm 0.2$  for PTEG-1 **29** was observed (Figure 6), and this value was constant over a wide frequency range (from 100 to  $10^6$  Hz). Remarkably, further substitution of the fullerene derivative with a second TEG side chain slightly decreased the dielectric constant compared to PTEG-1. Based on this finding, the authors conclude that the increase of  $\epsilon_r$  is more complex than just increasing the number of polar(izable) substituents. In this case, the interplay between the TEG side chains and the fullerene cage also plays a crucial role on the relative permittivity. The electron mobility of the fullerene derivatives did not significantly change, which is of great relevance for acceptor moieties since they efficiently need to transport the electrons to the cathode. Furthermore, the electro-optical properties were not devaluated by the introduction of ethylene glycol units and also the LUMO energy level remained similar. Moreover, strongly improved solubility was achieved in common organic solvents (e.g. chloroform, *o*-dichlorobenzene, ...).

The Hummelen group recently also presented a promising strategy to improve charge separation by installing permanent dipoles in fullerene adducts (**31** and **32**; Figure 6).<sup>[53]</sup> Although no dielectric constants were measured for the synthesized fullerene derivatives, enhanced dipole moments were calculated when specific functional groups were introduced to increase the electronic polarization. Modeling showed that addition of a certain amount of derivative **31** to the active layer blend facilitated charge separation in the proximity of the central donor-acceptor complex. Installing a permanent dipole is presented as a promising strategy, but further experiments need be done to illustrate this concept in BHJ organic solar cells.

Zhang *et al.* recently reported on fullerene derivatives with 2-cyano-ethoxyphenyl side chains.<sup>[30]</sup> The cyano-functionalized fullerenes (FCN-*n* **33-36**; Figure 6) with different alkyl side chain lengths showed good solubility in common organic solvents (e.g. chloroform, chlorobenzene, toluene, ...) and improved thermal stabilities compared to [60]PCBM. The optical and electrochemical properties were almost identical, whereas the electron mobilities of the novel fullerenes were

slightly higher than the one of [60]PCBM. Surface energies were found to be somewhat larger for the FCN-*n* compounds, as expected because of the enhanced polarity, but still in the same range and therefore not disturbing the compatibility with the donor material PCDTBT. The dielectric constants were analyzed using impedance spectroscopy and all CN-functionalized fullerenes exhibited similar  $\epsilon_r$  values of  $4.9 \pm 0.1$  (Table 2), considerably higher than PC[60]BM ( $3.9 \pm 0.1$ ). These larger values can not only be attributed to the cyano moieties, but also to the ethylenoxy spacer, providing a higher degree of rotation along the side chain and a more easy response to an applied electric field. The photovoltaic performances of the novel fullerene adducts were evaluated in blends with PCDTBT and a maximum device efficiency of 5.55% was achieved for FCN-2 **33** (compared to 4.56% for [60]PCBM; Table 2). It should be mentioned that 2 out of the 4 FCN-*n* fullerene derivatives performed less compared to [60]PCBM, especially due to the significantly lower fill factors. Morphology studies were performed by means of TEM and AFM (atomic force microscopy) and, although higher surface energies were reported for the FCN-*n* compounds, a finer fibrillar morphology was obtained for the best-performing device based on FCN-2 **33** (Figure 7).

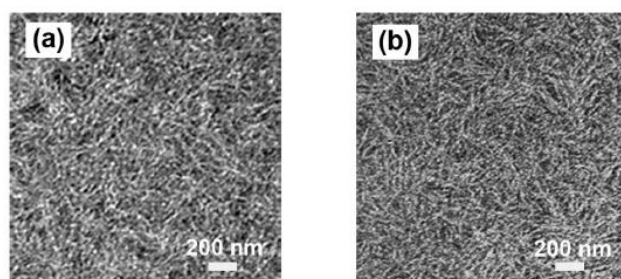


**Figure 7.** TEM images of the active layer blends containing a) PCDTBT:**33** and b) PCDTBT:[60]PCBM. Reproduced with permission.<sup>[30]</sup> Copyright 2016, Wiley.

The group of Burn and Meredith reported the first and so far only investigation on the dielectric constants of non-fullerene small molecule acceptors.<sup>[54]</sup> They showed that the introduction of DEG side chains on either a fluorene or 4*H*-cyclopenta[2,1-*b*:3,4-*b'*]dithiophene (CPDT) increased the static dielectric constant up to 8.5 for **38** and 9.8 for **39** (at 100 Hz) (Figure 6, Table 2). The optical and electrochemical properties of the chromophores remained unaffected

upon the DEG introduction, with reduction potentials similar to [60]PCBM. The electron mobility of **38** was almost similar as compared to the alkylated reference compound, but for the CPDT based material **39** it improved with one order of magnitude upon the introduction of DEG. CELIV and impedance measurements showed that the glycolated compounds have larger static and low frequency dielectric constants, although the dielectric constants at high frequencies were slightly lower. Initial OPV tests were presented as well, combining the small molecule acceptors with P3HT, but rather low efficiencies were observed, up to 0.12% for the best performing device (Table 2). Slightly enhanced  $J_{sc}$  values compared to the hydrocarbon counterparts were obtained, but the differences are so small that other factors besides  $\epsilon_r$  (e.g. film morphology) can play a (more) decisive role.

### **2.2.3 (In)organic additives to increase the blend $\epsilon_r$**

Engel *et al.* investigated the effect of substrate permittivity on an organic semiconductor active layer.<sup>[55]</sup> Different substrates with varying permittivities were used with pentacene as the photoactive material spin-coated on top. SiO<sub>2</sub>, TiO<sub>2</sub> and SrTiO<sub>3</sub> substrates were compared, with dielectric constants of 3.7, 88 and 305, respectively. The photo-charge carrier density ratio was investigated in dependence of the applied voltage and was found to increase with substrate permittivity. This can be attributed to the enhanced permittivity in the vicinity of the substrate-semiconductor interface, which results in a reduced Coulombic interaction and thereby facilitated charge separation and collection. Different active layer thicknesses were studied and, as expected, layer thicknesses up to the exciton diffusion length were most affected since all generated excitons can migrate to the organic-inorganic interface. This study suggested that introducing high- $\epsilon_r$  (in)organic materials (dopants) in close proximity of the active layer could increase the photocurrent generation for organic photovoltaics. Moreover, it could be concluded that when a high permittivity inorganic material ( $\epsilon_r = 300$ ) comes in the neighborhood of an organic material, the electric field strength between the respective charges in the organic material is reduced by a factor of almost 2, while the electric field in the inorganic material is screened almost completely (Figure 8). Although this particular study focused merely on the substrate, it clearly shows the potential of high- $\epsilon_r$  additives when blended in a photoactive layer. As a result,

several attempts in this direction were taken by other groups, using various approaches.

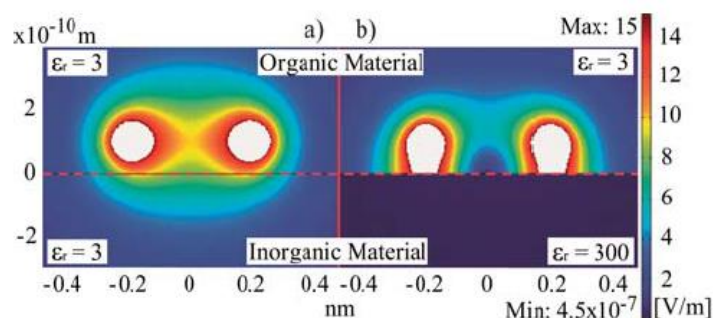


**Figure 8.** Electric field intensity between complementary point charges at an organic-inorganic interface, simulated by a finite element for (a)  $\epsilon_{r,\text{organic}} = \epsilon_{r,\text{inorganic}} = 3$  and (b)  $\epsilon_{r,\text{organic}} = 3$ ,  $\epsilon_{r,\text{inorganic}} = 300$ . Reproduced with permission.<sup>55</sup> Copyright 2012, Wiley.

In 2011, the group of Ginger reported results on charge generation and recombination in organic and hybrid solar cells.<sup>[56]</sup> Different donor host materials were blended with organic acceptors ([60]PCBM), inorganic acceptors (ZnO, TiO<sub>2</sub>) or colloidal quantum dots (PbS, CdSe). In general, longer average carrier lifetimes were measured in blends with inorganic acceptors compared to the [60]PCBM blends. The higher dielectric constants of the inorganic particles induce an increased dielectric screening of the photo-induced holes and electrons. The experimentally observed polaron lifetimes were also 10 times longer for the inorganic nanoparticles blends compared to different polymer:[60]PCBM blends.

Nalwa *et al.* were the first to investigate the influence of a ferroelectric additive in the OPV active layer. They performed a study on P3HT:[60]PCBM doped with a high- $\epsilon_r$  ( $\sim 11$ ) ferroelectric polymer PVDF-TrFE (**41**; Figure 9) to induce dipoles and to introduce a localized, increased electric field with the purpose to enhance charge dissociation.<sup>[57]</sup> A PCE increase up to 50% was presented, with internal quantum efficiencies (IQE's) approaching 100%, which represents a clear evidence that complete exciton dissociation at certain photon energies is achieved. An efficiency enhancement from 2.5 to 3.9% was observed upon incorporation of 10% PVDF-TrFE in the blend, especially increasing the photocurrent and FF (Table

3). The rather low reference PCE was ascribed to the co-solvent (THF) needed to dissolve the additive. Although no dielectric constants were measured for the blend layers, the enhanced dissociation rate of the excitons was put forward as a main cause for the efficiency enhancement, which is inherently connected to the higher relative permittivity of the active layer.

In 2015, Chaudhary and co-workers also investigated the effects of the addition of BaTiO<sub>3</sub> (BTO) nanoparticles to a P3HT:[60]PCBM active layer to increase the exciton dissociation and light scattering.<sup>[58]</sup> The BTO particles were functionalized (f-BTO) with methyl-terminated agents via a silanization process in which the surface hydroxyl groups were converted with the aid of *p*-tolyltrimethoxysilane to prevent precipitation of the particles. Addition of 5 wt% methyl-terminated BTO afforded a large increase (40%) in  $J_{sc}$  when the photoactive layer was spin-coated outside the glovebox, which was mainly done to enable immediate use of the solutions after sonication (Table 3). Solar cell fabrication in an inert atmosphere led to overall more efficient devices, but, remarkably, almost no effect of the f-BTO addition was observed (Table 3). The density of trap states was investigated and revealed an increase of trap states when f-BTO particles were added to the active layer, which increases recombination instead of reducing it, despite the (potentially) higher dielectric constant. Simulations with the exciton drift-diffusion model also demonstrated that the bare nanoparticles enhance exciton dissociation, while the methyl termination could cancel this effect. This suggests that the f-BTO nanoparticles can enhance the OPV characteristics because of light scattering rather than improved charge dissociation.

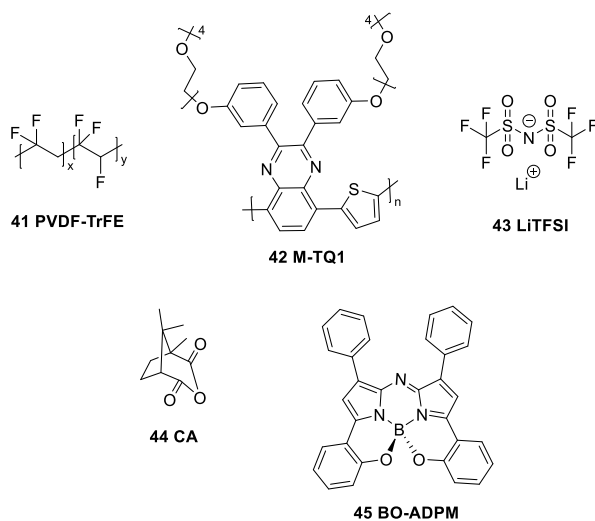


**Figure 9.** High- $\epsilon_r$  additives and host materials for BHJ organic/hybrid solar cells.

The group of Asbury reported an increased density of holes and a higher static dielectric permittivity of a polymer blend via salt doping.<sup>[59]</sup> Lithium bis(trifluoromethylsulfonyl)imide (LiTFSI) was added to a quinoxaline-based low bandgap polymer M-TQ1 (**42**; Figure 9) to increase the dielectric properties of the blend photoactive layer. The conjugated polymer was functionalized with long tetra(ethylene glycol) side chains to chelate small cations, permitting dispersal of salt ion pairs in the polymer phase. Dielectric constant measurements by means of impedance spectroscopy revealed an  $\epsilon_r$  of  $5.1 \pm 0.3$  in the range of Hz to MHz for the pure polymer without the addition of LiTFSI, while a very large increase up to  $145 \pm 20$  was reported when the polymer was doped with a 0.015 Li/O ratio (Table 3). It should, however, be noted that a steep decrease in  $\epsilon_r$  was observed at low frequencies (10–100 Hz). Since the influence on the high frequency regime is minimal, exciton dissociation in BHJ OPV devices will not largely be influenced because bimolecular recombination occurs at a  $\mu\text{s}$  timescale. This was confirmed when making OPV devices (Table 3). The addition of LiTFSI did not result in improved device parameters and the final devices even performed a bit worse.

**Table 3.** Photovoltaic parameters for BHJ OPV devices prepared from high- $\epsilon_r$  dopants added to the photoactive layer.

Compound	$\epsilon_r$	Active layer blend	$J_{sc}$ [mA cm <sup>-2</sup> ]	$V_{oc}$ [V]	FF	PCE [%] <sup>c)</sup>	Ref
<b>41</b>		P3HT:PC <sub>61</sub> BM + 0% <b>41</b>	9.6	0.55	0.48	2.5	[57]
<b>41</b>	11	P3HT:PC <sub>61</sub> BM + 10% <b>41</b>	11.3	0.57	0.60	3.9	[57]
<b>f-BTO</b>	-	P3HT:PC <sub>61</sub> BM + 0% f-BTO (air)	5.13	0.59	0.62	1.87	[58]
<b>f-BTO</b>	-	P3HT:PC <sub>61</sub> BM + 5% f-BTO (air)	7.21	0.60	0.63	2.72	[58]
<b>f-BTO</b>	-	P3HT:PC <sub>61</sub> BM + 0% f-BTO (N <sub>2</sub> )	9.30	0.61	0.55	3.08	[58]
<b>f-BTO</b>	-	P3HT:PC <sub>61</sub> BM + 5% f-BTO (N <sub>2</sub> )	9.88	0.61	0.51	3.07	[58]
<b>42</b>	5.1 ± 0.3	M-TQ1:PC <sub>61</sub> BM	~2.2 <sup>a)</sup>	~0.76 <sup>a)</sup>	~0.62 <sup>a)</sup>	~1.1 <sup>a)</sup>	[59]
<b>42 + 43</b> (0.015 Li <sup>+</sup> /O)	145 ± 20	M-TQ1:PC <sub>61</sub> BM + 0.01 Li <sup>+</sup> /O	~2.5 <sup>a)</sup>	~0.62 <sup>a)</sup>	~0.55 <sup>a)</sup>	~0.8 <sup>a)</sup>	[59]
<b>45</b>	4.5	bilayer with C <sub>60</sub>	4.65	0.55	0.53	1.34	[60]
<b>44:45 (30:70)</b>	8	bilayer with C <sub>60</sub>	4.95	0.62	0.56	1.72	[60]
<b>44:45 (50:50)</b>	10.8	bilayer with C <sub>60</sub>	4.41	0.65	0.50	1.43	[60]
\	~4.7 <sup>a,b)</sup>	MDMO-PPV:PC <sub>61</sub> BM	~1.45 <sup>a)</sup>	~0.90 <sup>a)</sup>	~0.29 <sup>a)</sup>	~0.38 <sup>a)</sup>	[61]
<b>MDMO-PPV:PC<sub>61</sub>BM + 10% 44</b>	~6.1 <sup>a,b)</sup>	MDMO-PPV:PC <sub>61</sub> BM + 20% <b>44</b>	~2.0 <sup>a)</sup>	~0.89 <sup>a)</sup>	~0.35 <sup>a)</sup>	~0.63 <sup>a)</sup>	[61]

<sup>a)</sup> Estimated values deduced from figures as no exact values were reported. <sup>b)</sup> Blend dielectric constants. <sup>c)</sup> Average efficiencies.

A different strategy was employed by Leblebici *et al.*<sup>[60]</sup> They blended an organic small molecule additive, camphoric anhydride (CA **44**; Figure 9), in a B,O-chelated azadipyrromethene donor material (BO-ADPM **45**; Figure 9), selected because of its broad absorption spectrum up to the near-infrared, to increase the film relative permittivity. The small molecule addition to the pristine donor film more than doubled the dielectric constant, from ~4.5 to ~11, with reduced exciton binding energies and an improved IQE. The relative permittivity of the film linearly

increased from 4.5 to 10.8 upon the addition of CA up to 50 wt%, but this goes hand in hand with a significant drop in film absorption properties because CA does not absorb in the visible region. Bilayer solar cell devices were investigated using C<sub>60</sub> as the acceptor layer. Despite the clear enhancement in IQE, no significant increase of the short-circuit current was observed (Table 3). The increase in IQE is probably counteracted by the lower hole mobilities (from  $\sim 10^{-5}$  to  $\sim 10^{-7}$  cm<sup>2</sup>/V s) observed upon increasing the amount of CA. On the other hand, an increase in  $V_{oc}$  from 0.55 to 0.65 was seen when going to a 1:1 BO-ADPM:CA blend, which was attributed to the increase in dipole moment at the interface between BO-ADPM:CA and C<sub>60</sub>.

Further studies by the same group employing CA as an additive for a different system, i.e. MDMO-PPV:[60]PCBM, again showed an increased film relative permittivity with reduced CT state energy. In this case, a PCE increase was achieved by the addition of 20 wt% CA, although the efficiency remained very low ( $\sim 0.6\%$ , Table 3).<sup>[61]</sup> Improved dielectric constants, from  $\sim 4.7$  to  $\sim 6$ , were obtained by the addition of 10 wt% of CA, while further increasing the amount of CA led to a drop in  $\epsilon_r$ . In contrast to the previous study, an increase in  $J_{sc}$  and FF was seen going from 0 to 20 wt% CA, whereas the  $V_{oc}$  slightly decreased (Table 3). The drop in  $V_{oc}$  was attributed to the reduced energy of the CT state. AFM analysis showed that more and larger separate domains were formed upon the addition of CA. This indicates that CA does phase separate when too much of it is added, which is detrimental for the photovoltaic performance.

### 2.3 Conclusions and outlook

Over the past 10 years, only a limited number of studies have been devoted to the enhancement of the dielectric properties of organic semiconducting materials developed for organic photovoltaics, as outlined in more detail above. Different functionalities (e.g. (oligo)ethylene glycol, fluoro and cyano) were introduced on the backbone or periphery of electron donor type conjugated polymers with the aim to increase the polarizability and relative permittivity of the resulting bulk heterojunction blends. Addition of oligo(ethylene glycol) side chains is the most widely used approach. As the polymer backbone remains unaffected, the dielectric constants can be increased without significantly altering the charge carrier mobilities. The enhanced  $\epsilon_r$  values result from the larger dipole moment of the C-

O units and the higher degree of flexibility, enabling a fast response to an applied electric field. This increased flexibility also induces a closer  $\pi$ - $\pi$  stacking of the polymer chains.<sup>[62]</sup> In most cases, increased HOMO energy levels are observed due to the electron-donating ability of the glycol side chains, which has a negative impact on the open-circuit voltage. In this respect, fluorination is more beneficial, as it allows simultaneous improvement of the dielectric properties and the  $V_{oc}$ . On the electron acceptor side, most studies focused on fullerene materials and very similar structural modifications (*i.e.* mainly introduction of short glycol chains) have been made to increase  $\epsilon_r$ . Only one single report mentions non-fullerene electron acceptors.<sup>[54]</sup> In a totally different way of working, dopants with very high permittivities were added to the photoactive layer.

When analyzing the available literature more critically, a few important observations can be made, which can serve as guidelines for future work in the field:

- (i) Very limited structural variations, as well in the active materials as the substituents employed to enhance  $\epsilon_r$ , have been applied so far to establish structure – dielectric constant – device efficiency relationships. As such, there is certainly plenty of room for improvement. Lots of questions remain on which structural modifications are most beneficial to enhance the dielectric constant. On the other hand, the conjugated polymer backbones have also shown quite some variations in  $\epsilon_r$  and also in this respect more research is needed to understand these differences.
- (ii) Although enhanced permittivities were obtained in multiple cases, this did not automatically result in better solar cell performances. The increased polarity of the functionalized materials often led to compatibility issues in the active layer blend. In general, studies were done on either the electron donor or acceptor material, whereas simultaneous efforts on both classes of compounds are needed to adjust their polarities, surface energies and miscibility. Eventually, when very high dielectric constant materials can be achieved, homojunction (*i.e.* single layer) devices could be realized – which was

initially the main goal for setting up high- $\epsilon_r$  studies<sup>[23]</sup> – and miscibility issues would be inherently resolved.

- (iii) Also when adding dielectric dopants with very high  $\epsilon_r$  values, minor effects have usually been observed. This can be attributed to the very large interface surface, inducing trap states and thereby counteracting the enhanced dielectric constants. Especially the strong interfacial polarization (Maxwell-Wagner effect) results in a strong dispersion of  $\epsilon_r$ .<sup>[63]</sup> Introducing a third phase in ternary blends may also affect other properties and high dielectric losses were observed. On the other hand, the large surface energies and interface areas can also induce more light scattering in the blend and thereby enhance light absorption.
- (iv) The higher hydrophilicity of most high- $\epsilon_r$  organic semiconductors enables processing from more environmentally benign, non-halogenated solvents (e.g. alcohols). Despite the high importance of 'green' processing for future OPV commercialization, this aspect has been undervalued so far.
- (v) Non-fullerene acceptors have recently afforded record device performances comparable to and even outperforming those achieved with fullerene-based OPV blends.<sup>[12]</sup> Also for the purpose of dielectric constant enhancement, non-fullerene acceptors give new possibilities. More structural variations are possible because of the different suitable backbones (ITIC, perylene diimides, ...)<sup>[64]</sup> and the ease to introduce polar/polarizable units on various locations.
- (vi) Different strategies have been applied to measure the dielectric constants (impedance or CELIV) using diverse device stacks (e.g. SiO<sub>2</sub> or glass substrates, different electric contacts, ...) and making certain assumptions, complicating straightforward comparison of the obtained values. In a few cases, the employed technique is even not mentioned. Furthermore, almost no active layer (blend or pristine material) roughness data have been reported, although significant errors can be made when rough, non-uniform layers are used for the measurements. Only a few groups report error bars on the  $\epsilon_r$  measurements. As a result, there are doubts on the interpretation of

certain literature values, which is obviously hindering further progress. A unified, standard protocol for the determination of  $\epsilon_r$  should therefore be defined to achieve reliable dielectric constants and to draw proper conclusions on structure – dielectric constant – device efficiency trends. This will most certainly give a new impetus to the field and attract other researchers to the remaining challenges to exploit the full potential of high dielectric constant conjugated materials for organic photovoltaics (and organic electronics in general).

## 2.4 References

- [1] Dennler, G.; Scharber, M. C.; Brabec, C. J. *Adv. Mater.* **2009**, *21*, 1323.
- [2] Kaltenbrunner, M.; White, M. S.; Głowacki, E. D.; Sekitani, T.; Someya, T.; Sariciftci, N. S.; Bauer, S. *Nat. Commun.* **2012**, *3*, 770.
- [3] Su, Y. W.; Lan S. C.; Wei, K. H. *Mater. Today* **2012**, *15*, 554.
- [4] Dou, L.; You, J.; Hong, Z.; Xu, Z.; Li, G.; Street R. A.; Yang, Y. *Adv. Mater.* **2013**, *25*, 6642.
- [5] Mazzi K. A.; Luscombe, C. K. *Chem. Soc. Rev.* **2015**, *44*, 78.
- [6] Darling S. B.; You, F. *RSC Adv.* **2013**, *3*, 17633.
- [7] Lizin, S.; Van Passel, S.; De Schepper, E.; Maes, W.; Lutsen, L.; Manca J.; Vanderzande, D. *Energy Environ. Sci.* **2013**, *6*, 3136.
- [8] Kang, H.; Kim, G.; Kim, J.; Kwon, S.; Kim H.; Lee, K. *Adv. Mater.* **2016**, *28*, 7821.
- [9] Müllen, K.; Pisula, W. *J. Am. Chem. Soc.* **2015**, *137*, 9503.
- [10] Holliday, S.; Li, Y.; Luscombe, C. K. *Prog. Polym. Sci.* **2017**, *70*, 34.
- [11] Zhao, J.; Li, Y.; Yang, G.; Jiang, K.; Lin, H.; Ade, H.; Ma, W.; Yan, H. *Nat. Energy* **2016**, *1*, 15027.
- [12] Zhao, W. C.; Qian, D. P.; Zhang, S. Q.; Li, S. S.; Inganäs, O.; Gao, F.; Hou, J. H. *Adv. Mater.* **2016**, *28*, 4734.
- [13] Brabec, C. J.; Sariciftci, N. S.; Hummelen, J. C. *Adv. Funct. Mater.* **2001**, *11*, 15.
- [14] Knupfer, M. *Appl. Phys. A* **2003**, *77*, 623.
- [15] Hiramoto, M.; Fujiwara, H.; Yokoyama, M. *Appl. Phys. Lett.* **1991**, *58*, 1062.
- [16] Yu, G.; Gao, J.; Hummelen, J. C.; Wudl, F.; Heeger, A. J. *Science* **1995**, *270*, 1789.
- [17] Halls, J. J. M.; Walsh, C. A.; Greenham, N. C.; Marseglia, E. A.; Friend, R. H.; Moratti, S. C.; Holmes, A. B. *Nature* **1995**, *376*, 498.
- [18] Park, S. H.; Roy, A.; Beaupré, S.; Cho, S.; Coates, N.; Moon, J. S.; Moses, D.; Leclerc, M.; Lee, K.; Heeger, A. J. *Nature Photon.* **2009**, *3*, 297.
- [19] Van Franeker, J. J.; Turbiez, M.; Li, W.; Wienk, M. M.; Janssen, R. A. J. *Nat. Commun.* **2015**, *6*, 6229.
- [20] Scharber, M. C.; Mühlbacher, D.; Koppe, M.; Denk, P.; Waldauf, C.; Heeger, A. J.; Brabec, C. J. *Adv. Mater.* **2006**, *18*, 789.

- [21] Zhou, H.; Yang, L.; You, W. *Macromolecules* **2012**, *45*, 607.
- [22] Uy, R. L.; Price, S. C.; You, W. *Macromol. Rapid Commun.* **2012**, *33*, 1162.
- [23] Koster, L. J. A.; Shaheen, S. E.; Hummelen, J. C. *Adv. Energy Mater.* **2012**, *2*, 1246.
- [24] Kirchartz, T.; Taretto, K.; Rau, U. *J. Phys. Chem. C* **2009**, *113*, 17958.
- [25] Clarke, T. M.; Durrant, J. R. *Chem. Rev.* **2010**, *110*, 6736.
- [26] Lenes, M.; Koster, L. J. A.; Mihailetschi, V. D.; Blom, P. W. M. *Appl. Phys. Lett.* **2006**, *88*, 243502.
- [27] Camaioni, N.; Po, R. *J. Phys. Chem. Lett.* **2013**, *4*, 1821.
- [28] Ibrahim, M. L. I.; Ahmad, Z.; Sulaiman, K.; Muniandy, S. V. *AIP Adv.* **2014**, *4*, 057133.
- [29] Torabi, S.; Jahani, F.; Van Severen, I.; Kanimozhi, C.; Patil, S.; Havenith, R. W. A.; Chiechi, R. C.; Lutsen, L.; Vanderzande, D. J. M.; Cleij, T. J.; Hummelen, J. C.; Koster, L. J. A. *Adv. Funct. Mater.* **2015**, *25*, 150.
- [30] Zhang, S.; Zhang, Z.; Liu, J.; Wang, L. *Adv. Funct. Mater.* **2016**, *26*, 6107.
- [31] Galagan, Y.; de Vries, I. G.; Langen, A. P.; Andriessen, R.; Verhees, W. J. H.; Veenstra, S. C.; Kroon, J. M. *Chem. Eng. Process* **2011**, *50*, 454.
- [32] Tait, J. G.; Merckx, T.; Li, W.; Wong, C.; Gehlhaar, R.; Cheyns, D.; Turbiez, M.; Heremans, P. *Adv. Funct. Mater.* **2015**, *25*, 3393.
- [33] Zhang, S.; Ye, L.; Zhang, H.; Hou, J. *Mater. Today* **2016**, *19*, 533.
- [34] Yao, Y.; Hou, J.; Xu, Z.; Li, G.; Yang, Y. *Adv. Funct. Mater.* **2008**, *18*, 1783.
- [35] Y. Chen, S. Zhang, Y. Wu and J. Hou, *Adv. Mater.*, 2014, **26**, 2744.
- [36] Andersen, T. R.; Larsen-Olsen, T. T.; Andreasen, B.; Böttiger, A. P. L.; Carlé, J. E.; Helgesen, M.; Bundgaard, E.; Norrman, K.; Andreasen, J. W.; Jorgensen, J. W.; Krebs, F. C. *ACS Nano* **2011**, *5*, 4188.
- [37] Bresselge, M.; Van Severen, I.; Lutsen, L.; Adriaensens, P.; Manca, J.; Vanderzande, D.; Cleij, T. *Thin Solid Films* **2006**, *511-512*, 328.
- [38] Lenes, M.; Kooistra, F. B.; Hummelen, J. C.; Van Severen, I.; Lutsen, L.; Vanderzande, D.; Cleij, T. J.; Blom, P. W. M. *J. Appl. Phys.* **2008**, *104*, 114517.
- [39] Chang, W.-H.; Gao, J. G.; Dou, L.; Chen, C.-C.; Liu, Y.; Yang, Y. *Adv. Energy Mater.* **2014**, *4*, 1300864.
- [40] Chen, X.; Zhang, Z.; Ding, Z.; Liu, J.; Wang, L. *Angew. Chem. Int. Ed.* **2016**, *55*, 10376.

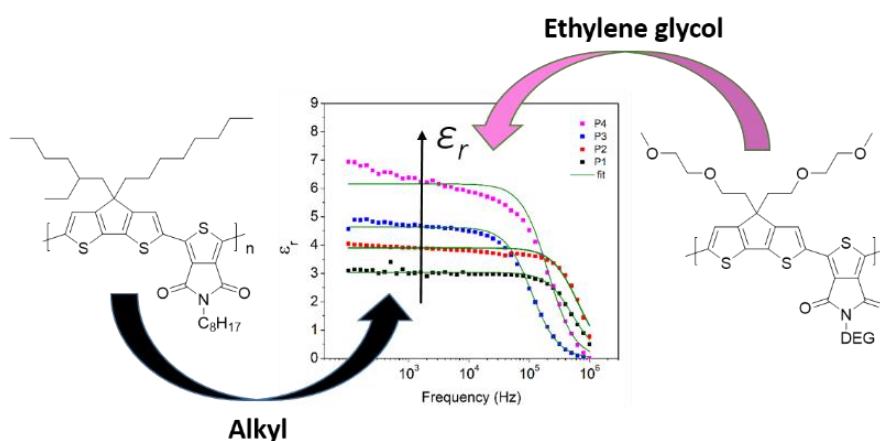
- [41] Bijleveld, J. C.; Zoombelt, A. P.; Mathijssen, S. G. J.; Wienk, M. M.; Turbiez, M.; de Leeuw, D. M.; Janssen, R. A. J. *J. Am. Chem. Soc.* **2009**, *131*, 16616.
- [42] Meng, B.; Song, H. Y.; Chen, X. X.; Xie, Z.; Y.; Liu, J.; Wang, L. X. *Macromolecules* **2015**, *48*, 4357.
- [43] Lu, Y.; Xiao, Z.; Yuan, Y.; Wu, H.; An, Z.; Hou, Y.; Gao, C.; Huang, J. *J. Mater. Chem. C* **2013**, *1*, 630.
- [44] Chen, H.-Y.; Hou, J.; Zhang, S.; Liang, Y.; Yang, G.; Yang, Y.; Yu, L.; Wu, Y.; Li, G. *Nat. Photonics* **2009**, *3*, 649.
- [45] Verstappen, P.; Kesters, J.; Vanormelingen, W.; Heintges, G.; Drijkoningen, J.; Vangerven, T.; Marin, L.; Koudjina, S.; Champagne, B.; Manca, J.; Lutsen, L.; Vanderzande, D.; Maes, W. *J. Mater. Chem. A* **2015**, *3*, 2960.
- [46] Yang, P.; Yuan, M.; Zeigler, D. F.; Watkins, S. E.; Lee, J. A.; Luscombe, C. K. *J. Mater. Chem. C* **2014**, *2*, 3278.
- [47] Vandewal, K.; Gadisa, A.; Oosterbaan, W. D.; Bertho, S.; Banishoeib, F.; Van Severen, I.; Lutsen, L.; Cleij, T. J.; Vanderzande, D.; Manca, J. V. *Adv. Funct. Mater.* **2008**, *18*, 2064.
- [48] Chen, S.; Tsang, S.-W.; Lai, T.-H.; Reynolds, R.; So, F. *Adv. Mater.* **2014**, *26*, 6125.
- [49] Cho, N.; Schlenker, C. W.; Knesting, K. M.; Koelsch, P.; Yip, H. L.; Ginger, D. S.; Jen, A. K. Y. *Adv. Energy Mater.* **2014**, *4*, 1301857.
- [50] Sun, Y.; Chien, S. C.; Yip, H. L.; Chen, K. S.; Zhang, Y.; Davies, J. A.; Chen, F. C.; Lin, B.; Jen, A. K. Y. *J. Mater. Chem.* **2012**, *22*, 5587.
- [51] Zhang, G.; Clarke, T. M.; Mozer, A. J. *J. Phys. Chem. C* **2016**, *120*, 7033.
- [52] Jahani, F.; Torabi, S.; Chiechi, R. C.; Koster, L. J. A.; Hummelen, J. C. *Chem. Commun.* **2014**, *50*, 10645.
- [53] De Gier, H. D.; Jahani, F.; Broer, R.; Hummelen, J. C.; Havenith, R. W. A. *J. Phys. Chem. A* **2016**, *120*, 4664.
- [54] Donaghey, J. E.; Armin, A.; Burn, P. L.; Meredith, P. *Chem. Commun.* **2015**, *51*, 14115.
- [55] Engel, M.; Kunze, F.; Lupascu, D. C.; Benson, N.; Schmechel, R. *Phys. Status Solidi RRL* **2012**, *6*, 68.
- [56] Noone, K. M.; Subramaniyan, S.; Zhang, Q.; Cao, G.; Jenekhe, S. A.; Ginger, D. S. *J. Phys. Chem. C* **2011**, *115*, 24403.

- [57] Nalwa, K. S.; Carr, J. A.; Mahadevapuram, R. C.; Kodali, H. K.; Bose, S.; Chen, Y.; Petrich, J. W.; Ganapathysubramanian, B.; Chaudhary, S. *Energy Environ. Sci.* **2012**, *5*, 7042.
- [58] Gebhardt, R. S.; Du, P.; Peer, A.; Rock, M.; Kessler, M. R.; Biswas, R.; Ganapathysubramanian, B.; Chaudhary, S. *J. Phys. Chem. C* **2015**, *119*, 23883.
- [59] Liu, X.; Jeong, K. S.; Williams, B. P.; Vakhshouri, K.; Guo, C.; Han, K.; Gomez, E. D.; Wang, Q.; Asbury, J. B. *J. Phys. Chem. B* **2013**, *117*, 15866.
- [60] Leblebici, S. Y.; Chen, T. L.; Olalde-Velasco, P.; Yang, W.; Ma, B. *ACS Appl. Mater. Interfaces* **2013**, *5*, 10105.
- [61] Leblebici, S.; Lee, J.; Weber-Bargioni, A.; Ma, B. *J. Phys. Chem. C* **2017**, *121*, 3279.
- [62] Boese, R.; Weiss, H. C.; Bläser, D. *Angew. Chem. Int. Ed.* **1999**, *38*, 988.
- [63] Smyth, C. P. *Dielectric Behavior and Structure: Dielectric Constant and Loss, Dipole Moment and Molecular Structure*. McGraw-Hill Book Company, New York, **1955**.
- [64] Li, S.; Zhang, Z.; Shi, M.; Li, C.-Z.; Chen, H. *Phys. Chem. Chem. Phys.* **2017**, *19*, 3440.



# Chapter 3

## An Effective Strategy to Enhance the Dielectric Constant of Organic Semiconductors - CPDTTPD-Based Low Bandgap Polymers Bearing Oligo(Ethylene Glycol) Side Chains



Brebels, J.; Douvogianni, E.; Devisscher, D.; Eachambadi, R. T.; Manca, J.; Lutsen, L.; Vanderzande, D.; Hummelen, J. C.; Maes, W. *Manuscript submitted*.

## Abstract

State of the art conjugated polymers applied in organic electronics (notably photovoltaics and photodetectors) exhibit relatively low dielectric constants ( $\epsilon_r = 3-4$ ), which leads to significant recombination losses of photogenerated excitons. As a direct consequence, the current output of the resulting devices is inherently restricted. Some efforts have been directed toward increasing  $\epsilon_r$  of the photoactive organic compounds, but the general knowledge on the impact of specific structural variations on the dielectric constant and the final device performance remains rather limited. In this study, this problem is addressed. A series of push-pull type alternating copolymers is synthesized based on 4*H*-cyclopenta[2,1-*b*:3,4-*b'*]dithiophene (CPDT) and 4*H*-thieno[3,4-*c*]pyrrole-4,6(5*H*)-dione (TPD) subunits, with the aim to increase the dielectric constant using oligo(ethylene glycol) side chains. The number of glycol substituents on the polymer backbone is gradually raised to systematically investigate its influence on the dielectric properties. Impedance measurements reveal a doubling of the dielectric constant (up to  $\epsilon_r = 6.3$ ) with respect to the reference polymer. Upon applying these materials in bulk heterojunction polymer solar cells, an efficiency of 4.4% is obtained for the best-performing device, with a particularly higher short-circuit current compared to the pristine alkyl-substituted polymer. Importantly, a non-halogenated solvent – beneficial toward 'green' processing – can also be applied for the active layer deposition, affording comparable results.

### 3.1 Introduction

Organic semiconductors are versatile active materials for high-performance (opto)electronic devices such as light-emitting diodes (OLEDs),<sup>[1]</sup> field-effect transistors (OFETs),<sup>[2]</sup> photodetectors (OPDs),<sup>[3]</sup> photovoltaics (organic and hybrid perovskite PVs)<sup>[4]</sup> and thermoelectrics.<sup>[5]</sup> Because of their high potential toward fully flexible, solution processed and low-cost organic solar cells, a lot of research has been done in this direction.<sup>[6–11]</sup> Many studies have focused on the variation of the building blocks of so-called 'push-pull', low bandgap, electron donor-type polymers, targeting optimal absorption features and energy level alignment, while the solubilizing side chains are tuned to optimize the miscibility with the electron acceptor component in the bulk heterojunction (BHJ) photoactive layer.<sup>[12]</sup> Thorough understanding of structure-property relations has been achieved and recent advances have pushed the power conversion efficiencies (PCEs) over 11%.<sup>[13]</sup> Intimate mixing of the electron donor and acceptor materials is essential to achieve these high efficiencies because of the limited diffusion length of the excitons formed upon the absorption of light.<sup>[14]</sup> This is a direct consequence of the strong Coulombic interactions of holes and electrons, caused by the rather low dielectric constants (i.e. static relative permittivity;  $\epsilon_r = \sim 3-4$ ) and high exciton binding energies in organic semiconductors.<sup>[15]</sup> The modest  $\epsilon_r$  of current generation organic semiconductors hence puts a limit on the PCE in comparison with inorganic or hybrid organic-inorganic solar cells.

Somewhat surprisingly, research on alternative high- $\epsilon_r$  conjugated small molecules and polymers has remained rather limited, although a number of specific features of high interest for OPV and other organic electronic applications can be achieved upon increasing the dielectric constant.<sup>[16]</sup> Simulations have shown that PCEs of more than 20% can be realized by taking into account an increased (active layer)  $\epsilon_r$  up to 10.<sup>[17]</sup> Higher dielectric constants can diminish important loss processes originating from Coulombic interactions between oppositely charged carriers.<sup>[17]</sup> The beneficial effect of an increasing  $\epsilon_r$  can easily be understood as the resulting lower binding energy of the charge transfer excitons (precursors to the free electrons and holes) will allow faster charge separation (with reduced energy losses) and thereby afford a higher photovoltaic efficiency.<sup>[18]</sup> Furthermore, reduction of the bimolecular recombination process

allows the production of OPV devices with thicker films for better light harvesting and further improved performance.<sup>[19]</sup> In this case, even single junction organic solar cells could be foreseen.<sup>[17]</sup> When applying these high- $\epsilon_r$  organic semiconductors as charge selective electrode materials in hybrid perovskite PVs, the dielectric contrast between the perovskite active layer and the charge selective transport layer can be lowered.<sup>[20]</sup> In applications where the organic semiconductor is doped, an increased  $\epsilon_r$  is also very beneficial. Thus, a wide range of applications can be targeted with high- $\epsilon_r$  organic semiconducting materials.

Most studies aiming to increase  $\epsilon_r$  have focused on polarizable oligo(ethylene glycol) (OEG) side chains.<sup>[16,19b,21]</sup> These glycol substituents are easily introduced and do not only increase the polarity of the organic semiconducting materials, but also provide a higher chain flexibility, facilitating closer  $\pi$ - $\pi$  stacking and thereby promoting charge carrier mobility.<sup>[22]</sup> Because of this improved chain flexibility, reorientation of the dipoles occurs much faster, which potentially increases  $\epsilon_r$ .<sup>[21]</sup> Moreover, OEG moieties are also known to increase the material solubility in more hydrophilic solvents, enabling to reduce the ecological footprint of the device preparation by allowing processing from environmentally more acceptable solvents (e.g. alcohols).<sup>[23]</sup> Greener processing is for instance highly desired to enhance the credibility and facilitate commercialization of organic photovoltaics as a truly renewable energy source.<sup>[24]</sup>

The first attempt to increase the dielectric constant of an organic semiconductor using OEG was done by Breselge *et al.* using a PPV (poly(*p*-phenylene vinylene)) polymer.<sup>[16a]</sup> A maximum  $\epsilon_r$  of 5.5 (vs. 3 for MDMO-PPV) was achieved by the introduction of 2 tri(ethylene glycol) (TEG) side chains on the polymer backbone (diPEO-PPV). Initial solar cell results were reported as well, but they remained very low. Later results from the same group showed a non-optimal BHJ morphology for a similar PPV with one single TEG side chain (PEO-PPV) because of compatibility issues with the applied fullerene acceptor, an issue more often encountered when adding glycol substituents.<sup>[25]</sup> As a result, again a low PCE (0.5%) was achieved. Nevertheless, an enhanced charge dissociation was obtained compared to standard PPV derivatives. More recent results by Chen *et al.* illustrate the strong potential of OEG-decorated materials for  $\epsilon_r$  (and OPV) enhancement.<sup>[19b]</sup> Diketopyrrolopyrrole (DPP) based polymers bearing different

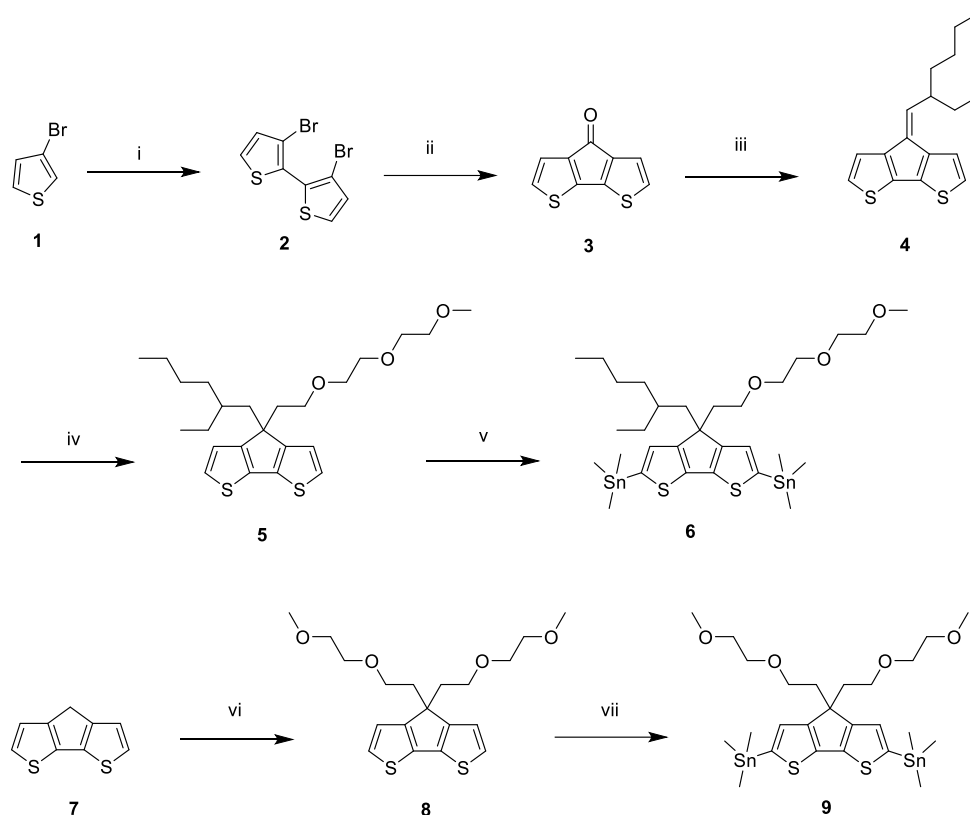
OEG side chains were reported to show reasonably high  $\epsilon_r$  values (up to 5.5) and a polymer solar cell efficiency up to 5.4% was achieved, similar to the reference polymer with regular alkyl side chains. On the other hand, Jahani *et al.* reported an  $\epsilon_r$  increase up to 5.7 for a fullerene derivative with a TEG substituent (vs. 3.9 for regular [60]PCBM), without severely affecting the optical and electrochemical material properties.<sup>[16b]</sup>

Despite the exciting prospects, the promises of a 'novel OPV efficiency regime'<sup>[17]</sup> by increasing the dielectric constant have not been realized so far.<sup>[26]</sup> It is clear that more dedicated studies are required to establish proper structure – dielectric constant – device efficiency relations. Lots of questions remain with respect to the effect of both the backbone and side chain structures. The impact of the enhanced  $\epsilon_r$  on the final solar cell efficiency is also hard to evaluate, as it cannot be isolated from other effects (e.g. on blend morphology, crystallinity and charge transport) imposed by the structural variations. Moreover, the dielectric constant measurements should be performed with great care to obtain reliable  $\epsilon_r$  values, allowing proper comparison. In the present study, four novel low bandgap copolymers are synthesized based on 4*H*-cyclopenta[2,1-*b*:3,4-*b'*]dithiophene (CPDT) as the donor and 1,3-dibromo-4*H*-thieno[3,4-*c*]pyrrole-4,6(5*H*)-dione (TPD) as the acceptor building block.<sup>[27,28]</sup> These subunits were specifically selected for the ease of gradual introduction of multiple OEG side chains on these materials, allowing a systematic study. The dielectric constants are evaluated by means of impedance spectroscopy, resulting in a maximum  $\epsilon_r$  value of 6.3, among the highest values reported so far for organic semiconductors, and with very low error bars.<sup>[16,19b,21,26,29]</sup>

## 3.2 Results and discussion

### *Material synthesis and characterization*

To allow systematic evaluation of the effect of the number of OEG substituents, these were introduced on either of the two building blocks required for the push-pull polymer synthesis via Stille polycondensation. For the synthesis of the stannylated CPDT monomer with one single TEG side chain, different literature procedures were combined to come up with a shorter and easier reaction sequence to synthesize CPDT precursor **4** (Scheme 1), allowing asymmetric side chain substitution.<sup>[30,31]</sup> The first step involved the coupling of 3-bromothiophene via the *Gronowitz* dithienyl synthesis, employing lithiation of the 2-position with lithium diisopropylamide (LDA) followed by coupling through the use of CuCl<sub>2</sub>. In the next step, cyclization was performed using dimethylcarbamoyl chloride to obtain 4*H*-cyclopenta[2,1-*b*:3,4-*b'*]dithiophen-4-one (**3**). A Wittig-type carbonyl olefination reaction with 2-ethylhexylphosphonium bromide was then applied to obtain product **4**. The exocyclic double bond was reduced with LiAlH<sub>4</sub> and an *in-situ* reaction was performed with 1-chloro-2-(2-(2-methoxyethoxy)ethoxy)ethane. In the last step, distannylation afforded CPDT monomer **6**. The standard conditions for stannylation were slightly adapted to obtain a better yield. A larger excess of *n*-BuLi was needed to force the reaction toward the distannylated product, probably due to the hygroscopic character of the TEG side chain.

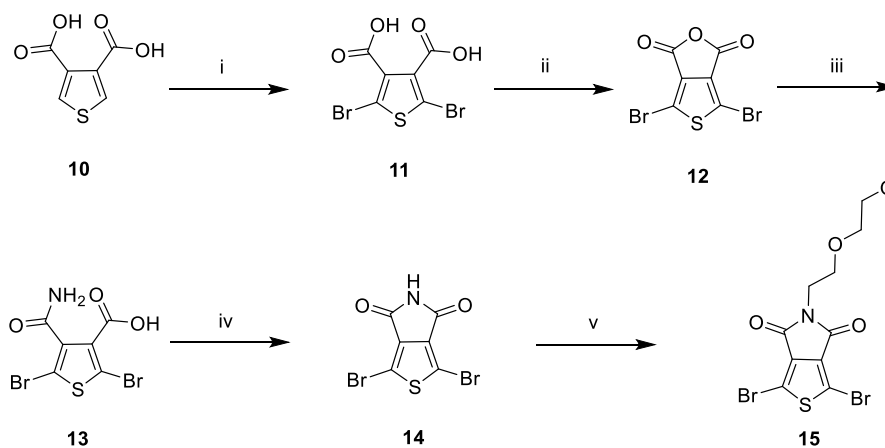


**Scheme 1.** Synthesis of bis(stannyl)-CPDT monomers **6** and **9**: i) LDA, CuCl<sub>2</sub>, THF, RT overnight at RT; 72%; ii) *n*-BuLi, ClCONMe<sub>2</sub>, THF, overnight at RT; 76%; iii) 2-ethylhexylphosphonium bromide, *n*-BuLi, THF, 2 h at -78 °C, overnight at RT; 77%; iv) LiAlH<sub>4</sub>, 1-chloro-2-(2-(2-methoxyethoxy)ethoxy)ethane, MTBE, 60 °C, overnight at RT; 62%; v) *n*-BuLi, SnMe<sub>3</sub>Cl, 1.5 h at -78 °C, overnight at RT; 54%; vi) 1-chloro-2-(2-methoxyethoxy)ethane, KI, KOH, DMSO, overnight at RT; 58%; vii) *n*-BuLi, SnMe<sub>3</sub>Cl, 1.5 h at -78 °C, overnight at RT; 65%.

A shorter sequence was used to synthesize symmetrical di(ethylene glycol) (DEG) substituted CPDT monomer **9** (Scheme 1). The two side chains were introduced on commercially available CPDT with the aid of KOH and KI, followed by a distannylation reaction to obtain the desired monomer. Also in this case it was

important to use at least 6 equivalents of *n*-BuLi to force the reaction toward the distannylated product. The final CPDT monomers (**6** and **9**) were purified by (recycling) preparative size exclusion chromatography (prep-SEC) to eliminate residual impurities, allowing a proper stoichiometric balance in the polymerization reactions.

To synthesize the TPD acceptor building block, a literature procedure was used (Scheme 2),<sup>[32]</sup> starting from thiophene-3,4-dicarboxylic acid (**10**) which was first brominated. Acetic anhydride was then added in the next step, which resulted in a ring closure to obtain compound **12**. Ammonia was subsequently added, which again opened up the ring, resulting in compound **13** containing a carbamoyl and a carboxylic acid group. In the next reaction, another ring closure was performed to obtain the bare TPD unit **14** without any side chain attached. Through reaction with 1-bromo-2-(2-methoxyethoxy)ethane in the presence of KOH, the DEG substituted TPD monomer **15** was finally obtained. Recrystallization from methanol afforded the molecule in high purity, ready for the polymerization reaction.



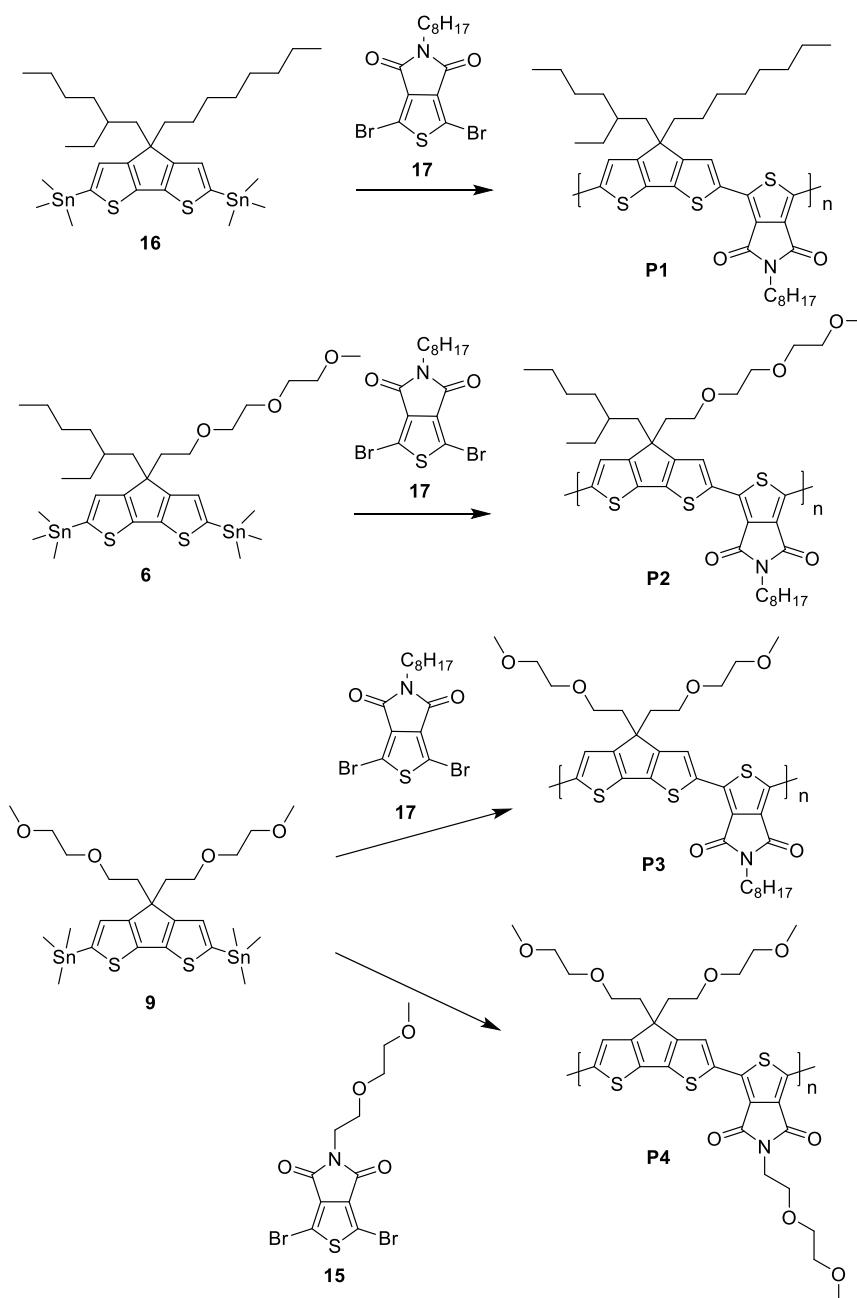
**Scheme 2.** Synthesis of dibromo-TPD monomer **15**: i)  $\text{Br}_2$ , acetic acid, overnight at 85 °C; 67%; ii) acetic anhydride, overnight at 140 °C; 96%; iii)  $\text{NH}_3$  (7 M in MeOH), THF, 30 min, then HCl (12 M), 30 min; 73%; iv)  $\text{Et}_3\text{N}$ , 1,1'-carbonyldiimidazole, THF, 12 h at RT; 81%; v) NaH (60%), DMF, 1 h at RT, then 1-bromo-2-(2-methoxyethoxy)ethane, 12 h at 50 °C; 56%.

The different monomers (**6**, **9**, **15** and regular 1,3-dibromo-5-octyl-4*H*-thieno[3,4-*c*]pyrrole-4,6(5*H*)-dione) were then copolymerized using a Stille polycondensation approach under standard conditions (2 mol% Pd<sub>2</sub>dba<sub>3</sub>, 8 mol% P(*o*-tol)<sub>3</sub>, toluene/DMF 5/1, 16 h at reflux; Scheme 3). Moving from **P1** to **P4**, the number of glycol side chains was increased in a stepwise manner. The resulting crude polymer materials were precipitated in methanol and further purified using Soxhlet extractions to remove catalyst residues and low molar mass species. All polymers were soluble in common organic solvents such as chloroform and THF. Number averaged molar masses (*M<sub>n</sub>*) as obtained by analytical SEC were 9, 10, 17 and 22 kg mol<sup>-1</sup> for **P1**, **P2**, **P3** and **P4**, respectively (Table 1).

**Table 1.** Characterization data for PCPDTPD polymers **P1–P4**.

	<i>M<sub>n</sub></i> <sup>a</sup> / kg mol <sup>-1</sup>	<i>D</i>	<i>ε<sub>r</sub></i>	<i>λ</i> <sub>max</sub> <sup>b</sup> / nm	<i>E<sub>g</sub></i> ,film <sup>c</sup> / eV	<i>E<sub>g</sub></i> ,cv <sup>e</sup> / eV	<i>E</i> <sub>HOMO</sub> <sup>f</sup> / eV	<i>E</i> <sub>LUMO</sub> <sup>f</sup> / eV
<b>P1</b>	9	1.4	3.1±0.1	677	1.72	2.19	-5.54	-3.35
<b>P2</b>	10	1.3	3.8±0.1	627	1.66	1.98	-5.44	-3.46
<b>P3</b>	17	1.6	4.9±0.1	641	1.62	1.85	-5.34	-3.49
<b>P4</b>	22	1.6	6.3±0.1	649	1.63	1.74	-5.30	-3.56

<sup>a</sup> Measured by SEC at 40 °C in THF. <sup>b</sup> Films were prepared by drop-casting a solution of the polymer onto a quartz disc. <sup>c</sup> Optical bandgap, determined by the onset of the solid-state UV-Vis spectrum. <sup>d</sup> Onset potential vs. Fc/Fc<sup>+</sup>. <sup>e</sup> Electrochemical bandgap. <sup>f</sup> Determined from the onset of oxidation/reduction in CV.



**Scheme 3.** P(CPDT-*alt*-TPD) copolymer synthesis by Stille cross-coupling (similar reaction conditions were used for all polymerizations: 2 mol% Pd<sub>2</sub>dba<sub>3</sub>, 8 mol% P(*o*-tol)<sub>3</sub>, toluene/DMF 5/1, 16 h at reflux).

To analyze the exact chemical composition of the polymers, MALDI-TOF (matrix-assisted laser desorption ionization time-of-flight) mass spectrometry was performed. The spectrum of **P4** (Figure S1) clearly reveals the expected alternating copolymer structure, but also the occurrence of homo-coupling species resulting from side reactions in the Stille polycondensation.<sup>[33]</sup> Furthermore, when looking in more detail at the peak distribution (Figure S2), especially methyl terminated oligomeric chains are observed. This implies that a methyl shift occurred during the transmetalation step of the Stille cross-coupling, impeding further chain growth.<sup>[33c,34]</sup>

The thermal properties of the novel polymers were evaluated by means of thermogravimetric analysis (TGA) and rapid heat-cool calorimetry (RHC) (Figure S3-S4). TGA showed that all polymers are thermally stable (i.e. they do not lose any mass) up to 300–325 °C. RHC analysis, preferred over regular differential scanning calorimetry (DSC) because of the improved sensitivity to thermal shifts as a result of the fast scanning rate and the low quantities needed,<sup>[35]</sup> indicated that **P1** and **P2** show a melting trajectory, whereas **P3** and **P4** do not show any kind of melting behavior up to 300 °C (Figure S4). Two different explanations can be given for the absence of a melting behavior for **P3** and **P4**: i) the different side chains prevent crystallization, or ii) the melting peak of both polymers is out of range (i.e. above 300 °C, when degradation sets in).

Figure 1 shows the normalized UV-Vis absorption spectra for all polymers in chloroform solution and as thin films. The optical properties are summarized in Table 1. A bathochromatic shift is observed for all polymers when going from solution to thin film, indicating the tendency to aggregate in the solid state. Besides the red-shift, also some peak broadening and an increase of the absorption at approximately 610 nm (at the expense of the shoulder at ~680 nm) can be seen. **P3** and **P4** show the most pronounced peak broadening and strongest tendency to aggregate in the solid state, probably because of the more flexible OEG side chains.<sup>[19b]</sup> On the other hand, **P1** already shows a pronounced shoulder at higher wavelength in solution, while the absorption onset remains almost unaffected in thin film. The optical bandgaps, measured in terms of the onset of absorption in the solid state, are 1.72, 1.66, 1.62 and 1.63 eV for **P1**,

**P2**, **P3** and **P4**, respectively, showing a progressive decrease in bandgap upon the replacement of alkyl side chains with OEG.

The electrochemical features of the polymers were investigated by cyclic voltammetry (CV) via the onset potentials of the oxidation and reduction (Figure S5-S6). It can be seen that the HOMO energy levels of the polymers gradually shift up from **P1** to **P4**, whereas the LUMO energy levels slightly go down. This results in a decrease of the electrochemical bandgap of the polymers, in agreement with the UV-Vis absorption trend. The shifts in the energy levels can be attributed to the higher chain flexibility of the OEG side chains, resulting in stronger interchain interactions and closer  $\pi$ - $\pi$  stacking, as mentioned before for OEG substituted materials.<sup>[22]</sup>

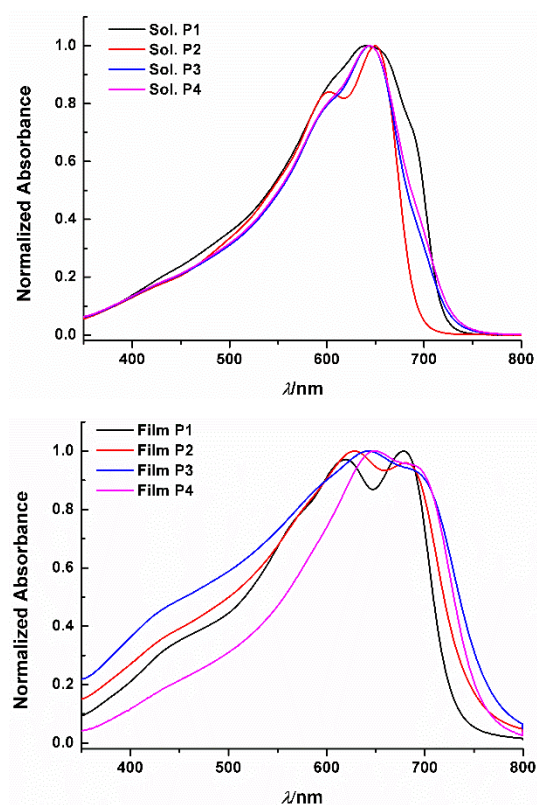


**Figure 1.** Normalized UV-Vis absorption spectra for **P1**, **P2**, **P3** and **P4** in chloroform solution (top) and thin film (bottom).

### **Dielectric constant analysis**

The dielectric constants of the semiconducting polymers were evaluated by means of impedance spectroscopy measurements on ITO/PEDOT:PSS/polymer/Al sandwich structures. The samples consisted of a glass substrate with four ITO areas acting as the bottom electrode, a PEDOT:PSS layer, a spin-cast sample polymer layer acting as the dielectric and four evaporated aluminum contacts as the top electrode. Varying the film thickness of the polymer layer was achieved by changing the spin-coating conditions, in such a way that thicknesses between 100 and 150 nm were obtained for each material. The examined frequencies ranged from 100 Hz to 1 MHz and the acquired data were fitted to model the response of the equivalent circuit of a real capacitor - i.e. resistance  $R_s$  in series with parallel circuit of ideal capacitor  $C$  and parallel resistance  $R_p$  - with less than 1% error (Figure S7 and S8). Table 1 and Figure 2 list the obtained  $\epsilon_r$  values of the pure polymers along with their errors (0.1 for all tested capacitors). During the impedance measurements of various capacitors, very small deviations were obtained, resulting in reliable values for  $\epsilon_r$ . There is a clear trend of increasing  $\epsilon_r$  upon addition of the OEG chains on the polymer backbone. The reference polymer **P1** has a 'standard'  $\epsilon_r$  of  $3.1 \pm 0.1$ , characteristic for conjugated polymers bearing regular alkyl side chains. Upon the gradual addition of glycol chains,  $\epsilon_r$  increases in a stepwise fashion, to  $3.8 \pm 0.1$  for **P2** and  $4.9 \pm 0.1$  for **P3**, and reaching a maximum of  $6.3 \pm 0.1$  for polymer **P4** bearing 3 OEG chains. Such a substantial increase of the dielectric constant can be attributed to the enhanced  $\pi$ - $\pi$  stacking and the higher flexibility of the glycol substituents, which enable a fast change in the direction of the dipoles,<sup>[21,22]</sup> rendering **P4** one of the push-pull polymers with the highest  $\epsilon_r$  values reported thus far.<sup>[26]</sup>

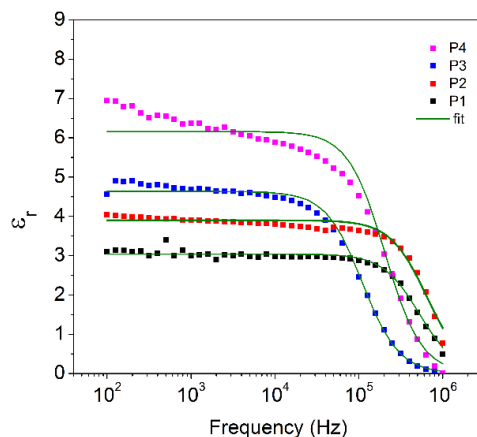


**Figure 2.** Dielectric constants of polymers **P1–P4** plotted vs. frequency.

#### ***OPV device fabrication and analysis***

To evaluate the influence of the side chain modification and the dielectric constant enhancement on the device efficiency of organic solar cells encompassing these materials, the four polymers were blended with [70]PCBM and applied as active layers in BHJ polymer solar cells with a traditional device architecture (glass/ITO/PEDOT:PSS/active layer/Ca/Al). The photovoltaic performances of all polymers are summarized in Table 2 (with additional data in Table S1). First of all, the devices were optimized by targeting optimal layer thicknesses and varying the donor:acceptor ratios (from 1:1.5 to 1:3). The photoactive layer thicknesses affording maximum PCEs depend on the polymer material. The devices based on **P1** and **P2** showed optimal layer thicknesses of 70 and 90 nm, respectively, whereas the solar cells made from **P3** and **P4** afforded the highest efficiencies for layers around 120 nm. This might be related to the higher  $\epsilon_r$  values for these materials, which should in principle reduce recombination processes in the active layer blend. The polymer to [70]PCBM weight ratios showed an optimum at 1:1.5 or 1:2, depending on the polymer material. Different processing (co)solvents were then tested for acquiring favorable nanostructured blend morphologies. All polymers exhibited different optimal solvent systems (Table 2). **P1** showed the best photovoltaic properties ( $J_{sc} = 8.29 \text{ mA cm}^{-2}$ ,  $V_{oc} = 0.82 \text{ V}$ ,  $FF = 0.49$ ; Table 2) when processed from chlorobenzene without any additive, resulting in a best PCE of 3.3%. This efficiency is very similar to what was achieved before for an

analogous PCPDTPD polymer (bearing two 2-ethylhexyl side chains on the CPDT unit and the same octyl-substituted TPD; PCE = 3.5%).<sup>[27]</sup>

**Table 2.** OPV device parameters for the BHJ polymer solar cells based on **P1–P4** (in combination with [70]PCBM).

Polymer	Solvent <sup>a</sup>	Ratio <sup>b</sup> / wt%	Additive	V <sub>oc</sub> / V	J <sub>sc</sub> / mA cm <sup>-2</sup>	FF	PCE <sup>d</sup> / %
<b>P1</b>	CB	1:2	/	0.82	8.29	0.49	3.30 (2.88)
<b>P2</b>	ODCB	1:2	/	0.78	8.77	0.46	3.14 (2.91)
<b>P3</b>	ODCB	1:1.5	2% DIO <sup>c</sup>	0.64	13.01	0.53	4.42 (4.31)
<b>P3</b>	Anisole	1:1.5	2% DIO <sup>c</sup>	0.64	10.91	0.57	3.97 (3.88)
<b>P4</b>	ODCB	1:2	1% DIO <sup>c</sup>	0.62	11.91	0.51	3.75 (3.72)
<b>P4</b>	Anisole	1:2	1% DIO <sup>c</sup>	0.60	11.04	0.53	3.48 (3.33)

<sup>a</sup> CB = chlorobenzene, ODCB = *ortho*-dichlorobenzene. <sup>b</sup> Polymer:[70PCBM]. <sup>c</sup> DIO = 1,8-diodooctane. <sup>d</sup> Best efficiencies, with averages over at least 4 devices in brackets.

The substitution of one CPDT alkyl side chain for a tri(ethylene glycol) substituent in **P2** afforded no real enhancement of the OPV characteristics and very similar average efficiencies were achieved for **P1** and **P2** (Table 2). However, a further increase of the OEG/alkyl ratio in **P3** did result in an increased performance, with a best device efficiency of 4.4% ( $J_{sc} = 13.01 \text{ mA cm}^{-2}$ ,  $V_{oc} = 0.64 \text{ V}$ ,  $FF = 0.53$ ; Table 2, Figure 3). As anticipated, the output parameter which is influenced most is the short-circuit current density, increasing from  $\sim 8$  to  $13 \text{ mA cm}^{-2}$ . This can tentatively be attributed to the enhanced dielectric constant of the donor material, resulting in a more efficient charge generation because of the lower binding energy of the photogenerated excitons. The fill factor is also slightly higher, which could be due to diminished recombination. External quantum efficiencies were measured for all polymer solar cells to investigate the photo-response (Figure 4). All current densities obtained from the integration of the EQE spectra are within

5% of the  $J_{sc}$  values. For the device based on **P3**, an enhancement over the whole wavelength range is seen, with a maximum up to 70% at lower wavelengths. Remarkably, the best performing **P3**:[70]PCBM device showed a larger contribution at  $\sim 300\text{--}550\text{ nm}$  as compared to the other polymer devices, boosting the photocurrent. On the other hand, a drastic decrease of the open-circuit voltage (by 0.18 V as compared to **P1**) was observed as well, limiting the device efficiency. Finally, further substitution of a di(ethylene glycol) substituent on the TPD units in **P4** did not result in an improved device efficiency, although this material still performs better than the reference polymer **P1**, especially due to a higher  $J_{sc}$ , whereas the  $V_{oc}$  dropped even further. The decrease in  $V_{oc}$  when moving from **P1** to **P4** can be correlated to the upward shift in the HOMO levels of the polymers upon replacement of the alkyl side chains by more flexible OEG substituents (Table 1, 2).

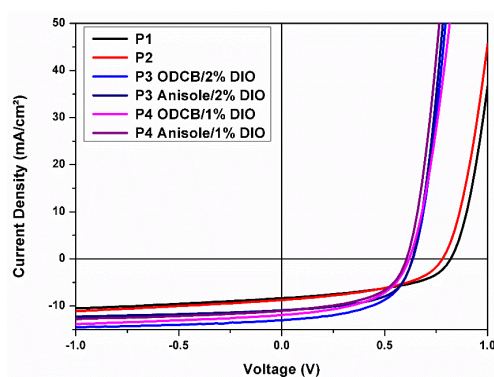


**Figure 3.**  $J$ - $V$  curves for the best polymer solar cells based on **P1–P4**.

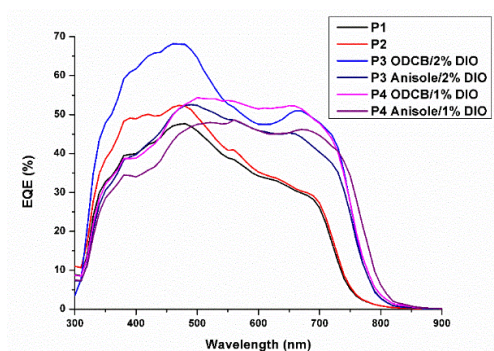


**Figure 4.** EQE spectra for the best polymer solar cells based on **P1–P4**.

Because of the higher polarity of (in particular) polymers **P3** and **P4**, alternative non-halogenated solvent systems were also studied to reduce the exposure to toxic solvents, of high relevance for industrial upscaling by roll-to-roll manufacturing. Comparable results were obtained for both **P3** and **P4** when processed from anisole with 1,8-diiodooctane as a co-solvent. Slightly lower short-circuit currents, but higher fill factors were measured, illustrating the beneficial green solvent processability of high- $\epsilon_r$  organic semiconductors.

To shed more light on the origin of the improved device performance achieved for high- $\epsilon_r$  polymers **P3** and **P4**, especially the higher  $J_{sc}$  values, the hole mobilities of the polymer materials were determined from OFET measurements and the BHJ active layer morphology was studied by means of atomic force microscopy (AFM) in tapping mode. All polymers displayed similar hole mobilities ( $\mu_{hole} = 9.9 \cdot 10^{-5}$ ,  $4.4 \cdot 10^{-5}$ ,  $5.4 \cdot 10^{-5}$ , and  $2.1 \cdot 10^{-5}$  cm<sup>2</sup>/Vs for **P1**, **P2**, **P3**, and **P4**, respectively). These results are in accordance with literature observations wherein organic semiconductors with OEG side chains exhibit similar hole mobilities as their hydrocarbon counterparts. <sup>[16b,1c,19b,21a]</sup> This implies that the higher  $J_{sc}$  values cannot simply be attributed to enhanced hole mobilities. The AFM topographic images of the best BHJ polymer solar cells are shown in Figure 5. The blends consisting of either **P1** or **P2** in combination with [70]PCBM show a very fine, fully intermixed morphology, with almost no distinct phase separation. On the other hand, the active layers based on **P3** and **P4** display a more rough morphology, both when processed from *ortho*-dichlorobenzene and anisole. Regarding the higher device performances of these solar cells, it seems important that a fine intermixing of the donor and acceptor is achieved, but also enriched domains of the pure materials are required to create efficient percolation pathways for the charge carriers.

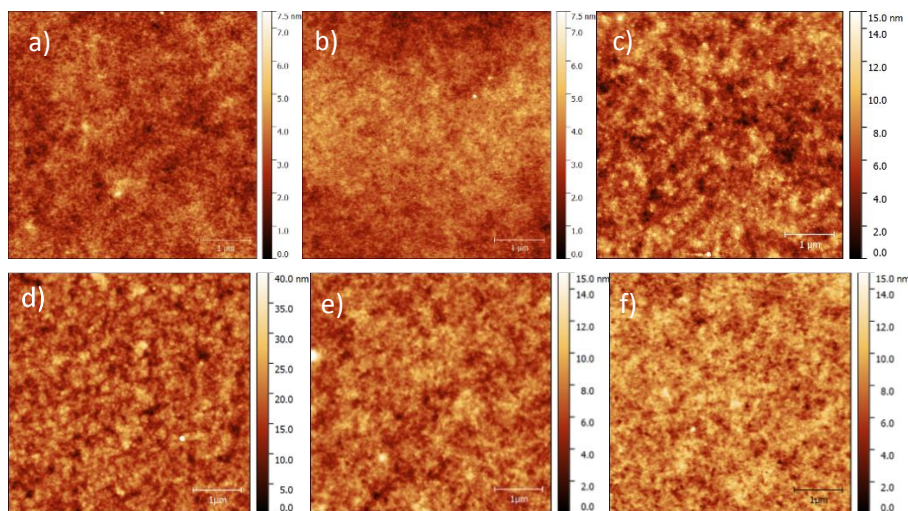


**Figure 5.** AFM images ( $5.0 \times 5.0 \mu\text{m}$ ) of the active layer blends (affording the best OPV devices) based on [70]PCBM in combination with a) **P1** (CB), b) **P2** (ODCB), c) **P3** (ODCB + 2% DIO), d) **P3** (anisole + 2% DIO), e) **P4** (ODCB + 1% DIO), and f) **P4** (anisole + 1% DIO).

### 3.3 Conclusions

In summary, four new PCPDTTPD-type donor-acceptor copolymers were designed, synthesized and characterized with the aim to enhance their dielectric properties. Glycol side chains were chosen to increase the polarizability of the resulting polymers, which is directly correlated to the permittivity. A clear trend in  $\epsilon_r$  was observed when gradually replacing the alkyl side chains with oligo(ethylene glycol) moieties, resulting in a PCPDTTPD-type low bandgap polymer with an  $\epsilon_r$  up to 6.3, more than doubled compared to the reference alkyl substituted polymer. This is a record dielectric constant for conjugated polymer materials in our hands. Higher short-circuit currents were obtained in polymer solar cells prepared from the most 'glycolated' polymers. Despite the fact that a simultaneous decrease in open-circuit voltage (as a result of the higher HOMO energy levels) limits the final efficiency improvement, an increased power conversion efficiency was achieved, which can likely partly be attributed to the higher dielectric constant of the donor material, facilitating charge extraction. Moreover, an alternative halogen-free

processing solvent (anisole) was also used and similar device parameters were obtained, a promising result in terms of sustainability. The enhanced dielectric properties and improved device characteristics illustrate the high potential of ethylene glycol-based side chains as alternatives to the widely used solubilizing alkyl side chains. Current work focuses on further enhancement of the dielectric properties of conjugated polymer materials and their application in OPD and PV (organic as well as hybrid perovskite) devices. Moreover, some efforts are done to translate these results to a system where a high- $\epsilon_r$  donor material (e.g. **P4**) is combined with a high- $\epsilon_r$  (glycolated) electron acceptor. The ultimate goal remains, however, to use a high- $\epsilon_r$  organic semiconductor in an efficient homojunction (*i.e.* single layer) PV device.

### 3.4 Experimental section

#### **Materials and methods**

(4-(2-Ethylhexyl)-4-octyl-4*H*-cyclopenta[2,1-*b*:3,4-*b'*]dithiophene-2,6-diyl) bis(trimethylstannane) (**16**) was prepared according to a literature procedure.<sup>[30b]</sup> All other reagents and chemicals were obtained from commercial sources and used without further purification. Solvents were dried by a solvent purification system (MBraun, MB-SPS-800) equipped with alumina columns. Preparative (recycling) size exclusion chromatography was performed on a JAI LC-9110 NEXT system equipped with JAIGEL 1*H* and 2*H* columns (eluent CHCl<sub>3</sub>, flow rate 3.5 mL min<sup>-1</sup>). NMR chemical shifts ( $\delta$ , in ppm) were determined relative to the residual CHCl<sub>3</sub> (7.26 ppm) absorption or the <sup>13</sup>C resonance shift of CDCl<sub>3</sub> (77.16 ppm). High resolution ESI-MS was performed using a LTQ Orbitrap Velos Pro mass spectrometer equipped with an atmospheric pressure ionization source operating in the nebulizer assisted electrospray mode. The instrument was calibrated in the *m/z* range 220–2000 using a standard solution containing caffeine, MRFA and Ultramark 1621. MALDI-TOF mass spectra were recorded on a Bruker Daltonics Ultraflex II ToF/ToF. A total of 1  $\mu$ L of the matrix solution (4 mg mL<sup>-1</sup> DTCB (*trans*-2-[3-(4-*tert*-butylphenyl)-2-methyl-2-propenylidene] malononitrile) in CHCl<sub>3</sub>) was spotted onto an MTP Anchorchip 600/384 MALDI plate. The spot was allowed to dry and 1  $\mu$ L of the analyte solution (0.5 mg mL<sup>-1</sup> in chloroform) was spotted on top of the matrix. UV-Vis absorption spectroscopy

measurements were performed on a VARIAN Cary 5000 UV-Vis spectrophotometer at a scan rate of 600 nm min<sup>-1</sup>. The films for the UV-Vis absorption measurements were prepared by drop casting a solution of the respective polymer in chloroform on a quartz substrate. The solid-state UV-Vis absorption spectra were used to estimate the optical bandgaps (from the wavelength at the intersection of the tangent line drawn at the low energy side of the absorption spectrum with the baseline:  $E_g$  (eV) = 1240/(wavelength in nm)). Analysis of the molar masses and molar mass distributions of the polymers was performed on a Tosoh EcoSEC System, comprising of an autosampler, a PSS guard column SDV (50 x 7.5 mm) followed by three PSS SDV analytical linear XL columns (5  $\mu$ m, 300 x 7.5 mm), and a UV-detector using THF as the eluent at 40 °C with a flow rate of 1.0 mL min<sup>-1</sup>. The SEC system was calibrated using linear narrow polystyrene standards ranging from 474 to 7.5 x 10<sup>6</sup> g/mol ( $K = 14.1 \times 10^{-5}$  dL g<sup>-1</sup> and  $\alpha = 0.70$ ). Electrochemical measurements (cyclic voltammetry) were performed with an Eco Chemie Autolab PGSTAT 30 potentiostat/galvanostat using a three-electrode microcell with a platinum working electrode, a platinum counter electrode and a Ag/AgNO<sub>3</sub> reference electrode (silver wire dipped in a solution of 0.01 M AgNO<sub>3</sub> and 0.1 M NBu<sub>4</sub>PF<sub>6</sub> in anhydrous acetonitrile). The reference electrode was calibrated against ferrocene/ferrocenium as an external standard. Samples were prepared by dip coating the platinum working electrode in the respective polymer solutions (also used for the solid-state UV-Vis measurements). The CV measurements were done on the resulting films with 0.1 M NBu<sub>4</sub>PF<sub>6</sub> in anhydrous acetonitrile as electrolyte solution. To prevent air from entering the system, the experiments were carried out under a curtain of argon. Cyclic voltammograms were recorded at a scan rate of 100 mV s<sup>-1</sup>. For the conversion of V to eV, the onset potentials of the first oxidation/reduction peaks were used and referenced to ferrocene/ferrocenium, which has an ionization potential of -4.98 eV vs. vacuum. This correction factor is based on a value of 0.31 eV for Fc/Fc<sup>+</sup> vs. SCE<sup>[36]</sup> and a value of 4.68 eV for SCE vs. vacuum<sup>[37]</sup>:  $E_{\text{HOMO/LUMO}}$  (eV) = -4.98 -  $E_{\text{onset ox/red}}^{\text{Ag/AgNO}_3}$  (V) +  $E_{\text{onset Fc/Fc}^+}^{\text{Ag/AgNO}_3}$  (V). The accuracy of measuring redox potentials by CV is ~0.01–0.02 V. Reproducibility can be less because the potentials depend on concentration and temperature. Rapid heat-cool calorimetry (RHC) experiments were performed on a prototype RHC of TA Instruments, equipped with liquid nitrogen cooling and specifically designed

for operation at high scanning rates. RHC measurements were performed at 500 K min<sup>-1</sup> (after cooling at 20 K min<sup>-1</sup>) using aluminum crucibles filled with samples of 200–250 µg, using helium (10 mL min<sup>-1</sup>) as a purge gas. TGA experiments were performed at 20 K min<sup>-1</sup> in platinum crucibles on a TA Instruments Q5000 TGA using nitrogen (50 mL min<sup>-1</sup>) as purge gas.

### **Materials synthesis and characterization**

**3,3'-Dibromo-2,2'-bithiophene (2).**<sup>[30c]</sup> 3-Bromothiophene (32.6 g, 200 mmol) was dissolved in dry THF and LDA (100 mL, 200 mmol) was added dropwise at –78 °C under inert atmosphere. The solution was then stirred for 1.5 h at –78 °C. CuCl<sub>2</sub> (29.6 g, 220 mmol) was added and the reaction mixture was stirred overnight at room temperature. The reaction was quenched with a 1 M HCl solution, dichloromethane was added and the organic phase was washed with water (2×), dried over anhydrous MgSO<sub>4</sub> and filtered. The solvent was removed under reduced pressure and the crude product was purified by flash chromatography (silica, *n*-hexane: dichloromethane, 50:50) and Kugelrohr distillation (2×10<sup>-2</sup> mbar, 110 °C). After recrystallization from ethanol, 3,3'-dibromo-2,2'-bithiophene was obtained as white crystals (22.0 g, 72%). <sup>1</sup>H NMR (400 MHz, CDCl<sub>3</sub>), δ (ppm): 7.41 (d, *J* = 5.4 Hz, 2H), 7.08 (d, *J* = 5.4 Hz, 2H).

**4*H*-Cyclopenta[2,1-*b*:3,4-*b'*]dithiophen-4-one (3).**<sup>[31]</sup> 3,3'-Dibromo-2,2'-bithiophene (10.0 g, 30.8 mmol) was dissolved in dry diethyl ether and the solution was cooled to –78 °C under inert atmosphere. *n*-BuLi (27.2 mL, 67.9 mmol) was added dropwise to the solution and after stirring the solution for 1 h at –78 °C, dimethylcarbamoyl chloride (3.1 mL, 33.9 mmol) was added dropwise. The solution was then allowed to stir overnight at room temperature. Diethyl ether was added and the organic phase was washed with water (2×), dried over anhydrous MgSO<sub>4</sub> and filtered. The solvent was removed under reduced pressure. To obtain a pure product, recrystallization from ethanol was performed to obtain 4*H*-cyclopenta[2,1-*b*:3,4-*b'*]dithiophen-4-one as red crystals (4.5 g, 76%). <sup>1</sup>H NMR (400 MHz, CDCl<sub>3</sub>), δ (ppm): 7.04 (d, *J* = 4.8 Hz, 2H), 7.00 (d, *J* = 4.8 Hz, 2H).

**4-(2-Ethylhexylidene)-4*H*-cyclopenta[2,1-*b*:3,4-*b'*]dithiophene (4).**<sup>[30b]</sup> (2-Ethylhexyl)triphenylphosphonium bromide (12.26 g, 32.7 mmol) was

dissolved in dry THF and the solution was cooled to  $-78$  °C under inert atmosphere. *n*-BuLi (10.8 mL, 11.7 mmol) was added dropwise and the solution was allowed to stir for 30 min at this temperature. 4*H*-cyclopenta[2,1-*b*:3,4-*b'*]dithiophen-4-one (4.00 g, 20.9 mmol) was dissolved in dry diethyl ether (30 mL) and added to the previously prepared solution. The reaction mixture was then stirred overnight at room temperature. Diethyl ether was added and the organic phase was washed with water (2×), dried over anhydrous MgSO<sub>4</sub> and filtered. The crude product was purified by column chromatography (silica, eluent petroleum ether) to yield 4-(2-ethylhexylidene)-4*H*-cyclopenta[2,1-*b*:3,4-*b'*]dithiophene as a yellow solid (4.6 g, 77%). <sup>1</sup>H NMR (400 MHz, CDCl<sub>3</sub>), δ (ppm): 7.28 (d, *J* = 4.9 Hz, 2H), 7.15 (d, *J* = 4.9 Hz, 2H), 6.16 (d, *J* = 10.5 Hz, 1H), 2.94–2.83 (m, 1H), 1.72–1.58 (m, 2H), 1.50–1.39 (m, 2H), 1.33–1.25 (m, 4H), 0.92 (t, *J* = 7.4 Hz, 3H), 0.85 (t, *J* = 7.0 Hz, 3H).

**4-(2-Ethylhexyl)-4-(2-(2-(2-methoxyethoxy)ethoxy)ethyl)-4*H*-cyclopenta[2,1-*b*:3,4-*b'*]di-thiophene (5).** A solution of 4-(2-ethylhexylidene)-4*H*-cyclopenta[2,1-*b*:3,4-*b'*]dithiophene (0.33 g, 1.14 mmol) and 1-chloro-2-(2-(2-methoxyethoxy)ethoxy)ethane (0.27 g, 1.48 mmol) in dry methyl *tert*-butyl ether (MTBE) was added to a suspension of LiAlH<sub>4</sub> (0.115 g, 1.37 mmol) in dry MTBE at 60 °C under inert atmosphere. The reaction was stirred overnight at room temperature. 1 M HCl solution and dichloromethane were added and the organic phase was washed with NaHCO<sub>3</sub> and water (2×), dried over anhydrous MgSO<sub>4</sub> and filtered. The crude product was purified by column chromatography (silica, eluent petroleum ether:diethyl ether, 70:30) to obtain 4-(2-ethylhexyl)-4-(2-(2-(2-methoxyethoxy)ethoxy)ethyl)-4*H*-cyclopenta[2,1-*b*:3,4-*b'*]dithiophene as a pale oil (0.31 g, 62%). <sup>1</sup>H NMR (300 MHz, CDCl<sub>3</sub>), δ (ppm): 7.13 (d, *J* = 4.9 Hz, 2H), 6.99–6.88 (m, 2H), 3.61–3.53 (m, 2H), 3.54–3.44 (m, 4H), 3.36 (s, 3H), 3.32 (t, *J* = 4.8 Hz, 2H), 2.94 (t, *J* = 7.5 Hz, 2H), 2.22 (t, *J* = 7.7 Hz, 2H), 1.96–1.80 (m, 2H), 1.11–0.78 (m, 8H), 0.75 (t, *J* = 6.9 Hz, 3H), 0.67–0.52 (m, 4H). <sup>13</sup>C NMR (75 MHz, CDCl<sub>3</sub>), δ (ppm): 157.1, 157.0, 136.8, 124.6, 122.0, 72.0, 70.7, 70.6, 70.1, 67.8, 59.1, 51.3, 42.3, 38.6, 35.1, 34.2, 28.7, 27.3, 22.8, 14.2, 10.8. HRMS (ESI+): calcd. for C<sub>24</sub>H<sub>36</sub>O<sub>3</sub>S<sub>2</sub> [M+H]<sup>+</sup>: 437.2186, measured: 437.2168.

**(4-(2-Ethylhexyl)-4-(2-(2-(2-methoxyethoxy)ethoxy)ethyl)-4H-cyclopenta[2,1-*b*:3,4-*b'*]di-thiophene-2,6-diyl)bis(trimethylstannane)**

**(6).** 4-(2-Ethylhexyl)-4-(2-(2-(2-methoxyethoxy)-ethoxy)ethyl)-4H-cyclopenta[2,1-*b*:3,4-*b'*]dithiophene (0.30 g, 0.687 mmol) was dissolved in dry THF under inert atmosphere. The reaction mixture was protected from light and cooled down to  $-78$  °C before *n*-BuLi (1.9 mL, 4.8 mmol) was added dropwise to the solution and the reaction mixture was stirred for another 30 min under inert atmosphere at  $-78$  °C. Trimethyltin chloride (5.5 mL, 5.5 mmol) was added and the reaction mixture was stirred overnight at room temperature. Diethyl ether was added and the organic phase was washed with water (2×), dried over anhydrous MgSO<sub>4</sub> and filtered. Further purification was done by recycling prep-SEC (CHCl<sub>3</sub>) to yield (4-(2-ethylhexyl)-4-(2-(2-(2-methoxyethoxy)ethoxy)ethyl)-4H-cyclopenta[2,1-*b*:3,4-*b'*]dithiophene-2,6-diyl)bis(trimethylstannane) (0.28 g, 54%). <sup>1</sup>H NMR (400 MHz, CDCl<sub>3</sub>), δ (ppm): 6.98–6.90 (m, 2H), 3.59–3.55 (m, 2H), 3.52–3.47 (m, 4H), 3.35 (s, 3H), 3.34–3.31 (m, 2H), 2.99–2.93 (t, *J* = 7.6 Hz, 2H), 2.23 (t, *J* = 7.7 Hz, 2H), 1.92–1.78 (m, 2H), 1.03–0.84 (m, 8H), 0.73 (t, *J* = 7.0 Hz, 3H), 0.68–0.55 (m, 4H), 0.44–0.29 (m, 18H).

**4,4-Bis(2-(2-methoxyethoxy)ethyl)-4H-cyclopenta[2,1-*b*:3,4-*b'*]dithiophene (8).**

4H-Cyclopenta[2,1-*b*:3,4-*b'*]dithiophene (0.200 g, 1.12 mmol), 1-chloro-2-(2-methoxyethoxy)ethane (0.621 g, 4.48 mmol) and KI (5.6 mg, 0.034 mmol) were dissolved in DMSO (20 mL) and KOH (0.22 g, 3.9 mmol) was slowly added in portions at 0 °C. The reaction mixture was stirred overnight at room temperature. Dichloromethane was added and the organic phase was washed with water (2×), dried over anhydrous MgSO<sub>4</sub> and filtered. The crude product was purified by column chromatography (silica, eluent petroleum ether:ethyl acetate, 70:30) to yield 4,4-bis(2-(2-methoxyethoxy)ethyl)-4H-cyclopenta[2,1-*b*:3,4-*b'*]dithiophene (0.251 g, 58%). <sup>1</sup>H NMR (400 MHz, CDCl<sub>3</sub>), δ (ppm): 7.15 (d, *J* = 4.9 Hz, 2H), 6.96 (d, *J* = 4.9 Hz, 2H), 3.39–3.36 (m, 4H), 3.31 (s, 6H), 3.31–3.28 (m, 4H), 2.99 (t, *J* = 7.6 Hz, 4H), 2.28 (t, *J* = 7.5 Hz, 4H). <sup>13</sup>C NMR (100 MHz, CDCl<sub>3</sub>), δ (ppm): 156.5, 136.6, 125.1, 121.8, 71.9, 70.1, 67.7, 59.1, 49.2, 37.7. HRMS (ESI+): calcd. for C<sub>19</sub>H<sub>26</sub>O<sub>4</sub>S<sub>2</sub> [M+H]<sup>+</sup>: 383.1353, measured: 383.1344.

**(4,4-Bis(2-(2-methoxyethoxy)ethyl)-4H-cyclopenta[2,1-*b*:3,4-*b'*]dithiophene-2,6-diyl)bis(trimethylstannane) (9).** 4,4-Bis(2-(2-methoxyethoxy)ethyl)-4H-cyclopenta[2,1-*b*:3,4-*b'*]dithiophene (0.247 g, 0.644 mmol) was dissolved in dry THF under inert atmosphere. The reaction mixture was cooled to -40 °C before *n*-BuLi (1.55 mL, 3.87 mmol) was added dropwise to the solution and the reaction mixture was stirred for another 30 min under inert atmosphere at -40 °C. Trimethyltin chloride (4.2 mL, 4.2 mmol) was added and the reaction mixture was stirred overnight at room temperature. Diethyl ether was added and the organic phase was washed with water (2×), dried over anhydrous MgSO<sub>4</sub> and filtered. Further purification was done by recycling prep-SEC (CHCl<sub>3</sub>) to yield (4,4-bis(2-(2-methoxyethoxy)ethyl)-4H-cyclopenta[2,1-*b*:3,4-*b'*]dithiophene-2,6-diyl)bis(trimethylstannane) (0.269 g, 65%). <sup>1</sup>H NMR (400 MHz, CDCl<sub>3</sub>), δ (ppm): 6.96 (s, 2H), 3.40–3.36 (m, 4H), 3.33–3.30 (m, 10H), 3.00 (t, *J* = 7.6 Hz, 4H), 2.28 (t, *J* = 7.6 Hz, 4H), 0.45–0.30 (m, 18H).

**2,5-Dibromothiophene-3,4-dicarboxylic acid (11).** Prepared according to a reported procedure.<sup>[32]</sup>

**4,6-Dibromo-1H,3H-thieno[3,4-*c*]furan-1,3-dione (12).** Prepared according to a reported procedure.<sup>[32]</sup>

**2,5-Dibromo-4-carbamoylthiophene-3-carboxylic acid (13).** Prepared according to a reported procedure.<sup>[32]</sup>

**1,3-Dibromo-4H-thieno[3,4-*c*]pyrrole-4,6(5H)-dione (14).** Prepared according to a reported procedure.<sup>[32]</sup>

**1,3-Dibromo-5-(2-(2-methoxyethoxy)ethyl)-4H-thieno[3,4-*c*]pyrrole-4,6(5H)-dione (15).** NaH (60%; 0.19 g, 4.76 mmol) was added slowly to 1,3-dibromo-4H-thieno[3,4-*c*]pyrrole-4,6(5H)-dione (1.14 g, 3.66 mmol) in dry DMF under inert atmosphere. The reaction mixture was stirred at room temperature for 1 h and then added dropwise to a 50 °C solution of 1-bromo-2-(2-methoxyethoxy)ethane (1.00 mL, 7.43 mmol) in dry DMF. The reaction mixture was subsequently stirred overnight at room temperature. Dichloromethane was added and the organic phase was washed with water (2×), dried over anhydrous MgSO<sub>4</sub> and filtered. The solvent was removed under reduced pressure and the residue was purified by column chromatography (silica, eluent *n*-

hexane:dichloromethane, 50:50). The solvent was removed under reduced pressure and the crude product was recrystallized from methanol to yield pure *1,3-dibromo-5-(2-(2-methoxyethoxy)ethyl)-4H-thieno[3,4-c]pyrrole-4,6(5H)-dione* (0.70 g, 46 %). <sup>1</sup>H NMR (400 MHz, CDCl<sub>3</sub>), δ (ppm): 3.82 (t, *J* = 5.8 Hz, 2H), 3.72 (t, *J* = 5.7 Hz, 2H), 3.66–3.62 (m, 2H), 3.52–3.49 (m, 2H), 3.35 (s, 3H). <sup>13</sup>C NMR (75 MHz, CDCl<sub>3</sub>), δ (ppm): 160.1, 134.6, 113.1, 71.8, 69.8, 67.5, 59.0, 37.7. HRMS (ESI+): calcd. for C<sub>11</sub>H<sub>11</sub>Br<sub>2</sub>NO<sub>4</sub>S [M+H]<sup>+</sup>: 411.8856, measured: 411.8850.

**1,3-Dibromo-5-octyl-4H-thieno[3,4-c]pyrrole-4,6(5H)-dione (17).**

Prepared according to a reported procedure.<sup>[38]</sup>

**(4-(2-Ethylhexyl)-4-octyl-4H-cyclopenta[2,1-*b*:3,4-*b'*]dithiophene-2,6-diyl)bis(trimethyl-stannane) (16).** Prepared according to a reported procedure.<sup>[30b]</sup>

**PCPDTPD P1. General polymerization method:** A mixture of (4-(2-ethylhexyl)-4-octyl-4H-cyclopenta[2,1-*b*:3,4-*b'*]dithiophene-2,6-diyl)bis(trimethylstannane) (**16**) (139 mg, 0.191 mmol) and 1,3-dibromo-5-octyl-4H-thieno[3,4-c]pyrrole-4,6(5H)-dione (**17**) (80.7 mg, 0.191 mmol) was dissolved in dry toluene (2.5 mL) and dry DMF (0.5 mL) and the solution was degassed for 20 min. Subsequently, Pd<sub>2</sub>(dba)<sub>3</sub> (3.48 mg, 3.8 μmol) and P(*o*-tol)<sub>3</sub> (4.6 mg, 15.2 μmol) were added and the mixture was stirred overnight at reflux temperature. The resulting crude polymer material was precipitated in methanol and purified by repetitive Soxhlet extractions with acetone, *n*-hexane and chloroform. The chloroform fraction was again precipitated in methanol and filtered, yielding a blue solid (102 mg, 80%). SEC (THF, 40 °C, PS standards): *M<sub>n</sub>* = 9 kg/mol, *D* = 1.4. UV-Vis (film): λ<sub>max</sub> = 677 nm.

**PCPDTPD P2.** Synthesis according to the general polymerization procedure: (4-(2-ethylhexyl)-4-(2-(2-(2-methoxyethoxy)ethoxy)ethyl)-4H-cyclopenta[2,1-*b*:3,4-*b'*]dithiophene-2,6-diyl)bis(trimethylstannane) (**6**) (75.7 mg, 0.099 mmol), TPD **17** (42.0 mg, 0.099 mmol), dry toluene (2.0 mL), dry DMF (0.4 mL). The polymer was obtained as a blue solid (43 mg, 62%). SEC (THF, 40 °C, PS standards): *M<sub>n</sub>* = 10 kg/mol, *D* = 1.3. UV-Vis (film): λ<sub>max</sub> = 627 nm.

**PCPDTPD P3.** Synthesis according to the general polymerization procedure: (4,4-bis(2-(2-methoxyethoxy)ethyl)-4*H*-cyclopenta[2,1-*b*:3,4-*b'*]dithiophene-2,6-diyl)bis(trimethylstan-nane) (**9**) (139 mg, 0.196 mmol), TPD **17** (83 mg, 0.196 mmol), dry toluene (2.5 mL), dry DMF (0.5 mL). The polymer was obtained as a blue solid (76 mg, 60%). SEC (THF, 40 °C, PS standards):  $M_n = 17$  kg/mol,  $\bar{D} = 1.6$ . UV-Vis (film):  $\lambda_{\max} = 641$  nm.

**PCPDTPD P4.** Synthesis according to the general polymerization procedure: (4,4-bis(2-(2-methoxyethoxy)ethyl)-4*H*-cyclopenta[2,1-*b*:3,4-*b'*]dithiophene-2,6-diyl)bis(trimethylstan-nane) (**9**) (50.5 mg, 0.0713 mmol), 1,3-dibromo-5-(2-(2-methoxyethoxy)ethyl)-4*H*-thieno[3,4-*c*]pyrrole-4,6(5*H*)-dione (**15**) (29.5 mg, 0.0713 mmol), dry toluene (2 mL), dry DMF (0.4 mL). The polymer was obtained as a blue solid (36 mg, 79%). SEC (THF, 40 °C, PS standards):  $M_n = 22$  kg/mol,  $\bar{D} = 1.6$ . UV-Vis (film):  $\lambda_{\max} = 649$  nm.

#### ***Dielectric constant measurements***

Impedance spectroscopy was performed in the range of 100 Hz to 1 MHz using a Solatron 1260 impedance gain-phase analyser with an AC drive voltage of 10 mV. All measurements were performed in N<sub>2</sub> at room temperature. Commercially available glass substrates patterned with ITO in four different dimensions (0.095, 0.1616, 0.357, and 0.995 cm<sup>2</sup>) were used as bottom electrode of the capacitors. The substrates were cleaned with soap/water solution, de-ionized water flushing, and sonication with acetone and isopropyl alcohol, followed by oven drying and UV-O<sub>3</sub> treatment. PEDOT:PSS (VP AI4083, H.C. Starck) was spin-cast in ambient conditions and oven dried at 140 °C for 10 min. All films were spun from chloroform under N<sub>2</sub> atmosphere and the Al top electrodes were deposited at a pressure of ca. 10<sup>-6</sup> mbar by thermal evaporation.

#### ***Solar cell and OFET fabrication and characterization***

Before device processing, the indium tin oxide (ITO, Kintec, 100 nm, 20 Ohm sq<sup>-1</sup>) containing substrates were thoroughly cleaned through sonication using soap, demineralized water, acetone, isopropyl alcohol, and a UV-O<sub>3</sub> treatment. Subsequently, a layer of PEDOT:PSS (Heraeus Clevios AI 4083) was spin-coated on top of the pre-patterned ITO substrates. Further processing was performed

under N<sub>2</sub> atmosphere in a glove box, starting with an annealing step at 130 °C for 15 min to remove any residual water. The polymer:[70]PCBM (> 99%, Solenne) active layers were spin-coated targeting thicknesses between 80 and 120 nm, as confirmed by profilometry (DEKTAK). The blend solutions providing highest efficiencies (**P3**) contained a 1:1.5 (polymer:[70]PCBM) ratio, with polymer concentrations of 10 mg mL<sup>-1</sup>, using *o*-dichlorobenzene as the processing solvent (see Table 2). On top of the active layer, Ca was evaporated *in vacuo* with a thickness of 30 nm, and the devices were finished off with Al as the top electrode, with a thickness of 80 nm. The active area (3.08 mm<sup>2</sup>) was defined using a mask. The output parameters of the BHJ polymer solar cells were measured using a Newport class A solar simulator (model 91195A), calibrated with a silicon solar cell to give a 1 sun AM 1.5G spectrum. EQE measurements were performed with a Newport Apex illuminator (100 W xenon lamp, 6257) as light source, a Newport Cornerstone 130 monochromator and a Stanford SR830 lock-in amplifier for the current measurements. Calibration was done with a certificated Si FDS-100 photodiode. For AFM imaging, a Park NX10 (manufactured by Park Systems) was used to image topography in non-contact mode. In non-contact mode, the AFM cantilever is vibrated near the surface of the sample. The distance between the cantilever and the sample during operation can be in the order of angstroms. This distance is dictated by the van der Waals forces that repel the cantilever at very close distances. Acta probes were used, manufactured by AppNano, which have a nominal spring constant of 37 N/m and a nominal cantilever length of 125 μm.

Field-effect transistors were prepared by spin-coating the polymers from chloroform with a concentration of 5 mg mL<sup>-1</sup> on 200 nm of thermally grown SiO<sub>2</sub>. The gate contact consisted of highly n-doped Si. Interdigitated source and drain electrodes were pre-patterned, comprising of a stack of Ti/Au (10/100 nm). FET substrates were acquired from Philips. The channel length was 10 μm. Two Keithley 2400 source meters were used to measure the *I*<sub>DS</sub> and correct it for leakage through the gate electrode. All FET preparations and characterizations were carried out in a N<sub>2</sub> filled glovebox.

### 3.5 References

- [1] Sax, S.; Rugen-Penkalla, N.; Neuhold, A.; Schuh, S.; Zojer, E.; List, E. J. W.; Müllen, K. *Adv. Mater.* **2010**, *22*, 2087.
- [2] Kanimozhi, C.; Yaacobi-Gross, N.; Chou, K. W.; Amassian, A.; Anthopoulos, T. D.; Patil, S. *J. Am. Chem. Soc.* **2012**, *134*, 16532.
- [3] Jansen-van Vuuren, R. D.; Armin, A.; Pandey, A. K.; Burn, P. L.; Meredith, P. *Adv. Mater.* **2016**, *28*, 4766.
- [4] Polman, A.; Knight, M.; Garnett, E. C.; Ehrler, B.; Sinke, W. C. *Science* **2016**, *352* (6283), aad4424.
- [5] Russ, B.; Glaudell, A.; Urban, J. J.; Chabinyk, M. L.; Segalman, R. A. *Nat. Rev. Mater.* **2016**, *1*, 16050.
- [6] a) Dennler, G.; Scharber, M. C.; Brabec, C. J. *Adv. Mater.* **2009**, *21* (13), 1323; b) Kaltenbrunner, M.; White, M. S.; Glowacki, E. D.; Sekitani, T.; Someya, T.; Sariciftci, N. S.; Bauer, S. *Nat. Commun.* **2012**, *3*, 770.
- [7] a) Su, Y. W.; Lan, S. C.; Wei, K. H. *Mater. Today* **2012**, *15* (12), 554; b) Darling, S. B.; You, F. *RSC Adv.* **2013**, *3*, 17633.
- [8] Lizin, S.; Van Passel, S.; De Schepper, E.; Maes, W.; Lutsen, L.; Manca, J.; Vanderzande, D. *Energy Environ. Sci.* **2013**, *6*, 3136.
- [9] Dou, L.; You, J.; Hong, Z.; Xu, Z.; Li, G.; Street, R. A.; Yang, Y. *Adv. Mater.* **2013**, *25* (46), 6642.
- [10] Mazzio, K. A.; Luscombe, C. K. *Chem. Soc. Rev.* **2015**, *44*, 78.
- [11] Kang, H.; Kim, G.; Kim, J.; Kwon, S.; Kim, H.; Lee, K. *Adv. Mater.* **2016**, *28* (36), 7821.
- [12] Müllen, K.; Pisula, W. *J. Am. Chem. Soc.* **2015**, *137* (30), 9503.
- [13] Zhao, W. C.; Li, S.; Yao, H.; Zhang, S.; Zhang, Y.; Yang, B.; Hou, J. *J. Am. Chem. Soc.* **2017**, *139* (21), 7148–7151.
- [14] Park, S. H.; Roy, A.; Beaupré, S.; Cho, S.; Coates, N.; Moon, J. S.; Moses, D.; Leclerc, M.; Lee, K.; Heeger, A. J. *Nat. Photonics* **2009**, *3*, 297.
- [15] Knupfer, M. *Appl. Phys. A* **2003**, *77* (5), 623.
- [16] a) Bresselge, M.; Van Severen, I.; Lutsen, L.; Adriaensens, P.; Manca, J.; Vanderzande, D.; Cleij, T. *Thin Solid Films* **2006**, *511-512*, 328.; b) Jahani, F.; Torabi, S.; Chiechi, R. C.; Koster, L. J. A.; Hummelen, J. C. *Chem. Commun.*

- 2014**, *50*, 10645; c) Donaghey, J. E.; Armin, A.; Burn, P. L.; Meredith, P. *Chem. Commun.* **2015**, *51*, 14115.
- [17] Koster, L. J. A.; Shaheen, S. E.; Hummelen, J. C. *Adv. Energy Mater.* **2012**, *2* (10), 1246.
- [18] Zhang, G.; Clarke, T. M.; Mozer, A. J. *J. Phys. Chem. C* **2016**, *120* (13), 7033.
- [19] a) Lenes, M.; Koster, L. J. A.; Mihailetchi, V. D.; Blom, P. W. M. *Appl. Phys. Lett.* **2006**, *88*, 243502; b) Chen, X.; Zhang, Z.; Ding, Z.; Liu, J.; Wang, L. *Angew. Chem. Int. Ed.* **2016**, *55* (35), 10376.
- [20] Deng, Q.; Li, Y.; Chen, L.; Wang, S.; Wang, G.; Sheng, Y.; Shao, G. *Mod. Phys. Lett. B* **2016**, *30*, 1650341.
- [21] a) Lu, K.; Fang, J.; Zhu, X. W.; Yan, H.; Li, D. H.; Di, C. A.; Yang, Y. L.; Wei, Z. X. *New J. Chem.* **2013**, *37*, 1728; b) Gedefaw, D. A.; Zhou, Y.; Ma, Z.; Genene, Z.; Hellström, S.; Zhang, F.; Mammo, W.; Inganäs, O.; Andersson, M. R. *Polym. Int.* **2014**, *63* (1), 22; c) Torabi, S.; Jahani, F.; Van Severen, I.; Kanimozhi, C.; Patil, S.; Havenith, R. W. A.; Chiechi, R. C.; Lutsen, L.; Vanderzande, D. J. M.; Cleij, T. J.; Hummelen, J. C.; Koster, L. J. A. *Adv. Funct. Mater.* **2015**, *25* (1), 150.
- [22] Meng, B.; Song, H. Y.; Chen, X. X.; Xie, Z. Y.; Liu, J.; Wang, L. X. *Macromolecules* **2015**, *48* (13), 4357.
- [23] Chen, Y.; Zhang, S.; Wu, Y.; Hou, J. *Adv. Mater.* **2014**, *26* (17), 2744.
- [24] Andersen, T. R.; Larsen-Olsen, T. T.; Andreasen, B.; Böttiger, A. P. L.; Carlé, J. E.; Helgesen M.; Bundgaard, E.; Norrman, K.; Andreasen, J. W.; Jorgensen, J. W.; Krebs, F. C. *ACS Nano* **2011**, *5* (5), 4188.
- [25] Lenes, M.; Kooistra, F. B.; Hummelen, J. C.; Van Severen, I.; Lutsen, L.; Vanderzande, D.; Cleij, T. J.; Blom, P. W. M. *J. Appl. Phys.* **2008**, *104*, 114517.
- [26] Brebels, J.; Lutsen, L.; Manca, J.; Vanderzande, D.; Maes, W.; High Dielectric Constant Conjugated Materials for Organic Photovoltaics. Manuscript submitted.
- [27] MacNeill, C. M.; Peterson, E. D.; Noftle, R. E.; Carroll, D. L.; Coffin, R. C. *Synth. Met.* **2011**, *161*, 1137.
- [28] Li, Z.; Tsang, S.-W.; Du, X.; Scoles, L.; Robertson, G.; Zhang, Y.; Toll, F.; Tao, Y.; Lu, J.; Ding, J. *Adv. Funct. Mater.* **2011**, *21* (17), 3331.
- [29] a) Guo, M.; Hayakawa, T.; Kakimoto, M.-A.; Goodson, T. *J. Phys. Chem. B* **2011**, *115*, 13419; b) Lu, Y.; Xiao, Z.; Yuan, Y.; Wu, H.; An, Z.; Hou, Y.; Gao,

C.; Huang, J. *J. Mater. Chem. C* **2013**, *1*, 630; c) Yang, P.; Yuan, M.; Zeigler, D. F.; Watkins, S. E.; Lee, J. A.; Luscombe, C. K. *J. Mater. Chem. C* **2014**, *2*, 3278; d) Cho, N.; Schlenker, C. W.; Kesting, K. M.; Koelsch, P.; Yip, H.-L.; Ginger, D. S.; Jen, A. K.-Y. *Adv. Energy Mater.* **2014**, *4*, 1301857.

[30] Van Mierloo, S.; Adriaensens, P.; Maes, W.; Lutsen, L.; Cleij, T.; Botek, E.; Champagne, B.; Vanderzande, D. *J. Org. Chem.* **2010**, *75*, 7202; b) Vanormelingen, W.; Verstappen, P.; Maes, V.; Bevk, D.; Lutsen, L.; Vanderzande, D.; Maes, W. *Synlett* **2013**, *24* (18), 2389; c) Kawabata, K.; Takeguchi, M.; Goto, H. *Macromolecules* **2013**, *46* (6), 2078.

[31] Shi, J.; Zhao, W.; Xu, L.; Kan, Y.; Li, C.; Song, J.; Wang, H. *J. Phys. Chem. C* **2014**, *118* (15), 7844.

[32] Griffini, G.; Douglas, J. D.; Piliago, C.; Holcombe, T. W.; Turri, S.; Fréchet, J. M. J.; Mynar, J. L. *Adv. Mater.* **2011**, *23* (14), 1660.

[33] a) Vangerven, T.; Verstappen, P.; Drijkoningen, J.; Dierckx, W.; Himmelberger, S.; Salleo, A.; Vanderzande, D.; Maes, W.; Manca, J. V. *Chem. Mater.* **2015**, *27*, 3726; b) Verstappen, P.; Cardinaletti, I.; Vangerven, T.; Vanormelingen, W.; Verstraeten, F.; Lutsen, L.; Vanderzande, D.; Manca, J.; Maes, W. *RSC Adv.* **2016**, *6*, 32298; c) Pirotte, G.; Verstappen, P.; Vanderzande, D.; Maes, W. *Adv. Electron. Mater.*, manuscript submitted.

[34] Brouwer, F.; Alma, J.; Valkenier, H.; Voortman, T. P.; Hillebrand, J.; Chiechi, R. C.; Hummelen, J. C. *J. Mater. Chem.* **2011**, *21*, 1582.

[35] Danley, R. L., Caulfield, P. A., Aubuchon, S. R. *Am. Lab.* **2008**, *40*, 9.

[36] Trasatti, S. *Pure Appl. Chem.* **1986**, *58* (7), 955.

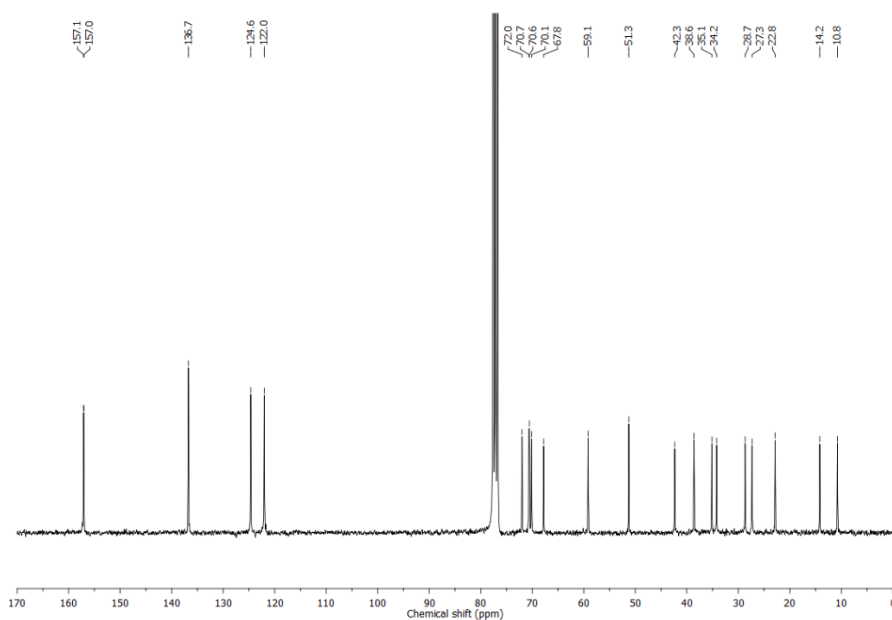
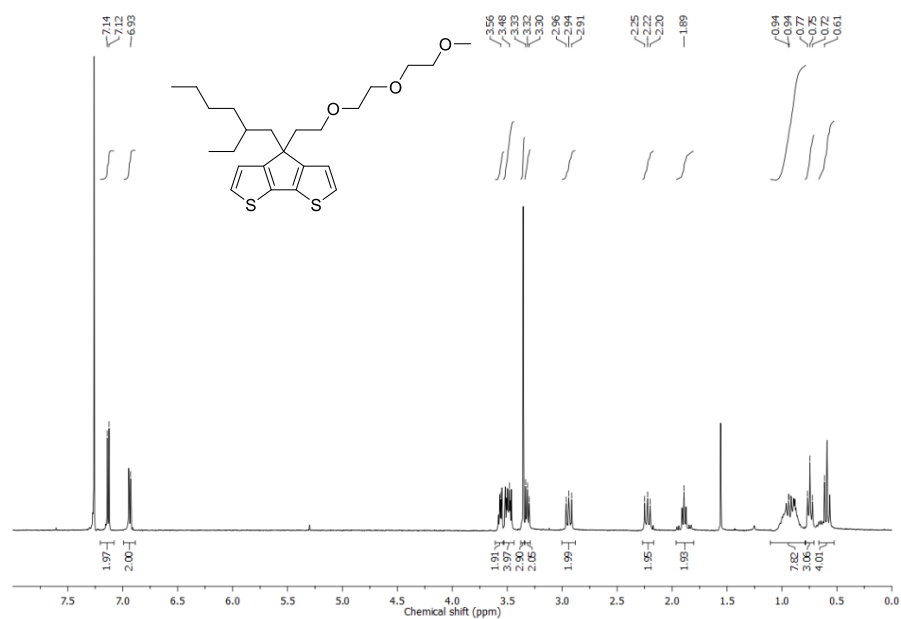
[37] Bard, J.; Faulkner, L. R. *Electrochemical Methods: Fundamentals and Applications*, 2nd Ed., **2001**, Wiley.

[38] Piliago, C.; Holcombe, T. W.; Douglas, J. D.; Woo, C. H.; Beaujuge, P. M.; Fréchet, J. M. J. *J. Am. Chem. Soc.* **2010**, *132* (22), 7595.

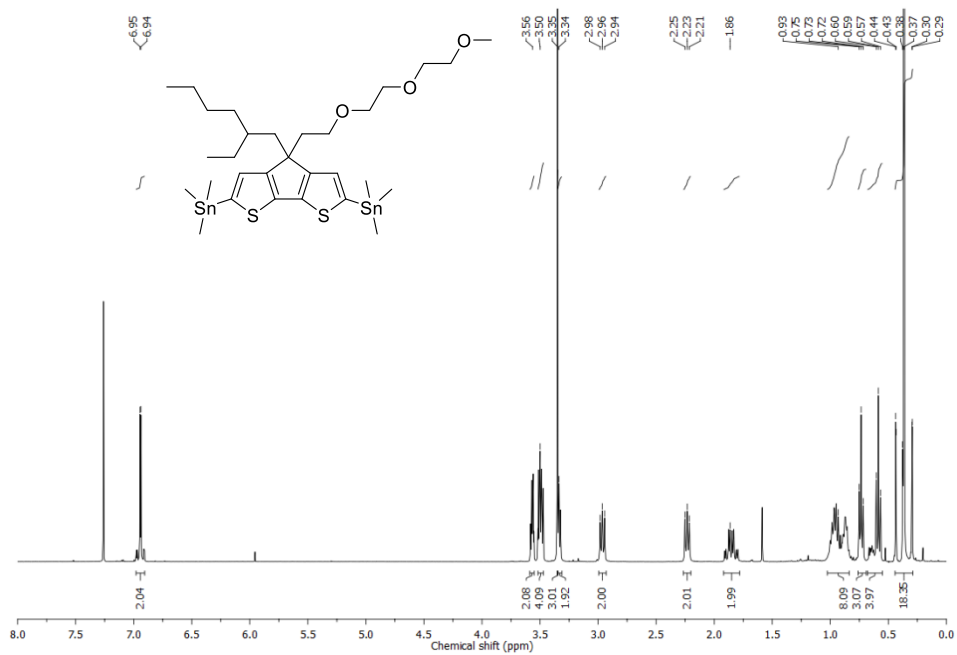
### 3.6 Supporting information

#### *<sup>1</sup>H and <sup>13</sup>C NMR spectra*

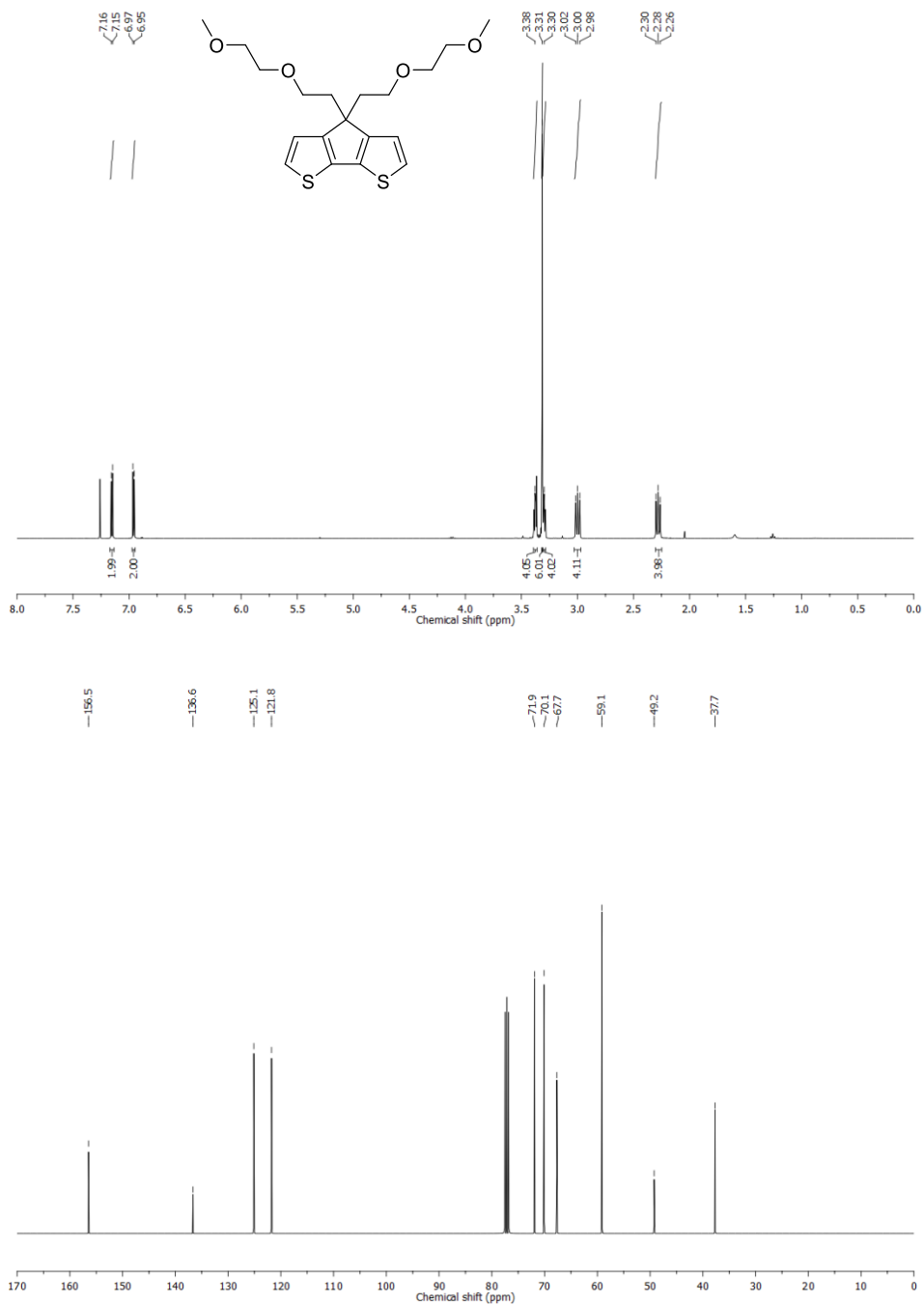
#### 4-(2-ethylhexyl)-4-(2-(2-(2-methoxyethoxy)ethoxy)ethyl)ethyl-4H-cyclopenta[2,1-b:3,4-b']dithiophene (5)



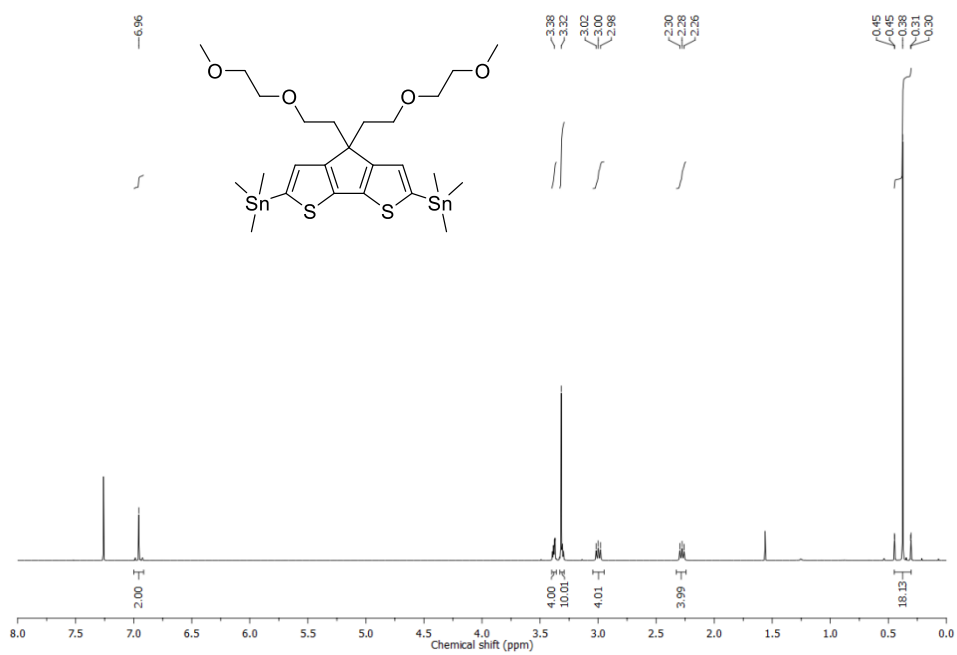
**(4-(2-ethylhexyl)-4-(2-(2-(2-methoxyethoxy)ethoxy)ethyl)-4*H*-cyclopenta[2,1-*b*:3,4-*b'*]dithiophene-2,6-diyl)bis(trimethylstannane)**  
**(6)**



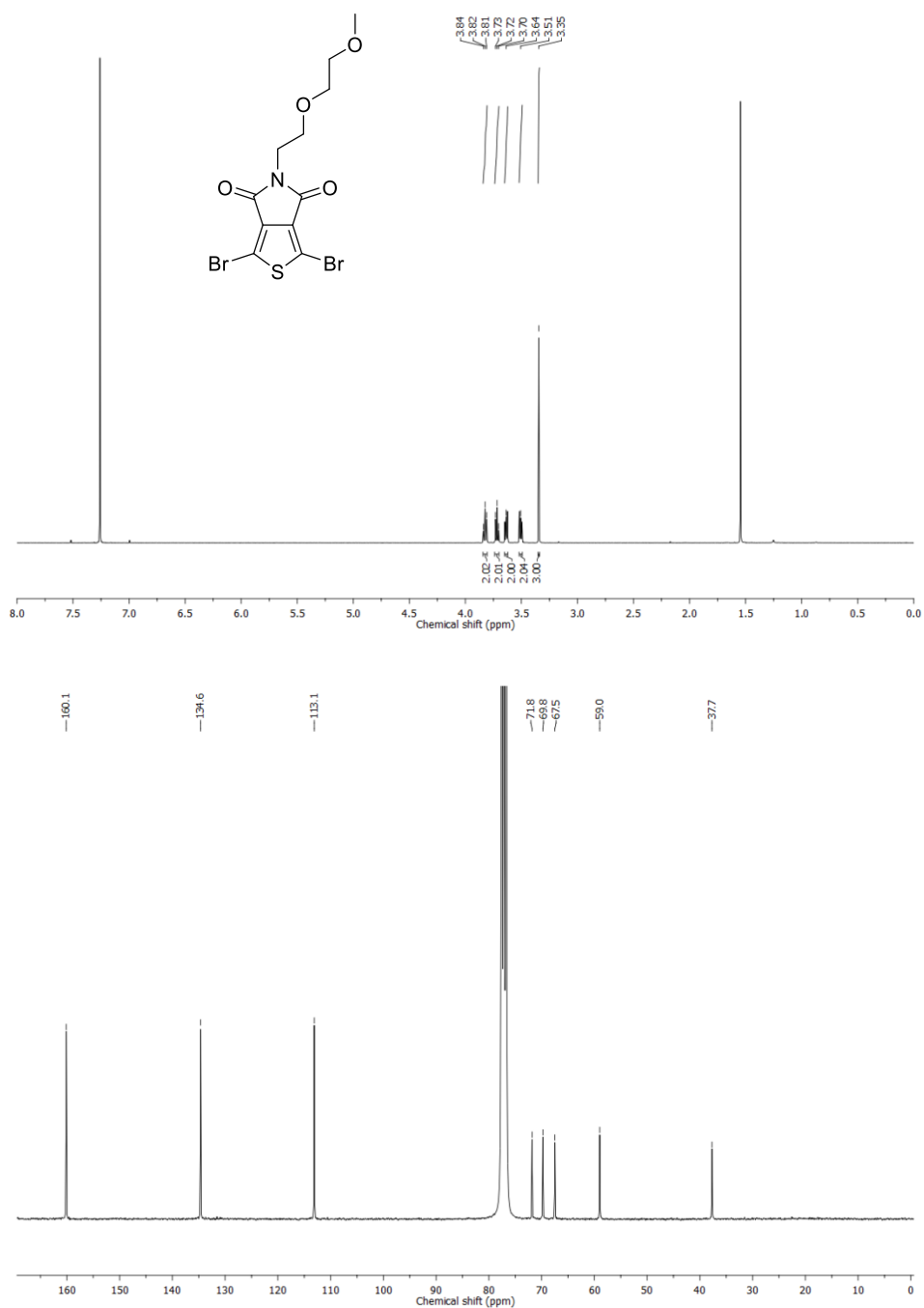
**4,4-bis(2-(2-methoxyethoxy)ethyl)-4*H*-cyclopenta[2,1-*b*:3,4-*b'*]dithiophene (8)**



**(4,4-bis(2-(2-methoxyethoxy)ethyl)-4H-cyclopenta[2,1-b:3,4-b']dithiophene-2,6-diyl)bis(trimethylstannane) (9)**



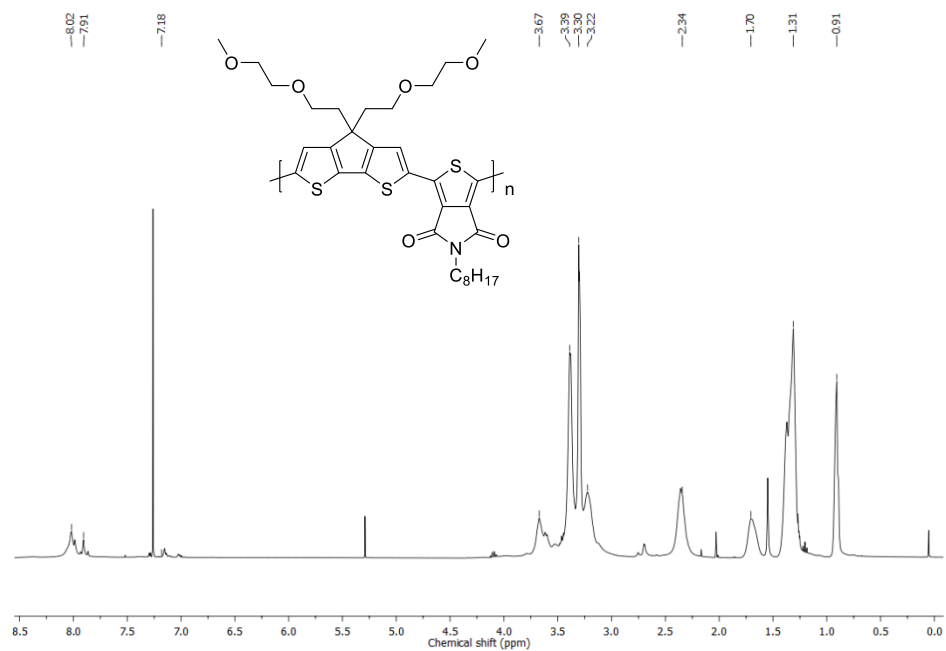
**1,3-dibromo-5-(2-(2-methoxyethoxy)ethyl)-4*H*-thieno[3,4-*c*]pyrrole-4,6(5*H*)-dione (15)**



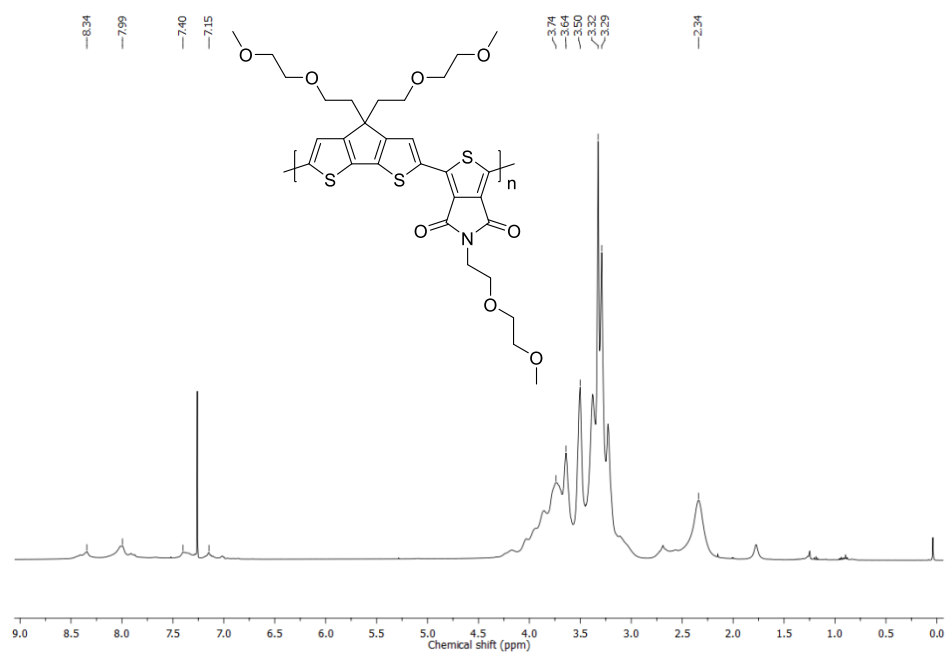


## CPDTPD-Based High Dielectric Constant Polymers Bearing OEG Side Chains

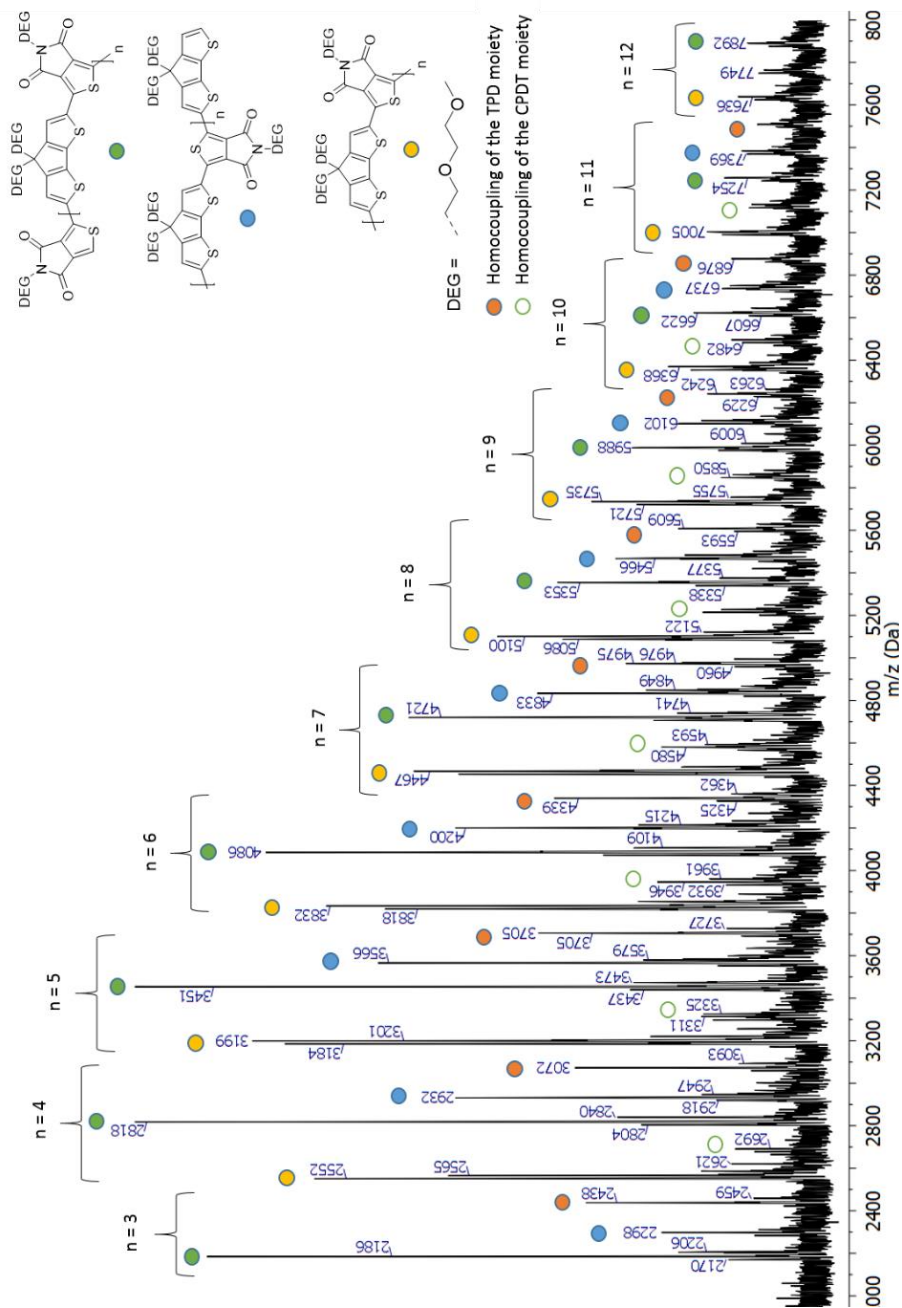
**P3**



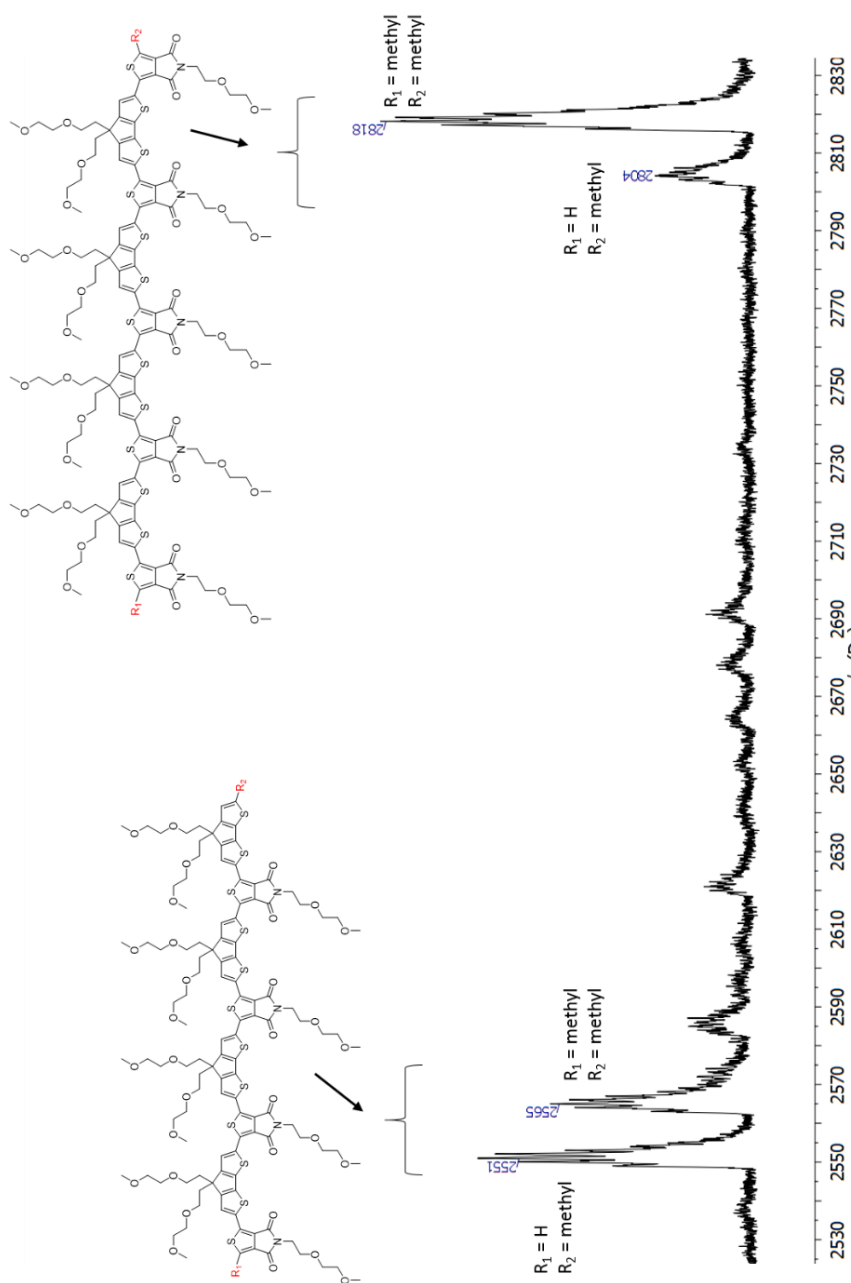
**P4**



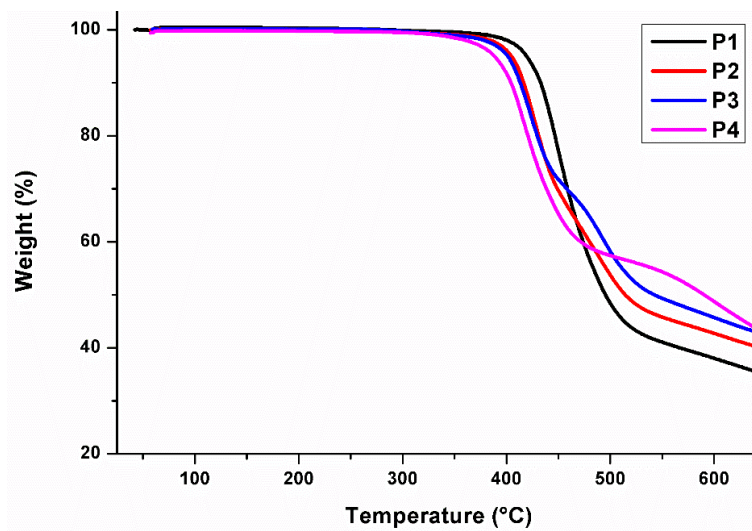
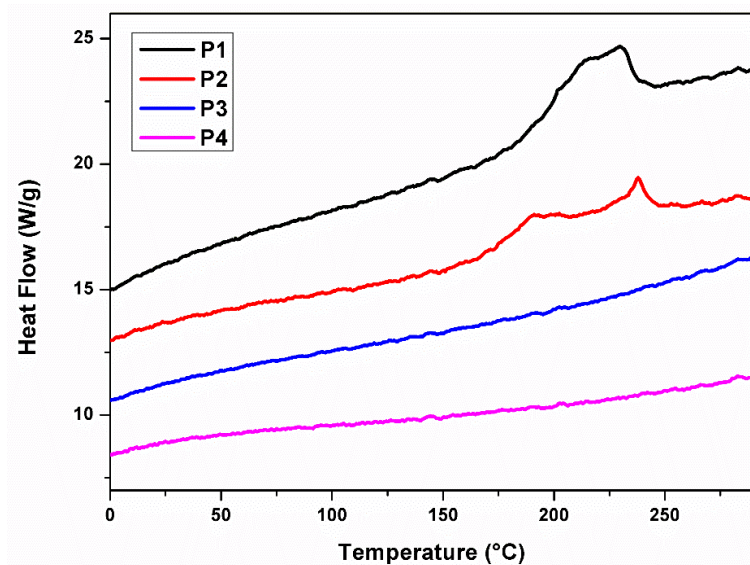
**MALDI-TOF analysis**



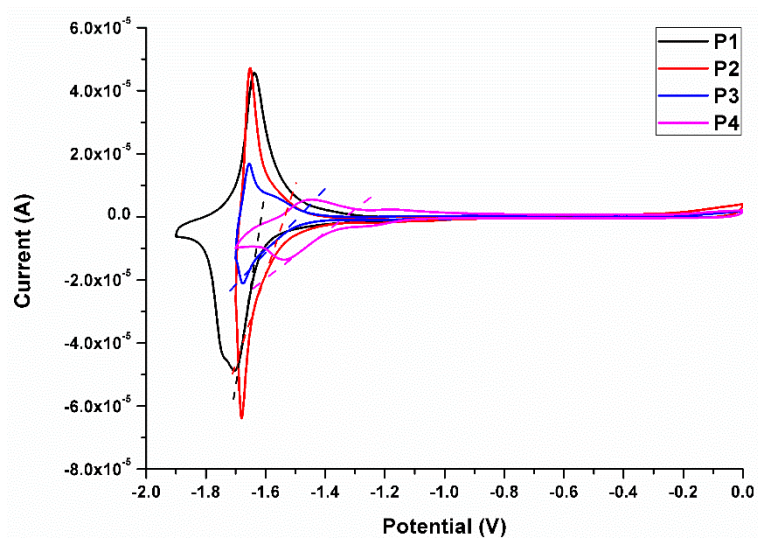
**Figure S1.** MALDI-TOF spectrum of polymer P4.



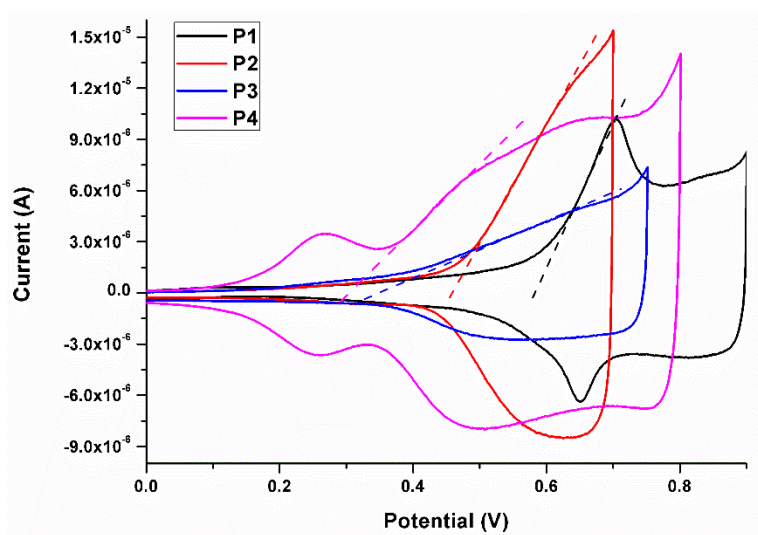
**Figure S2.** MALDI-TOF mass spectrum of **P4** (zoom from  $m/z$  2525 to 2835  $\text{g mol}^{-1}$ ), with the assignment and end group identification.

**Thermal analysis****Figure S3.** TGA analysis of polymers **P1–P4**.**Figure S4.** RHC second heating profiles for polymers **P1–P4** (heating at 500 K  $\text{min}^{-1}$  after cooling at 20 K  $\text{min}^{-1}$ ; curves shifted vertically for clarity, endo up).

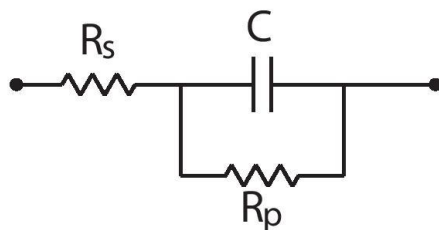
**Cyclic voltammetry**



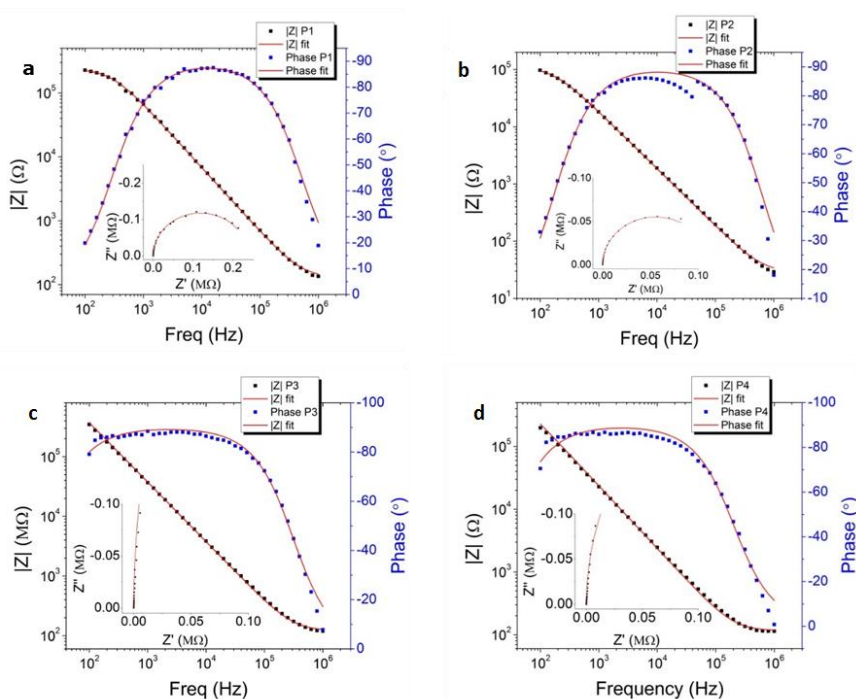
**Figure S5.** Cyclic voltammograms (reduction) of polymers **P1–P4**.



**Figure S6.** Cyclic voltammograms (oxidation) of polymers **P1–P4**.

**Impedance spectroscopy**

**Figure S7.** Equivalent circuit used for fitting the impedance data.  $R_s$  represents the series resistance (in the range of  $\Omega$ ) due to plate resistance and probe effects. The parallel resistance ( $R_p$ , in the range of  $M\Omega$ ) originates from the fact that dielectric materials used within the capacitor are not perfect insulators and allow some amount of current to pass through when the voltage is applied.  $C$  represents the ideal capacitor.



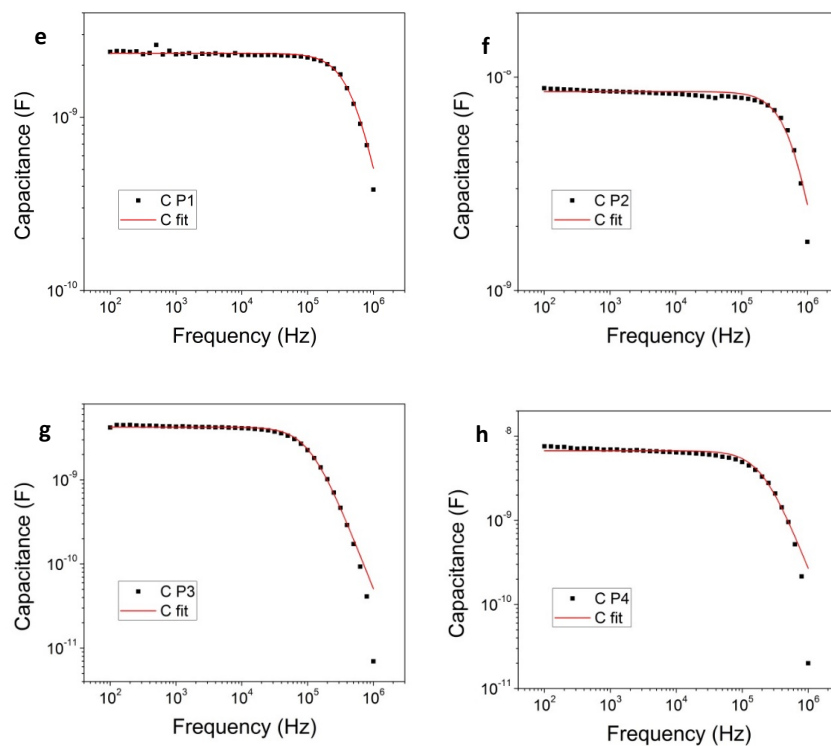


**Figure S8.** Impedance measurements for polymers **P1–P4**. (**a, b, c, d**) The measured data of the magnitude ( $|Z|$ , black square) and the phase (blue square) are plotted against the frequency, while the red lines represent the fit over the measured data. In the insets, the Nyquist diagrams of the devices are plotted, showing the behavior of a real capacitor. (**e, f, g, h**) Capacitance plotted over frequency (black squares) and the applied fitting (red line).

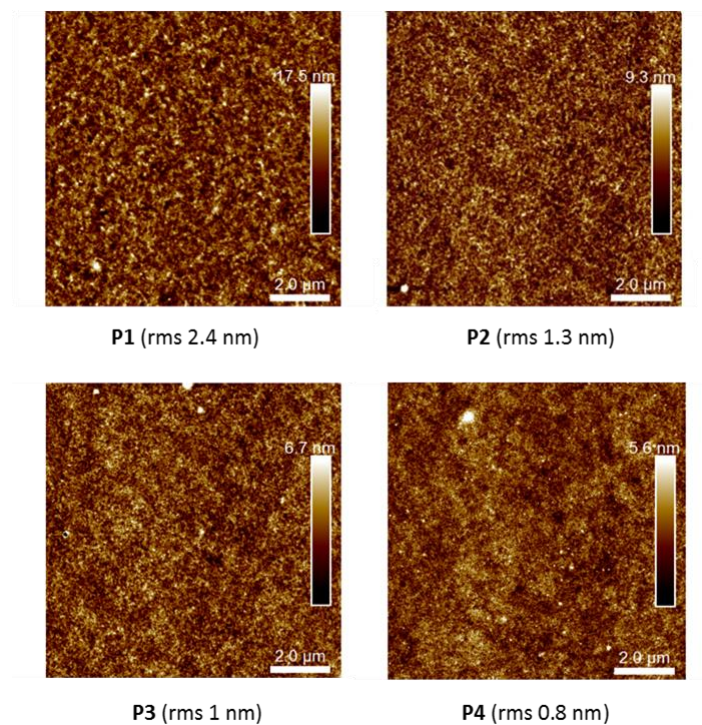


**Figure S9.** AFM height images of the films applied for the impedance measurements.

**Solar cell optimization data**

**Table S1.** Most important optimization data of the solar cell devices based on **P1-P4** and [70]PCBM.

<b>Polymer</b>	<b>Solvent<sup>a</sup></b>	<b>Ratio<sup>b</sup> / wt%</b>	<b>Additive<sup>c</sup></b>	<b>V<sub>oc</sub> / V</b>	<b>J<sub>sc</sub> / mA cm<sup>-2</sup></b>	<b>FF</b>	<b>Best PCE<sup>d</sup> / %</b>
<b>P1</b>	ODCB	1:2	/	0.82	6.25	0.42	2.13 (1.8)
<b>P1</b>	ODCB	1:2	2% CN	0.84	7.16	0.41	2.44 (2.34)
<b>P1</b>	CB	1:2	2% DIO	0.78	5.93	0.54	2.52 (2.07)
<b>P2</b>	ODCB	1:2	2% CN	0.46	6.73	0.33	1.01 (0.90)
<b>P2</b>	ODCB	1:2	2% DIO	0.72	4.36	0.59	1.85 (1.74)
<b>P2</b>	ODCB	1:2	3% DIO	0.68	4.47	0.59	1.79 (1.60)
<b>P3</b>	CB	1:1.5	/	0.64	4.25	0.44	1.20 (1.12)
<b>P3</b>	CB	1:1.5	2% CN	0.68	10.05	0.54	3.69 (3.62)
<b>P3</b>	CB	1:1.5	2% DIO	0.64	11.02	0.60	4.22 (4.22)
<b>P3</b>	ODCB	1:1.5	4% DIO	0.64	10.99	0.55	3.90 (3.77)
<b>P3</b>	Anisole	1:1.5	/	0.66	4.81	0.48	1.54 (1.48)
<b>P3</b>	Anisole	1:1.5	2% AA	0.66	3.97	0.52	1.36 (1.21)

---

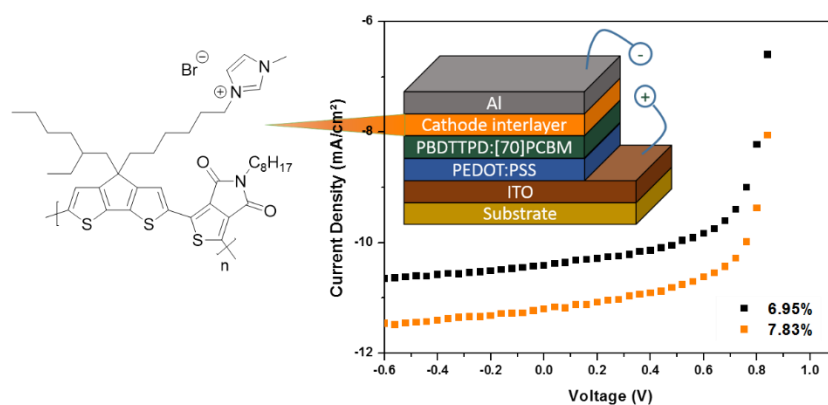
<b>Polymer</b>	<b>Solvent<sup>a</sup></b>	<b>Ratio<sup>b</sup></b>	<b>Additive<sup>c</sup></b>	<b>V<sub>oc</sub> / V</b>	<b>J<sub>sc</sub> / mA cm<sup>-2</sup></b>	<b>FF</b>	<b>Best PCE<sup>d</sup> / %</b>
<b>P4</b>	ODCB	1:2	/	0.64	9.47	0.56	3.40 (3.37)
<b>P4</b>	ODCB	1:2	2% DIO	0.60	11.26	0.51	3.46 (3.43)
<b>P4</b>	ODCB	1:2	2% CN	0.62	11.17	0.50	3.49 (3.32)
<b>P4</b>	Anisole	1:2	/	0.62	4.35	0.49	1.32 (1.30)

---

<sup>a</sup> CB = chlorobenzene, ODCB = *ortho*-dichlorobenzene. <sup>b</sup> Polymer:[70]PCBM. <sup>c</sup> CN = 1-chloronaphthalene, DIO = 1,8-diiodooctane, AA = *p*-anisaldehyde. <sup>d</sup> Average efficiencies over at least 3 devices in brackets.

# Chapter 4

## A CPDTPD-Based Narrow Bandgap Conjugated Polyelectrolyte for Organic Solar Cells



Brebels, J.; Kesters, J.; Defour, M.; Pirotte, G.; Van Mele, B.; Manca, J.; Lutsen, L.; Vanderzande, D.; Maes, W. *Manuscript submitted*.

## Abstract

Extensive research on organic photovoltaics has granted impressive power conversion efficiencies, nowadays exceeding 13% for state-of-the-art photoactive material combinations. Nevertheless, different strategies can be adopted to further enhance the efficiency and the competitiveness with alternative photovoltaic technologies. Conjugated polyelectrolytes have been applied as anode or cathode interlayers to optimize ohmic contacts and lower the contact resistance, thereby improving the ultimate device efficiency. Here, we present an interlayer material belonging to the emerging class of narrow bandgap conjugated polyelectrolytes, based on an imidazolium functionalized 4*H*-cyclopenta[2,1-*b*:3,4-*b'*]dithiophene (CPDT) as the electron-rich polymer building block and 4*H*-thieno[3,4-*c*]pyrrole-4,6(5*H*)-dione (TPD) as the electron-deficient subunit. The ionic polymer is applied as cathode interlayer for PBDTTPD:[70]PCBM bulk heterojunction polymer solar cells, improving the overall device performance from 6.9 to 7.8%.

## 4.1 Introduction

Organic photovoltaics (OPV's) have witnessed a strong growth over the last two decades as a promising technology to convert solar irradiation into electricity.<sup>[1-4]</sup> In contrast to their silicon-based counterparts, fully flexible and light-weight devices can be targeted via large-area production methods and with a reduced cost.<sup>[5-8]</sup> On the active organic material side, strong efforts have been directed toward the development of new low bandgap materials (polymers as well as small molecules) that optimally match with the solar spectrum.<sup>[9,10]</sup> Furthermore, perfect frontier orbital (HOMO and LUMO) energy level alignment of the electron donor and acceptor materials combined in the bulk heterojunction (BHJ) blend and an optimal interpenetrating nanostructured BHJ morphology are required to maximize the device performance.<sup>[11,12]</sup> This has resulted in power conversion efficiencies (PCE's) nowadays exceeding 13% for the best donor-acceptor combinations.<sup>[13-15]</sup> An important point of attention is the efficient charge extraction of the created excitons upon light absorption because of the inherent recombination processes present in (blends of) organic materials.<sup>[16,17]</sup> BHJ OPV devices typically consist of different layers stacked on top of each other (see Figure 2). Interface engineering is hence of utmost importance to realize ohmic contacts (with low contact resistance) of the photoactive layer with the metal electrodes and to improve the selectivity of charge transport.<sup>[18]</sup> Recent studies in this direction have demonstrated the high potential of interface engineering to reduce charge accumulation and to increase charge extraction, enhancing the device performance.<sup>[19-21]</sup>

Conjugated polyelectrolytes (CPE's), combining a conjugated polymer backbone with ionic (mostly side chain) pendant groups, have already proven to be successful as cathode and anode modification layers to boost the photovoltaic performance of OPV devices.<sup>[22-25]</sup> Furthermore, the pending polar groups give rise to additional interesting features. An inherent benefit of creating more hydrophilic polymers is their processability from more environmentally friendly, low-boiling solvents (e.g. alcohols).<sup>[23,26]</sup> The detailed working principle of CPE interlayers is, however, not always fully understood, in particular with respect to the structural features giving rise to the observed improvements of the different photovoltaic output parameters. Lai *et al.* investigated the effect of different

interlayers for diverse systems and summarized the different roles these interlayers have.<sup>[17]</sup> They found that the interlayers control i) the electrode-polymer energy alignment, ii) the built-in electric field, iii) the surface energy, and iv) the surface recombination. Furthermore, interlayers are also applied to prevent penetration of the thermally evaporated electric contact (e.g. Al) into the organic layer. Most importantly, CPE's serve as a simple and powerful tool to enhance the OPV device parameters.<sup>[22]</sup> The open-circuit voltage ( $V_{oc}$ ) often improves, mainly because of a higher built-in potential created by the hydrophilic surface and better dipole alignment. The fill factor (FF) also increases due to the ohmic contact with more balanced charge injection and better charge carrier transportation and collection at the respective electrode, hence also improving the short-circuit current density ( $J_{sc}$ ).<sup>[18-20,22,27]</sup>

For the design of cathode interlayers, it is preferable to have a low work function and good (thermal) stability. Most CPE's are derived from polythiophenes (mostly functionalized P3HT derivatives) or polyfluorenes (e.g. PFN).<sup>[28]</sup> Although PFN is the most commonly used CPE interlayer material, polythiophenes have recently shown slightly better device performances.<sup>[21-23,29]</sup> A drawback of these CPE's is their tendency to not uniformly distribute on top of the active layer when spin-coated, leading to the formation of clusters.<sup>[21,23]</sup> Narrow bandgap conjugated polyelectrolytes (NBGCPE's) are an emerging class of CPE's, aiming to combine the advantages of conjugated low bandgap polymers (e.g. improved compatibility<sup>[30]</sup>, conductivity<sup>[31]</sup> and charge carrier mobilities<sup>[32,33]</sup>) and CPE interlayer materials. In 2013, the group of Bazan was the first to demonstrate that NBGCPE's can exhibit superior characteristics (e.g. charge transport properties) as compared to conventional CPE's.<sup>[32,33]</sup> Nevertheless, very limited research has been devoted to these types of CPE's, likely because of the synthetic efforts required.<sup>[30-35]</sup>

In the current manuscript, the concept of ionic side chain functionalization to achieve NBGCPE's has been translated to a 'push-pull' system based on 4*H*-cyclopenta[2,1-*b*:3,4-*b'*]dithiophene (CPDT) as the push and 1,3-dibromo-4*H*-thieno[3,4-*c*]pyrrole-4,6(5*H*)-dione (TPD) as the pull building block. As such, we demonstrate that the incorporation of an imidazolium functionalized PCPDTPD-

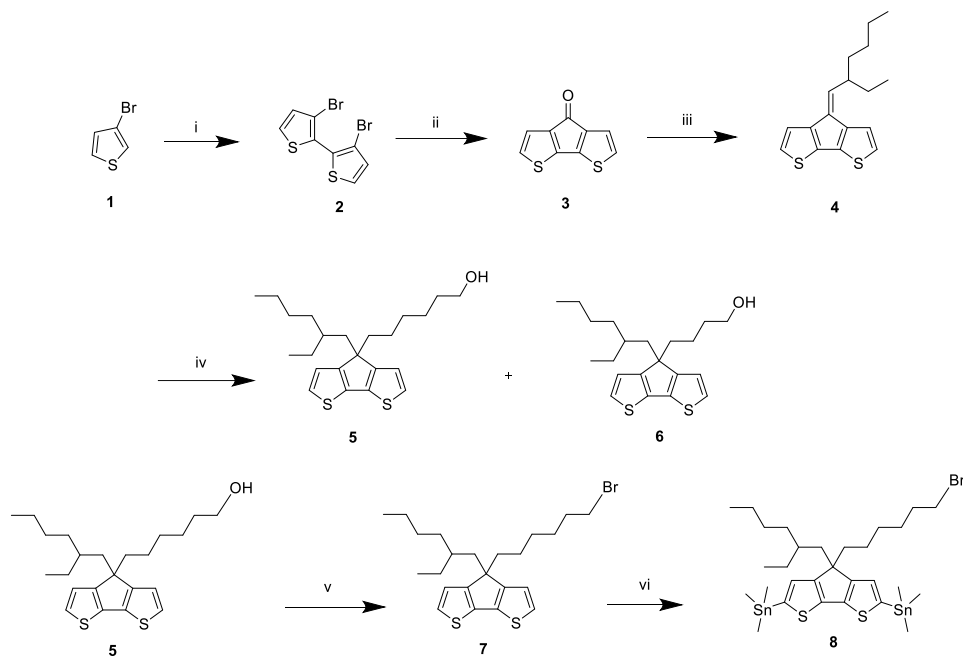
based low bandgap copolymer as cathode interlayer leads to an enhancement of the overall OPV device efficiency with 13% (from 6.9 to 7.8%).

## 4.2 Results and discussion

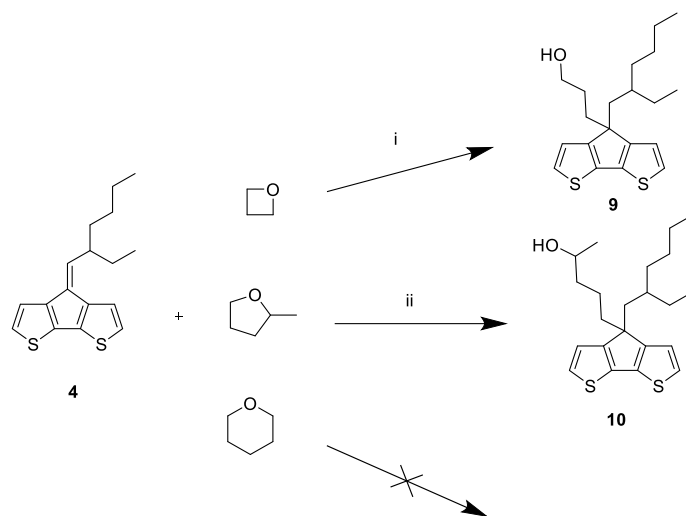
### ***Material synthesis and characterization***

To prepare the PCPDTPD interlayer material, a Stille polycondensation approach was envisaged, combining the distannylated CPDT precursor with a dibrominated TPD. For the synthesis of the CPDT monomer, different literature procedures were combined to come up with a simplified reaction sequence providing good yields (Scheme 1).<sup>[36-38]</sup> The first step in the reaction sequence was the synthesis of 3,3'-dibromo-2,2'-bithiophene (**2**) via the *Gronowitz* dithienyl synthesis.<sup>[36]</sup> 3-Bromothiophene (**1**) was lithiated at the 2-position with lithium diisopropylamide (LDA), followed by coupling with the aid of CuCl<sub>2</sub>. Next, a cyclization reaction was performed in the presence of N,N-dimethylcarbamoyl chloride, yielding 4*H*-cyclopenta[2,1-*b*:3,4-*b'*]dithiophen-4-one (**3**).<sup>[37]</sup> The synthesis of precursor **4** involved a Wittig-type reaction, in which the ketone functionality of compound **3** was converted into an exocyclic double bond with *n*-BuLi and 2-ethylhexylphosphonium bromide.<sup>[38]</sup> An alcohol functionalized side chain was then introduced in the next step in a one pot reduction-substitution reaction. However, an unwanted side product appeared in this reaction. After NMR and mass analysis, it turned out to be compound **6**, lacking 2 carbon atoms in the functionalized side chain. Further studies on this reaction showed that the solvent used for the reaction (tetrahydrofuran) ring opened and was attached to precursor **4**. This hypothesis was confirmed through the introduction of other cyclic ethers under the same reaction conditions. 2-Methyltetrahydrofuran (MeTHF) and oxetane were also incorporated when used as solvents for this reaction. Incorporation of larger cyclic ethers was not possible, probably because of their low ring strain, providing less driving force for the ring opening reaction (Scheme 2). Although only minor amounts of the unwanted side product (up to 10%) were obtained, it still poses problems in the next reaction steps. Due to their structural similarity, purification is not straightforward. Different solvents were then tested and methyl-*tert*-butylether (MTBE) turned out to be a good substitute, providing a satisfying yield. The alcohol functionality of precursor **5** was then converted into a bromine group

by an Appel reaction. In the final step, lithiation and subsequent stannylation were performed to afford the CPDT monomer **8**. To enhance the purity of the stannylated monomer, (recycling) preparative size exclusion chromatography (prep-SEC) was performed.

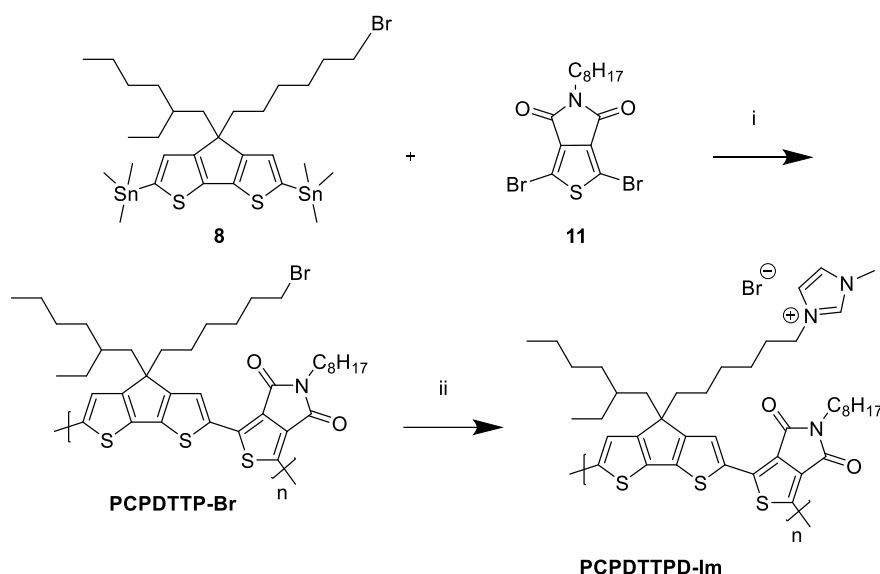


**Scheme 1.** CPDT monomer synthesis: i) LDA, CuCl<sub>2</sub>, THF, overnight at RT (72%); ii) *n*-BuLi, CICONMe<sub>2</sub>, THF, overnight at RT (76%); iii) 2-ethylhexylphosphonium bromide, *n*-BuLi, THF, 2 h at -78 °C, overnight at RT (77%); iv) 1. (6-broomhexyloxy)triisopropylsilane, LiAlH<sub>4</sub>, MTBE, overnight at 0 °C; 2. TBAF (71% over two steps); v) PPh<sub>3</sub>, CBr<sub>4</sub>, 3 h at RT (94%); vi) *n*-BuLi, SnMe<sub>3</sub>Cl, 1.5 h at -78 °C (54% after prep-SEC).



**Scheme 2.** Reactions of precursor **4** with cyclic ethers: i) MTBE, LiAlH<sub>4</sub>, overnight at 60 °C (65%); ii) MeTHF, LiAlH<sub>4</sub>, overnight at 75 °C (44%).

CPDT monomer **8** was then copolymerized with regular *N*-octyl-2,5-dibromothiemo[3,4-*c*]pyrrole-4,6-dione (octyl-TPD **11**), prepared through the standard literature procedure,<sup>[39]</sup> via a Stille cross-coupling polycondensation in the presence of Pd<sub>2</sub>dba<sub>3</sub> (2 mol%) as a catalyst and P(*o*-tol)<sub>3</sub> (8 mol%) as a ligand (Scheme 3). The reaction was performed in a toluene/DMF (4/1) mixture at 115 °C for 5 hours. The crude polymer was purified using soxhlet extractions with different solvents (acetone, hexanes and chloroform) to remove catalyst residues and low molar mass fractions. A PCPDTPD polymer with number-average molar mass (*M<sub>n</sub>*) of 13 kg mol<sup>-1</sup> was obtained (Table 1).



**Scheme 3.** PCPDTTPD-Im synthesis: i) Pd<sub>2</sub>dba<sub>3</sub>, P(*o*-tol)<sub>3</sub>, toluene/DMF (4/1), reflux overnight (58%); ii) 1-methylimidazole, CH<sub>3</sub>CN, microwave, 4 h at 100 °C (69%).

Subsequently, the ionic imidazolium moiety was introduced by post-polymerization substitution of the Br-functionalized CPDT side chains (Scheme 3). A large excess of the functionalization agent (1-methylimidazole) was added to the polymer in acetonitrile and the ionic substitution reaction was activated with microwave irradiation. The polymer was purified again by soxhlet extraction using diethyl ether as a washing solvent to remove the excess of 1-methylimidazole, followed by methanol to collect the ionic polymer. Owing to the ionic imidazole substituent, **PCPDTTPD-Im** is very soluble in polar solvents (e.g. methanol) and can hence be processed 'orthogonally' on top of the active layer without interface erosion or disruption of the underlying morphology.

The thermal properties of the polymers were investigated by thermogravimetric analysis (TGA) and rapid heat-cool calorimetry (RHC) (Figure S1-S2). RHC was chosen above regular differential scanning calorimetry (DSC) because of its increased sensitivity to thermal transitions resulting from the fast scanning rates and the low sample amounts required.<sup>[40]</sup> TGA showed that **PCPDTTPD-Br** is more thermally stable and only starts to degrade at 280 °C, while **PCPDTTPD-**

**Im** slowly starts to lose weight above 200 °C (Figure S1). RHC analysis indicated that **PCPDTPD-Br** has a broad melting transition around 150–200 °C (after a preceding cooling at 20 K min<sup>-1</sup>), whereas no clear melting transition can be observed for **PCPDTPD-Im** (Figure S2). No clear glass transitions could be observed for these polymers.

Prior to device investigation, the optoelectronic material properties (absorption behavior, bandgap and energy levels) were investigated by means of ultraviolet-visible (UV-Vis) absorption spectroscopy and cyclic voltammetry (CV). The UV-Vis absorption spectra were recorded for **PCPDTPD-Br** and **PCPDTPD-Im** in chloroform and methanol, respectively. No single solvent was found for both materials to simplify comparison. Figure 1 depicts both the solution and solid-state UV-Vis spectra. Peak broadening and a red-shift in the onset of absorption is observed for both polymers when going from solution to thin film, likely due to aggregation in the solid state. The optical bandgap, determined from the onset of absorption in thin film, was estimated at 1.70 and 1.67 eV for **PCPDTPD-Br** and **PCPDTPD-Im**, respectively. The frontier orbital energy levels for both polymers, obtained from the onset potentials of oxidation and reduction via CV, are listed in Table 1.

**Table 1.** Molar mass, optical, thermal and electrochemical data for **PCPDTPD-Br** and **PCPDTPD-Im**.

	$M_n^a / \text{kg mol}^{-1}$	$D$	$\lambda_{\text{max film}}^b / \text{nm}$	$E_{\text{g film}}^c / \text{eV}$	$E_{\text{g cv}}^d / \text{eV}$	$E_{\text{HOMO}}^e / \text{eV}$	$E_{\text{LUMO}}^e / \text{eV}$
<b>CPDTPD-Br</b>	13	1.5	690	1.70	1.96	-5.42	-3.46
<b>CPDTPD-Im</b>	-	-	622	1.67	1.79	-5.31	-3.52

<sup>a</sup> Measured by SEC at 40 °C in THF. <sup>b</sup> Films were prepared by drop-casting a solution of the polymer onto a quartz disc. <sup>c</sup> Optical bandgap, determined by the onset of the solid-state UV-Vis spectrum. <sup>d</sup> Electrochemical bandgap. <sup>e</sup> Determined from the onset of oxidation/reduction in cyclic voltammetry.

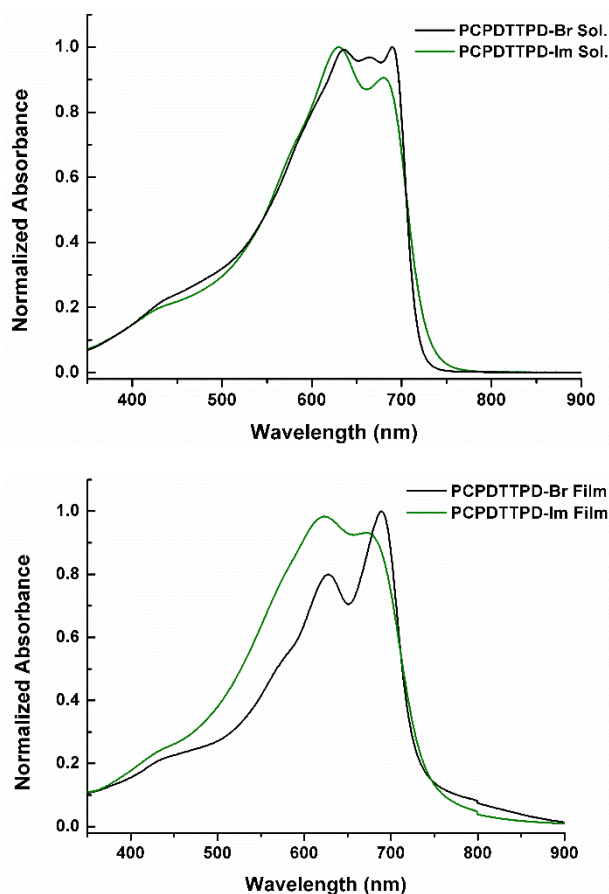


**Figure 1.** Normalized UV-Vis absorption spectra for **PCPDTTPD-Br** and **PCPDTTPD-Im** in solution (top) and thin film (bottom).

#### ***OPV device fabrication and analysis***

To investigate the photovoltaic effect of the novel CPE material, BHJ organic solar cells with a standard configuration glass/ITO/PEDOT:PSS/PBDTTPD:[70]PCBM/CPE (or Ca)/Al were fabricated (Figure 2). For the photoactive layer, PBDTTPD was chosen because of its relatively high efficiency, comparatively low synthetic complexity and the ease by which this polymer can be synthesized on a large scale using continuous flow chemistry.<sup>[41]</sup> The blend solution of PBDTTPD:[70]PCBM (1:1.5) was spin-coated on top of PEDOT:PSS from chlorobenzene using 5% 1-chloronaphthalene (CN) as the co-solvent.<sup>[41]</sup> **PCPDTTPD-Im** was then spin-coated on top of the active layer

from methanol using various concentrations (0.25, 0.5, 1, 2 and 4 mg mL<sup>-1</sup>). As shown in Table 2, the photovoltaic performance significantly increased across the entire CPE concentration range, mainly due to the increase in  $J_{sc}$  and a small gain in FF. The best results were obtained when employing a CPE concentration of 1 mg mL<sup>-1</sup>, granting an average PCE increase from 6.9 to 7.5% (Figure 2), with a top PCE of 7.8%. External quantum efficiency (EQE) measurements (Figure 2) revealed an increased photocurrent in the 300–550 nm range for the CPE bearing device, surpassing 65% at ~450 nm.<sup>[21]</sup> The integrated current densities from the EQE ( $J_{EQE}$ ) were found to be 10.43 and 11.05 mA cm<sup>-2</sup> for the reference device and the CPE device, respectively, correlating well with the measured  $J_{sc}$ 's.

**Table 2.** Photovoltaic parameters for PBDTTPD:[70]PCBM organic solar cells employing either Ca or the **PCPDTPD-Im** interlayer.

<b>CPE concentration / mg mL<sup>-1</sup></b>	<b><math>V_{oc}</math> / V</b>	<b><math>J_{sc}</math> / mA cm<sup>-2</sup></b>	<b>FF</b>	<b>Average PCE<sup>a</sup> / %</b>	<b>Best PCE / %</b>
Reference (Ca)	0.92	10.53	0.71	6.89	6.95
0.25	0.92	10.87	0.74	7.39	7.54
0.5	0.92	11.08	0.73	7.49	7.80
1	0.92	11.18	0.73	7.54	7.83
2	0.92	11.07	0.73	7.44	7.79
4	0.92	10.37	0.72	6.91	7.22

<sup>a</sup> Average efficiencies over at least 4 devices.

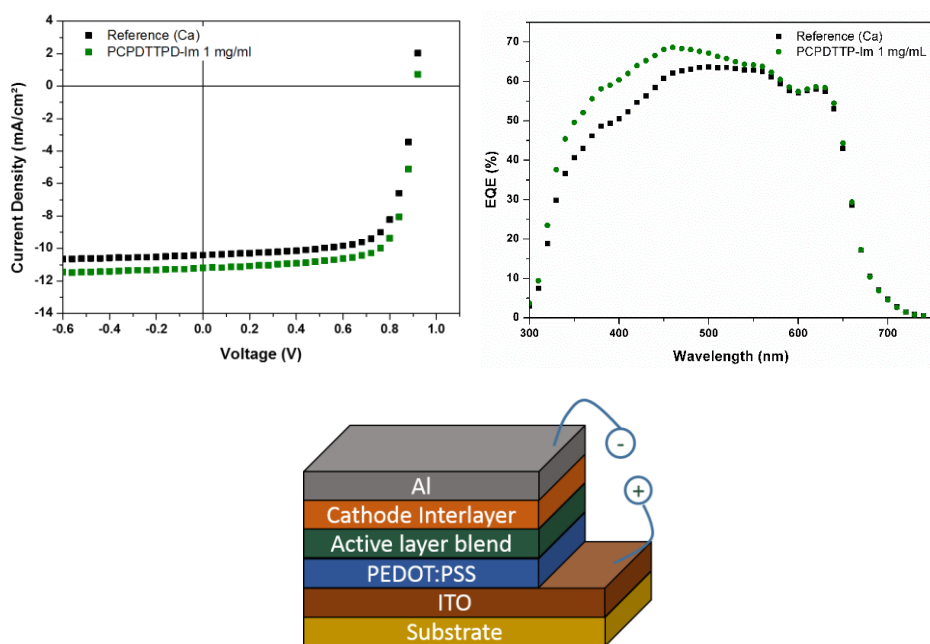


**Figure 2.** *J-V* curves (top left) and EQE spectra (top right) of average performing BHJ solar cell devices containing either Ca or the **PCPDTTPD-Im** CPE interlayer (spin-coated from a 1 mg mL<sup>-1</sup> solution in methanol). Representation of the employed solar cell stack (bottom).

Atomic force microscopy (AFM) measurements were performed on the polymer solar cells treated with varying CPE concentrations to investigate possible trends (Figure 3). The CPE material seems uniformly distributed on top of the active layer, without formation of large clusters. However, no real fluctuations in topography can be observed upon changing the CPE concentration. Only when employing a solution of 4 mg mL<sup>-1</sup>, a small enlargement of the domains can be seen.

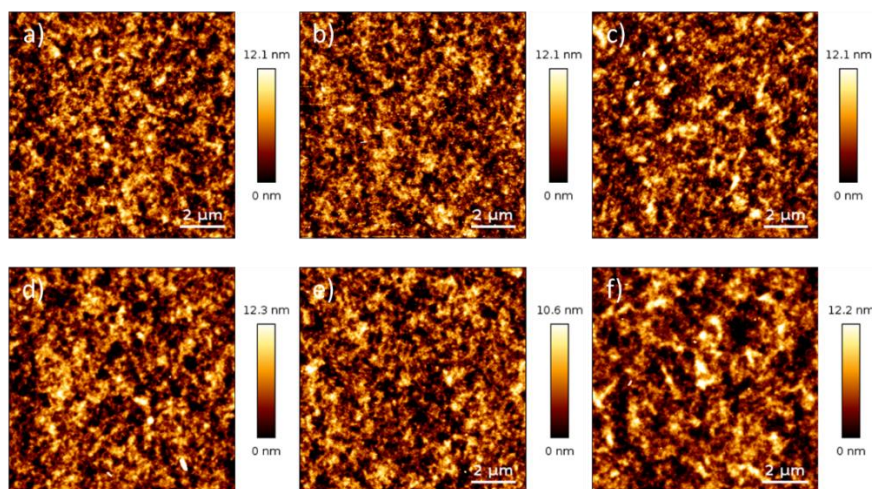


**Figure 3.** AFM images ( $10 \times 10 \mu\text{m}$ ) of PBDTTPD:[70]PCBM organic solar cells employing a) no CPE, b) 0.25, c) 0.5, d) 1, e) 2 and f)  $4 \text{ mg mL}^{-1}$  of **PCPDTPD-Im** methanolic solution spin-coated on top of the active layer.

### 4.3 Conclusions

We have synthesized a PCPDTPD-based narrow bandgap conjugated polyelectrolyte bearing imidazolium-type ionic side chains as a cathode interlayer for organic solar cells. A significant improvement in power conversion efficiency was demonstrated when this interlayer material was applied in combination with a PBDTTPD:[70]PCBM photoactive layer. An efficiency increase of 13% was achieved for the best performing device, especially due to the improved short-circuit current. In contrast to (some) other reported CPEs,<sup>[21,23]</sup> the cathode interlayer seems to cover the active layer in a uniform way. Further efforts are currently done to translate these results to different active layer blends with different monomer compositions to enhance the impact of this study.

## 4.4 Experimental section

### ***Material synthesis and characterization***

All reagents and chemicals were obtained from commercial sources and used without further purification. Solvents were dried by a solvent purification system (MBraun, MB-SPS-800) equipped with alumina columns. Preparative (recycling) size exclusion chromatography (prep-SEC) was performed on a JAI LC-9110 NEXT system equipped with JAIGEL 1H and 2H columns (eluent CHCl<sub>3</sub>, flow rate 3.5 mL min<sup>-1</sup>). NMR chemical shifts ( $\delta$ , in ppm) were determined relative to the residual CHCl<sub>3</sub> (7.26 ppm), CH<sub>2</sub>Cl<sub>2</sub> (5.32 ppm) or CH<sub>3</sub>OH (3.31 ppm) absorption or the <sup>13</sup>C resonance shift of CDCl<sub>3</sub> (77.16 ppm) or CD<sub>2</sub>Cl<sub>2</sub> (54.00 ppm). High resolution ESI-MS was performed using a LTQ Orbitrap Velos Pro mass spectrometer equipped with an atmospheric pressure ionization source operating in the nebulizer assisted electrospray mode. The instrument was calibrated in the *m/z* range 220–2000 using a standard solution containing caffeine, MRFA and Ultramark 1621. UV-Vis absorption spectroscopy measurements were performed on a VARIAN Cary 5000 UV-Vis spectrophotometer at a scan rate of 600 nm min<sup>-1</sup>. The films for the UV-Vis absorption measurements were prepared by drop casting a solution of the respective polymer in chloroform or methanol on a quartz substrate. The solid-state UV-Vis absorption spectra were used to estimate the optical bandgaps (from the wavelength at the intersection of the tangent line drawn at the low energy side of the absorption spectrum with the baseline:  $E_g$  (eV) = 1240/(wavelength in nm)). Analysis of the molar mass and molar mass distribution of **PCPDTTPD-Br** was performed on a Tosoh EcoSEC System, comprising of an autosampler, a PSS guard column SDV (50 x 7.5 mm), followed by three PSS SDV analytical linear XL columns (5  $\mu$ m, 300 x 7.5 mm) and a UV-detector using THF as the eluent at 40 °C with a flow rate of 1.0 mL min<sup>-1</sup>. The SEC system was calibrated using linear narrow polystyrene standards ranging from 474 to 7.5 x 10<sup>6</sup> g mol<sup>-1</sup> ( $K = 14.1 \times 10^{-5}$  dL g<sup>-1</sup> and  $\alpha = 0.70$ ). Electrochemical measurements (cyclic voltammetry) were performed with an Eco Chemie Autolab PGSTAT 30 potentiostat/galvanostat using a three-electrode microcell with a platinum working electrode, a platinum counter electrode and a Ag/AgNO<sub>3</sub> reference electrode (silver wire dipped in a solution of 0.01 M AgNO<sub>3</sub> and 0.1 M NBu<sub>4</sub>PF<sub>6</sub> in anhydrous acetonitrile). The reference electrode was calibrated against ferrocene/ferrocenium as an external

standard. The **PCPDTPD-Br** sample was prepared by dip coating the platinum working electrode in a polymer solution in chloroform (the same solution as used for the solid-state UV-Vis measurements), while **PCPDTPD-Im** was measured in MeCN solution. The CV measurements were done with 0.1 M NBu<sub>4</sub>PF<sub>6</sub> in anhydrous acetonitrile as electrolyte solution. To prevent air from entering the system, the experiments were carried out under a curtain of argon. Cyclic voltammograms were recorded at a scan rate of 100 mV s<sup>-1</sup>. For the conversion of V to eV, the onset potentials of the first oxidation/reduction peaks were used and referenced to ferrocene/ferrocenium, which has an ionization potential of -4.98 eV vs. vacuum. This correction factor is based on a value of 0.31 eV for Fc/Fc<sup>+</sup> vs. SCE<sup>[42]</sup> and a value of 4.68 eV for SCE vs. vacuum<sup>[43]</sup>:  $E_{\text{HOMO/LUMO}} \text{ (eV)} = -4.98 - E_{\text{onset ox/red}}^{\text{Ag/AgNO}_3} \text{ (V)} + E_{\text{onset Fc/Fc}^+}^{\text{Ag/AgNO}_3} \text{ (V)}$ . The accuracy of measuring redox potentials by CV is about 0.01–0.02 V. Reproducibility can be less because the potentials depend on concentration and temperature. Rapid heat-cool calorimetry experiments were performed on a prototype RHC of TA Instruments, equipped with liquid nitrogen cooling and specifically designed for operation at high scanning rates. RHC measurements were performed at 500 K min<sup>-1</sup> (after cooling at 20 K min<sup>-1</sup>) using aluminum crucibles filled with samples of 200–250 µg, using helium (10 mL min<sup>-1</sup>) as a purge gas. TGA experiments were performed at 20 K min<sup>-1</sup> in platinum crucibles on a TA Instruments Q5000 TGA using nitrogen (50 mL min<sup>-1</sup>) as purge gas.

### ***Solar cell fabrication and characterization***

Before device processing, the indium tin oxide (ITO, Kintec, 100 nm, 20 Ohm sq<sup>-1</sup>) containing substrates were thoroughly cleaned through sonication using soap, demineralized water, acetone, isopropyl alcohol and a UV/O<sub>3</sub> treatment. Subsequently, a layer of PEDOT:PSS (poly(3,4-ethylenedioxythiophene):poly(styrenesulfonic acid); Heraeus Clevios AI 4083) was spin-coated on top of the pre-patterned ITO substrates. Further processing was performed under N<sub>2</sub> atmosphere in a glove box, starting with an annealing step at 130 °C for 15 min to remove any residual water. The PBDTPD:[70]PCBM (Solenne) active layers were spin-coated targeting thicknesses of ~100–120 nm, as confirmed by profilometry (DEKTAK). The blend solutions providing highest efficiencies contained a 1:1.5 (PBDTPD:[70]PCBM) ratio, with polymer

concentrations of 20 mg mL<sup>-1</sup>, using chlorobenzene as the processing solvent and 5% CN as co-solvent (see Table 2).<sup>[41]</sup> On top of the active layer, **PCPDTTPD-Im** was spin-coated from methanol with various concentrations or Ca was evaporated *in vacuo* with a thickness of 30 nm (as reference device). The devices were finished off with Al as the top electrode, with a thickness of 80 nm. The active area (3.08 mm<sup>2</sup>) was defined using a mask. The output parameters of the polymer solar cells were measured using a Newport class A solar simulator (model 91195A), calibrated with a silicon solar cell to give a 1 sun AM 1.5G spectrum. EQE measurements were performed with a Newport Apex illuminator (100 W xenon lamp, 6257) as light source, a Newport Cornerstone 130 monochromator and a Stanford SR830 lock-in amplifier for the current measurements. Calibration was done with a certificated Si FDS-100 photodiode. AFM experiments were performed with a JPK NanoWizard 3 AFM (JPK Instruments AG, Berlin, Germany) using AC mode in air. Silicon ACTA-50 tips from AppNano with cantilever length ~125 nm, spring constant ~40 N/m and resonance frequency ~300 kHz were used. The scan angle, set point height, gain values and scan rate were adjusted according to the calibration of the AFM tip.

### Experimental

**3,3'-Dibromo-2,2'-bithiophene (2).**<sup>[36]</sup> 3-Bromothiophene (32.6 g, 200 mmol) was dissolved in dry THF and LDA (100 mL, 200 mmol) was added dropwise at -78 °C under inert atmosphere. The solution was stirred for 1.5 h at -78 °C. CuCl<sub>2</sub> (29.6 g, 220 mmol) was then added and the reaction mixture was stirred overnight at room temperature. The reaction was quenched with a 1M HCl solution, dichloromethane was added and the organic phase was washed with water (2×), dried over anhydrous MgSO<sub>4</sub> and filtered. The solvent was removed under reduced pressure and the crude product was purified by flash chromatography (silica, *n*-hexane: dichloromethane, 50:50) and Kügelröhr distillation (2\*10<sup>-2</sup> mbar, 110 °C). After recrystallization from ethanol, 3,3'-dibromo-2,2'-bithiophene was obtained as white crystals (22.0 g, 72%). <sup>1</sup>H NMR (400 MHz, CDCl<sub>3</sub>), δ (ppm): 7.41 (d, *J* = 5.4 Hz, 2H), 7.08 (d, *J* = 5.4 Hz, 2H).

**4H-Cyclopenta[2,1-*b*:3,4-*b'*]dithiophen-4-one (3).**<sup>[37]</sup> 3,3'-Dibromo-2,2'-bithiophene (10.0 g, 30.8 mmol) was dissolved in dry diethyl ether and the solution was cooled to -78 °C under inert atmosphere. *n*-BuLi (27.2 mL, 67.9

mmol) was added dropwise and after stirring the solution for 1 h at  $-78\text{ }^{\circ}\text{C}$ , dimethylcarbamoyl chloride (3.1 mL, 33.9 mmol) was added dropwise. The solution was then stirred overnight at room temperature. Diethyl ether was added and the organic phase was washed with water ( $2\times$ ), dried over anhydrous  $\text{MgSO}_4$  and filtered. The solvent was removed under reduced pressure. To obtain pure product, recrystallization from ethanol was performed to afford *4H-cyclopenta[2,1-*b*:3,4-*b'*]dithiophen-4-one* as red crystals (4.5 g, 76%).  $^1\text{H}$  NMR (400 MHz,  $\text{CDCl}_3$ ),  $\delta$  (ppm): 7.04 (d,  $J = 4.8$  Hz, 2H), 7.00 (d,  $J = 4.9$  Hz, 2H).

**4-(2-Ethylhexylidene)-4H-cyclopenta[2,1-*b*:3,4-*b'*]dithiophene (4).**<sup>[38]</sup> (2-Ethylhexyl)triphenylphosphonium bromide (12.26 g, 32.7 mmol) was dissolved in dry THF (30 mL) and the solution was cooled to  $-78\text{ }^{\circ}\text{C}$  under inert atmosphere. *n*-BuLi (10.8 mL, 11.7 mmol) was added dropwise and the solution was allowed to stir for 30 min at this temperature. *4H*-Cyclopenta[2,1-*b*:3,4-*b'*]dithiophen-4-one (4.00 g, 20.9 mmol) was dissolved in dry diethyl ether (30 mL) and added to the previously prepared solution. The reaction mixture was stirred overnight at room temperature. Diethyl ether was added and the organic phase was washed with water ( $2\times$ ), dried over anhydrous  $\text{MgSO}_4$  and filtered. The crude product was purified by column chromatography (silica, eluent petroleum ether) to yield *4-(2-ethylhexylidene)-4H-cyclopenta[2,1-*b*:3,4-*b'*]dithiophene* as a yellow solid (4.6 g, 77%).  $^1\text{H}$  NMR (400 MHz,  $\text{CDCl}_3$ ),  $\delta$  (ppm): 7.28 (d,  $J = 5.0$  Hz, 2H), 7.15 (d,  $J = 4.9$  Hz, 2H), 6.16 (d,  $J = 10.5$  Hz, 1H), 2.94–2.83 (m, 1H), 1.72–1.58 (m, 2H), 1.50–1.39 (m, 2H), 1.33–1.25 (m, 4H), 0.92 (t,  $J = 7.4$  Hz, 3H), 0.85 (t,  $J = 7.0$  Hz, 3H).

**6-[4-(2-Ethylhexyl)-4H-cyclopenta[2,1-*b*:3,4-*b'*]dithiophen-4-yl]hexan-1-ol (5).** Prepared according to a modified literature procedure.<sup>[38]</sup> A solution of *4-(2-ethylhexylidene)-4H-cyclopenta[2,1-*b*:3,4-*b'*]dithiophene* (1.01 g, 3.47 mmol) and (6-bromohexyloxy)triisopropylsilane (1.17 g, 3.47 mmol) in dry methyl-*tert*-butyl ether (MTBE, 25 mL) was added to a suspension of  $\text{LiAlH}_4$  (0.292 g, 3.47 mmol) in dry MTBE (10 mL) at  $60\text{ }^{\circ}\text{C}$  under inert atmosphere. The reaction was stirred overnight at  $60\text{ }^{\circ}\text{C}$ . 1M HCl solution and diethyl ether (50 mL) were carefully added and the organic phase was washed with  $\text{NaHCO}_3$  and water ( $2\times$ ), dried over anhydrous  $\text{MgSO}_4$  and filtered. After removing the solvent under reduced pressure, the resulting product was dissolved in THF (15 mL) and TBAF

(1.13 g, 4.33 mmol) was added under inert atmosphere. The solution was stirred overnight at room temperature, followed by the addition of diethyl ether and water. The organic phase was washed with water (2×), dried over anhydrous MgSO<sub>4</sub> and filtered. The solvent was removed under reduced pressure and the crude product was purified by column chromatography (silica, eluent petroleum ether:diethyl ether, 70:30). 6-[4-(2-Ethylhexyl)-4H-cyclopenta[2,1-b:3,4-b']dithiophen-4-yl]hexan-1-ol was obtained as a yellow oil (0.966 g, 71%). <sup>1</sup>H NMR (400 MHz, CDCl<sub>3</sub>), δ (ppm): 7.12 (d, *J* = 4.9 Hz, 2H), 6.90 (2d, *J* = 4.9, 1.7 Hz, 2H), 3.54 (t, *J* = 6.6 Hz, 2H), 1.93–1.75 (m, 4H), 1.46–1.37 (m, 3H), 1.25–1.08 (m, 5H), 1.02–0.81 (m, 10H), 0.74 (t, *J* = 7.1 Hz, 3H), 0.66–0.50 (m, 4H).

During this reaction, 4-[4-(2-ethylhexyl)-4H-cyclopenta[2,1-b:3,4-b']dithiophen-4-yl]butan-1-ol was also obtained due to a reaction with THF (0.13 g, 10%). <sup>1</sup>H NMR (400 MHz, CDCl<sub>3</sub>), δ (ppm): 7.12 (d, *J* = 4.9 Hz, 2H), 6.91 (2d, *J* = 4.9, 1.9 Hz, 2H), 3.45 (t, *J* = 6.6 Hz, 2H), 1.93–1.79 (m, 4H), 1.35–1.25 (m, 3H), 0.99–0.85 (m, 10H), 0.74 (t, *J* = 7.0 Hz, 3H), 0.66–0.55 (m, 4H). <sup>13</sup>C NMR (100 MHz, CDCl<sub>3</sub>), δ (ppm): 157.51, 157.47, 136.7, 124.4, 121.84, 121.81, 62.6, 53.1, 41.7, 39.3, 35.2, 34.0, 33.0, 28.5, 27.2, 22.7, 20.1, 14.1, 10.6.

**4-(6-Bromohexyl)-4-(2-ethylhexyl)-4H-cyclopenta[2,1-b:3,4-b']dithiophene (7).** Prepared according to a literature procedure.<sup>[38]</sup> A solution of triphenylphosphine (0.713 g, 2.72 mmol) in dry CH<sub>2</sub>Cl<sub>2</sub> (5 mL) was added drop wise to a solution of 6-[4-(2-ethylhexyl)-4H-cyclopenta[2,1-b:3,4-b']dithiophen-4-yl]hexan-1-ol (0.760 g, 1.94 mmol) and tetrabromomethane (0.837 g, 2.52 mmol) in dry CH<sub>2</sub>Cl<sub>2</sub> (10 mL) at 0 °C. After stirring the solution for 3 h at room temperature, diethyl ether and water were added and the organic phase was washed with NaHCO<sub>3</sub> (2×) and water (2×), dried over anhydrous MgSO<sub>4</sub> and filtered. The solvent was removed under reduced pressure and the crude product was purified by column chromatography (silica, eluent petroleum ether) to yield 4-(6-bromohexyl)-4-(2-ethylhexyl)-4H-cyclopenta[2,1-b:3,4-b']dithiophene as a yellow oil (0.83 g, 94%). <sup>1</sup>H NMR (400 MHz, CDCl<sub>3</sub>), δ (ppm): 7.13 (d, *J* = 6.5 Hz, 2H), 6.92 (2d, *J* = 6.5, 1.7 Hz, 2H), 3.32 (t, *J* = 9.1 Hz, 2H), 1.91–1.67 (m, 6H), 1.30–1.21 (m, 2H), 1.17–1.07 (m, 2H), 1.01–0.82 (m, 10H), 0.75 (t, *J* = 9.2 Hz, 3H), 0.66–0.55 (m, 4H).

**[4-(6-Bromohexyl)-4-(2-ethylhexyl)-4H-cyclopenta[2,1-*b*:3,4-*b'*]dithiophene-2,6-diyl]bis(trimethylstannane) (8).** 4-(6-Bromohexyl)-4-(2-ethylhexyl)-4H-cyclopenta[2,1-*b*:3,4-*b'*]dithiophene (0.200 g, 0.327 mmol) was dissolved in dry THF (2.5 mL) and the solution was cooled down to  $-78$  °C under inert atmosphere. *n*-BuLi (0.26 mL, 0.661 mmol) was added dropwise and the mixture was stirred for 30 min at  $-78$  °C. Trimethyltin chloride (0.72 mL, 0.720 mmol) was added and the reaction mixture was allowed to gently warm to room temperature. After 1.5 h, diethyl ether was added and the organic phase was washed with water (2×), dried over anhydrous MgSO<sub>4</sub> and filtered. Further purification of the monomer was done by recycling prep-SEC (CHCl<sub>3</sub>) to yield [4-(6-bromohexyl)-4-(2-ethylhexyl)-4H-cyclopenta[2,1-*b*:3,4-*b'*]dithiophene-2,6-diyl]bis(trimethylstannane) as a yellow oil (0.137 g, 54%). <sup>1</sup>H NMR (300 MHz, CD<sub>2</sub>Cl<sub>2</sub>): 6.99 (2s, 2H), 3.34 (t, *J* = 6.9 Hz, 2H), 1.91–1.68 (m, 6H), 1.33–1.24 (m, 2H), 1.20–1.10 (m, 2H), 1.02–0.83 (m, 10H), 0.74 (t, *J* = 6.9 Hz, 3H), 0.59 (t, *J* = 7.4 Hz, 4H), 0.47–0.27 (m, 18H).

**3-[4-(2-ethylhexyl)-4H-cyclopenta[2,1-*b*:3,4-*b'*]dithiophen-4-yl]propan-1-ol (9).** Oxetane (0.06 g, 1.04 mmol) was slowly added to a suspension of LiAlH<sub>4</sub> (0.026 g, 0.693 mmol) in dry MTBE (10 mL) under inert atmosphere. The reaction mixture was subsequently heated to 50 °C and a solution of 4-(2-ethylhexylidene)-4H-cyclopenta[2,1-*b*:3,4-*b'*]dithiophene (0.100 g, 0.347 mmol) in dry MTBE (2 mL) was added dropwise. The reaction was stirred overnight at 50 °C. 1M HCl solution was then carefully added, followed by diethyl ether (20 mL) and the organic phase was washed with NaHCO<sub>3</sub> and water (2×), dried over anhydrous MgSO<sub>4</sub> and filtered. The solvent was removed under reduced pressure and the crude product was purified by column chromatography (silica, eluent petroleum ether:diethyl ether, 60:40) to obtain 3-[4-(2-ethylhexyl)-4H-cyclopenta[2,1-*b*:3,4-*b'*]dithiophen-4-yl]propan-1-ol as a colorless oil (0.079 g, 65%). <sup>1</sup>H NMR (400 MHz, CDCl<sub>3</sub>),  $\delta$  (ppm): 7.12 (d, *J* = 4.9 Hz, 2H), 6.91 (2d, *J* = 4.9, 1.7 Hz, 2H), 3.39 (t, *J* = 6.5 Hz, 2H), 1.95–1.84 (m, 4H), 1.27–1.19 (br, 1H), 1.09–0.85 (m, 10H), 0.73 (t, *J* = 7.0 Hz, 3H), 0.67–0.60 (m, 1H), 0.57 (t, *J* = 7.4 Hz, 3H); <sup>13</sup>C NMR (100 MHz, CD<sub>2</sub>Cl<sub>2</sub>),  $\delta$  (ppm): 158.13, 158.07, 137.31, 137.28, 125.10, 125.06, 122.50, 122.47, 63.3, 42.3, 36.0, 35.9, 34.5, 29.1, 28.2, 27.7, 23.3, 14.4, 11.0.

**5-[4-(2-ethylhexyl)-4*H*-cyclopenta[2,1-*b*:3,4-*b'*]dithiophen-4-yl]pentan-2-ol (10).** 4-(2-Ethylhexylidene)-4*H*-cyclopenta[2,1-*b*:3,4-*b'*]dithiophene (0.100 g, 0.347 mmol) in dry 2-methyltetrahydrofuran (MeTHF, 2 mL) was added to a suspension of LiAlH<sub>4</sub> (0.026 g, 0.693 mmol) in dry MeTHF (10 mL) at 75 °C under inert atmosphere. The reaction was stirred overnight at 75 °C. 1M HCl solution and diethyl ether (50 mL) were carefully added and the organic phase was washed with NaHCO<sub>3</sub> and water (2×), dried over anhydrous MgSO<sub>4</sub> and filtered. The solvent was removed under reduced pressure and the crude product was purified by column chromatography (silica, eluent petroleum ether:diethyl ether, 75:25) to obtain 5-[4-(2-ethylhexyl)-4*H*-cyclopenta[2,1-*b*:3,4-*b'*]dithiophen-4-yl]pentan-2-ol as a light-yellow oil (0.058 g, 44%). <sup>1</sup>H NMR (400 MHz, CDCl<sub>3</sub>), δ (ppm): 7.13 (2d, *J* = 4.9, 1.2 Hz, 2H), 6.94–6.90 (m, 2H), 3.68–3.55 (m, 1H), 1.93–1.78 (m, 4H), 1.33–1.18 (m, 5H), 1.01–0.83 (m, 11H), 0.74 (t, *J* = 7.0 Hz, 3H), 0.66–0.54 (m, 4H); <sup>13</sup>C NMR (100 MHz, CDCl<sub>3</sub>), δ (ppm): 158.01, 157.97, 137.2, 124.89, 124.88, 122.34, 122.30, 122.26, 68.3, 53.6, 42.2, 30.0, 39.9, 35.7, 34.5, 29.0, 27.7, 23.9, 23.2, 21.1, 14.5, 11.1.

**1,3-Dibromo-5-octyl-4*H*-thieno[3,4-*c*]pyrrole-4,6(5*H*)-dione (11).** Prepared according to a reported procedure.<sup>[39]</sup>

**PCPDTPD-Br.** A mixture of [4-(6-bromohexyl)-4-(2-ethylhexyl)-4*H*-cyclopenta[2,1-*b*:3,4-*b'*]dithiophene-2,6-diyl]bis(trimethylstannane) (0.215 g, 0.276 mmol) and 1,3-dibromo-5-octyl-4*H*-thieno[3,4-*c*]pyrrole-4,6(5*H*)-dione (0.117 g, 0.276 mmol) was dissolved in a mixture of dry toluene (4 mL) and dry DMF (1 mL) and the solution was degassed for 20 min with N<sub>2</sub>. Subsequently, Pd<sub>2</sub>(dba)<sub>3</sub> (5.0 mg, 5.5 μmol) and P(*o*-tol)<sub>3</sub> (6.7 mg, 22 μmol) were added and the mixture was heated at reflux overnight. The crude polymer was precipitated in methanol and purified by repetitive soxhlet extractions with acetone, *n*-hexane and chloroform. The chloroform fraction was again precipitated in methanol and filtered, yielding a blue solid (115 mg, 58%). SEC (THF, 40 °C, PS standards): *M*<sub>n</sub> = 13 kg mol<sup>-1</sup>, *D* = 1.5; λ<sub>max</sub> = 690 nm.

**PCPDTPD-Im.** 1-Methylimidazole (3 mL) and acetonitrile (2 mL) were added to **PCPDTPD-Br** (115 mg) and the suspension was placed in a microwave vial and heated for 4 h at 100 °C. The functionalized polymer was precipitated in diethyl ether and subsequently purified by soxhlet extraction with diethyl ether and

methanol. The methanol fraction was again precipitated in diethyl ether and filtered, yielding the functionalized polymer **PCPDTPD-Im** as a blue solid (88 mg, 69%).  $\lambda_{\text{max}} = 622 \text{ nm}$ .

## 4.5 References

- [1] Dennler, G.; Scharber, M. C.; Brabec, C. J. *Adv. Mater.* **2009**, *21* (13), 1323.
- [2] Polman, A.; Knight, M.; Garnett, E. C.; Ehrler, B.; Sinke, W. C. *Science* **2016**, *352* (6283), aad4424.
- [3] Su, Y. W.; Lan, S. C.; Wei, K. H. *Mater. Today* **2012**, *15* (12), 554.
- [4] Dou, L.; You, J.; Hong, Z.; Xu, Z.; Li, G.; Street, R. A.; Yang, Y. *Adv. Mater.* **2013**, *25* (46), 6642.
- [5] Mazzio, K. A.; Luscombe, C. K. *Chem. Soc. Rev.* **2015**, *44*, 78.
- [6] Darling, S. B.; You, F. *RSC Adv.* **2013**, *3*, 17633.
- [7] Lizin, S.; Van Passel, S.; De Schepper, E.; Maes, W.; Lutsen, L.; Manca, J.; Vanderzande, D. *Energy Environ. Sci.* **2013**, *6*, 3136.
- [8] Kang, H.; Kim, G.; Kim, J.; Kwon, S.; Kim, H.; Lee, K. *Adv. Mater.* **2016**, *28* (36), 7821.
- [9] Müllen, K.; Pisula, W. *J. Am. Chem. Soc.* **2015**, *137* (30), 9503.
- [10] Vogelbaum, H. S.; Sauvé, G. *Synthetic Met.* **2017**, *223*, 107.
- [11] Hoppe, H.; Sariciftci, N. S. *J. Mater. Chem.* **2006**, *16*, 45.
- [12] Park, S. H.; Roy, A.; Beaupré, S.; Cho, S.; Coates, N.; Moon, J. S.; Moses, D.; Leclerc, M.; Lee, K.; Heeger, A. J. *Nat. Photonics* **2009**, *3*, 297.
- [13] Holliday, S.; Li, Y.; Luscombe, C. K. *Prog. Polym. Sci.* **2017**, *70*, 34.
- [14] Zhao, J.; Li, Y.; Yang, G.; Jiang, K.; Lin, H.; Ade, H.; Ma, W.; Yan, H. *Nat. Energy* **2016**, *1*, 15027.
- [15] Zhao, W. C.; Li, S.; Yao, H.; Zhang, S.; Zhang, Y.; Yang, B.; Hou, J. *J. Am. Chem. Soc.* **2017**, *139* (21), 7148.
- [16] Knupfer, M. *Appl. Phys. A* **2003**, *77* (5), 623.
- [17] Lai, T.-H.; Tsang, S.-W.; Manders, J. R.; Chen, S.; So, F. *Mater. Today* **2013**, *16* (11), 424.
- [18] Steim, R.; Kogler, F. R.; Brabec, C. J. *J. Mater. Chem.* **2010**, *20*, 2499.
- [19] Yin, Z.; Wei, J.; Zheng, Q. *Adv. Sci.* **2016**, *3*, 1500362.
- [20] Lim, K.-G.; Park, S. M.; Woo, H. Y.; Lee, T.-W. *ChemSusChem* **2015**, *8*, 3062.
- [21] Kesters, J.; Govaerts, S.; Pirotte, G.; Drijkoningen, J.; Chevrier, M.; Van den Brande, N.; Liu, X.; Fahlman, M.; Van Mele, B.; Lutsen, L.; Vanderzande, D.;

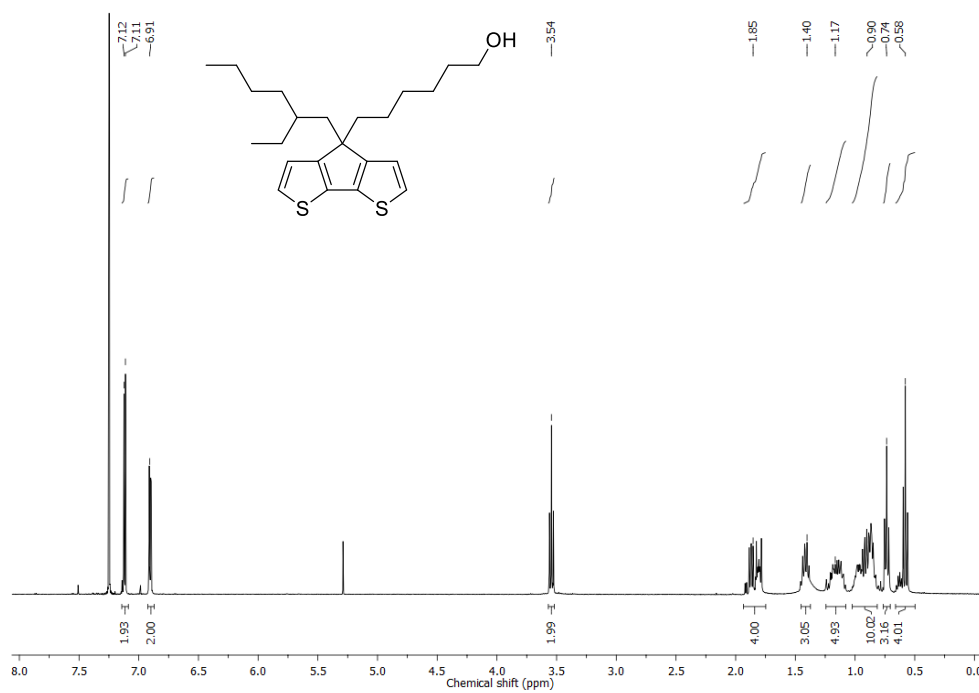
- Manca, J.; Clément, S.; Von Hauff, E.; Maes, W. *ACS Appl. Mater. Interfaces* **2016**, 8 (10), 6309.
- [22] He, Z.; Zhong, C.; Huang, X.; Wong, W.-Y.; Wu, H.; Chen, L.; Su, S.; Cao, Y. *Adv. Mater.* **2011**, 23 (40), 4636.
- [23] Kesters, J.; Ghooos, T.; Penxten, H.; Drijkoningen, J.; Vangerven, T.; Lyons, D. M.; Verreert, B.; Aernouts, T.; Lutsen, L.; Vanderzande, D.; Manca, J.; Maes, W. *Adv. Energy Mater.* **2013**, 3 (9), 1180.
- [24] Zhou, H.; Chen, Q.; Li, G.; Luo, S.; Song, T.-B.; Duan, H.-S.; Hong, Z.; You, J.; Liu, Y.; Yang, Y. *Photovoltaics. Science* **2014**, 345 (6196), 542.
- [25] Zhang, H.; Azimi, H.; Hou, Y.; Ameri, T.; Przybilla, T.; Spiecker, E.; Kraft, M.; Scherf, U.; Brabec, C. J. *Chem. Mater.* **2014**, 26, 5190.
- [26] Hu, Z.; Zhang, K.; Huang, F.; Cao, Y. *Chem. Commun.* **2015**, 51, 5572.
- [27] Chen, L.-M.; Xu, Z.; Hong, Z.; Yang, Y. *J. Mater. Chem.* **2010**, 20, 2575.
- [28] Houston, J. E.; Richeter, S.; Clément, S.; Evans, R. C. *Polym. Int.* **2017**, 66 (10), 1333.
- [29] Seo, J. H.; Gutacker, A.; Sun, Y.; Wu, H.; Huang, F.; Cao, Y.; Scherf, U.; Heeger, A. J.; Bazan, G. C. *J. Am. Chem. Soc.* **2011**, 133 (22), 8416.
- [30] Zhang, W.; Li, Y.; Zhu, L.; Liu, X.; Song, C.; Li, X.; Sun, X.; Fang, J. *Chem. Commun.* **2017**, 53, 2005.
- [31] Hu, L.; Wu, F.; Li, C.; Hu, A.; Hu, X.; Zhang, Y.; Chen L.; Chen, Y. *Macromolecules* **2015**, 48 (16), 5578.
- [32] Henson, Z. B.; Zhang, Y.; Nguyen, T.-Q.; Seo, J. H.; Bazan, G. C. *J. Am. Chem. Soc.* **2013**, 135 (11), 4163.
- [33] Mai, C.-K.; Zhou, H.; Zhang, Y.; Henson, Z. B.; Nguyen, T.-Q.; Heeger, A. J.; Bazan, G. C. *Angew. Chem. Int. Ed.* **2013**, 52, 12874.
- [34] Page, Z. A.; Liu, F.; Russell T. P.; Emrick, T. J. *Polym. Sci., Part A: Polym. Chem.* **2015**, 53 (2), 327.
- [35] Zhou, H.; Zhang, Y.; Mai, C.-K.; Collins, S. D.; Nguyen, T.-Q.; Bazan G. C.; Heeger, A. J. *Adv. Mater.* **2013**, 26 (5), 780.
- [36] Kawabata, K.; Takeguchi, M.; Goto, H. *Macromolecules* **2013**, 46 (6), 2078.
- [37] Shi, J.; Zhao, W.; Xu, L.; Kan, Y.; Li, C.; Song, J.; Wang, H. *J. Phys. Chem. C* **2014**, 118 (15), 7844.
- [38] Vanormelingen, W.; Verstappen, P.; Maes, V.; Bevk, D.; Lutsen, L.; Vanderzande, D.; Maes, W. *Synlett* **2013**, 24 (18), 2389.

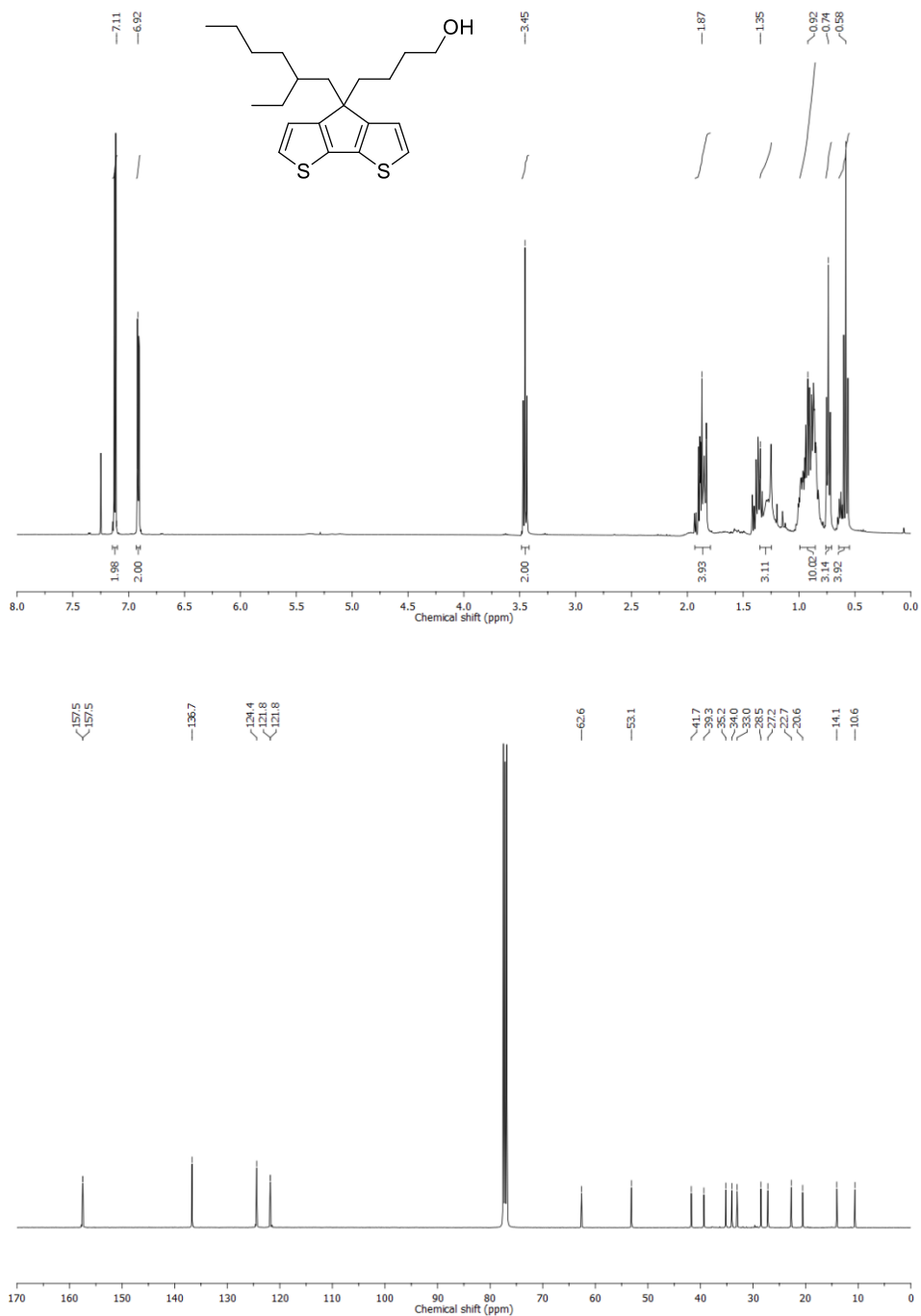
- [39] Piliego, C.; Holcombe, T. W.; Douglas, J. D.; Woo, C. H.; Beaujuge, P. M.; Fréchet, J. M. J. *J. Am. Chem. Soc.* **2010**, *132* (22), 7595.
- [40] Danley, R. L.; Caulfield, P. A.; Aubuchon, S. R. *Am. Lab.* **2008**, *40*, 9.
- [41] Pirotte, G.; Kesters, J.; Verstappen, P.; Govaerts, S.; Manca, J.; Lutsen, L.; Vanderzande, D.; Maes, W. *ChemSusChem* **2015**, *8* (19), 3228.
- [42] Trasatti, S. *Pure Appl. Chem.* **1986**, *58* (7), 955.
- [43] Bard, J.; Faulkner, L. R. *Electrochemical Methods: Fundamentals and Applications*, 2nd Ed., **2001**, Wiley.

## 4.6 Supporting information

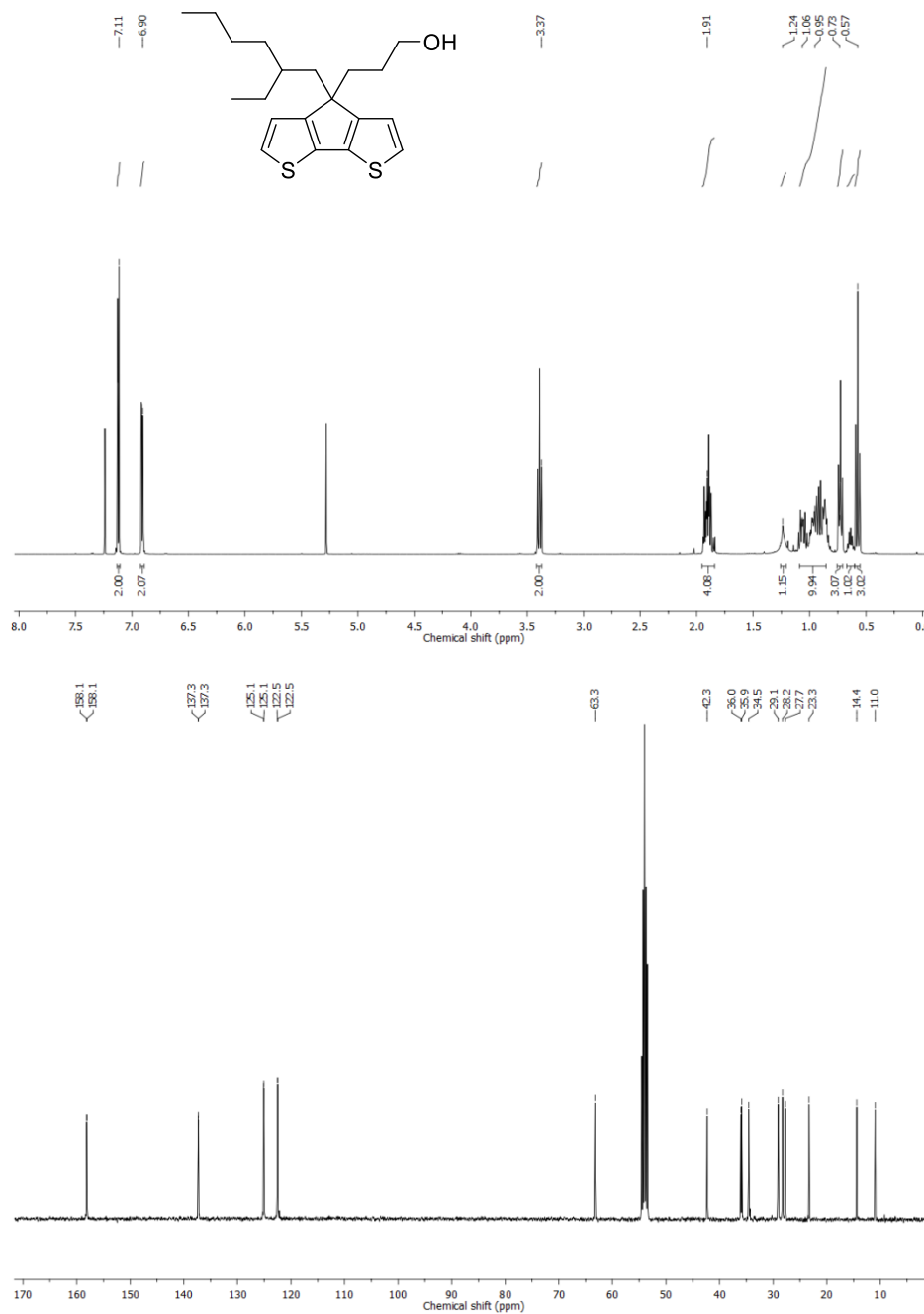
### <sup>1</sup>H and <sup>13</sup>C NMR spectra

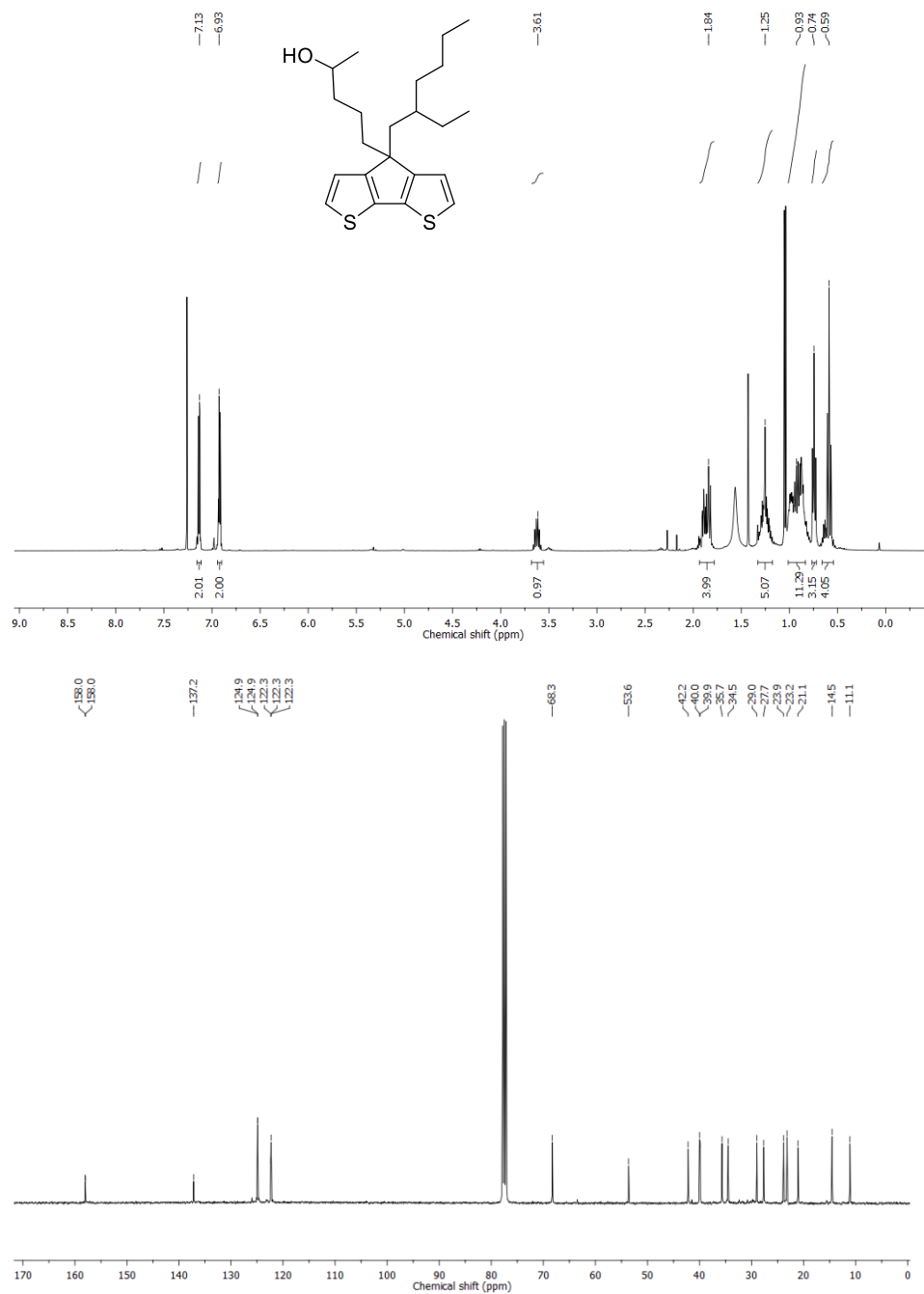
#### 6-[4-(2-ethylhexyl)-4*H*-cyclopenta[2,1-*b*:3,4-*b'*]dithiophen-4-yl]hexan-1-ol (5)



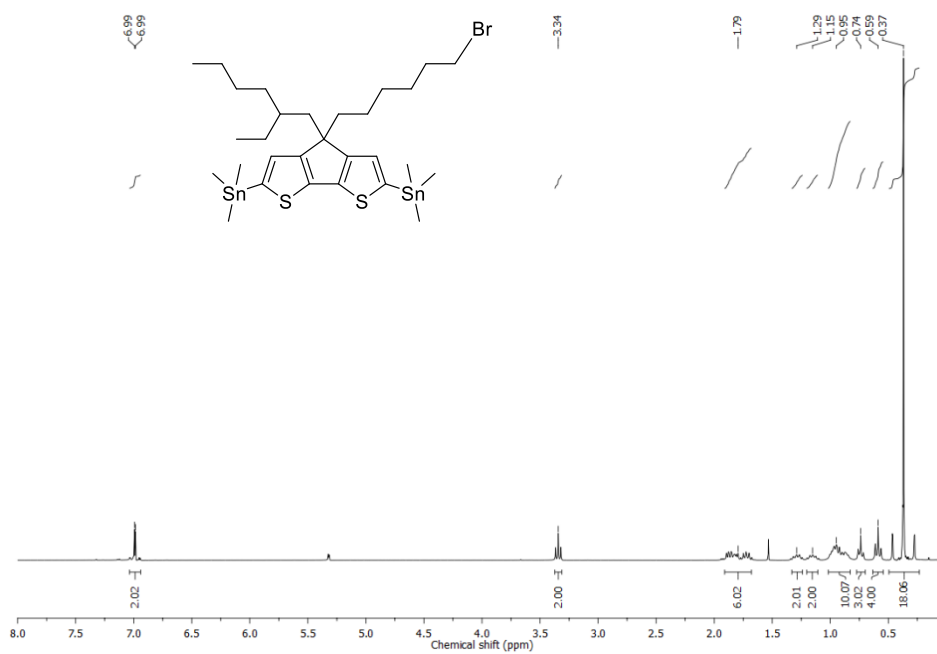
**4-[4-(2-ethylhexyl)-4*H*-cyclopenta[2,1-*b*:3,4-*b'*]dithiophen-4-yl]butan-1-ol (6)**

**3-[4-(2-ethylhexyl)-4*H*-cyclopenta[2,1-*b*:3,4-*b'*]dithiophen-4-yl]propan-1-ol (9)**

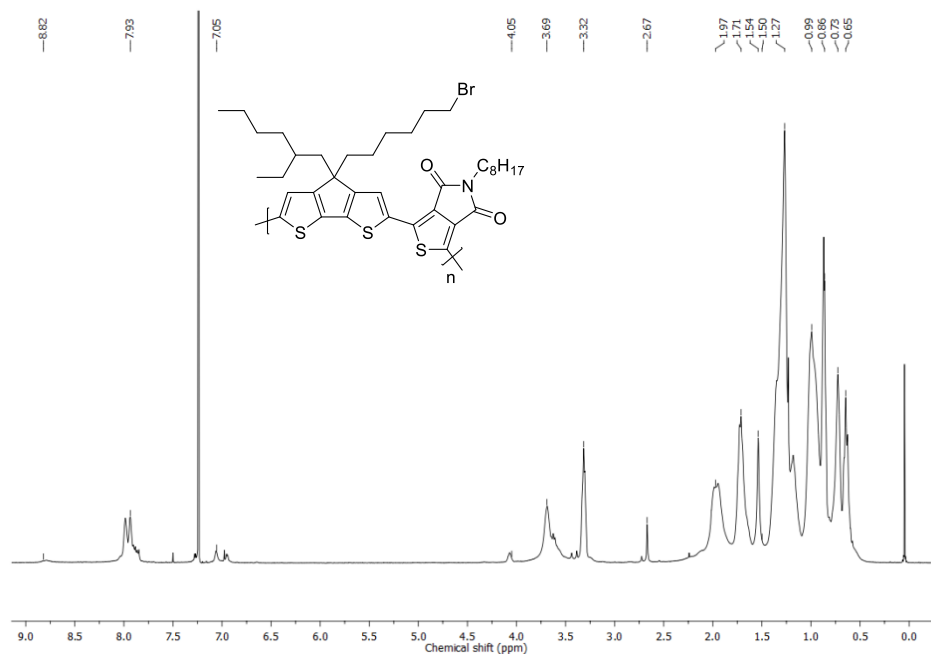


**5-[4-(2-ethylhexyl)-4*H*-cyclopenta[2,1-*b*:3,4-*b'*]dithiophen-4-yl]pentan-2-ol (10)**

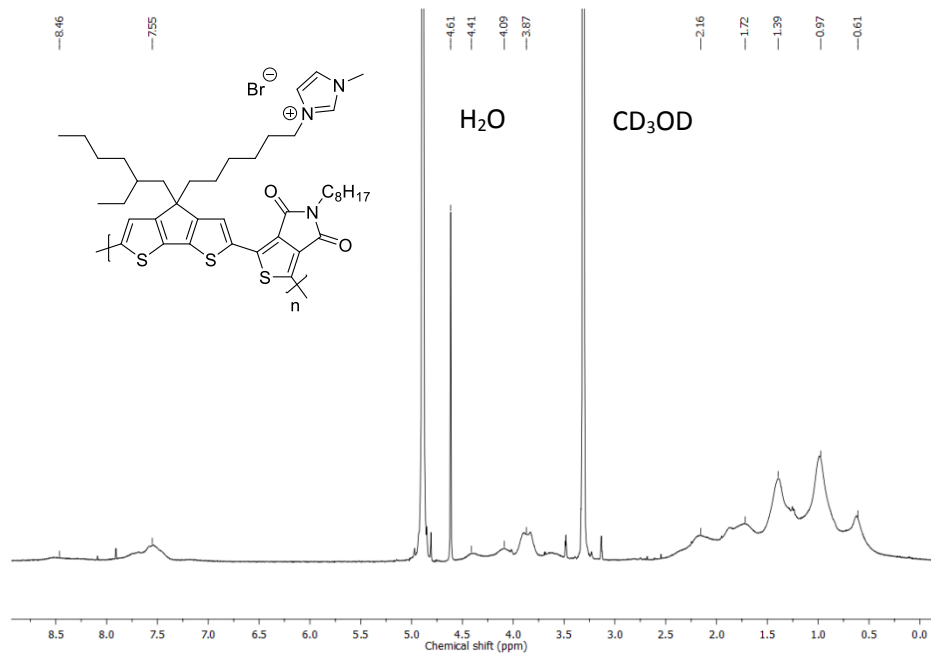
**[4-(6-bromohexyl)-4-(2-ethylhexyl)-4*H*-cyclopenta[2,1-*b*:3,4-*b'*]dithiophene-2,6-diyl]bis(tri-methylstannane) (8)**



**PCPDTTPD-Br**



**PCPDTTPD-Im**



**Thermal analysis**

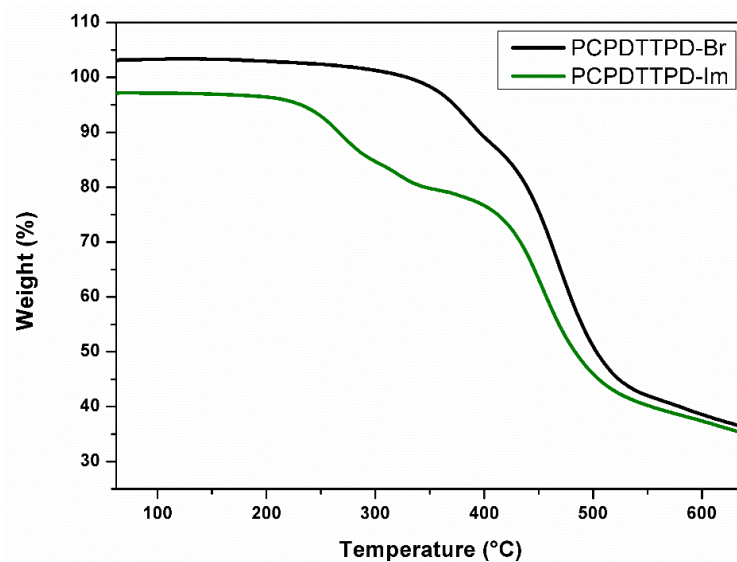


**Figure S1.** TGA analysis of **PCPDTPD-Br** and **PCPDTPD-Im**.

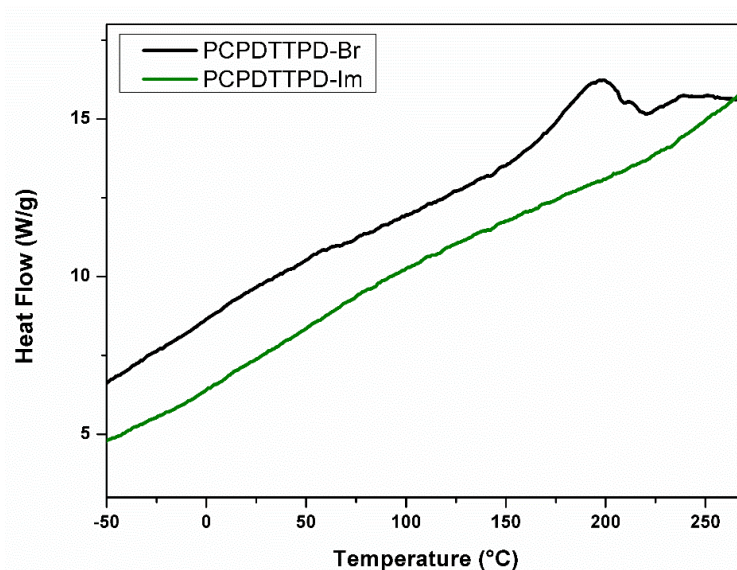


**Figure S2.** RHC (second) heating profiles for **PCPDTPD-Br** and **PCPDTPD-Im** (heating at  $500 \text{ K min}^{-1}$  after cooling at  $20 \text{ K min}^{-1}$ ; curves shifted vertically for clarity).

**Cyclic voltammetry**

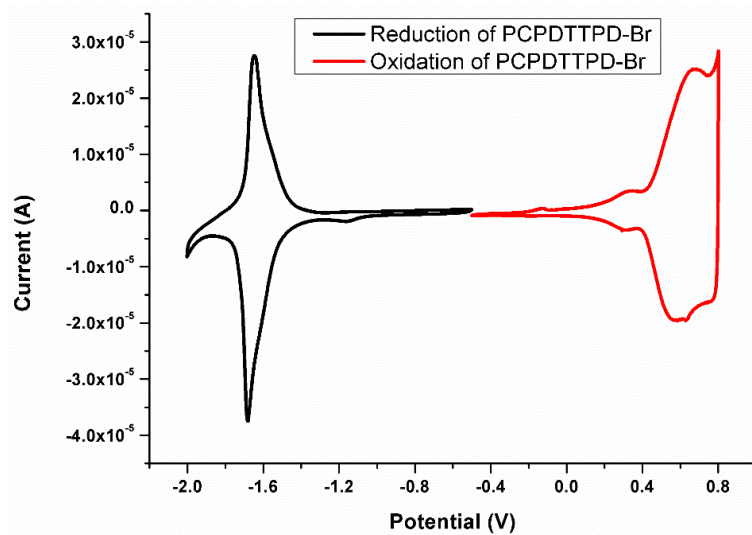


**Figure S3.** Oxidation and reduction curves (cyclic voltammetry) for **PCPDTPD-Br**.

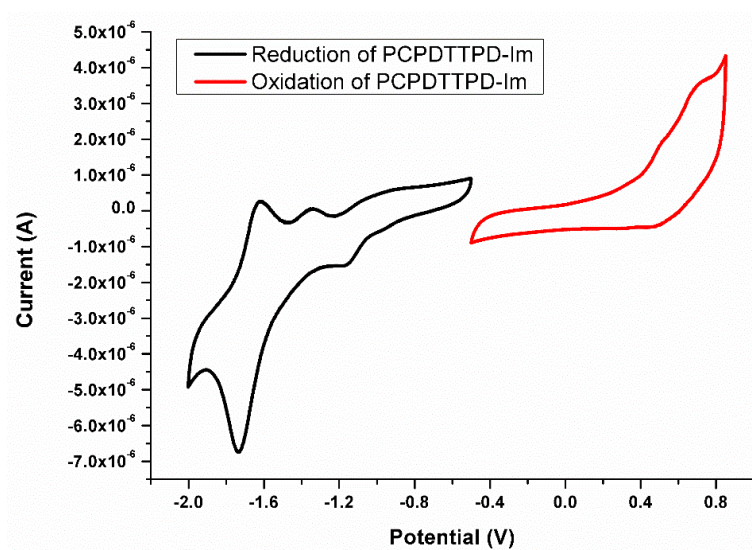
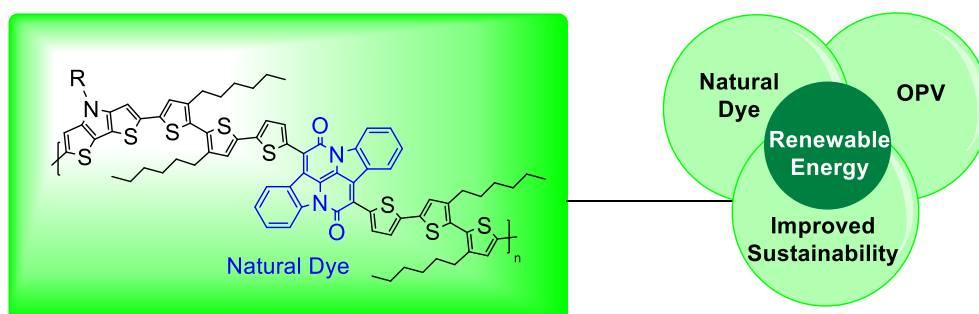


**Figure S4.** Oxidation and reduction curves (cyclic voltammetry) for **PCPDTPD-Im**.

# Chapter 5

## Low Bandgap Polymers Based on Bay-Annulated Indigo for Organic Photovoltaics: Enhanced Sustainability in Material Design and Solar Cell Fabrication

---



Brebels, J.; Klider, K. C. C. W. S.; Kelchtermans, M.; Verstappen, P.; Van Landeghem, M.; Van Doorslaer, S.; Goovaerts, E.; Garcia, J. R.; Manca, J.; Lutsen, L.; Vanderzande, D.; Maes, W., *Org. Electron.* **2017**, *50*, 264.

## Abstract

Although research in the field of organic photovoltaics (OPV) still merely focuses on efficiency, efforts to increase the sustainability of the production process and the materials encompassing the device stack are of equally crucial importance to fulfil the promises of a truly renewable source of energy. In this study, a number of steps in this direction are taken. The photoactive polymers all contain an electron-deficient building block inspired on the natural indigo dye, bay-annulated indigo, combined with electron-rich thiophene and 4*H*-dithieno[3,2-*b*:2',3'-*d*]pyrrole units. The synthetic protocol (starting from indigo) is optimized and the final materials are thoroughly analyzed. MALDI-TOF mass spectrometry provides detailed information on the structural composition of the polymers. Best solar cell efficiencies are obtained for polymer:fullerene blends spin-coated from a pristine non-halogenated solvent (*o*-xylene), which is highly recommended to reduce the ecological footprint of OPV and is imperative for large scale production and commercialization.

## 5.1 Introduction

Low bandgap conjugated (co)polymers consisting of alternating electron-rich (donor or 'push') and electron-poor (acceptor or 'pull') moieties in the polymer backbone have attracted a lot of attention during the last decade because of their interesting properties for organic electronics, in particular field-effect transistors (OFETs)<sup>[1,2]</sup> and photovoltaics (OPVs).<sup>[3]</sup> Because of the high absorptivity and suitability for printing of these types of organic semiconductors, fully flexible, ultra-thin photovoltaic devices can be produced. Other interesting properties such as semi-transparency and a better performance in diffuse light render OPV especially attractive for portable electronics and textile or building integration.<sup>[4-11]</sup> To absorb a maximum amount of solar light – from the UV throughout the visible up to the near-infrared (NIR) range – to be converted into electricity, the energy levels of the polymer absorbers must be fine-tuned on a molecular level.<sup>[12,13]</sup> This implies variation of the molecular structure to optimize the frontier orbital energy levels (HOMO and LUMO) and the resulting (low) bandgap. Simultaneously, appropriate solubility and miscibility with the electron-acceptor material is needed to achieve a near-ideal nanostructured bulk heterojunction (BHJ) active layer and a blend morphology maximizing charge extraction.<sup>[14]</sup>

A key step in improving OPV device efficiency is the quest for highly efficient donor and acceptor units creating photoactive push-pull type low bandgap copolymers or analogous small molecules. Recently, a novel acceptor chromophore based on the natural indigo dye, bay-annulated indigo (BAI), was reported as a promising building block for organic semiconducting materials.<sup>[15-20]</sup> The optical, electrochemical and charge carrier (hole/electron) mobility characteristics of the resulting low bandgap compounds are attractive for both electron donor and acceptor type OPV materials.<sup>[20]</sup> BAI shows several similarities with other lactam-based building blocks<sup>[21-24]</sup> affording highly efficient OPV materials (e.g. isoindigo<sup>[21]</sup> and diketopyrrolopyrrole or DPP; Figure 1). It is a strongly electron-deficient moiety because of the presence of two lactam units, resulting in a low-lying LUMO level, thereby rendering it an attractive acceptor unit for push-pull type low bandgap copolymers.<sup>[25]</sup> Furthermore, when proceeding from indigo to BAI, an enlarged planar structure is created, which improves the  $\pi$ - $\pi$  stacking tendency of the resulting materials and hence facilitates intermolecular charge

transport. Moreover, the BAI unit could also be used as an attractive precursor to design non-fullerene acceptor<sup>[26]</sup> materials.

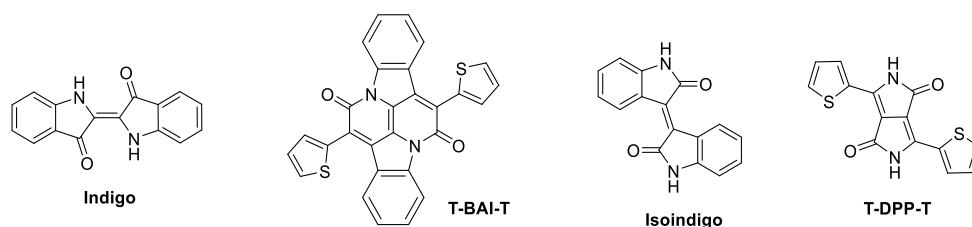


**Figure 1.** Lactam-based electron deficient building blocks.

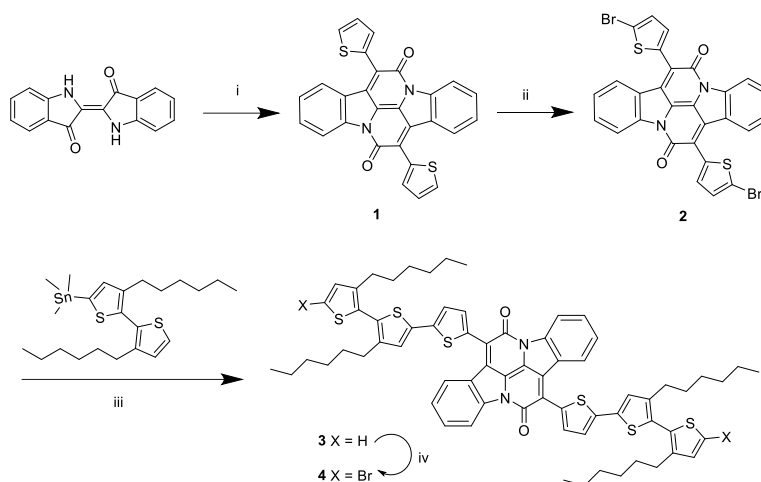
Although recent achievements have pushed up the power conversion efficiencies (PCEs) of polymer solar cells to over 11% for single junction devices,<sup>[27]</sup> there is an eminent need for short, simple and scalable processes to reduce the synthesis costs of the active materials.<sup>[28-30]</sup> Furthermore, at present, the photoactive layers of the top-efficiency BHJ organic solar cells are most often produced from solutions in high-boiling chlorinated solvents with significant toxicity, such as (*ortho*-di)chlorobenzene.<sup>[26,31,32]</sup> These aromatic solvents are selected based on their solubilizing properties and the high boiling points lead to slow drying conditions, allowing for self-organization of the active components and the generation of favorable nanoscale blend morphologies. To reduce the ecological footprint of the OPV production process, especially upon upscaling, deposition from less harmful, non-halogenated solvents is highly desirable.<sup>[27,33-35]</sup> Recent studies have shown that *o*-xylene can be used as an alternative casting solvent, affording similar results as for chlorinated solvents.<sup>[36-42]</sup>

In the present study, *o*-xylene was found to be a superior processing solvent for active layer combinations of BAI-based copolymers and [70]PCBM ([6,6]-phenyl-C<sub>71</sub>-butyric acid methyl ester). A device efficiency of 2.41% was achieved. Although the efficiency remains modest, this is among the highest values reported so far for OPV devices made from potentially bio-sustainable BAI-based materials.<sup>[15-20]</sup> The main importance of the reported results resides, however, in the reduced environmental impact of the active material development as well as the device processing. Moreover, MALDI-TOF mass spectrometry analysis of the final BAI-based polymers provided useful insights on the noticeably large variety of structures present in presumably simple alternating low bandgap copolymers.

## 5.2 Results and discussion

### *Material synthesis and characterization*

Because of the increasing scarceness of crude oil, chemicals derived from non-fossil fuel resources are obviously gaining importance. In this respect, the natural dye indigo is highly attractive. Bay-annulated indigo (diindolonaphtyridine-6,13-dione) can be prepared from indigo in a single step. In this work, we have optimized the synthetic sequence toward thiophene-extended BAI derivative **2** (Scheme 1).<sup>[15]</sup> In the first step, a double annulation on indigo was performed with thiophene-2-acetyl chloride. Because of the (very) low solubility of precursor **1** and the formation of tar-like side products, more optimal reaction and purification conditions were pursued. *o*-Xylene was replaced by toluene as the reaction solvent, which resulted in less tar-like materials being formed, tentatively attributed to the lower boiling point of the applied solvent. After the reaction, it was found to be crucial to first purify the product by Soxhlet extractions with acetone and chloroform (recovering the material) before final recrystallization. This approach provides a more pure product (see <sup>1</sup>H NMR spectrum in the supporting information). No elaborate purification methods were required, in contrast to other literature procedures affording comparable yields.<sup>[19,20]</sup> In the next step, dibromination was performed with *N*-bromosuccinimide (NBS) in DMF, which reduced the solubility of the BAI core even further. Bromination was performed at 60 °C to completely solubilize the starting material and hence obtain complete conversion without too much (over)heating.

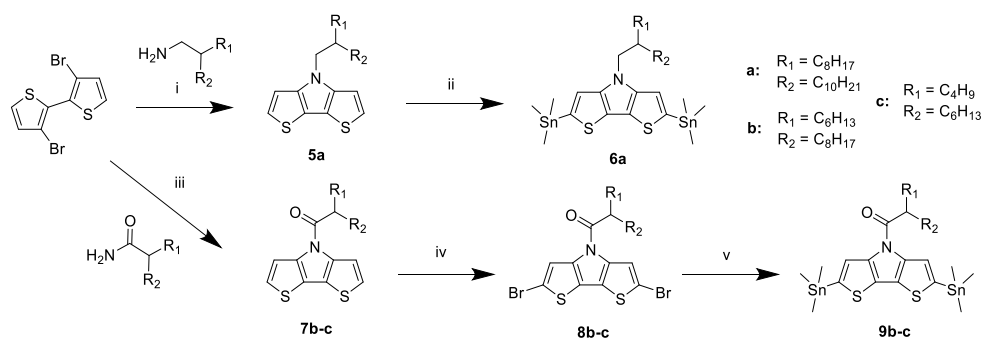


**Scheme 1.** BAI monomer synthesis: i) thiophene-2-acetyl chloride, toluene, reflux, 72 h (27%); ii) NBS, DMF, 60 °C, 3 h (84%); iii) Pd(PPh<sub>3</sub>)<sub>4</sub>, toluene, DMF, reflux, 16 h (55%); iv) NBS, CHCl<sub>3</sub>, RT, 16 h (76%).

To increase the solubility of the BAI precursor, we decided to extend the chromophore with an alkylated bithiophene moiety (Scheme 1). To this extent, mono-stannylation of a hexylated 2,2'-bithiophene unit was performed first, and then this moiety was introduced on BAI compound **2** via a Stille cross-coupling reaction employing Pd(PPh<sub>3</sub>)<sub>4</sub> as the catalyst. An analogous Suzuki protocol was tested as well, affording similar results and avoiding the formation of toxic tin residues. Product **3** was considerably more soluble and therefore it was easily purified by column chromatography. The moderate yield (55%) might be due to remaining impurities in the starting product **2**. In the final step, bromination with NBS in CHCl<sub>3</sub> was performed and the desired monomer **4** was readily obtained.

From this novel BAI monomer, a first polymer was prepared by combining it with 2,5-bis(trimethylstannyl)thiophene in a Stille cross-coupling polycondensation. However, an insoluble material was obtained, indicating that alkylated donor building blocks are required to render the final low bandgap polymers soluble and processable. Because of our previous successes with 4*H*-dithieno[3,2-*b*:2',3'-*d*]pyrrole (DTP) derivatives,<sup>[43-45]</sup> we turned to these electron-rich precursors. At first, the *N*-alkylated DTP unit **5a** was synthesized starting from 3,3'-dibromo-2,2'-bithiophene and 2-octyldodecan-1-amine (Scheme 2). Subsequently,

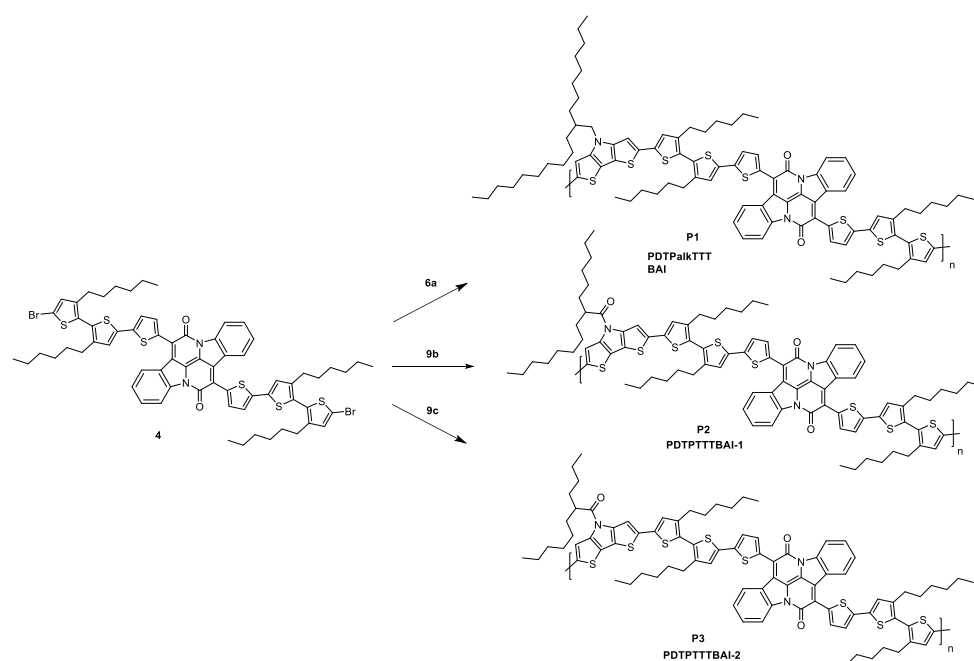
distannylation with trimethyltin chloride was performed to obtain DTP monomer **6a**.<sup>[46]</sup> A relatively long branched side chain was introduced to overcome solubility problems in the resulting polymer. Two other DTP-*alt*-BAI polymers were synthesized as well. However, for these polymers, the N-alkyl substituent on the DTP part was replaced by an N-acyl unit, which has been shown before to lower the HOMO level of the resulting polymers and hence afford an increased open-circuit voltage ( $V_{oc}$ ) in the final solar cells.<sup>[43-47]</sup> The required bis(trimethylstannyl)-DTP monomers, 1-[2,6-bis(trimethylstannyl)-4*H*-dithieno[3,2-*b*:2',3'-*d*]pyrrol-4-yl]-2-hexyldecan-1-one (**9b**) and 1-[2,6-bis(trimethylstannyl)-4*H*-dithieno[3,2-*b*:2',3'-*d*]pyrrol-4-yl]-2-butyloctan-1-one (**9c**) (Scheme 2), were prepared according to literature procedures.<sup>[43,47]</sup> A copper-catalyzed reaction between 3,3'-dibromo-2,2'-bithiophene and the respective amide-functionalized side chain was performed, followed by dibromination with NBS and final distannylation with hexamethylditin (Scheme 2). All final monomers were purified by (recycling) preparative size exclusion chromatography (prep-SEC) to eliminate residual impurities, allowing a proper stoichiometric balance in the polymerization reactions. This is essential to achieve high molar masses, as generally required for efficient polymer solar cells.<sup>[48-51]</sup>



**Scheme 2.** DTP monomer synthesis: i)  $t\text{BuONa}$ ,  $\text{Pd}_2(\text{dba})_3$ , BINAP, toluene, reflux, 16 h (86%); ii)  $n\text{-BuLi}$ ,  $(\text{CH}_3)_3\text{SnCl}$ ,  $-78\text{ }^\circ\text{C}$ , 5 h (58%); iii)  $\text{K}_2\text{CO}_3$ ,  $\text{CuI}$ , DMEDA, toluene, reflux, 24 h (57%); iv) NBS,  $\text{CHCl}_3$ ,  $0\text{ }^\circ\text{C}$ , 2 h (93%); v)  $(\text{CH}_3)_3\text{SnSn}(\text{CH}_3)_3$ ,  $\text{LiCl}$ ,  $\text{Pd}(\text{PPh}_3)_4$ , toluene, reflux, 1 h (59%).

The different monomers were then copolymerized using a Stille polycondensation approach under standard conditions (2 mol%  $\text{Pd}_2\text{dba}_3$ , 8 mol%  $\text{P}(o\text{-tol})_3$ , toluene/DMF, reflux, 16 h; Scheme 3). After the reactions, the crude polymer

materials were precipitated in methanol and further purified using Soxhlet extractions with different solvents (acetone, *n*-hexane and chloroform successively, for at least 2 hours) to remove catalyst residues and low molar mass species. Finally, polymers with number-averaged molar masses ( $M_n$ ) of 29, 55 and 20 kg/mol for **P1**, **P2** and **P3**, respectively, were obtained (Table 1). The lower  $M_n$  observed for **P3** can be attributed to the fact that it already precipitated during the polymerization, prohibiting it to react any further. The final polymer material (**P3**) was only soluble in high boiling point solvents (e.g. hot chlorobenzene).



**Scheme 3.** BAI-*alt*-DTP polymer synthesis by Stille cross-coupling (similar reaction conditions for all polymerizations: 2 mol% Pd<sub>2</sub>dba<sub>3</sub>, 8 mol% P(*o*-tol)<sub>3</sub>, toluene/DMF, reflux, 16 h).

MALDI-TOF (matrix-assisted laser desorption ionization time-of-flight) mass spectrometry was applied to gain more information on the exact nature of the products within the polymer distribution. Although such analysis is rarely performed for low bandgap copolymers, MALDI-TOF can provide important insights on the polymer composition that cannot trivially be obtained by other techniques. The MALDI-TOF spectra (Figure 2, 3 and S1-S4) are similar for the

three polymers. Besides the expected alternating oligomer-like species, homocoupling of both the acceptor (BAI) and donor (DTP) monomers was observed as well, probably generating a stoichiometric imbalance during the polymerization and thereby hindering the formation of high molar masses. The strong impact of homocoupling 'defects' on the final solar cell performance has recently been elucidated in a number of studies.<sup>[45,50,52-54]</sup> As such, direct identification of homocoupling via MALDI-TOF is very relevant. Furthermore, MALDI-TOF also allows identifying the end groups of the different polymer chains. In this particular case, reactive bromide end groups were still observed for polymers **P1** and **P3**. Moreover, methyl end-capping is also seen regularly, pointing to methyl transfer from the trimethylstannyl precursors as an important polymer termination reaction.<sup>[55]</sup> The lower molar masses observed in the MALDI-TOF spectra as compared to the SEC data are a result of the overestimation of the molar masses derived from SEC (because of the polystyrene standards used and the tendency of the polymers to aggregate) and the use of lower molar mass fractions for the MALDI-TOF analysis (to facilitate the sample preparation, improve the signal to noise ratio and allow structural analysis).

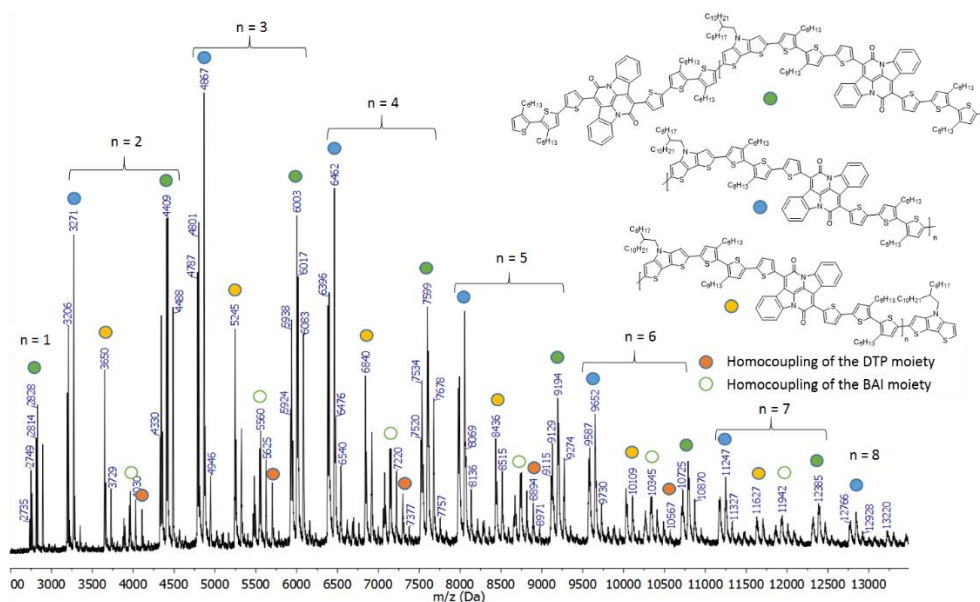


**Figure 2.** MALDI-TOF mass spectrum of **P1**.

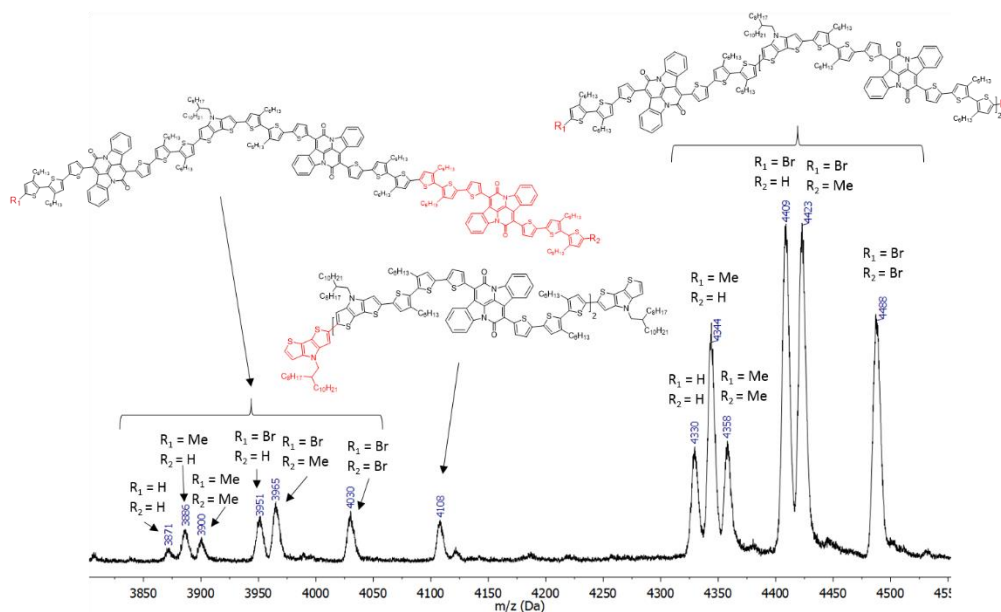


**Figure 3.** MALDI-TOF mass spectrum of **P1** (zoom from  $m/z$  3800 to 4550  $\text{g mol}^{-1}$ ), with the assignment of homocoupling and end group identification.

The thermal properties of the polymers were investigated by thermogravimetric analysis (TGA) and rapid heat-cool calorimetry (RHC) (Figure S5-S6, Table 1). TGA showed that the polymers are thermally stable (i.e. they do not lose any mass) up to 300 °C. RHC was chosen above regular differential scanning calorimetry (DSC) because of its increased sensitivity to thermal transitions resulting from the fast scanning rates and the low sample amounts required.<sup>[56]</sup> RHC analysis indicated that all polymers are fully amorphous in the second heating (after a preceding cooling at 20 K  $\text{min}^{-1}$ ), whereas some endo/exothermic behavior between 70 and 150 °C was seen in the first heating (Figure S6). A glass transition ( $T_g$ ) between 130 and 150 °C was observed in the second heating for all three materials. These high  $T_g$ 's are beneficial for the thermal stability of the bulk heterojunction blends.<sup>[57-60]</sup>

The optical and electrochemical properties of the three polymers were also investigated to analyze the suitability of the novel materials for polymer solar cells and to establish structure-property relations. Figure 4 shows the UV-Vis-NIR absorption spectra in chlorobenzene solution and in the solid state. All polymers exhibit a broad dual band absorption in the 350–900 nm region. A notable

extension to the NIR is observed compared to standard low bandgap polymers because of the highly electron-deficient nature of the BAI moiety. Polymer **P1** shows the largest bathochromic shift, which can be attributed to the increased donor strength of the N-alkylated DTP component. In all cases, peak broadening is observed when going from solution to the solid state, pointing to  $\pi$ - $\pi$  stacking and therefore strong electronic interactions in the films. The optical bandgaps, estimated from the absorption edges of the polymer films, are all similar and around 1.4 eV (Table 1). The absorption coefficients of the three polymers in chlorobenzene solution are in the range of 40–55 L g<sup>-1</sup> cm<sup>-1</sup> (Figure S7). The differences can be due to the different DTP monomers employed (N-alkyl vs N-acyl), molar mass and/or side chain (volume fraction) variations.<sup>[61]</sup>

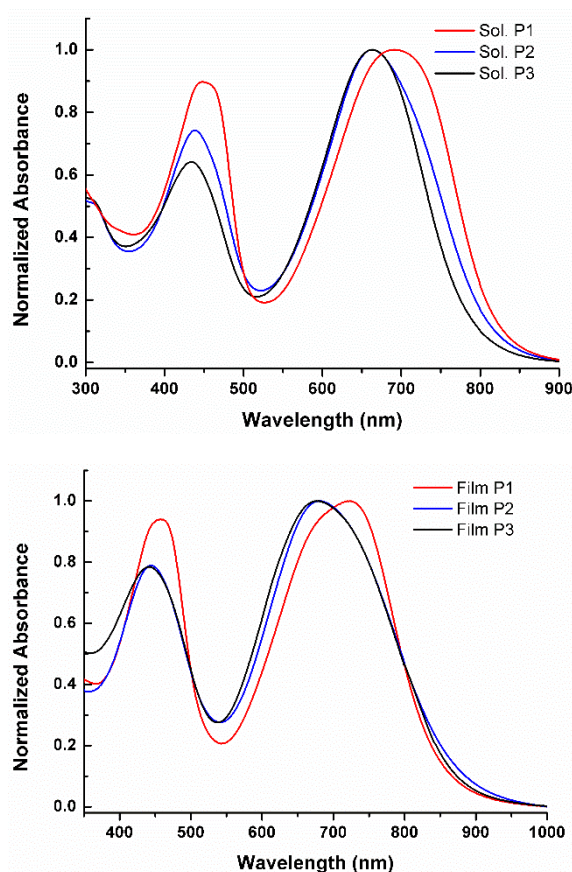


**Figure 4.** Normalized UV-Vis-NIR absorption spectra for **P1**, **P2** and **P3** in chlorobenzene solution (top) and thin film (bottom).

**Table 1.** Molar mass, optical, thermal and electrochemical data for copolymers **P1**, **P2** and **P3**.

	$M_n^a /$ kg mol <sup>-1</sup>	$\bar{D}$	$\lambda_{\max}$ film <sup>b</sup> / nm	$\epsilon^c /$ L g <sup>-1</sup> cm <sup>-1</sup>	$E_{g\text{film}}^d$ / eV	$T_g^e /$ °C	$E_{g\text{cv}}^f$ / eV	$E_{\text{HOMO}}^g /$ eV	$E_{\text{LUMO}}^g$ / eV
<b>P1</b>	29	4.4	723	43.0	1.46	130	1.40	-5.2(6)	-3.9
<b>P2</b>	55	3.3	680	54.9	1.41	134	1.44	-5.3(0)	-3.9
<b>P3</b>	20	1.7	677	52.4	1.41	149	1.50	-5.3(1)	-3.8

<sup>a</sup> Measured by SEC at 60 °C in chlorobenzene. <sup>b</sup> Films were prepared by drop-casting a solution of the polymer onto a quartz disc. <sup>c</sup> Extinction coefficient of the polymers in solution at  $\lambda_{\max}$ . <sup>d</sup> Optical bandgap, determined by the onset of the solid-state UV-Vis-NIR spectrum. <sup>e</sup> Glass transition temperature (2<sup>nd</sup> heating). <sup>f</sup> Electrochemical bandgap. <sup>g</sup> Determined from the onset of oxidation/reduction in cyclic voltammetry.

The electrochemical features of the polymers were investigated by cyclic voltammetry (CV; Figure S8, Table 1). HOMO and LUMO energy levels were estimated from the oxidation and reduction onset potentials. As expected, a deeper HOMO level was observed when introducing the N-acyl substituent on the DTP part.<sup>[43,47]</sup> From the data obtained, there seems to be no (substantial) LUMO-LUMO offset with [70]PCBM ( $E_{\text{red}} = -1.26$  eV under the same experimental CV conditions; Figure S8), suggesting that the polymers might not act as efficient electron donors in combination with [70]PCBM. To investigate the charge-transfer mechanism between the polymers and [70]PCBM, light-induced electron paramagnetic resonance (LI-EPR) experiments were performed on the **P2**: [70]PCBM (1:4) blend. The X-band (9.4 GHz) and W-band (94 GHz) LI-EPR spectra (Figure S11) enabled the identification of the positive and negative radicals formed in the blend after charge transfer, based on their respective electronic g-tensors. By comparison of the experimental g-values with those obtained from our density functional theory (DFT) calculations (Table S1, Figure S10, S11) and literature values for the [70]PCBM anion,<sup>[62]</sup> the EPR spectra could be unambiguously assigned to positive radicals on the **P2** polymer (with the deepest LUMO in the series) and negative radicals on the fullerene molecules, thereby confirming the donor character of the polymers relative to [70]PCBM.

**OPV device fabrication and analysis**

The photovoltaic performances of the novel materials were then investigated by fabricating BHJ organic solar cells with a traditional device architecture consisting of glass/ITO/PEDOT:PSS/polymer:[70]PCBM/Ca/Al. The device measurements were carried out under illumination of AM1.5G simulated solar light ( $100 \text{ mW cm}^{-2}$ ) and the photovoltaic properties are summarized in Table 2.

Polymer **P1** showed a good solubility in all common processing solvents. On the other hand, due to the low solubility of **P2** and **P3**, high-boiling aromatic solvents (e.g. chlorobenzene, *o*-xylene, ...) were needed to completely dissolve these polymers and to process the active layers. The performance of the BHJ solar cells was first optimized by changing the polymer to [70]PCBM ratios and layer thicknesses of the blends. **P1** showed an optimal polymer:fullerene weight ratio of 1:3, whereas for **P2** and **P3**, 1:4 turned out to be the best ratio, with optimal layer thicknesses around 80–90 nm for all devices. At first, the devices made from **P1** were further optimized. Unfortunately, however, modest efficiencies (up to a PCE of 1.24%) were obtained in all cases. Especially the  $V_{oc}$  and fill factor (FF) turned out to be the limiting factors (Table 2, S2). Replacement of the alkyl substituents on the DTP units by acyl derivatives notably improved the  $V_{oc}$ ,<sup>[43,47]</sup> in accordance with the electrochemical data. Careful optimization of the processing solvent for the **P3**:[70]PCBM blends afforded a best performing device with a PCE of 1.84% from chlorobenzene (Table S2). Upon annealing at 85 °C for 10 minutes, the efficiency further improved to 2.22% ( $J_{sc} = 6.83 \text{ mA cm}^{-2}$ ,  $V_{oc} = 0.80 \text{ V}$ ,  $FF = 0.41$ ; Table 2). Despite the higher  $M_n$  of **P2**, similar device results were initially achieved. However, as this polymer is also soluble in *o*-xylene, this processing solvent could also be applied. *o*-Xylene is a 'greener' alternative for the most commonly used halogenated processing solvents. It has a high boiling point and is a suitable candidate for high-throughput OPV production.<sup>[36-42]</sup> In our case, *o*-xylene turned out to be the best choice and a record PCE of 2.41% ( $J_{sc} = 6.67 \text{ mA cm}^{-2}$ ,  $V_{oc} = 0.82 \text{ V}$ ,  $FF = 0.44$ ; Figure 5, Table 2) was achieved after annealing at 110 °C for 10 minutes. To further improve the efficiency, anisaldehyde was used as a co-solvent in various volume concentrations (1 to 2% v/v).<sup>[37]</sup> Unfortunately, however, the PCE did not increase any further (Table 2). The EQE spectrum shows a broad charge photogeneration ( $J_{EQE} = 6.82 \text{ mA cm}^{-2}$ )

range from 300 up to 900 nm, hence extending into the NIR (Figure S12). Expansion to the NIR is considered to be a main challenge for OPV and is important to further improve the efficiency of state-of-the-art devices.<sup>[20,52]</sup> Despite extensive optimization efforts, modest device efficiencies were still obtained, which can tentatively be attributed to the low/average molar masses obtained, the presence of homocoupling in all three polymer compositions and the modest driving force for electron transfer. Nevertheless, one of the highest PCE's for a BHJ solar cell made from a BAI-based polymer material was achieved.<sup>[15-20]</sup>

**Table 2.** Photovoltaic output parameters for the BHJ organic solar cells based on copolymers **P1**, **P2** and **P3** (in combination with [70]PCBM).

Polymer	Solvent <sup>a</sup>	Ratio <sup>b</sup> /wt%	Additive	V <sub>oc</sub> / V	J <sub>sc</sub> / mA cm <sup>-2</sup>	FF	Best PCE <sup>d</sup> / %
<b>P1</b>	CF	1:3	/	0.64	5.37	0.36	1.24 (1.22)
<b>P2</b>	CB	1:4	10% TCE <sup>c</sup> (annealed @85 °C)	0.78	6.99	0.42	2.28 (2.25)
<b>P2</b>	<i>o</i> -xylene	1:4	/ (annealed @110 °C)	0.82	6.67	0.44	2.41 (2.28)
<b>P2</b>	<i>o</i> -xylene	1:4	1% anisaldehyde (annealed @110 °C)	0.80	6.47	0.45	2.31 (2.13)
<b>P3</b>	CB	1:4	/ (annealed @85 °C)	0.80	6.83	0.41	2.22 (2.06)

<sup>a</sup> CF = chloroform, CB = chlorobenzene. <sup>b</sup> Polymer:[70]PCBM. <sup>c</sup> TCE = tetrachloroethane.

<sup>d</sup> Average efficiencies over at least 3 devices in brackets.

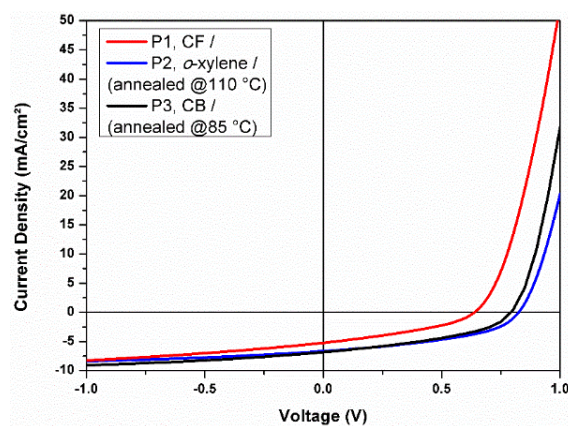


**Figure 5.** *J-V* characteristics of the best polymer solar cells prepared from the **P1–P3**: $[70]$ PCBM blends.

The limited FF and  $J_{sc}$  values cannot simply be attributed to a too low hole mobility of the new donor polymers. The saturated hole mobilities for the **P1** and **P2** polymers as measured in OFETs were similar and in the appropriate range ( $1 \times 10^{-3} \text{ cm}^2/\text{Vs}$  for **P1** and  $3 \times 10^{-3} \text{ cm}^2/\text{Vs}$  for **P2**). Most often, a less than optimal active layer morphology is at the origin of OPV blends performing below expectations. The surface morphology of the best performing active layer blend was investigated with atomic force microscopy (AFM) in tapping mode (Figure S13). A rather rough morphology was observed, with large particles remaining in the active layer, which is in agreement with the moderate FF values observed. These large domains also reduce the donor-acceptor interface and hence the dissociation of excitons into free charges, thereby limiting the  $J_{sc}$ . The addition of 1% (v/v) anisaldehyde as co-solvent did not improve the surface morphology, providing even larger domains (Figure S18), in accordance with the values of the OPV parameters.

### 5.3 Conclusions

Three push-pull type copolymers employing bay-annulated indigo as the electron deficient and 4*H*-dithieno[3,2-*b*:2',3'-*d*]pyrrole as the electron rich building block were synthesized, with particular attention for the synthetic protocol of the nature-inspired BAI monomer. MALDI-TOF mass spectrometry provided detailed information on the structural composition of the polymers, indicating homocoupling defects as well as methyl shift termination reactions. Photophysical

and electrochemical analysis pointed out that the polymers possess relatively small bandgaps ( $\sim 1.4$  eV) and low-lying LUMO levels. Nevertheless, EPR analysis showed that the polymers act as electron donors in combination with [70]PCBM. The polymers were then all tested in bulk heterojunction solar cells, affording a maximum efficiency of 2.41%, which is among the highest efficiencies reported so far for organic photovoltaics prepared from BAI-containing active materials. Photocurrent is generated throughout the complete visible spectrum up to the NIR range. Noteworthy, the optimal result was achieved using a non-halogenated processing solvent (*o*-xylene), which is beneficial from an ecological point of view. As the device performance seems to be partly limited by the non-favorable active layer morphology, current efforts focus on the introduction of different donor building blocks to increase the miscibility of the final BAI-based polymers with suitable electron acceptors, in particular non-fullerene materials with low-lying LUMO levels. On the other hand, the NIR activity of the blends can also beneficially be applied in organic photodetectors.<sup>[63]</sup> Finally, further efforts are required toward a truly 'green' synthesis of BAI-based organic semiconductors.<sup>[64]</sup>

## 5.4 References

- [1] Kim, G.; Kang, S.-J.; Dutta, G. K.; Han, Y.-K.; Shin, T. J.; Noh, Y.-Y.; Yang, C. *J. Am. Chem. Soc.* **2014**, *136* (26), 9477.
- [2] Yamashita, Y.; Hinkel, F.; Marszalek, T.; Zajaczkowski, W.; Pisula, W.; Baumgarten, M.; Matsui, H.; Müllen, K.; Takeya, J. *Chem. Mater.* **2016**, *28* (2), 420.
- [3] Müllen, K.; Pisula, W. *J. Am. Chem. Soc.* **2015**, *137* (30), 9503.
- [4] Dennler, G.; Scharber, M. C.; Brabec, C. J. *Adv. Mater.* **2009**, *21* (13), 1323.
- [5] Kaltenbrunner, M.; White, M. S.; Glowacki, E. D.; Sekitani, T.; Someya, T.; Sariciftci, N. S.; Bauer, S. *Nat. Commun.* **2012**, *3*, 770.
- [6] Su, Y. W.; Lan, S. C.; Wei, K. H. *Mater. Today* **2012**, *15* (12), 554-562.
- [7] Darling, S. B.; You, F. *RSC Adv.* **2013**, *3*, 17633.
- [8] Lizin, S.; Van Passel, S.; De Schepper, E.; Maes, W.; Lutsen, L.; Manca, J.; Vanderzande, D. *Energy Environ. Sci.* **2013**, *6*, 3136.
- [9] Dou, L.; You, J.; Hong, Z.; Xu, Z.; Li, G.; Street, R. A.; Yang, Y. *Adv. Mater.* **2013**, *25* (46), 6642.
- [10] Mazziro, K. A.; Luscombe, C. K. *Chem. Soc. Rev.* **2015**, *44*, 78.
- [11] Kang, H.; Kim, G.; Kim, J.; Kwon, S.; Kim, H.; Lee, K. *Adv. Mater.* **2016**, *28* (36), 7821.
- [12] Havinga, E. E.; Ten Hoeve, W.; Wynberg, H. *Polym. Bull.* **1992**, *29* (1), 119.
- [13] Kitamura, C.; Tanaka, S.; Yamashita, Y. *Chem. Mater.* **1996**, *8* (2), 570.
- [14] Park, S. H.; Roy, A.; Beaupré, S.; Cho, S.; Coates, N.; Moon, J. S.; Moses, D.; Leclerc, M.; Lee, K.; Heeger, A. J. *Nature Photon.* **2009**, *3*, 297.
- [15] He, B.; Pun, A. B.; Zherebetskyy, D.; Liu, Y.; Liu, F.; Klivansky, L.; McGough, A. M.; Zhang, B. A.; Lo, K.; Russell, T. P.; Wang, L.; Liu, Y. *J. Am. Chem. Soc.* **2014**, *136* (42), 15093.
- [16] He, B.; Zherebetskyy, D.; Wang, H.; Kolaczowski, M.; Klivansky, L. M.; Tan, T.; Wang, L.; Liu, Y. *Chem. Sci.* **2016**, *7*, 3857.
- [17] He, B.; Neo, W. T.; Chen, T. L.; Klivansky, L. M.; Wang, H.; Tan, T.; Teat, S. J.; Xu, J.; Liu, Y. *ACS Sustainable Chem. Eng.* **2016**, *4* (5), 2797.
- [18] Kolaczowski, M.; He, B.; Liu, Y. *Org. Lett.* **2016**, *18* (20), 5224.
- [19] Fallon, K. J.; Wijeyasinghe, N.; Manley, E. F.; Dimitrov, S. D.; Yousaf, S. A.; Ashraf, R. S.; Duffy, W.; Guilbert, A. A. Y.; Freeman, D. M. E.; Al-Hashimi, M.;

- Nelson, J.; Durrant, J. R.; Chen, L. X.; McCulloch, I.; Marks, T. J.; Clarke, T. M.; Anthopoulos, T. D.; Bronstein, H. *Chem. Mater.* **2016**, *28* (22), 8366.
- [20] Fallon, K. J.; Wijeyasinghe, N.; Yaacobi-Gross, N.; Ashraf, R. S.; Freeman, D. M. E.; Palgrave, R. G.; Al-Hashimi, M.; Marks, T. J.; McCulloch, I.; Anthopoulos, T. D.; Bronstein, H. *Macromolecules* **2015**, *48* (15), 5148.
- [21] Wang, E.; Mammo, W.; Andersson, M. R. *Adv. Mater.* **2014**, *26* (12), 1801.
- [22] Cao, J.; Liao, Q.; Du, X.; Chen, J.; Xiao, Z.; Zuo, Q.; Ding, L. *Energy Environ. Sci.* **2013**, *6*, 3224.
- [23] Qian, L.; Cao, J.; Ding, L. *J. Mater. Chem. A* **2015**, *3*, 24211.
- [24] Cao, J.; Qian, L.; Ding, L. *Polym. Chem.* **2016**, *7*, 1027.
- [25] Guo, X.; Facchetti, A.; Marks, T. J. *Chem. Rev.* **2014**, *114* (18), 8943.
- [26] Zhao, W. C.; Qian, D. P.; Zhang, S. Q.; Li, S. S.; Inganäs, O.; Gao, F.; Hou, J. H. *Adv. Mater.* **2016**, *28* (23), 4734.
- [27] Zhao, J.; Li, Y.; Yang, G.; Jiang, K.; Lin, H.; Ade, H.; Ma, W.; Yan, H. *Nat. Energy* **2016**, *1*, 15027.
- [28] Osedach, T. P.; Andrew, T. L.; Bulovic, V. *Energy Environ. Sci.* **2013**, *6*, 711.
- [29] Po, R.; Bianchi, G.; Carbonera, C.; Pellegrino, A. *Macromolecules* **2015**, *48* (3), 453.
- [30] Pirotte, G.; Kesters, J.; Verstappen, P.; Govaerts, S.; Manca, J.; Lutsen, L.; Vanderzande, D.; Maes, W. *ChemSusChem* **2015**, *8* (19), 3228.
- [31] Yao, Y.; Hou, J.; Xu, Z.; Li, G.; Yang, Y. *Adv. Funct. Mater.* **2008**, *18* (12), 1783.
- [32] Rogers, J. T.; Schmidt, K.; Toney, M. F.; Kramer, E. J.; Bazan, G. C. *Adv. Mater.* **2011**, *23* (20), 2284.
- [33] Galagan, Y.; de Vries, I. G.; Langen, A. P.; Andriessen, R.; Verhees, W. J. H.; Veenstra, S. C.; Kroon, J. M. *Chem. Eng. Process* **2011**, *50* (5-6), 454.
- [34] Tait, J. G.; Merckx, T.; Li, W.; Wong, C.; Gehlhaar, R.; Cheyns, D.; Turbiez, M.; Heremans, P. *Adv. Funct. Mater.* **2015**, *25* (22), 3393.
- [35] Zhang, S.; Ye, L.; Zhang, H.; Hou, J. *Mater. Today* **2016**, *19* (9), 533.
- [36] Aïch, B. R.; Beaupré, S.; Leclerc, M.; Tao, Y. *Org. Electron.* **2014**, *15* (2), 543.
- [37] Sprau, C.; Buss, F.; Wagner, M.; Landerer, D.; Koppitz, M.; Schulz, A.; Bahro, D.; Schabel, W.; Scharfer, P.; Colsmann, A. *Energy Environ. Sci.* **2015**, *8*, 2744.

- [38] Zhang, H.; Yao, H.; Zhao, W.; Ye, L.; Hou, J. *Adv. Energy Mater.* **2016**, *6* (6), 1502177.
- [39] Heo, H.; Kim, H.; Lee, D.; Jang, S.; Ban, L.; Jim, B.; Lee, J.; Lee, Y. *Macromolecules* **2016**, *49* (9), 3328.
- [40] Zhang, Z.; Zhang, X.; Zhang, J.; Gong, X.; Liu, Y.; Lu, H.; Li, C.; Bo, Z. *RSC Adv.* **2016**, *6*, 39074.
- [41] Guérette, M.; Najari, A.; Maltais, J.; Pouliot, J.-R.; Dufresne, S.; Simoneau, M.; Besner, S.; Charest, P.; Leclerc, M. *Adv. Energy Mater.* **2016**, *6* (9), 1502094.
- [42] Seri, M.; Gedefaw, D.; Prosa, M.; Tessarolo, M.; Bolognesi, M.; Muccini, M.; Andersson, M. R. *J. Polym. Sci. A Polym. Chem.* **2016**, *55* (2), 234.
- [43] Vanormelingen, W.; Kesters, J.; Verstappen, P.; Drijkoningen, J.; Kudrjasova, J.; Koudjina, S.; Liégeois, V.; Champagne, B.; Manca, J.; Lutsen, L.; Vanderzande, D.; Maes, W. *J. Mater. Chem. A* **2014**, *2*, 7535.
- [44] Kesters, J.; Verstappen, P.; Vanormelingen, W.; Drijkoningen, J.; Vangerven, T.; Devisscher, D.; Marin, L.; Champagne, B.; Manca, J.; Lutsen, L.; Vanderzande, D.; Maes, W. *Sol. Energy Mater. Sol. Cells* **2015**, *136*, 70.
- [45] Verstappen, P.; Cardinaletti, I.; Vangerven, T.; Vanormelingen, W.; Verstraeten, F.; Lutsen, L.; Vanderzande, D.; Manca, J.; Maes, W. *RSC Adv.* **2016**, *6* (38), 32298.
- [46] Ahmed, E.; Subramaniyan, S.; Kim, F. S.; Xin, H.; Jenekhe, S. *Macromolecules* **2011**, *44* (18), 7207.
- [47] Evenson, S. J.; Rasmussen, S. C. *Org. Lett.* **2010**, *12* (18), 4054.
- [48] Li, W.; Yang, L.; Tumbleston, J. R.; Yan, L.; Ade, H.; You, W. *Adv. Mater.* **2014**, *26* (26), 4456.
- [49] Spoltore, D.; Vangerven, T.; Verstappen, P.; Piersimoni, F.; Bertho, S.; Vandewal, K.; Van den Brande, N.; Defour, M.; Van Mele, B.; De Sio, A.; Parisi, J.; Lutsen, L.; Vanderzande, D.; Maes, W.; Manca, J. *Org. Electron.* **2015**, *21*, 160.
- [50] Vangerven, T.; Verstappen, P.; Drijkoningen, J.; Dierckx, W.; Himmelberger, S.; Salleo, A.; Vanderzande, D.; Maes, W.; Manca, J. *Chem. Mater.* **2015**, *27* (10), 3726.
- [51] Katsouras, A.; Gasparini, N.; Koulogiannis, C.; Spanos, M.; Ameri, T.; Brabec, C. J.; Chochos, C. L.; Avgeropoulos, A. *Macromol. Rapid Commun.* **2015**, *36* (20), 1778.

- [52] Hendriks, K. H.; Li, W.; Wienk, M. M.; Janssen, R. A. J. *J. Am. Chem. Soc.* **2014**, *136* (34), 12130.
- [53] Vangerven, T.; Verstappen, P.; Patil, N.; D'Haen, J.; Cardinaletti, I.; Benduhn, J.; Van den Brande, N.; Defour, M.; Lemaur, V.; Beljonne, D.; Lazzaroni, R.; Champagne, B.; Vandewal, K.; Andreasen, J. W.; Adriaensens, P.; Breiby, D. B.; Van Mele, B.; Vanderzande, D.; Maes, W.; Manca, J. *Chem. Mater.* **2016**, *28* (24), 9088.
- [54] Lu, L.; Zheng, T.; Xu, T.; Zhao, D.; Yu, L. *Chem. Mater.* **2015**, *27* (2), 537.
- [55] Brouwer, F.; Alma, J.; Valkenier, H.; Voortman, T. P.; Hillebrand, J.; Chiechi, R. C.; Hummelen, J. C. *J. Mater. Chem.* **2011**, *21*, 1582.
- [56] Ghoo, T.; Van den Brande, N.; Defour, M.; Brassinne, J.; Fustin, C.-A.; Gohy, J.-F.; Hoepfener, S.; Schubert, U. S.; Vanormelingen, W.; Lutsen, L.; Vanderzande, D. J.; Van Mele, B.; Maes, W. *Eur. Polym. J.* **2014**, *53*, 206.
- [57] Kesters, J.; Verstappen, P.; Raymakers, J.; Vanormelingen, W.; Drijkoningen, J.; D'Haen, J.; Manca, J.; Lutsen, L.; Vanderzande, D.; Maes, W. *Chem. Mater.* **2015**, *27* (4), 1332.
- [58] Cardinaletti, I.; Kesters, J.; Bertho, S.; Conings, B.; Piersimoni, F.; D'Haen, J.; Lutsen, L.; Nesladek, M.; Van Mele, B.; Van Assche, G.; Vandewal, K.; Salleo, A.; Vanderzande, D.; Maes, W.; Manca, J. V. *J. Photon. Energy* **2014**, *4*, 040997-1.
- [59] Vandenberg, J.; Conings, B.; Bertho, S.; Kesters, J.; Spoltore, D.; Esiner, S.; Zhao, J.; Van Assche, G.; Wienk, M. M.; Maes, W.; Lutsen, L.; Van Mele, B.; Janssen, R. A. J.; Manca, J.; Vanderzande, D. J. M. *Macromolecules* **2011**, *44* (21), 8470.
- [60] Drijkoningen, J.; Kesters, J.; Vangerven, T.; Lutsen, L.; Vanderzande, D.; Maes, W.; D'Haen, J.; Manca, J. *Org. Electron.* **2014**, *15* (6), 1282.
- [61] Vezie, M. S.; Few, S.; Meager, I.; Pieridou, G.; Dörfling, B.; Ashraf, R. S.; Goñi, A. R.; Bronstein, H.; McCulloch, I.; Hayes, S. C.; Campoy-Quiles, M.; Nelson, J. *Nat. Mater.* **2016**, *15* (7), 746.
- [62] Niklas, J.; Mardis, K. L.; Banks, B. P.; Grooms, G. M.; Sperlich, A.; Dyakonov, V.; Beaupré, S.; Leclerc, M.; Xu, T.; Yu, L.; Poluektov, O. G. *Phys. Chem. Chem. Phys.* **2013**, *15* (24), 9562.
- [63] Zhou, X.; Yang, D.; Ma, D. *Adv. Optical Mater.* **2015**, *3* (11), 1570.
- [64] Burke, D. J.; Lipomi, D. J. *Energy Environ. Sci.* **2013**, *6*, 2053.

## 5.5 Supporting information

### **Experimental section**

(3,3'-Dihexyl[2,2'-bithiophen]-5-yl)trimethylstannane was prepared according to a literature procedure.<sup>[1]</sup> All reagents and chemicals were obtained from commercial sources and used without further purification. Solvents were dried by a solvent purification system (MBraun, MB-SPS-800) equipped with alumina columns.

Preparative (recycling) size exclusion chromatography (prep-SEC) was performed on a JAI LC-9110 NEXT system equipped with JAIGEL 1H and 2H columns (eluent CHCl<sub>3</sub>, flow rate 3.5 mL min<sup>-1</sup>). NMR chemical shifts ( $\delta$ , in ppm) were determined relative to the residual CHCl<sub>3</sub> (7.26 ppm) or CDHCl<sub>2</sub> (5.32 ppm) absorption or the <sup>13</sup>C resonance shift of CDCl<sub>3</sub> (77.16 ppm) or CD<sub>2</sub>Cl<sub>2</sub> (54.00 ppm). High resolution ESI-MS was performed using a LTQ Orbitrap Velos Pro mass spectrometer equipped with an atmospheric pressure ionization source operating in the nebulizer assisted electrospray mode. The instrument was calibrated in the *m/z* range 220–2000 using a standard solution containing caffeine, MRFA and Ultramark 1621. MALDI-TOF mass spectra were recorded on a Bruker Daltonics Ultraflex II ToF/ToF. A total of 1  $\mu$ L of the matrix solution (4 mg mL<sup>-1</sup> DTCB (*trans*-2-[3-(4-*tert*-butylphenyl)-2-methyl-2-propenylidene]malononitrile) in CHCl<sub>3</sub>) was spotted onto an MTP Anchorchip 600/384 MALDI plate. The spot was allowed to dry and 1  $\mu$ L of the analyte solution (0.5 mg mL<sup>-1</sup> in chlorobenzene) was spotted on top of the matrix. UV-Vis-NIR absorption spectroscopy measurements were performed on a VARIAN Cary 5000 UV-Vis-NIR spectrophotometer at a scan rate of 600 nm min<sup>-1</sup>. The films for the UV-Vis-NIR absorption measurements were prepared by drop casting a solution of the respective polymer in chloroform or chlorobenzene on a quartz substrate. The solid-state UV-Vis-NIR absorption spectra were used to estimate the optical bandgaps (from the wavelength at the intersection of the tangent line drawn at the low energy side of the absorption spectrum with the baseline:  $E_g$  (eV) = 1240/(wavelength in nm)). Analysis of the molar masses and molar mass distributions of the polymers was performed by SEC using a Spectra Series P100 pump equipped with two mixed-B columns (10  $\mu$ m, 2 cm  $\times$  30 cm, Polymer Laboratories) and an Agilent 1100 diode array

detector with chlorobenzene as an eluent at 60 °C and a flow rate of 1.0 mL min<sup>-1</sup>. Electrochemical measurements (cyclic voltammetry) were performed with an Eco Chemie Autolab PGSTAT 30 potentiostat/galvanostat using a three-electrode microcell with a platinum working electrode, a platinum counter electrode and a Ag/AgNO<sub>3</sub> reference electrode (silver wire dipped in a solution of 0.01 M AgNO<sub>3</sub> and 0.1 M NBu<sub>4</sub>PF<sub>6</sub> in anhydrous acetonitrile). The reference electrode was calibrated against ferrocene/ferrocenium as an external standard. Samples were prepared by dip coating the platinum working electrode in the respective polymer solutions (also used for the solid-state UV-Vis measurements). The CV measurements were done on the resulting films with 0.1 M NBu<sub>4</sub>PF<sub>6</sub> in anhydrous acetonitrile as electrolyte solution. To prevent air from entering the system, the experiments were carried out under a curtain of argon. Cyclic voltammograms were recorded at a scan rate of 100 mV s<sup>-1</sup>. For the conversion of V to eV, the onset potentials of the first oxidation/reduction peaks were used and referenced to ferrocene/ferrocenium, which has an ionization potential of -4.98 eV vs. vacuum. This correction factor is based on a value of 0.31 eV for Fc/Fc<sup>+</sup> vs. SCE<sup>[2]</sup> and a value of 4.68 eV for SCE vs. vacuum<sup>[3]</sup>:  $E_{\text{HOMO/LUMO}} (\text{eV}) = -4.98 - E_{\text{onset}}^{\text{ox/red, Ag/AgNO}_3} (\text{V}) + E_{\text{onset}}^{\text{Fc/Fc}^+, \text{Ag/AgNO}_3} (\text{V})$ . The accuracy of measuring redox potentials by CV is about 0.01–0.02 V. Reproducibility can be less because the potentials do depend on concentration and temperature. Rapid heat-cool calorimetry (RHC) experiments were performed on a prototype RHC of TA Instruments, equipped with liquid nitrogen cooling and specifically designed for operation at high scanning rates. RHC measurements were performed at 500 K min<sup>-1</sup> (after cooling at 20 K min<sup>-1</sup>) using aluminum crucibles filled with samples of 200–250 µg, using helium (10 mL min<sup>-1</sup>) as a purge gas. TGA experiments were performed at 20 K min<sup>-1</sup> in platinum crucibles on a TA Instruments Q5000 TGA using nitrogen (50 mL min<sup>-1</sup>) as a purge gas. The samples for EPR were prepared from drop-cast films of a 1:4 **P2**:<sup>[70]</sup>PCBM solution in chlorobenzene (10 mg mL<sup>-1</sup> total weight of polymer and <sup>[70]</sup>PCBM). For the X-band measurements, a drop-cast film on a transparent flexible substrate was mounted in a quartz sample tube (I.D. 3 mm, O.D. 4 mm). W-band samples were prepared by scratching off a drop-cast film dried on a glass substrate and transferring the collected material into a quartz sample tube of appropriate size (I.D. 0.6 mm, O.D. 0.84 mm). To minimize photo-oxidation of the samples, the drop-cast films were dried in the dark under

N<sub>2</sub> atmosphere. The X-band continuous-wave (CW) EPR spectra were recorded at 50 K on a Bruker ESP300E spectrometer (microwave frequency: 9.44 GHz, microwave power: 0.5 mW, modulation amplitude: 1G) equipped with a liquid helium cryostat (Oxford Inc.). Photo-excitation of the sample was achieved by means of illumination with a CW 532 nm frequency-doubled Nd:YAG laser through an optical window in the microwave resonator (20 mW incident laser power). The W-band electron spin echo (ESE) detected EPR experiments were performed on a Bruker Elexsys E680 spectrometer (microwave frequency: 94 GHz) equipped with a continuous flow cryostat and a superconducting magnet from Oxford Inc. The W-band EPR spectra were recorded at 20 K in pulse mode to avoid distortions due to fast passage effects at low temperatures. For the ESE detection, the pulse sequence  $\pi/2$ - $\tau$ - $\pi$ - $\tau$ -echo was used, with  $t_{\pi/2} = 108$  ns,  $t_{\pi} = 216$  ns and interpulse distance  $\tau = 300$  ns. To remove unwanted echoes, a two-step phase cycle was applied. The shot repetition rate was taken to be 55.6 Hz. The sample was illuminated with the CW 532 nm Nd:YAG laser inside the cavity via an optical fiber (20 mW laser power at the end of the fiber). The simulations of the EPR spectra were performed with the Easyspin software package (version 5.1.3).<sup>[4]</sup> Spin-unrestricted DFT calculations were performed with the ORCA package.<sup>[5-7]</sup> The structure geometry was first optimized using the BP86 functional<sup>[8]</sup> and the SVP basis set<sup>[9]</sup> for all atoms. For polymer **P2**, the calculation was limited to a single monomer unit. Single-point computations of the principal g-values of the positive and negative radicals were performed using the B3LYP functional<sup>[8,10]</sup> combined with the EPR-II basis set<sup>[11]</sup> for H, C, N, O and the TZV\_PP basis set for S. Since no information on the dielectric constant of the polymer is available, computations were performed assuming a vacuum.

**2-(3,3'-Dihexyl[2,2'-bithiophen]-5-yl)-4,4,5,5-tetramethyl-1,3,2-dioxaborolane.** 3,3'-Dihexyl-2,2'-bithiophene (3.00 g, 8.97 mmol) was dissolved in dry THF (50 mL) and *n*-BuLi (3.9 mL, 9.86 mmol) was added drop wise to the solution at -78 °C. The reaction mixture was stirred at -78 °C for 30 min before 2-isopropoxy-4,4,5,5-tetramethyl-1,3,2-dioxaborolane (2.50 g, 13.4 mmol) was added. After stirring the reaction mixture at room temperature for 1.5 h, diethyl ether was added and the organic phase was washed with water (2×), 1 N HCL (1×) and a saturated NaCl solution (1×). The organic phase was subsequently dried over anhydrous MgSO<sub>4</sub> and filtered. The solvent was removed under reduced

pressure and the crude product was purified by column chromatography (silica, eluent petroleum ether:EtOAc, 90:10) to obtain the final product (3.47 g, 84 %).  $^1\text{H}$  NMR (400 MHz,  $\text{CDCl}_3$ ),  $\delta$  (ppm): 7.51 (s, 1H), 7.29 (d,  $J = 5.2$  Hz, 1H), 6.96 (d,  $J = 5.2$  Hz, 1H), 2.53–2.46 (m, 4H), 1.59–1.48 (m, 4H), 1.35 (s, 12H), 1.31–1.18 (m, 12H), 0.84 (t,  $J = 6.8$  Hz, 6H).

**7,14-Di(thiophen-2-yl)diindolo[3,2,1-de:3',2',1'-ij][1,5]naphthyridine-6,13-dione (1).** Prepared according to a modified literature procedure:<sup>[12]</sup> A solution of thiophene-2-acetyl chloride (5.24 g, 32.6 mmol) in anhydrous toluene (15 mL) was added dropwise over 30 min to a refluxing suspension of indigo (2.14 g, 8.15 mmol) in anhydrous toluene (150 mL). The reaction was monitored by thin layer chromatography (TLC). The half and doubly annulated indigo derivatives were observed as purple and red spots, respectively. After 72 h, complete conversion was observed and the mixture was cooled down to room temperature. The precipitate was recovered by filtration and further purification was done via Soxhlet extractions with acetone and chloroform (solubilizing the product). The solvent of the chloroform fraction was evaporated under reduced pressure. To further increase the purity of the product, recrystallization from methanol/chloroform (25:75) was performed, finally affording a red solid (1.04 g, 27%).  $^1\text{H}$  NMR (400 MHz,  $\text{CDCl}_3$ ),  $\delta$  (ppm): 8.60 (d,  $J = 8.2$  Hz, 2H), 8.18 (d,  $J = 7.8$  Hz, 2H), 7.73 (ddd,  $J = 6.3, 4.4, 1.1$  Hz, 4H), 7.61 (t,  $J = 7.2$  Hz, 2H), 7.35–7.30 (m, 2H), 7.29 (dd,  $J = 5.1, 3.6$  Hz, 2H).

**7,14-Bis(5-bromothiophen-2-yl)diindolo[3,2,1-de:3',2',1'-ij][1,5]naphthyridine-6,13-dione (2).** Prepared according to a literature procedure.<sup>[12]</sup> A purple product was obtained (1.16 g, 84%).  $^1\text{H}$  NMR (400 MHz,  $\text{CDCl}_3$ ),  $\delta$  (ppm): 8.59 (d,  $J = 8.3$  Hz, 2H), 8.24 (d,  $J = 7.8$  Hz, 2H), 8.02 (s, 2H), 7.64 (t,  $J = 7.1$  Hz, 2H), 7.57 (d,  $J = 3.9$  Hz, 2H), 7.36 (t,  $J = 7.2$  Hz, 2H).

**7,14-Bis(3'',4'-dihexyl[2,2':5',2''-terthiophen]-5-yl)diindolo[3,2,1-de:3',2',1'-ij][1,5]naphthyridine-6,13-dione (3).** A mixture of [3,3'-dihexyl(2,2'-bithiophen)-5-yl]trimethylstannane (0.960 g, 1.93 mmol) and 7,14-bis(5-bromothiophen-2-yl)diindolo[3,2,1-de:3',2',1'-ij][1,5]naphthyridine-6,13-dione (0.532 g, 0.84 mmol) was dissolved in toluene (3 mL) and DMF (0.6 mL) and purged with  $\text{N}_2$  for 20 min.  $\text{Pd}(\text{PPh}_3)_4$  (4.8 mg, 0.04 mmol) was added to the mixture, which was subsequently heated to reflux temperature. After 16 h,  $\text{CHCl}_3$

was added and the organic phase was washed with water (2×), dried over anhydrous MgSO<sub>4</sub> and filtered. The solvent was removed under reduced pressure and the crude product was purified by column chromatography (silica, eluent CHCl<sub>3</sub>:petroleum ether, 70:30) and recrystallized from toluene:petroleum ether (4:1). The pure product was obtained as a blue solid (0.521 g, 55%). <sup>1</sup>H NMR (300 MHz, CD<sub>2</sub>Cl<sub>2</sub>), δ (ppm): 7.93 (d, *J* = 7.9 Hz, 2H), 7.77 (d, *J* = 7.9 Hz, 2H), 7.35 (d, *J* = 5.3 Hz, 2H), 7.25 (d, *J* = 3.7 Hz, 2H), 7.16 (t, *J* = 7.7 Hz, 2H), 7.08 (s, 2H), 7.03 (d, *J* = 5.3 Hz, 2H), 6.99–6.91 (m, 4H), 2.60 (t, *J* = 7.5 Hz, 4H), 2.50 (t, *J* = 7.5 Hz, 4H), 1.76–1.49 (m, 8H), 1.45–1.19 (m, 24H), 1.00–0.78 (m, 12H); <sup>13</sup>C NMR (75 MHz, CD<sub>2</sub>Cl<sub>2</sub>), δ (ppm): 157.7, 144.1, 143.2, 142.8, 137.1, 134.3, 131.6, 131.4, 129.3, 128.8, 127.4, 126.4, 126.2, 126.1, 125.6, 124.8, 123.8, 122.8, 121.3, 117.6, 32.3, 32.2, 31.3, 31.2, 29.7, 29.5, 23.2, 14.5. HRMS (ESI): calcd. for C<sub>68</sub>H<sub>70</sub>N<sub>2</sub>O<sub>2</sub>S<sub>6</sub> [M]<sup>+</sup>: 1138.3762, measured: 1138.3765. UV-Vis: λ<sub>max</sub> (log ε) = 666 nm (4.60).

**7,14-Bis(5''-bromo-3'',4'-dihexyl[2,2':5',2''-terthiophen]-5-yl)diindolo[3,2,1-de:3',2',1'-ij][1,5]naphthyridine-6,13-dione (4).** 7,14-Bis(3'',4'-dihexyl[2,2':5',2''-terthiophen]-5-yl)diindolo[3,2,1-de:3',2',1'-ij][1,5]naphthyridine-6,13-dione (156 mg, 0.14 mmol) was dissolved in CHCl<sub>3</sub> (20 mL) and NBS (50 mg, 0.28 mmol) was added at 0 °C. After stirring at RT for 16 h, water and CHCl<sub>3</sub> were added, the two phases were separated and the organic phase was washed with water (2×), dried over anhydrous MgSO<sub>4</sub> and filtered. The solvent was removed under reduced pressure and the crude product was purified by column chromatography (silica, CHCl<sub>3</sub>:petroleum ether 50:50) and recycling prep-SEC (CHCl<sub>3</sub>) to yield a blue solid (138 mg, 76%). <sup>1</sup>H NMR (400 MHz, CDCl<sub>3</sub>), δ (ppm): 8.57 (d, *J* = 8.1 Hz, 2H), 8.29 (d, *J* = 8.0 Hz, 2H), 7.72 (d, *J* = 3.9 Hz, 2H), 7.58 (t, *J* = 7.8 Hz, 2H), 7.33 (t, *J* = 7.7 Hz, 2H), 7.30 (d, *J* = 3.9 Hz, 2H), 7.23 (s, 2H), 6.96 (s, 2H), 2.55–2.48 (m, 8H), 1.65–1.49 (m, 8H), 1.35–1.20 (m, 24H), 0.92–0.82 (m, 12H); <sup>13</sup>C NMR (75 MHz, CDCl<sub>3</sub>), δ (ppm): 158.5, 144.1, 143.6, 143.5, 142.4, 137.0, 133.9, 132.0, 131.5, 131.1, 129.6, 128.8, 127.5, 126.3, 126.0, 125.8, 124.8, 124.2, 122.9, 121.8, 117.8, 112.1, 31.6, 30.5, 29.0, 28.9, 22.6, 14.1. HRMS (ESI): calcd. for C<sub>68</sub>H<sub>68</sub>Br<sub>2</sub>N<sub>2</sub>O<sub>2</sub>S<sub>6</sub> [M]<sup>+</sup>: 1296.1951, measured: 1296.1955.

**4-(2-Octyldodecyl)-2,6-bis(trimethylstannyl)-4H-dithieno[3,2-*b*:2',3'-*d*]pyrrole (6a).** Prepared according to a literature procedure.<sup>[13]</sup> <sup>1</sup>H NMR (300 MHz, CDCl<sub>3</sub>),  $\delta$  (ppm): 6.93 (s, 2H), 4.03 (d, *J* = 7.2 Hz, 2H), 1.99 (s, 1H), 1.33-1.15 (m, 32H), 0.90-0.82 (m, 6H), 0.48-0.27 (m, 18H).

**1-[2,6-Bis(trimethylstannyl)-4H-dithieno[3,2-*b*:2',3'-*d*]pyrrol-4-yl]-2-hexyldecan-1-one (9b).**

Prepared according to a literature procedure.<sup>[14]</sup> <sup>1</sup>H NMR (300 MHz, CDCl<sub>3</sub>),  $\delta$  (ppm): 7.85 (s, 1H), 7.19 (s, 1H), 3.38-3.30 (m, 1H), 1.93-1.80 (m, 2H), 1.71-1.57 (m, 2H), 1.42-1.18 (m, 20H), 0.87-0.79 (m, 6H), 0.52-0.28 (m, 18H).

**1-[2,6-bis(trimethylstannyl)-4H-dithieno[3,2-*b*:2',3'-*d*]pyrrol-4-yl]-2-butyloctan-1-one (9c).** Prepared according to a literature procedure.<sup>[15]</sup>

**P1. General polymerization method:** A mixture of 7,14-bis(5''-bromo-3'',4''-dihexyl[2,2':5',2''-terthiophen]-5-yl)diindolo[3,2,1-*de*:3',2',1'-*ij*][1,5]naphthyridine-6,13-dione (**4**) (119 mg, 0.0916 mmol) and 4-(2-octyldodecyl)-2,6-bis(trimethylstannyl)-4H-dithieno[3,2-*b*:2',3'-*d*]pyrrole (**6a**) (72 mg, 0.0916 mmol) was dissolved in dry toluene (2.5 mL) and dry DMF (0.5 mL) and the solution was degassed for 20 min. Subsequently, Pd<sub>2</sub>(dba)<sub>3</sub> (1.65 mg, 1.83  $\mu$ mol) and P(*o*-tol)<sub>3</sub> (2.23 mg, 7.33  $\mu$ mol) were added and the mixture was stirred overnight at reflux temperature. The resulting crude polymer material was precipitated in methanol and purified by repetitive Soxhlet extractions with acetone, *n*-hexane and chloroform. The chloroform fraction was again precipitated in methanol and filtered, yielding a green solid (63 mg, 43%). SEC (CB, 60 °C, PS standards):  $M_n$  = 29 kg/mol,  $D$  = 4.4;  $\lambda_{max}$  = 715 nm.

**P2. Synthesis according to the general polymerization procedure with a minor adaptation:** **4** (52.9 mg, 0.0408 mmol), 1-[2,6-bis(trimethylstannyl)-4H-dithieno[3,2-*b*:2',3'-*d*]pyrrol-4-yl]-2-hexyldecan-1-one (**9b**) (30.4 mg, 0.0408 mmol), dry toluene (1.0 mL), dry DMF (0.2 mL). Soxhlet extraction with 1,1,2,2-tetrachloroethane was needed to extract the high molecular weight fraction. The 1,1,2,2-tetrachloroethane fraction was again precipitated in methanol and filtered, yielding a green solid (25.5 mg, 40%). SEC (CB, 60 °C, PS standards):  $M_n$  = 55 kg/mol,  $D$  = 3.3;  $\lambda_{max}$  = 680 nm.

**P3.** Synthesis according to the general polymerization procedure, with the same adaptation as for **P2**: **4** (86.3 mg, 0.0665 mmol), 1-[2,6-bis(trimethylstannyl)-4*H*-dithieno[3,2-*b*:2',3'-*d*]pyrrol-4-yl]-2-butyloctan-1-one (**9c**) (45.7 mg, 0.0665 mmol), dry toluene (2.0 mL), dry DMF (0.4 mL). The polymer was obtained as a green solid (51.4 mg, 52%). SEC (CB, 60 °C, PS standards):  $M_n = 20$  kg/mol,  $D = 1.7$ ;  $\lambda_{max} = 677$  nm.

### **Solar cell and OFET fabrication and characterization**

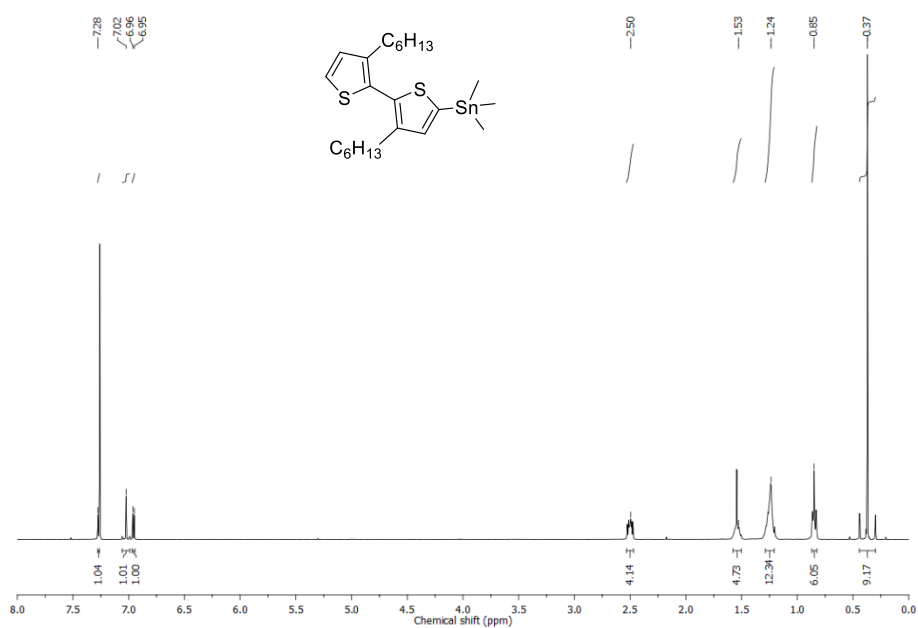
Before device processing, the indium tin oxide (ITO, Kintec, 100 nm, 20 Ohm sq<sup>-1</sup>) containing substrates were thoroughly cleaned through sonication using soap, demineralized water, acetone, isopropyl alcohol and a UV/O<sub>3</sub> treatment. Subsequently, a layer of PEDOT-PSS (Heraeus Clevis AI 4083) was spin-coated on top of the pre-patterned ITO substrates. Further processing was performed under N<sub>2</sub> atmosphere in a glove box, starting with an annealing step at 130 °C for 15 min to remove any residual water. The polymer:[70]PCBM (Solenne) active layers were spin-coated targeting thicknesses of ~80 nm, as confirmed by profilometry (DEKTA). The blend solutions providing highest efficiencies contained a 1:4 (polymer:[70]PCBM) ratio, with polymer concentrations of 5 mg mL<sup>-1</sup>, using chlorobenzene or *o*-xylene as the processing solvent (see Table 2). On top of the active layer, Ca was evaporated *in vacuo* with a thickness of 30 nm, and the devices were finished off with Al as the top electrode, with a thickness of 80 nm. The active area (3.08 mm<sup>2</sup>) was defined using a mask. The output parameters of the bulk heterojunction polymer solar cells were measured using a Newport class A solar simulator (model 91195A), calibrated with a silicon solar cell to give a 1 sun AM 1.5G spectrum. EQE measurements were performed with a Newport Apex illuminator (100 W xenon lamp, 6257) as light source, a Newport Cornerstone 130 monochromator and a Stanford SR830 lock-in amplifier for the current measurements. Calibration was done with a certificated Si FDS-100 photodiode. For AFM imaging, a Bruker Multimode 8 AFM was used in PeakForce tapping mode, employing ScanAsyst. The images were produced with a silicon tip on a nitride lever with a spring constant of 4 N m<sup>-1</sup>.

Field-effect transistors were prepared by spin-coating **P1** in chloroform with a concentration of 5 mg mL<sup>-1</sup> or **P2** in chlorobenzene with a concentration of 8 mg mL<sup>-1</sup> on 200 nm of thermally grown SiO<sub>2</sub>. The gate contact consisted of highly n-

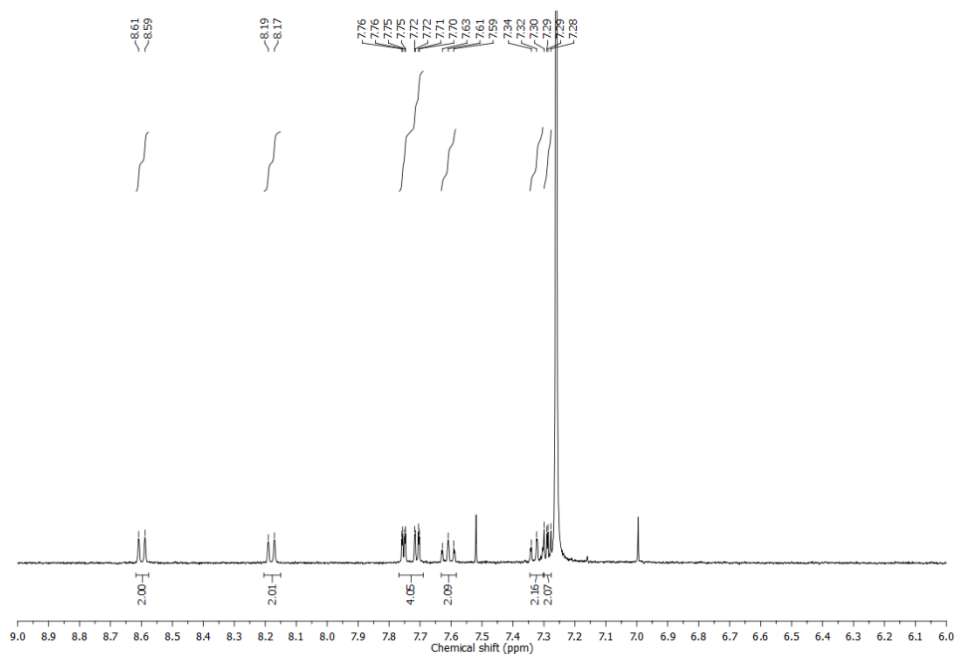
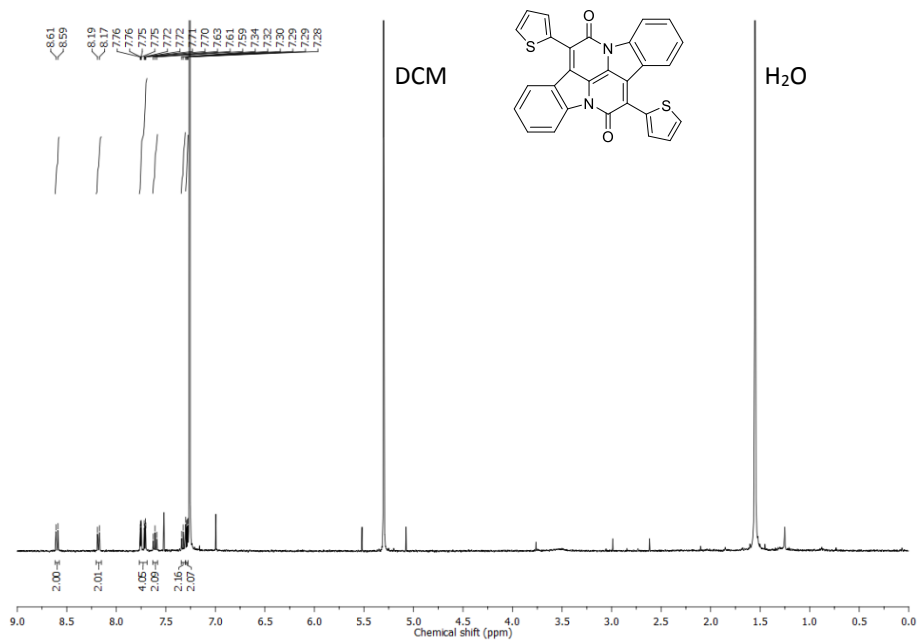
doped Si. Interdigitated source and drain electrodes were pre-patterned, comprising of a stack of Ti/Au (10/100 nm). FET substrates were acquired from Philips. The channel length was 10  $\mu\text{m}$ . Two Keithley 2400 source meters were used to measure the  $I_{DS}$  and correct it for leakage through the gate electrode. All FET preparations and characterizations were carried out in a  $\text{N}_2$  filled glovebox.

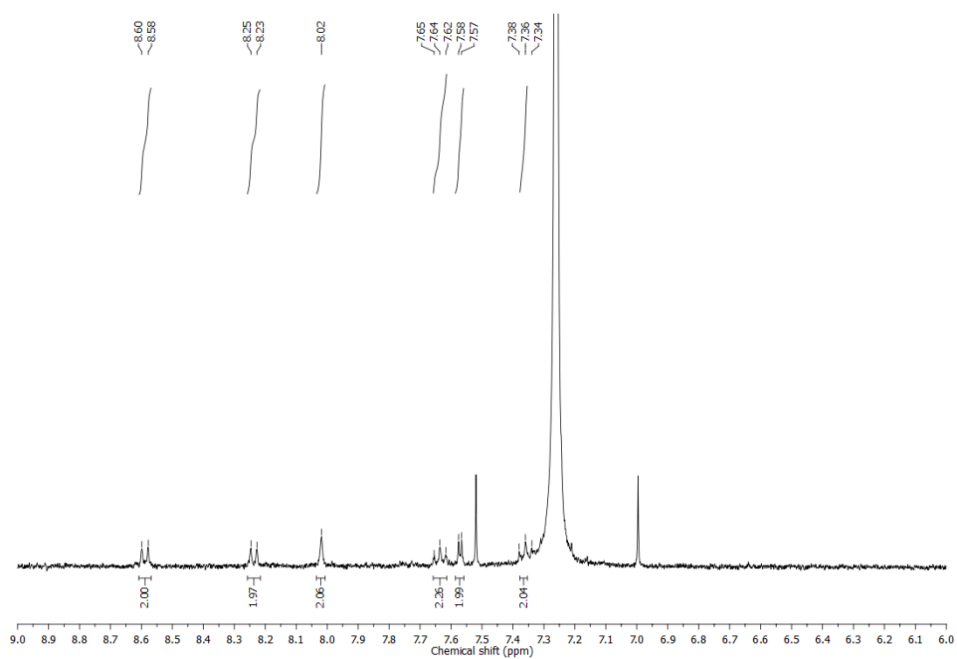
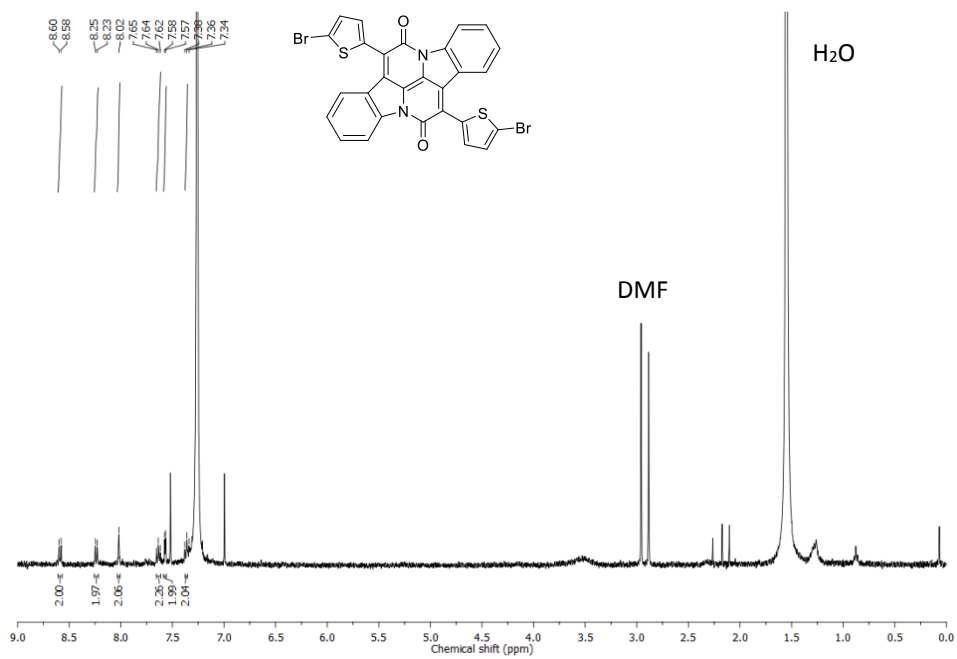
### **$^1\text{H}$ and $^{13}\text{C}$ NMR spectra**

#### **(3,3'-dihexyl-[2,2'-bithiophen]-5-yl)trimethylstannane**

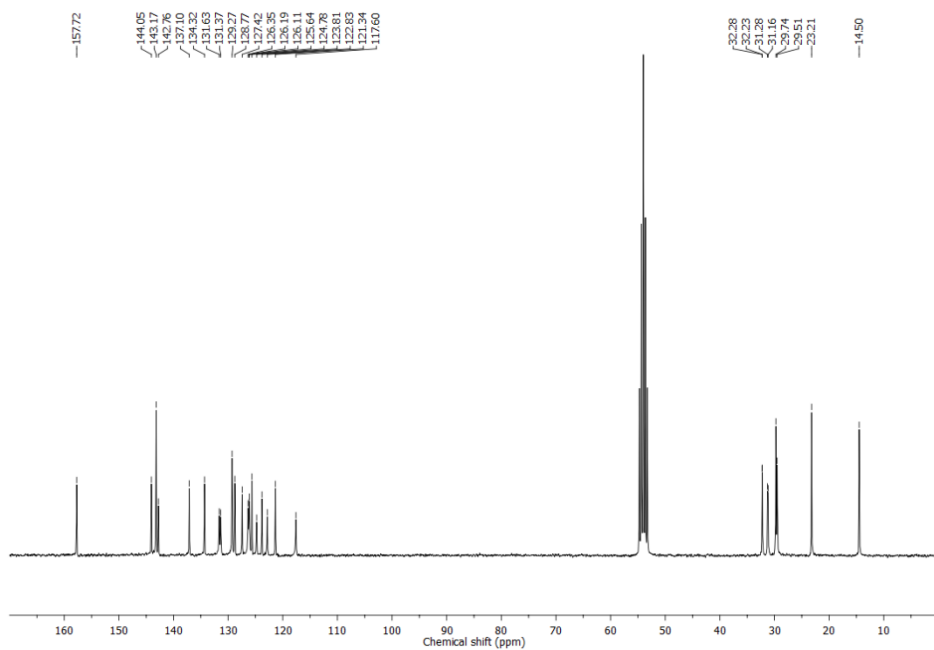
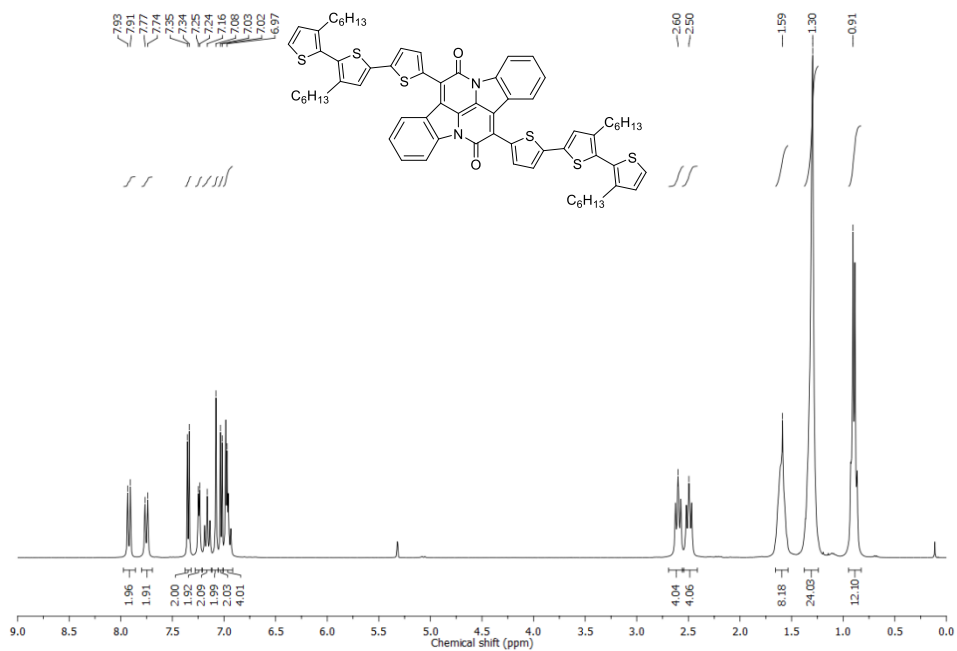


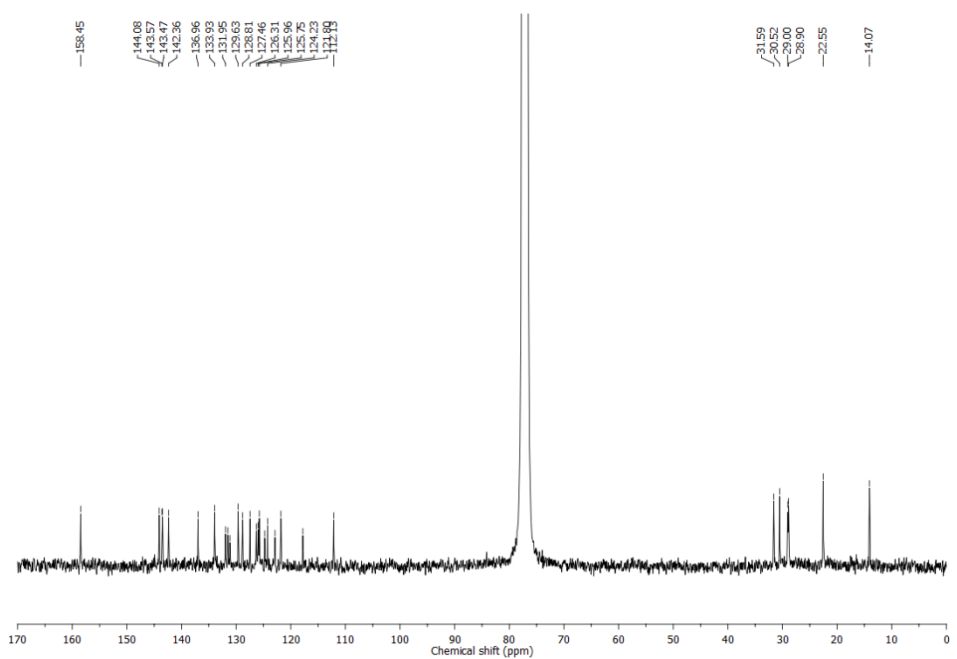
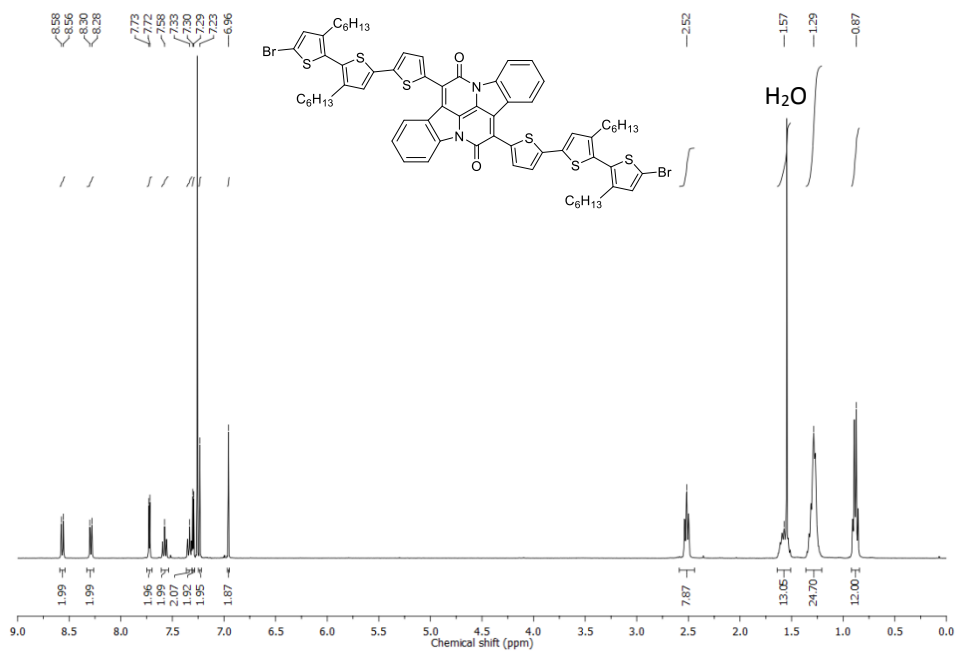
**7,14-di(thiophen-2-yl)diindolo[3,2,1-*de*:3',2',1'-*ij*][1,5]naphthyridine-6,13-dione (1)**



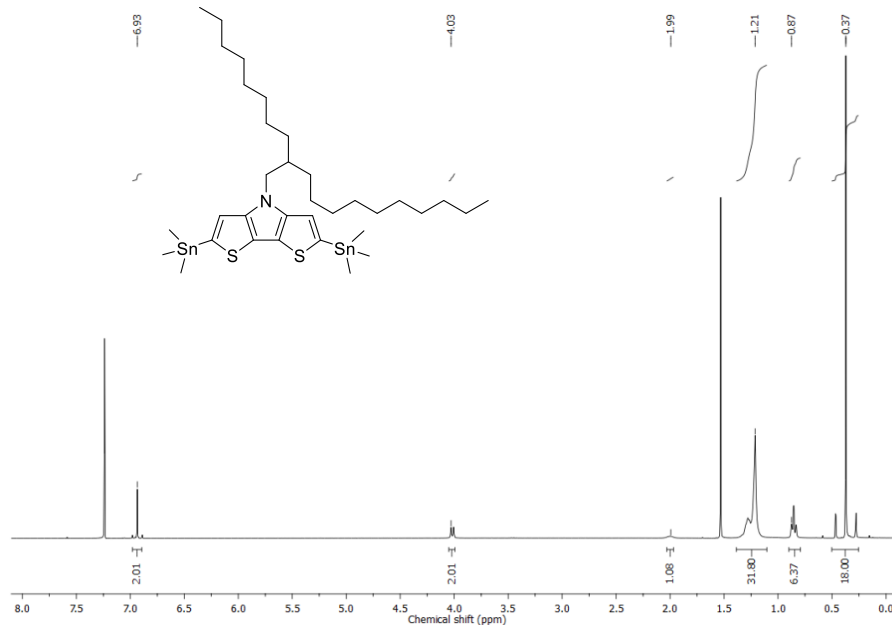
**7,14-bis(5-bromothiophen-2-yl)diindolo[3,2,1-de:3',2',1'-ij][1,5]naphthyridine-6,13-dione (2)**

**7,14-bis(3'',4'-dihexyl[2,2':5',2''-terthiophen]-5-yl)diindolo[3,2,1-de:3',2',1'-ij][1,5]naphthyridine-6,13-dione (3)**

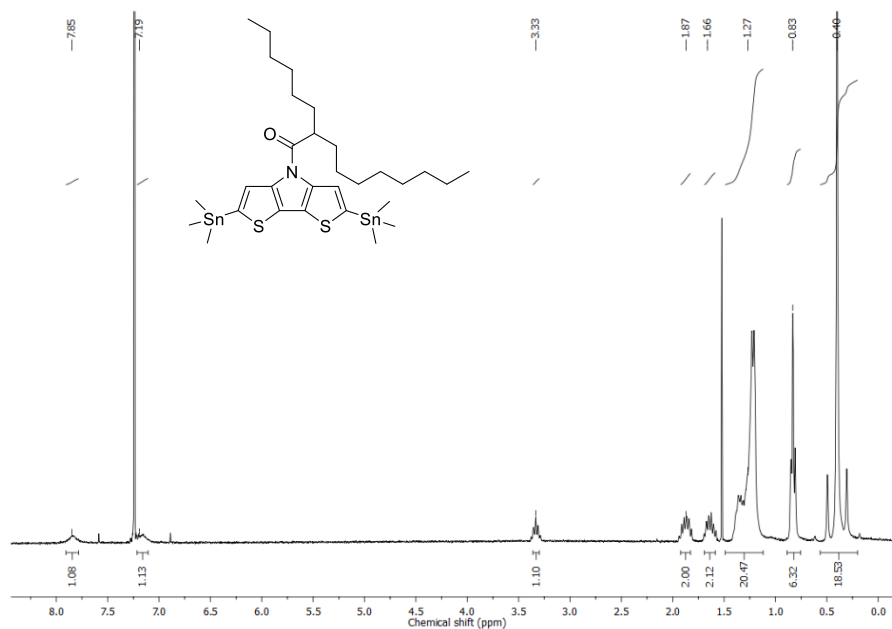


**7,14-bis(5''-bromo-3'',4''-dihexyl[2,2':5',2''-terthiophen]-5-yl)diindolo[3,2,1-de:3',2',1'-ij][1,5]naphthyridine-6,13-dione (4)**

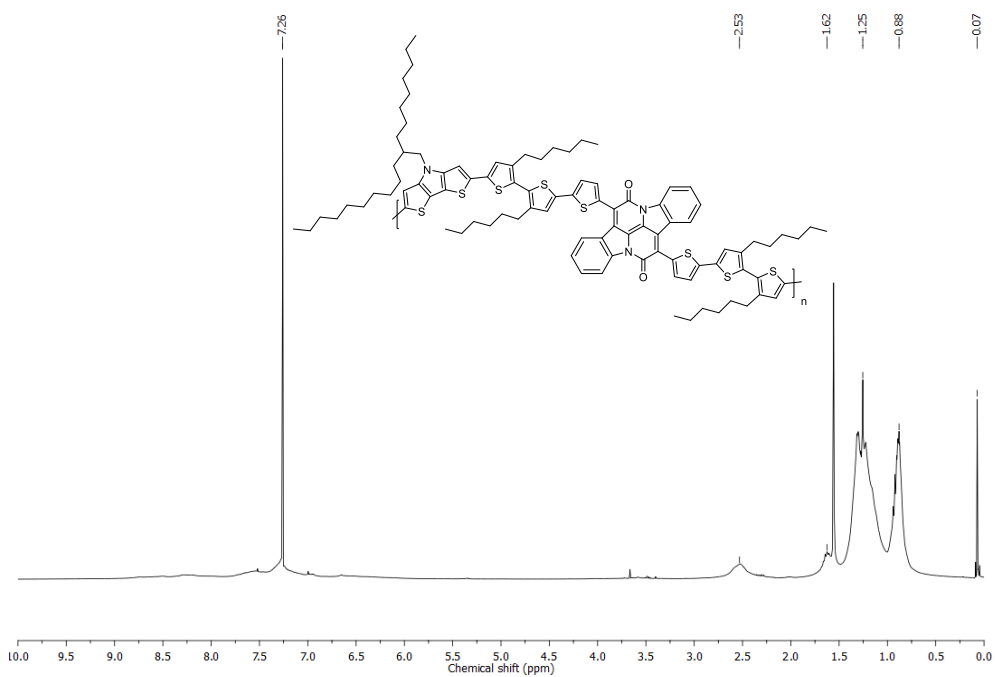
**4-(2-Octyldodecyl)-2,6-bis(trimethylstannyl)-4H-dithieno[3,2-b:2',3'-d]pyrrole (6a)**



**1-[2,6-Bis(trimethylstannyl)-4H-dithieno[3,2-b:2',3'-d]pyrrol-4-yl]-2-hexyldecan-1-one (9b)**

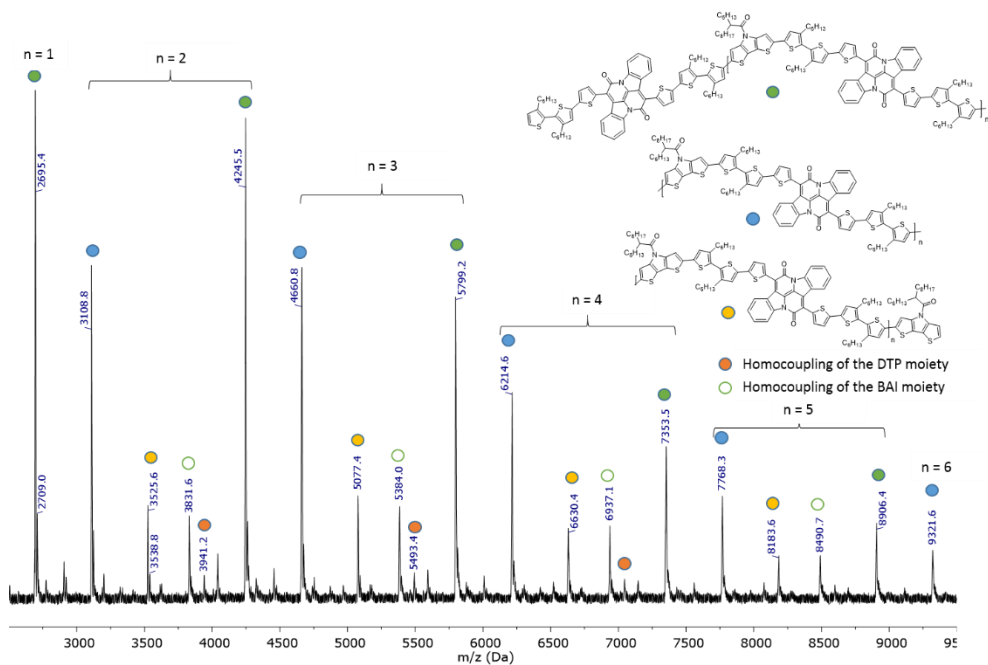


**P1 – PDTPalkTTTBAI**

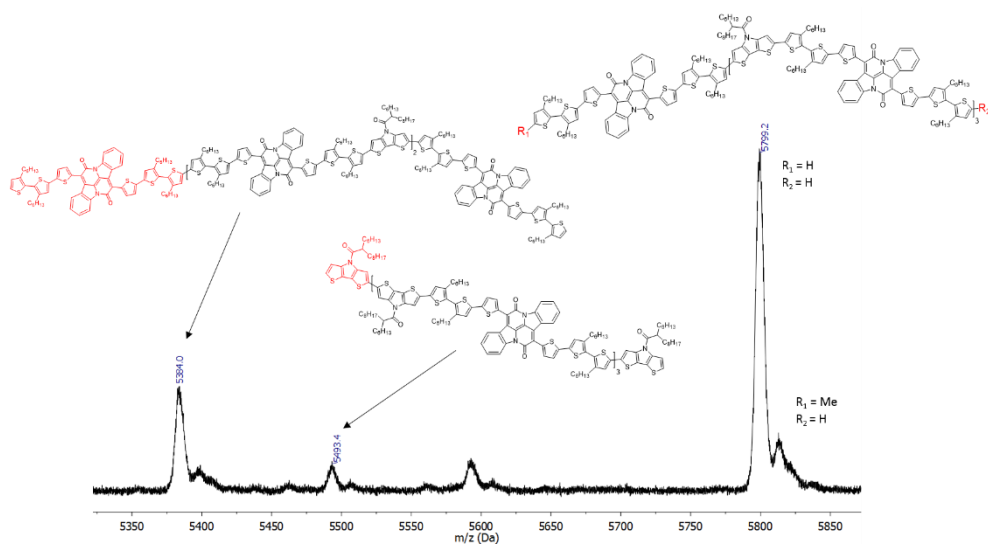


As <sup>1</sup>H NMR analysis of the most soluble polymer **P1** already showed very broad signals, not allowing to properly characterize the material by NMR, no efforts in this direction were undertaken for the less soluble polymers **P2** and **P3**.

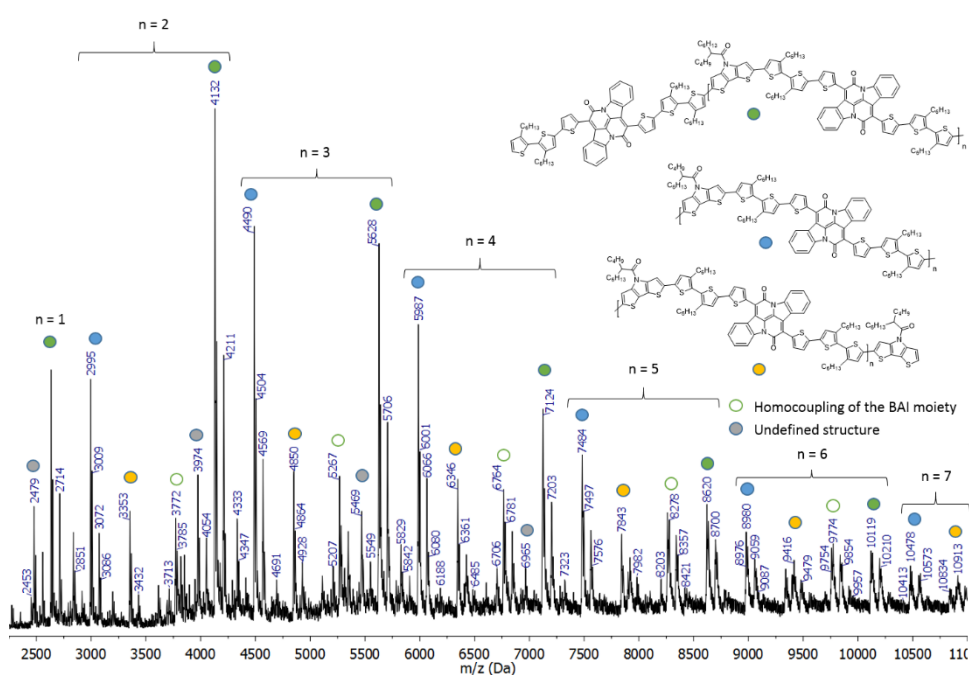
**MALDI-TOF**



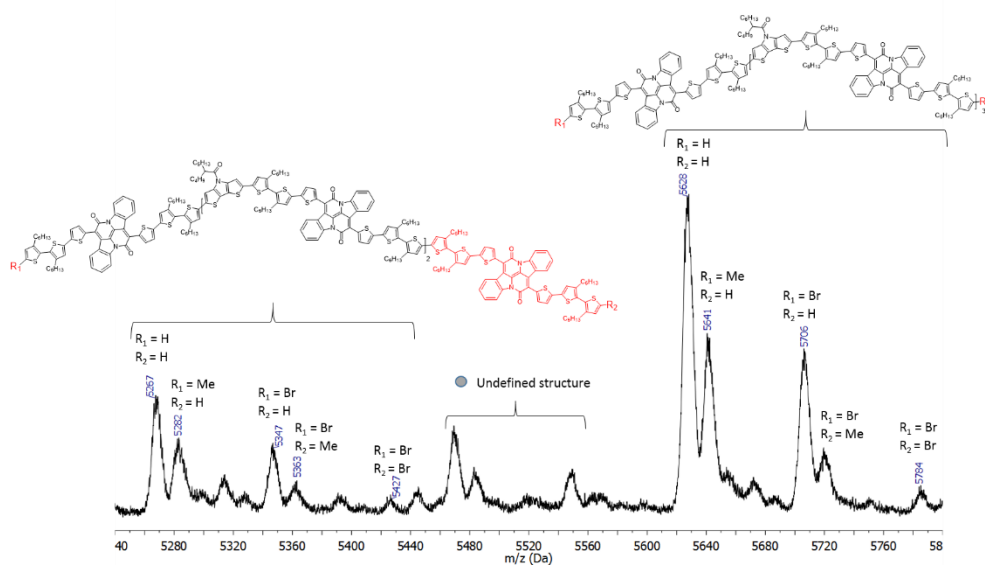
**Figure S1.** MALDI-TOF mass spectrum of **P2**.



**Figure S2.** MALDI-TOF mass spectrum of **P2** (zoom from  $m/z$  5300 to 5900  $\text{g mol}^{-1}$ ), with the assignment of homocoupling and end group identification.

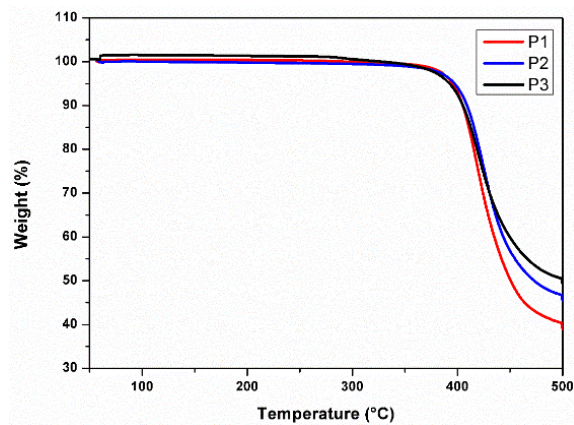


**Figure S3.** MALDI-TOF mass spectrum of **P3**.

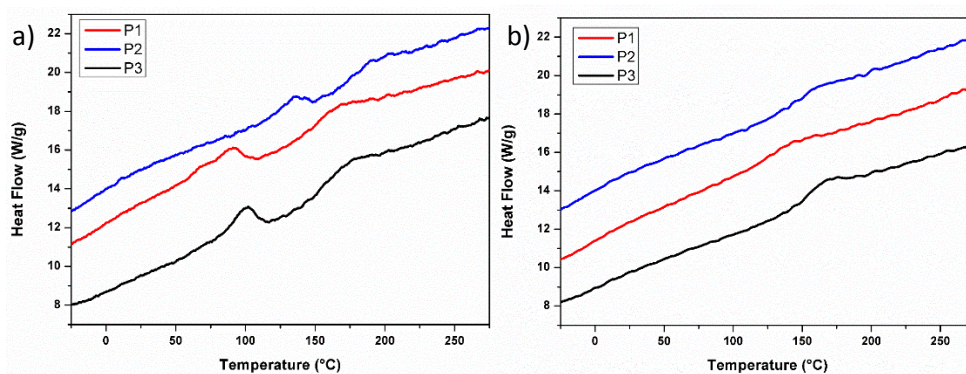


**Figure S4.** MALDI-TOF mass spectrum of **P3** (zoom from  $m/z$  5140 to 5800  $\text{g mol}^{-1}$ ), with the assignment of homocoupling and end group identification.

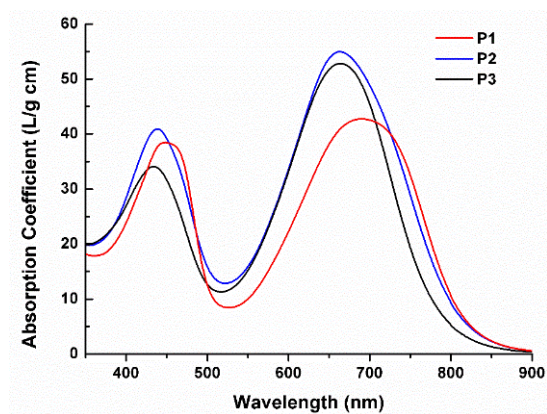
**Thermal analysis**



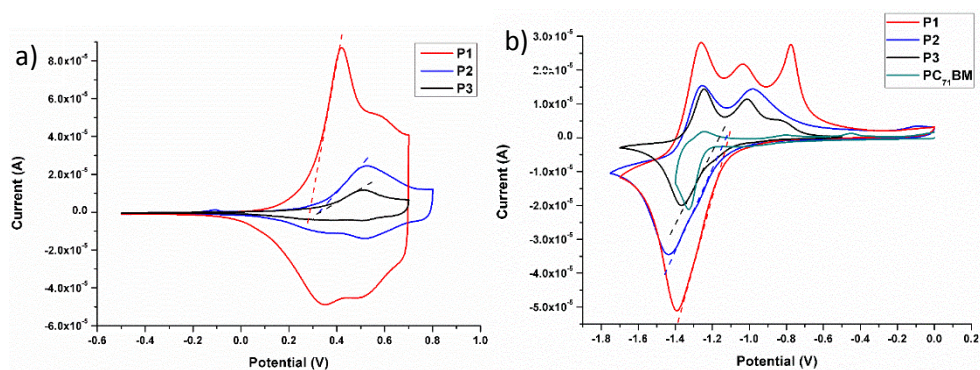
**Figure S5.** TGA analysis of polymers **P1–P3**.



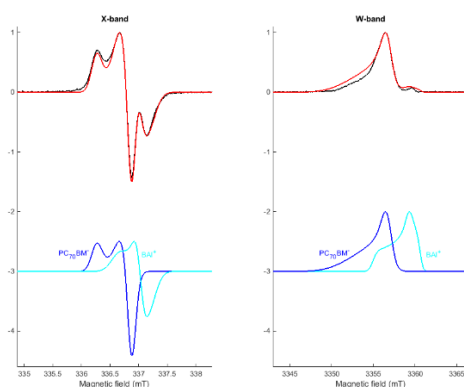
**Figure S6.** a) RHC first heating profiles for polymers **P1–P3** (heating at 500 K min<sup>-1</sup>) and b) RHC second heating profiles for polymers **P1–P3** (heating at 500 K min<sup>-1</sup> after cooling at 20 K min<sup>-1</sup>; curves shifted vertically for clarity).

**Absorption coefficients**

**Figure S7.** Absorption coefficients of the neat polymers in chlorobenzene solution.

**Cyclic voltammetry**

**Figure S8.** Overlay of a) the oxidation curves and b) the reduction curves (cyclic voltammetry) for polymers **P1–P3**.

**EPR**

**Figure S9.** Light-induced EPR spectra of **P2**:**[70]PCBM** (1:4) blend films. Left: CW X-band spectra yielding first derivative line shape. Right: W-band ESE-detected EPR spectra resulting in absorption line shape. Black: Experimental spectrum. Blue: Simulation of the **[70]PCBM** anion. Cyan: Simulation of the positive radical on the polymer **P2** based on DFT calculations. Red: Weighed sum of the two simulations.

**Table S1.** Comparison of the principal  $g$ -values from the simulations of the EPR spectra (Exp) and the  $g$ -values obtained from DFT calculations for positive and negative radical centers on a monomeric unit of polymer **P2** and on **[70]PCBM**. The error on the experimentally determined  $g$ -values is estimated to be 0.0001.

<b>P2</b>	$g_x$	$g_y$	$g_z$
<b>Exp</b>	2.0004	2.0015	2.0038
<b>DFT P2<sup>+</sup></b>	2.0009	2.0022	2.0037
<b>DFT P2<sup>-</sup></b>	2.0023	2.0035	2.0049
<b>[70]PCBM</b>	$g_x$	$g_y$	$g_z$
<b>Exp</b>	2.0025	2.0032	2.0061
<b>DFT [70]PCBM<sup>+</sup></b>	2.0012	2.0018	2.0021
<b>DFT [70]PCBM<sup>-</sup></b>	2.0022	2.0030	2.0054
<b>Ref<sup>[16]</sup></b>	2.0021	2.0028	2.0060

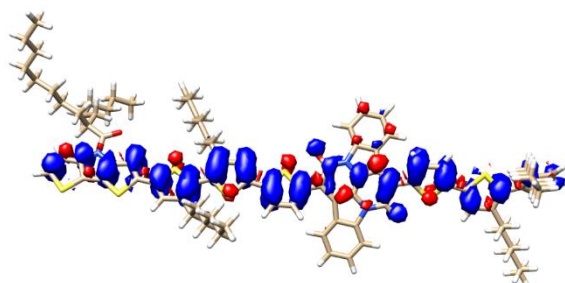


**Figure S10.** Spin density distribution of the positive radical on a monomeric unit of the polymer **P2** based on DFT calculations. Red: Negative spin density. Blue: Positive spin density. Contour levels were fixed at  $-0.0005$  and  $0.0005$ , respectively.

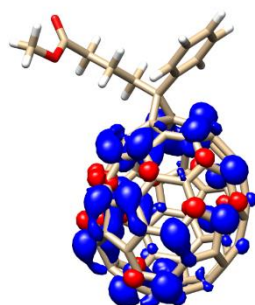


**Figure S11.** Spin density distribution of the [70]PCBM anion based on DFT calculations. Red: Negative spin density. Blue: Positive spin density. Contour levels were fixed at  $-0.001$  and  $0.001$ , respectively.

**Solar cell optimization data****Table S2.** Optimization of the solar cell devices based on **P1**, **P2** and **P3** in combination with [70]PCBM.

<b>Polymer</b>	<b>Solvent</b>	<b>Ratio<sup>a</sup></b>	<b>Additive</b>	<b>V<sub>oc</sub> / V</b>	<b>J<sub>sc</sub> / mA cm<sup>-2</sup></b>	<b>FF</b>	<b>Best PCE / %<sup>b</sup></b>
<b>P1</b>	<i>o</i> -xylene	1:4	/	0.68	4.45	0.33	0.99 (0.95)
<b>P1</b>	CB	1:4	/	0.66	4.74	0.34	1.06 (0.98)
<b>P1</b>	CB	1:4	/ (annealed @110 °C)	0.66	4.40	0.35	1.01 (0.94)
<b>P1</b>	CB	1:3	1% DIO	0.64	4.22	0.35	0.95 (0.92)
<b>P1</b>	CB	1:3	2% DIO	0.64	4.19	0.35	0.95 (0.92)
<b>P2</b>	<i>o</i> -xylene	1:4	/	0.84	6.59	0.39	2.15 (2.05)
<b>P2</b>	CB	1:4	/	0.83	6.73	0.37	2.04 (1.96)
<b>P2</b>	CB	1:4	/ (annealed @110 °C)	0.78	7.03	0.40	2.20 (2.15)
<b>P2</b>	CB	1:4	1% DIO (annealed @85 °C)	0.78	6.76	0.41	2.17 (2.15)
<b>P2</b>	CB	1:4	2% DIO (annealed @85 °C)	0.74	6.01	0.39	1.74 (1.65)

---

<b>P3</b>	CB	1:2	/	0.77	4.06	0.30	0.93 (0.88)
<b>P3</b>	CB	1:3	/	0.77	6.20	0.37	1.78 (1.66)
<b>P3</b>	CB	1:4	/	0.80	6.44	0.36	1.84 (1.82)
<b>P3</b>	CB	1:4	/	0.80	6.83	0.41	2.22 (2.06)

---

<sup>a</sup> Polymer:[70]PCBM. <sup>b</sup> Average efficiencies over at least 3 devices in brackets.

**EQE**

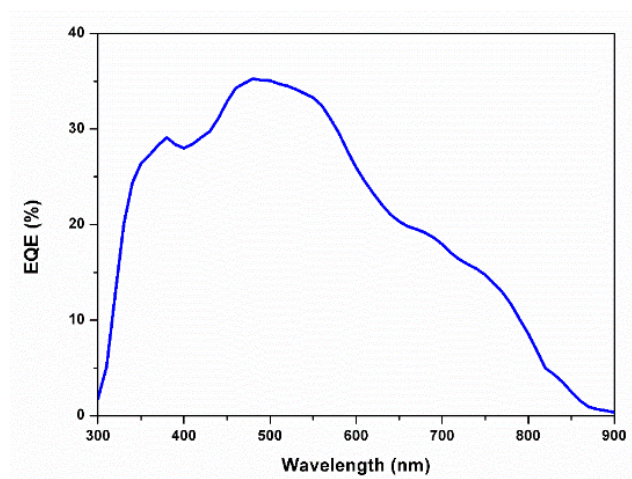


**Figure S12.** EQE spectrum for the best polymer solar cell prepared from **P2**.

**AFM**

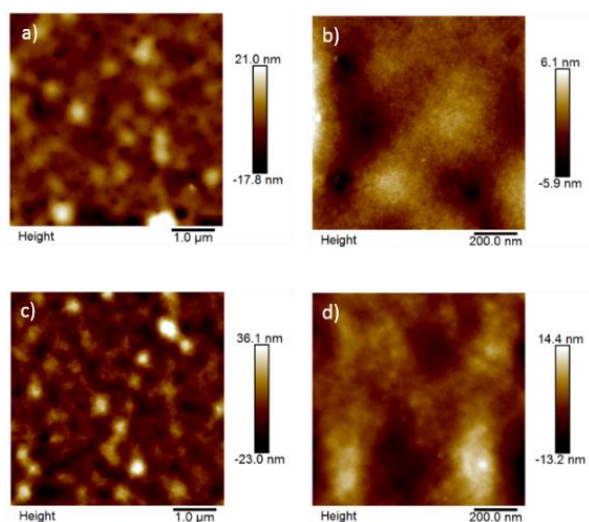


**Figure S13.** AFM images of the active layer blends composed of **P2** and [70]PCBM (1:4) processed from *o*-xylene (a,b) and *o*-xylene + 1% anisaldehyde (c,d).

**References**

- [1] Lai, L. F.; Love, J. A.; Sharenko, A.; Coughlin, J. E.; Gupta, V.; Tretiak, S.; Nguyen, T.-Q.; Wong, W.-Y.; Bazan, G. C. *J. Am. Chem. Soc.* **2014**, *136* (15), 5591.
- [2] Trasatti, S. *Pure Appl. Chem.* **1986**, *58* (7), 955.
- [3] Bard, J.; Faulkner, L. R. *Electrochemical Methods: Fundamentals and Applications*, 2nd Ed., **2001**, Wiley.
- [4] Stoll S.; Schweiger A. *J. Magn. Res.* **2006**, *178*, 42.
- [5] Neese, F. *WIREs Comput. Mol. Sci.* **2012**, *2*, 73.
- [6] Neese, F. *J. Chem. Phys.* **2001**, *115*, 11080.
- [7] Neese, F. *J. Chem. Phys.* **2005**, *122*, 034107.
- [8] Becke, A. D. *Phys. Rev. A* **1988**, *38*, 3098.
- [9] Schäfer, A.; Horn, H.; Ahlrichs, R. *J. Chem. Phys.* **1992**, *97* (4), 2571.
- [10] Lee, C.; Yang, W.; Parr, R. G. *Phys. Rev. B* **1988**, *37*, 785.
- [11] Barone, V. *Recent advances in density functional methods, part I.* **1997** Chong, D. P. (Ed.), World Scientific, Singapore.
- [12] He, B.; Pun, A. B.; Zherebetsky, D.; Liu, Y.; Liu, F.; Klivansky, L.; McGough, A. M.; Zhang, B. A.; Lo, K.; Russell, T. P.; Wang, L.; Liu, Y. *J. Am. Chem. Soc.* **2014**, *136* (42), 15093.
- [13] Ahmed, E.; Subramaniyan, S.; Kim, F. S.; Xin, H.; Jenekhe, S. A. *Macromolecules* **2011**, *44* (18), 7207.
- [14] Vanormelingen, W.; Kesters, J.; Verstappen, P.; Drijkoningen, J.; Kudrjasova, J.; Koudjina, S.; Liégeois, V.; Champagne, B.; Manca, J.; Lutsen, L.; Vanderzande, D.; Maes, W. *J. Mater. Chem. A* **2014**, *2*, 7535.
- [15] Evenson, S. J.; Rasmussen, S. C. *Org. Lett.* **2010**, *12* (18), 4054.
- [16] Niklas J.; Mardis, K. L.; Banks, B. P.; Grooms, G. M.; Sperlich, A.; Dyakonov, V.; Beaupré, S.; Leclerc, M.; Xu, T.; Yu, L.; Poluektov, O. G. *Phys. Chem. Chem. Phys.* **2013**, *15* (24), 9562.

---

# Chapter 6

## Summary and Outlook

---

### 6.1 Summary

Organic photovoltaics (OPV's) – based on organic semiconducting small molecules or low bandgap conjugated polymers for light absorption – have received a strong interest over the past two decades because of their appealing looks and fast and easy large scale fabrication using (roll-to-roll) printing techniques. Moreover, the opto-electronic properties of organic semiconductors are highly tunable, which enables precise optimization of the molecular properties. This has resulted in power conversion efficiencies nowadays surpassing 13% for state-of-the-art material combinations. However, most high-performance conjugated organic materials still require rather harsh processing conditions, i.e. the use of (heated) halogenated processing (co)solvents, to obtain high-efficiency devices, which is an important drawback as strict safety precautions need to be taken when converting this lab process to an industrial scale. These processing conditions are a direct consequence of the rather apolar conjugated materials employed to date. The photoactive materials are generally substituted with alkyl side chains to provide a good solubility to the conjugated backbone (to overcome the large stacking tendency) and allow processing from solution. However, substitution with (more) polar side chains allows processing from more environmentally benign solvents (e.g. alcohols) and thereby reduces the ecological footprint. Furthermore, light-harvesting materials decorated with more polar/polarizable substituents also

tend to possess higher dielectric constants ( $\epsilon_r$ ) and hence reduced bimolecular recombination.

At first instance, an overview on the high dielectric constant materials used in OPV over the last decade was made, in order to gain insight on the different strategies that have been used so far. Although research in this domain remained quite limited, several functionalities (e.g. (oligo)ethylene glycol, fluoro and cyano moieties) have been reported to increase the polarizability and dielectric properties. (Oligo)ethylene glycol (OEG) side chains were proven to be good candidates to replace regular hydrocarbon side chains as they facilitate fast reorientation of the dipole moment by their high (rotational) degree of freedom. The ease by which these rotations can occur directly translates to the dielectric constant. Furthermore, more environmentally friendly processing conditions were reported for glycolated polymers.

As such, we have implemented these findings by replacing the hydrocarbon side chains by (oligo)ethylene glycol substituents on a model push-pull polymer comprised of 4*H*-cyclopenta[2,1-*b*:3,4-*b'*]dithiophene (CPDT) as the electron-donating unit and 4*H*-thieno[3,4-*c*]pyrrole-4,6(5*H*)-dione (TPD) as the electron-deficient subunit. To allow systematic evaluation of the effect of the number of OEG substituents, these were introduced on either of the two building blocks. After careful optimization of a shorter and easier reaction sequence toward the CPDT monomer, four new PCPDTPD-type low bandgap copolymers were synthesized. The number of OEG substituents was gradually increased to systematically investigate the influence on the dielectric properties and solar cell parameters. Evaluation of the dielectric constants by impedance spectroscopy revealed a clear trend upon replacement of the side chains, with a more than doubled  $\epsilon_r$  (6.3) for the fully glycolated polymer with respect to the alkylated reference material. All polymers were then applied in bulk heterojunction OPV devices. Higher short-circuit currents were obtained for the OEG-substituted polymers, which could be due to reduced recombination losses as expected for high- $\epsilon_r$  materials. However, the simultaneous drop in open-circuit voltage (as a result of the higher HOMO energy levels) limits the final device efficiency. Nevertheless, an increased power conversion efficiency of 4.4% was achieved for this material class.

The same building blocks were then also combined in a hydrophilic polymer endowed with ionic functionalities in the side chains, resulting in a narrow bandgap conjugated polyelectrolyte. A similar synthetic sequence was used, but in this case a bromide-functionalized side chain was introduced on the CPDT unit, which was then converted into an ionic side chain using methylimidazole by a post-polymerization approach. Because of the hydrophilic nature of the conjugated polymer, a halogen-free processing solvent (methanol) could be used to spincoat the novel material as a cathode interlayer on top of the active layer blend. An overall increase of the OPV device parameters was achieved for this novel cathode interlayer in combination with a PBDTTPD:[70]PCBM photoactive blend. The power conversion efficiency increased with ~13% for the best-performing device, from 6.95% to 7.83%. In contrast to other reported conjugated polyelectrolytes, the interlayer seems to fully cover the active layer in a uniform way (according to AFM measurements).

Finally, further efforts were taken to improve the sustainability of the production process and the materials used in organic photovoltaics. A completely different conjugated polymer system was investigated as photoactive material, starting from the rather inexpensive and naturally available dye indigo. After extensive optimization of the synthetic protocol, indigo was converted into bay-annulated indigo (BAI) as the electron-deficient building block. This was then combined with electron-rich thiophene and 4*H*-dithieno[3,2-*b*:2',3'-*d*]pyrrole (DTP) units to produce three different low bandgap copolymers and these materials were applied as photoactive donor compounds in bulk heterojunction organic solar cells. MALDI-TOF mass spectrometry analysis was done to gain more insights into the structural composition of the low bandgap polymers, pointing out minor amounts of homocoupling in the different polymer batches. A solar cell efficiency of 2.41% was achieved using a halogen-free solvent (*o*-xylene), which is highly recommended to reduce the ecological footprint of OPV and is imperative for large scale production and commercialization.

## 6.2 Outlook

In this PhD thesis, it is demonstrated that more hydrophilic conjugated polymers can show benefits when applied in organic solar cells, enhancing in particular the current output of the devices. Moreover, an enhanced solubility in more environmentally friendly solvents is observed when increasing the hydrophilicity of organic semiconductors. In this work, we only addressed electron donor-type conjugated polymers, which were then combined with (apolar) [70]PCBM. This combination can lead to compatibility issues in the active layer blend, resulting in a non-optimal bulk heterojunction morphology. A photoactive layer encompassing two materials with similar polarities, surface energies and miscibilities would likely be more performant. More efforts also need to be taken to simultaneously enhance the dielectric properties of electron donor and acceptor materials. Most research on electron-accepting materials has focused on fullerene derivatives. However, non-fullerene acceptors have recently afforded similar and even better OPV efficiencies.<sup>[1]</sup> For the purpose of dielectric constant enhancement, non-fullerene acceptors are potentially viable candidates because of the ease to introduce polar/polarizable units on various locations of different systems (ITIC, perylene diimides, ...).<sup>[2]</sup> Eventually, when very high dielectric constant materials can be achieved, homojunction (*i.e.* single layer) devices could be realized and miscibility issues would be inherently resolved.

Hydrophilic organic semiconductors can also be applied as charge-selective interlayer materials. Interface engineering is of utmost importance to obtain perfectly balanced charge transport in OPV's and can boost the photovoltaic performance. However, research on narrow bandgap conjugated polyelectrolytes remains very limited and more efforts need to be taken to fundamentally understand the origin of the increased device performance to allow a more dedicated material design.

The improved hydrophilicity of the conjugated polymers reported in this thesis enables processing from more environmentally benign, non-halogenated solvents (e.g. alcohols). Despite the high importance of 'green' production for future OPV commercialization, this aspect has been undervalued so far. Some efforts were also taken to enhance the sustainability of the OPV material synthesis. Due to the low solubility of the unsubstituted bay-annulated indigo (BAI) building block,

upscaling of this process is unfortunately rather complicated. Functionalization of the BAI core with solubilizing side chains or using a functionalized 2-thiopheneacetyl chloride during the BAI synthesis could (partly) solve this. Additionally, this would also improve the solubility issues when synthesizing the corresponding polymers and could result in a better morphology of the active layer. On the other hand, different donor building blocks with enhanced solubility characteristics could also be used. Finally, further efforts are required toward a more 'green' synthesis of BAI-based organic semiconductors.<sup>[3]</sup>

### 6.3 References

- [1] Zhao, W. C.; Qian, D. P.; Zhang, S. Q.; Li, S. S.; Inganäs, O.; Gao, F.; Hou, J. H. *Adv. Mater.* **2016**, *28*, 4734.
- [2] Li, S.; Zhang, Z.; Shi, M.; Li, C.-Z.; Chen, H. *Phys. Chem. Chem. Phys.* **2017**, *19*, 3440.
- [3] Burke, D. J.; Lipomi, D. J. *Energy Environ. Sci.* **2013**, *6*, 2053.

## 6.4 Nederlandstalige samenvatting

Het onderzoek naar organische (polymere) zonnecellen ('*organic photovoltaics*' of OPV) heeft de laatste jaren een sterke groei doorgemaakt. Toch heeft OPV nog steeds te kampen met enkele specifieke problemen die het gebruik en de toepassing van de technologie limiteren. Het hoofddoel bij de productie van (organische) zonnecellen is natuurlijk het opdrijven van de efficiëntie, hetgeen verwezenlijkt kan worden door (subtiële) veranderingen aan de foto-actieve organische materialen. Hoewel deze actieve materialen uiteraard erg belangrijk zijn, wordt de efficiëntie bepaald door een samenspel van vele factoren. Het is hierbij van groot belang om een beter inzicht te verkrijgen in de relatie tussen de moleculaire structuur, de morfologie van de actieve laag en de finale efficiëntie van de zonnecel. Optimalisatie van de gehele devices is dus noodzakelijk, waarbij bijvoorbeeld ook de nodige aandacht besteed moet worden aan het creëren van ladingen en goede *interfaces* voor een efficiënt transport van deze ladingen. Een ander belangrijk aspect is de milieu-impact van het productieproces. Bij de verwerking van de actieve laag vanuit een oplossing (of 'inkt') zijn de gebruikte solventen van belang. Op dit moment worden voornamelijk hoogkokende gechloreerde solventen gebruikt om een ideale morfologie van de actieve laag te verkrijgen. Verder onderzoek is nodig om de oplosbaarheid van de materialen in minder milieubelastende solventen te verhogen. Dit kan bekomen worden door de hydrofiliciteit van de geconjugeerde structuren te verhogen, waardoor polaire solventen (bv. methanol) gebruikt kunnen worden om zo de ecologische voetafdruk van OPV verder te verkleinen. Een bijkomend voordeel van de polairdere structuren is dat ook de diëlektrische constante wordt verhoogd. Dit heeft als positief gevolg dat de relaxatie- en recombinatieprocessen verminderd worden. De verhoging van de diëlektrische constante van een foto-actief organisch materiaal geeft aanleiding tot een lagere bindingsenergie van de excitonen (zoals in anorganische materialen), waardoor de tegengestelde ladingen eenvoudiger kunnen scheiden en zich sneller kunnen verplaatsen doorheen het materiaal. Hierdoor zal er minder recombinatie optreden waardoor de zonnecel een hogere efficiëntie kan hebben.

In deze thesis werd in eerste instantie een overzicht gegeven van de verschillende materialen met een verhoogde diëlektrische constante die reeds gebruikt werden

in organische zonnecellen. Hierbij werd duidelijk dat een verhoging van de diëlektrische constante in een geconjugeerde structuur bekomen kan worden op verschillende manieren, maar voornamelijk door lokale structurele veranderingen, zoals het invoeren van polaire substituenten op de geconjugeerde *backbone* of op de alkyl-zijketens van de foto-actieve materialen. Deze laatste strategie wekte de meeste interesse, waarbij (oligo)ethyleenglycol-substituenten naar voor traden als interessante alternatieven voor de apolaire koolwaterstofketens die traditioneel gebruikt worden ter verhoging van de oplosbaarheid. Het voordeel van deze zijketens is hun snellere respons op een aangelegd elektrisch veld, waardoor de dipoolmomenten zich gemakkelijker kunnen heroriënteren. Daarnaast vertonen deze polymeren ook nog een verhoogde oplosbaarheid in meer milieuvriendelijke solventen.

Er werd ervoor gekozen om deze strategie toe te passen op een nieuw 'low bandgap' geconjugeerd polymeer bestaande uit 4*H*-cyclopenta[2,1-*b*:3,4-*b'*]dithiofeen (CPDT) als elektronenrijke en 4*H*-thiëno[3,4-*c*]pyrrool-4,6(5*H*)-dion (TPD) als elektronenarme component. Ten eerste werd de syntheseroute voor CPDT aangepast en vertaald naar een eenvoudiger en gemakkelijker opschaalbaar proces. Hiervoor werden verschillende bestaande procedures gecombineerd. Vier nieuwe polymeren werden vervolgens gesynthetiseerd, waarbij gradueel de apolaire alkyl-zijketens vervangen werden door (oligo)ethyleenglycol met het oog op een verhoogde diëlektrische constante. Dit werd vervolgens getest door middel van impedantiemetingen. Het referentiemateriaal, bestaande uit enkel alkyl-zijketens, had een diëlektrische constante van 3.1, hetgeen een normale waarde is voor een organische halfgeleider. Een verdubbeling (tot 6.3) werd vervolgens verkregen voor het polymeer volledig gesubstitueerd met (oligo)ethyleenglycol, een topresultaat vergeleken met andere waarden in de literatuur. De polymeren werden vervolgens ook getest in organische zonnecellen en een verhoging van de stroom werd waargenomen voor de materialen met een verhoogde diëlektrische constante. Verder werd ook vastgesteld dat een halogeen-vrij solvent (anisol) gelijkaardige resultaten gaf op het vlak van efficiëntie, wat zeer belangrijk is voor de commercialisering van OPV.

Vervolgens werd een ander polymeer gesynthetiseerd, eveneens bestaande uit CPDT en TPD. In dit geval werd er echter gekozen voor een ionische zijketen zodat

het resulterende materiaal gebruikt kon worden als interlaag in organische zonnecellen. Het PCPDTPD geconjugeerde polyelektroliet werd toegepast als kathode-interlaag ter vervanging van calcium (wat sterk onderhevig is aan oxidatie). De toepassing van een polyelektroliet heeft verder als positief effect dat het ladingstransport verbeterd wordt. Bovendien kan deze laag afgezet worden vanuit methanol (bovenop de foto-actieve laag). Een verhoging van de zonnecellefficiëntie met 13% werd waargenomen wanneer deze interlaag gecombineerd werd met PBDTTPD:[70]PCBM als actieve laag, met een maximale efficiëntie van 7.83% (tegenover 6.95% wanneer calcium gebruikt werd).

Tot slot werd er ook extra aandacht besteed aan het milieu-aspect van organische zonnecellen, zowel op het vlak van de materiaalsynthese als op het vlak van de verwerking van de actieve materialen. Drie nieuwe polymeren werden ontwikkeld met de doelstelling om de duurzaamheid van organische zonnecellen te verhogen. Hiervoor werd er gekozen om de syntheseroute te starten uitgaande van een natuurlijk voorkomende kleurstof en de keuze viel op indigo. De syntheseroute werd grondig geanalyseerd en geoptimaliseerd. De drie nieuwe polymeren werden vervolgens ook uitgebreid gekarakteriseerd, beginnende met MALDI-TOF, hetgeen een beter inzicht gaf in de werkelijke structuur van de polymeren. Kleine hoeveelheden homo-gekoppelde sequenties werden aangetroffen in elk polymeer. De bekomen zonnecelparameters bleken eerder matig te zijn, waarbij vooral de morfologie van de actieve laag en de bekomen energieniveaus niet optimaal bleken, wat de uiteindelijke prestaties van de zonnecellen limiteerde. De beste resultaten werden echter wel verkregen uitgaande van een halogeen-vrij solvent (*o*-xyleen), wat belangrijk is voor de opschaling en productie van de zonnecellen.

## List of Publications

Lou, X.; Van Dongen, J. L. J.; Braeken, Y.; Brebels, J.; Van Pruisen, G. W. P.; Li, W.; Wienk, M. W.; Janssen, R. A. J. Superheated High-Temperature Size-Exclusion Chromatography with Chloroform as the Mobile Phase for  $\pi$ -Conjugated Polymers. *Polym. Chem.* **2014**, *5*, 558–561.

Van Pruisen, G. W. P.; Brebels, J.; Hendriks, K. H.; Wienk, M. W.; Janssen, R. A. J. Effects of Cross-Conjugation on the Optical Absorption and Frontier Orbital Levels of Donor–Acceptor Polymers. *Macromolecules* **2015**, *48*, 2435–2443.

Maes, V.; Pirotte, G.; Brebels, J.; Verstappen, P.; Lutsen, L.; Vanderzande, D.; Maes, W. Synthesis of N,N'-dialkyl-6,6'-dibromoisindigo Derivatives by Continuous Flow. *J. Flow Chem.* **2015**, *5*, 201–209.

Kudrasjova, J.; Kesters, J.; Verstappen, P.; Brebels, J.; Vangerven, T.; Cardinaletti, I.; Drijkoningen, J.; Penxten, H.; Manca, J.; Lutsen, L.; Vanderzande, D.; Maes, W. A Direct Arylation Approach towards Efficient Small Molecule Organic Solar Cells. *J. Mater. Chem. A* **2016**, *4*, 791–795.

Brebels, J.; Klider, K. C. C. W. S.; Kelchtermans, M.; Verstappen, P.; Van Landeghem, M.; Van Doorslaer, S.; Goovaerts, E.; Garcia, J. R.; Manca, J.; Lutsen, L.; Vanderzande, D.; Maes, W. Low Bandgap Polymers Based on Bay-Annulated Indigo for Organic Photovoltaics: Enhanced Sustainability in Material Design and Solar Cell Fabrication. *Org. Electron.* **2017**, *50*, 264–272.

Brebels, J.; Manca, J.; Lutsen, L.; Vanderzande, D.; Maes, W. High Dielectric Constant Conjugated Materials for Organic Photovoltaics. *J. Mater. Chem. A* **2017**, *under revision*.

Brebels, J.; Douvogianni, E.; Devisscher, D.; Eachambadi, R. T.; Manca, J.; Lutsen, L.; Vanderzande, D.; Hummelen, J. C.; Maes, W. CPDTPD-Based Low Bandgap Polymers Bearing Oligo(Ethylene Glycol) Side Chains – An Effective

## List of Publications

---

Strategy to Enhance the Dielectric Constant of Organic Semiconductors.  
*Manuscript in progress.*

Brebels, J.; Kesters, J.; Defour, M.; Pirotte, G.; Van Mele, B.; Manca, J.; Lutsen, L.; Vanderzande, D.; Maes, W. A CPDTPD-based Narrow Bandgap Conjugated Polyelectrolyte for Organic Solar Cells. *Manuscript in progress.*

## Dankwoord

Ten eerste gaat mijn dank uit naar mijn promotor, Prof. Dr. Wouter Maes, voor het mogelijk maken van dit project. Je hebt me de vrijheid gegeven om zelf mijn eigen ding te doen in dit project. In het begin liep het onderzoek niet altijd als gepland, maar op het einde is alles toch op zijn pootjes terecht gekomen. Aan het schrijven kreeg je me misschien niet zo snel, maar ook dit is dik in orde gekomen en ik ben ook trots op de artikels die we samen hebben mogen uitbrengen. Je hebt me dan ook geholpen in de ontwikkeling van mijn professionele vaardigheden door je kennis en 'kritische pen' tijdens het verbeteren van mijn artikels en proefschrift.

Verder wil ik mijn 2 co-promotoren, Prof. Dr. Dirk Vanderzande en Prof. Dr. Jean Manca. We kenden niet zo veel succes met het 'Dirk-molecule' (zoals ik het noemde), maar toch wil ik jullie beiden bedanken voor de inbreng en het kritisch nalezen van de publicaties.

Furthermore, I would like to thank all the members of the jury for taking the time to evaluate my work and the IWT for financial support.

Het NMR-team, met in het bijzonder Gunther en Koen, mag ik zeker niet vergeten voor de vele NMR's die ze altijd voor me opnamen met de nodige professionele kunde. Verder ook een dankuwel aan Huguette voor al de CV-metingen die je voor me hebt uitgevoerd.

Verder wil ik toch ook even de naaste collega's en bureaugenoten - Yasmine, Sanne en Mathias - bedanken. De interessante (al dan niet wetenschappelijke) discussies zorgden voor de nodige afleiding gedurende mijn doctoraat. Zonder jullie had mijn doctoraat er toch anders uit gezien. In het bijzonder wil ik natuurlijk Mathias ook nog bedanken voor de leuke momenten en autoritten. Je hebt me toch wel wat geld bespaard doordat ik niet elke dag zelf met de auto de verplaatsing naar Diepenbeek heb moeten maken ☺. We hebben er een mooie tijd van kunnen maken, vind ik, al zal ik je flatulentie minder hard missen. Amuseert u daar nog een jaar en dan kunnen we misschien terug collega's worden!

## Dankwoord

---

Natuurlijk wil ik ook al de andere collega's van DSOS bedanken voor de fijne tijden in en buiten het labo gedurende de volle 4 jaar! Verder mag ik al de andere collega's binnen OBPC ook niet vergeten, bedankt allemaal!

En dan nog onze favoriete barvrouw: Marie-Jeanne. Ze zorgde er altijd voor dat onze werkweek goed afgesloten werd (met de nodige hapjes), zodat we ons weekend goed konden beginnen!

Als laatste wil ik zeker nog een woordje van dank plaatsen aan mijn ouders die mij ook gedurende het hele project gesteund hebben en het soms moesten ontgelden als het een dagje minder goed liep. Ze hebben me dikwijls gevraagd, hoe loopt je project, en lukt alles,... al was het niet altijd gemakkelijk om precies en verstaanbaar uit te leggen waar ik nu precies mee bezig was. Bedankt voor het luisterende oor en de steun!

**BEDANKT ALLEMAAL!**

